Search for Higgs bosons in the final state with b-quarks in the semi-leptonic channel with the CMS 2017 data

Dissertation

zur Erlangung des Doktorgrades

an der Fakultät für Mathematik, Informatik und Naturwissenschaften

Fachbereich Physik

der Universität Hamburg

vorgelegt von

Antonio Vagnerini

aus Bologna, Italy

Hamburg

2020

Eidesstattliche Erklärung

Hiermit versichere ich an Eides statt, die vorliegende Dissertationsschrift selbst verfasst und keine anderen als die angegebenen Hilfsmittel und Quellen benutzt zu haben. Die eingereichte schriftliche Fassung entspricht der auf dem elektronischen Speichermedium. Die Dissertation wurde in der vorgelegten oder einer ähnlichen Form nicht schon einmal in einem früheren Promotionsverfahren angenommen oder als ungenügend beurteilt.

Hamburg, den 5. Juni 2020.

Antonio Vagnerini

Gutachter der Dissertation:	Dr. Roberval Walsh Prof. Dr. Elisabetta Gallo
Zusammensetzung der Prüfungskommission:	Dr. Roberval Walsh Prof. Dr. Elisabetta Gallo Prof. Dr. Dieter Horns Dr. Sarah Heim Prof. Dr. Sven-Olaf Moch
Vorsitzender des Prüfungsausschusses:	Prof. Dr. Dieter Horns
Datum der Disputation:	28 Mai 2020
Vorsitzender Fach-Promotionsausschusses PHYSIK:	Prof. Dr. Günter Sigl
Leiter des Fachbereichs PHYSIK:	Prof. Dr. Wolfgang Hansen
Dekan des MIN-Fakultät:	Prof. Dr. Heinrich Graener

"Les hommes tiennent le monde.
Les mères tiennent l'éternel qui
tient le monde et les hommes."

Christian Bobin

To my beloved mother

Abstract

The existence of several neutral Higgs states is predicted in many models comprising an enlargement of the Standard Model (SM) scalar sector, notably the general Two-Higgs-Doublet Model (2HDM) and the Minimal Supersymmetric Extension of the Standard Model (MSSM). Many of these scenarios predict an enhancement of the coupling of the neutral Higgs bosons to bottom quarks. A search for neutral Higgs bosons decaying into a b-quark pair in the semi-leptonic channel and produced in association with at least an additional bottom quark at the LHC is presented. The corresponding data sample was collected at CMS during proton-proton collisions in 2017 at a centre-of-mass energy of $\sqrt{s} = 13$ TeV corresponding to an integrated luminosity of 36.5 fb^{-1}. In the final state, a muon must lie within the cone of any of the two most energetic b-jets in the event. The latter are initiated from the partons stemming from the Higgs boson decay. The soft muon requirement drives down considerably the trigger rates, allowing to probe Higgs bosons with masses as low as 125 GeV. The observed di-jet invariant mass distribution is compatible with the background-only prediction of the Standard Model. Therefore, stringent exclusion limits are extracted on the production cross-section times branching fraction of the signal process for Higgs boson masses ranging up to 700 GeV. The exclusion limits are further translated into the parameter space of several MSSM and 2HDM benchmark scenarios.

Zusammenfassung

Die Existenz mehrerer neutraler Higgsbosonen wird in vielen Modellen vorhergesagt, die eine Erweiterung des skalaren Sektors im Standardmodell beinhalten. Dies sind insbesondere das allgemeine Zwei-Higgs-Dublett Modell (2HDM) sowie die minimale supersymmetrische Erweiterung des Standardmodells (MSSM). Zahlreiche Szenarien sagen eine Verstärkung der Kopplung der neutralen Higgsbosonen an Bottomquarks vorher. In dieser Arbeit wird eine Suche nach neutralen Higgsbosonen präsentiert, die in Assoziation mit mindestens einem weiteren Bottomquark produziert werden und in ein Bottomquarkpaar zerfallen. Dabei soll mindestens ein b-Hadron semileptonisch im Myon-Kanal zerfallen. Der Datensatz wurde mit dem CMS Detektor am LHC im Jahr 2017 in Proton-Proton-Kollisionen mit einer Schwerpunktsenergie von $\sqrt{s} = 13$ TeV aufgenommen und entspricht einer integrierten Luminosität von $36.5 fb^{-1}$. Im Endzustand muss ein Myon innerhalb eines der beiden höchstenergetischen Jets im Ereignis liegen, die überwiegend aus der Fragmentation der Tochterpartonen des Higgsbosons stammen. Die Forderung dieses zusätzlichen Myons reduziert die Triggerraten erheblich, wodurch relativ niedrige Higgsbosonmassen bis herab zu 125 GeV getestet werden können. Die gemessene Verteilung der invarianten Masse der beiden Jets stimmt mit der Vorhersage des Standardmodelluntergrunds überein. Daher werden strenge Grenzen für das Produkt aus Produktionswirkungsquerschnitt und Zerfallsrate für Higgsbosonmassen bis zu 700 GeV extrahiert. Diese Grenzen werden im Parameterraum verschiedener MSSM und 2HDM Szenarien interpretiert.

Contents

Introduction

> ”La filosofia è scritta in questo grandissimo libro che continuamente ci sta aperto innanzi a gli occhi (io dico l'universo) [...]. Egli è scritto in lingua matematica, e i caratteri son triangoli, cerchi, ed altre figure geometriche, [...]; senza questi è un aggirarsi vanamente per un oscuro laberinto.”
>
> Galileo Galilei

In the early XVII century, Galileo Galilei was expressing in the *The Assayer* [1] his profound astonishment at the intrinsically mathematical character of the Book of Nature. In contrast with the immutable Aristotelian views of natural philosophy, the founding father of the scientific method established the centrality of the experiment for hypothesis testing. This mutation of paradigm marked the beginning of the scientific era. Ever since, generations of physicists have endeavoured to interpret and model natural phenomena in the search of an experimentally supported theory of everything: from Isaac Newton's *Principia Mathematica* [2] to James Clerk Maxwell's *Treatise on electricity and magnetism* [3]. The observation of non-classical physical phenomena, such as black body radiation and the photoelectric effect, paved the way to the development of a quantum theory, later complemented with special relativity. In the XX century, decades of experimental effort in high-energy physics culminated in the formulation of the Standard Model (SM) of particle physics [4–7]. This phenomenological model summarises our current understanding of the building blocks of matter and of the fundamental non-gravitational interactions governing our universe. It encompasses the electroweak and the strong force[1] in a single

[1]A review of the electroweak and the strong sector of the SM are presented in [8] and [9], respectively.

theoretical framework, described in terms of a quantum gauge field theory. Numerous elevated precision experiments have been designed to test it to high accuracy exploiting particle collider technology [10], thereby establishing its validity up to the TeV scale. In particular, the properties of the electroweak bosons such as the mass, total and partial decay widths [11] and coupling to fermions, as well the existence of the top quark [12] were found to be fully consistent with the SM. Furthermore, the discovery of a scalar particle with a mass at 125 GeV compatible with the Higgs boson of the Standard Model undeniably marked one of the greatest triumphs of the model and experimentation. Its properties are consistent with the electroweak symmetry breaking mechanism (EWSB) responsible for the masses of all the particles of the Standard Model, except neutrinos.

Despite its desirable phenomenological features, such as its renormalisability and UV-completeness [13], the Standard Model cannot represent the ultimate theory of particle physics. There are both unsolved theoretical problems as well as experimental evidence pointing to the existence of physics Beyond the SM (BSM). Notable examples of such observations are the discovery of neutrino oscillations and the cosmological observation of non-baryonic cold dark matter. One of the main theoretical shortcomings of the SM is the inability to incorporate the gravitational interaction into a coherent, self-consistent framework, since gravity is not perturbatively renormalisable unlike other SM fields. Thus, it is strongly conjectured that the validity of the Standard Model should cease at some energy scale, or *cut-off*, where quantum gravitational effects become significant, i.e. the Planck scale at 10^{19} GeV. Furthermore, the discovery of neutrino masses at the sub-eV level may indicate the existence of new physics already at a mass scale of 10^{9-15} GeV [14]. The large scale difference between the mass scale associated to new physics and the electroweak scale, denoted as the *gauge hierarchy problem*, is a notorious shortcoming of the SM which has important implications on the running masses of the scalar particles. The energy cut-off scale introduces unnaturally large, quadratically divergent loop corrections to the Higgs boson mass. Furthermore, the large mass hierarchy between fermions, the origin of the number of mass generations, as well as the quantisation of fermionic charge in units 1/3 of the elementary charge, may indicate that the SM is the low-energy limit of a more fundamental gauge theory.

Several Beyond the Standard Model theories comprise an enlargement of the SM scalar sector. The most basic addition is the inclusion of another electroweak Higgs doublet in a class of models collectively referred to as the Two-Higgs-Doublet Models (2HDM) [15]. The prediction of an extended Higgs sector is analogous to other non-minimal sectors present already in the SM, such as the flavour structure of the CKM matrix. In 2HDM models, after electroweak symmetry breaking there are five physical Higgs bosons, namely the neutral Higgs triplet $\Phi = \{h, H, A\}$, of which the first two states are CP-even while the A boson is a pseudoscalar, and two charged Higgs bosons $H^{\pm}$. The resulting richer phenomenology can provide additional sources of CP violation, needed to explain the observed matter-antimatter asymmetry of the universe. Moreover, the coupling structure of the Higgs doublets to fermions, which is constrained by discrete symmetries to enforce the absence of flavour–changing–neutral–currents at tree level, may shed some light on the observed fermion mass hierarchy. The inert Higgs model, which is also based on discrete symmetries of the Yukawa sector has been introduced to provide an explanation to non-vanishing neutrino masses [16] and to account for the number of fermion families. In the Minimal Supersymmetric extension of the SM (MSSM), a space-time symmetry between fermionic and bosonic degrees of freedom is introduced to tackle the hierarchy problem. This is achieved at the cost of doubling the particle content of the SM. Within this model, the lightest-supersymmetric particle (LSP) could prove a suitable dark matter candidate. Minimal gauge coupling unification can be achieved at a mass scale of 10^{16} GeV, when the MSSM is regarded as effective theory of some Grand Unified Model. These searches for an extended Higgs sector have to be conducted with a particle collider capable of operating at a high center-of-mass energy and delivering large amounts of integrated luminosity.

These requirements are met by the Large Hadron Collider (LHC) situated near Geneva, the most powerful circular proton-proton collider ever constructed. The high center-of-mass-energy of 13 TeV attained in correspondence of the interaction point is crucial to perform searches for the Higgs production modes of additional undiscovered resonances, probing a wide mass range from the GeV to the TeV scale. The Compact Muon Solenoid (CMS), one of the two multi-purpose detector installed at LHC, has been designed to identify the decay products of a Higgs-like particle with high accuracy. The detector achieves excellent vertexing, tracking and calorimeter resolution, which are essential ingredients in b-tagging and muon reconstruction. The present work focuses on a search for neutral Higgs boson produced in association with b-quarks and decaying to a b-quark pair with a muon within-a-jet in the final state.

The data sample used in this analysis was collected in 2017 data-taking during pp collisions at a centre-of-mass energy of $\sqrt{s} = 13$ TeV corresponding to an integrated luminosity of $36.5fb^{-1}$. In the Standard Model and in several BSM scenarios, the decay channel into b-quarks represents the prevailing decay mode. In the MSSM and in the 2HDM Type-II and flipped model, the coupling of the Higgs bosons to b-quarks is greatly enhanced, motivating the choice for this final state. However, in this hadronic environment, the huge QCD multi-jet production prevents an inclusive search for additional Higgs bosons with b-quarks in the final state. The $b\bar{b}$ associated production has been chosen since the signal process is accompanied by a lower fraction of background events than the main Higgs production mechanism at LHC, namely the gluon-gluon fusion process. The signature of the event is the presence of at least three highly energetic b-jets, of which the two most energetic ones are initiated by the Higgs boson daughter candidates. The third leading jet in transverse momentum is regarded as a spectator jet in the Higgs production mechanism, and it must also be initiated by a b-quark. The main observable of the analysis is the invariant mass of the two most energetic jets in the event, which is used to extract the total signal production rate in terms of the cross-section times the branching ratio of the process. In the final state, a muon stemming from the b-hadron decay must lie in the hadronisation cone of any of the two most energetic jets in the events. A dedicated semi-leptonic trigger permits to impose looser kinematic cuts on the two most energetic jets. This type of selection allows probing a Higgs boson mass ranging from 125 GeV to 700 GeV. Thus, the sensitivity reach of this analysis is sensibly extended with respect to the former analogous search in the fully-hadronic channel performed with 2016 data collected by CMS [17]. The resulting exclusion limits on the signal cross-section times branching ratio are extracted and translated into the parameter space of several MSSM and 2HDM benchmark scenarios to provide crucial information about these models.

This work is structured as follows. In the first chapter, a brief review of the particle content and interactions present in the SM precedes a discussion of the MSSM and 2HDM models, with a particular emphasis on the benchmark scenarios of interest. In the subsequent chapter, a concise overview of the LHC and of the CMS detector used to collect the data for this work is presented. In the third chapter, the main techniques behind the identification and reconstruction of muons and b-tagging of jets are discussed. The next chapter is devoted to the analysis strategy and methods, from the design of the dedicated semi-leptonic trigger to the statistical inference on the observed data. In the fifth chapter, the model-independent results and their interpretation within the most relevant models with an enlarged Higgs sector are illustrated. Finally, the conclusive chapter highlights the main results of this work, providing an outlook on the future prospects of this search.

CHAPTER 1

Theoretical framework

The Standard Model (SM) of particle physics provides an extremely accurate theoretical description of all known processes in high-energy physics. In spite of its spectacular success, supported by the numerous high-precision experiments, probing its scope of validity up to the TeV energy-scale, it is strongly conjectured that the SM cannot represent the ultimate, all-encompassing scientific theory. A series of unexplained theoretical queries as well as experimental observations point to the plausible existence of beyond Standard Model (BSM) physics. In this chapter, a description of the founding principles of the SM is followed by an overview of the BSM models. A particular emphasis is dedicated to a subset of such models containing an extended Higgs sector, which are of particular interest for this thesis work.

1.1 The Standard Model of particle physics

1.1.1 Quantum Field theory

Formulated in the late sixties, the Standard Model summarises our current knowledge of all known elementary particles and fundamental non-gravitational interactions. It incorporates the physical laws governing natural phenomena at microscopic level, namely quantum mechanics and special relativity in a single theoretical framework. Mathematically, the SM is a particular instance of a relativistic *Quantum Field Theory* (QFT). The underlying principle is the quantisation of the particle content, which comprises both matter constituents and force carriers as physical observables. Within this framework, all elementary particles are regarded as excitations of the corresponding quantum fields. Two classes of particles can be distinguished on the basis of their *spin*, a purely relativistic property, defining the intrinsic angular momentum of a particle (not arising from orbital motion): fermions carrying half-integer spin, such as the electron, which account for matter quantum fields, and bosons with integer spin representing force carriers, e.g.

the photon, the mediator of electromagnetism. Anti-particles are identical to their counterparts in ordinary matter, albeit oppositely charged, e.g. the positron is a positively charged analog of the electron. The spin-statistics theorem [18–20] of QFT dictates that the overall wavefunction of an ensemble of identical fermions (bosons) is totally antisymmetric (symmetric) under the exchange of any pair of such particles. As a corollary, the Pauli exclusion principle states that any pair of identical fermions cannot occupy the same quantum state. This leads to extremely different phenomenological features for bosons and fermions. The Fermi-Dirac statistics [18, 19] underpins the huge variety of atomic orbitals, while the Bose-Einstein condensation [20] is the underlying principle of cohesive streaming in laser beams.
In general, the equations of motions of any physical system can be derived by imposing the *principle of least action*. This variational principle prescribes the minimisation of the action S, defined as the following time integral:

$$S = \int \mathscr{L}(\psi(x), \partial_\mu \psi(x))\, \mathrm{d}t, \tag{1.1}$$

where the Lagrangian density $\mathscr{L}$ is a real-valued scalar, with dimension of the energy density to the fourth power. Its total space integral corresponds to the total kinetic energy of a system subtracted by the potential energy, i.e. $L = T - V$. In a quantum field theory, the physical system under scrutiny is generally an ensemble of interacting particles, and the Lagrangian density is a function solely of the particle fields ψ, and their first derivatives $\partial_\mu \psi$ with respect to the space time coordinates x.

Symmetries of the Lagrangian

The concept of symmetry is a fundamental tool to investigate and predict the behaviour of any physical system. In a field theory, symmetry translates into the invariance of the Lagrangian density under a set of transformations that preserves some observable quantities. Two different classes of symmetries can be distinguished, local or global in one dimension, discrete or continuous in the other. An important ingredient that relates the symmetries of the Lagrangian to physical observables is Noether's theorem. The latter prescribes that each continuous global symmetry of the Lagrangian is associated with a corresponding conserved quantity. In quantum field theories, elementary particles satisfy two main types of symmetries: *space-time* symmetries, acting directly on the coordinates x, and *internal* ones corresponding to the transformation of a quantum field ψ.

In a relativistic theory, Lorentz invariance ensures that the global, space-time symmetries predicted by special relativity are satisfied. The invariance of the Lagrangian under time, spatial translation and rotations codifies the conservation of energy, linear and angular momentum, respectively, of any system of particles. Noether's theorem permits also to classify elementary particles on the basis of their quantum numbers[1], which arise from the conservation laws of some internal symmetry, such as the electric charge.

The local gauge principle

Symmetries can also be used to construct a theory of interacting particles via the gauge principle. In a gauge theory, a global symmetry is promoted to a local symmetry of the Lagrangian density. The resulting additional interaction terms that have to be introduced contain the gauge fields. Such field terms are suitably chosen such that the action remains unchanged under the local gauge trasformations $U(x)$ of the fermionic field, viz:

$$S = \int \mathscr{L}(U(x)\psi)\,\mathrm{d}t \stackrel{!}{=} \int \mathscr{L}(\psi)\,\mathrm{d}t. \tag{1.2}$$

After quantisation, the gauge fields give rise to the gauge bosons, mediating the corresponding interaction. As an illustration of local gauge invariance, one may consider as a starting point the Lagrangian density of a non-interacting Dirac fermionic field $\psi = \psi(x)$ with mass m and charge q:

$$\mathscr{L}_f = i\bar{\psi}\gamma^\mu\partial_\mu\psi - m\bar{\psi}\psi, \tag{1.3}$$

where $\bar{\psi} \equiv \psi\gamma^0$ denotes the adjoint spinor and γ^μ stands for the Dirac matrices. This *free* Lagrangian consists of only two terms, a kinematic and a mass term:

$$\psi \to e^{iq\theta}\psi,\ \bar{\psi} \to e^{-iq\theta}\bar{\psi} \quad \textit{with} \quad \theta = \theta(x), \tag{1.4}$$

where $\theta(x)$ is the scalar phase of the fermionic field. The Lagrangian remains unchanged only under a global phase shift, i.e. provided that θ is constant[2]. However, it is manifestly not invariant under a local $U(1)$ gauge unitary transformation.

1.1.2 Electromagnetic interaction

In order to obtain an interaction theory for electrically charged, massive fermions, a gauge field vector $A^\mu = A^\mu(x)$ and the covariant derivative D_μ are introduced simultaneously:

$$A_\mu \to A_\mu + \partial_\mu\theta, \tag{1.5}$$

$$D_\mu = \partial_\mu - iqA_\mu, \tag{1.6}$$

such that the local gauge transformation $D_\mu\psi \to e^{iq\theta}D_\mu\psi$ is now satisfied. Henceforth, the Lagrangian can be cast into the following form:

$$\mathscr{L}_{QED} = \mathscr{L}_f + \mathscr{L}_{int} + \mathscr{L}_{gauge} = \mathscr{L}_f + q\bar{\psi}\gamma^\mu\psi A_\mu - \frac{1}{4}F_{\mu\nu}F^{\mu\nu}, \tag{1.7}$$

[1]Mathematically, a quantum number is defined as the time-like component of the corresponding conserved Noether current J^0, or charge.

[2]This global $U(1)$ invariance encodes the conservation of the electric charge.

where the second terms accounts for the interaction term; the third is the free-field term with field strength tensor $F_{\mu\nu} = \partial_\mu A_\nu - \partial_\nu A_\mu$. Thus, the Lagrangian of Quantum Electrodynamics (QED) is invariant under the local $U(1)$ gauge transformations, provided that the gauge boson A_μ is massless, as it is experimentally verified in case of the photon. The resulting electromagnetic current density $J_\mu = q(\bar{\psi}\gamma^\mu\psi)$ represents a three-point vertex describing the exchange of a photon between a fermion-anti-fermion pair.
Quantum Electrodynamics successfully describes all aspects of the electromagnetic interaction, starting from its strength as a function of the energy scale, quantified by the fine structure constant α_{EM}. A high precision test of QED is the prediction of the gyromagnetic *g-factor* of the electron. This quantity is defined as the ratio of the magnetic moment of a particle over its angular momentum. In the non-interacting Dirac picture, it is predicted to be exactly two for a spinning electron. However, inclusion of higher order corrections terms in QED gives:

$$g_\mathrm{e} = 2(1 + \frac{\alpha_{EM}}{2\pi} + \cdots). \tag{1.8}$$

For the electron, the g-factor was measured to be [21]:

$$g_\mathrm{e} = 2.00231930436182(52), \tag{1.9}$$

which is consistent with theory over ten significant figures, rendering it the most accurate prediction in the history of physics. This measurement allows probing the logarithmic dependence of α_{EM} on the interaction energy. The fine-structure constant tends to the value of $\frac{e^2}{4\pi} \approx \frac{1}{137}$ in the low energy regime. This has several important implications in optics and chemistry, since the value of α_{EM} fixes the Bohr radius, which in turn determines the size of the hydrogen atom.

1.1.3 Strong interaction

In the context of atomic nuclei, the strong nuclear force is observed "macroscopically" at a distance of O(fm) in the binding of nucleons, namely protons and neutrons. The elementary constituents defining the quantum numbers of protons and neutrons are up- (u-) and down (d-) valence quarks, elementary fermions carrying an electric charge of $+\frac{2}{3}e$ and -$\frac{1}{3}e$ respectively[3]. The quark model of the strong interactions was developed to account for the *eightfold way* [22]. The latter is the observed geometric arrangement of the mesons and baryons, bound states of two and three quarks respectively, into different groups according to their quantum numbers.
At distances below the nucleon radius around 0.8 fm, these bound states are held together via the exchange of force mediators called gluons. Thus, at fundamental level, the strong

[3] Besides valence quarks, nucleons contain also quark-antiquark pairs, referred to as "sea" quarks, produced in strong interactions.

nuclear force is interpreted as the interaction between particles carrying a *colour charge*, namely quarks and gluons. The colour quantum number C was originally introduced to preserve the total anti-symmetry of the wavefunction of the Δ^{++} baryon [23], a bound state of three u quarks with a highly symmetric configuration. Within the QFT framework, the strong interaction is encoded in the $SU(3)_c$ gauge symmetry group of Quantum Chromodynamics (QCD). The QCD Lagrangian can be defined in analogy to QED as :

$$\mathscr{L}_{QCD} = \mathscr{L}_f + g_s \bar{\psi} \gamma^\mu \lambda_a \psi G^a_\mu - \frac{1}{4} G^a_{\mu\nu} G^{\mu\nu}_a. \tag{1.10}$$

where the Einstein summation convention is assumed over the generator index $a = 1...8$, while λ_a denotes the eight generators of the SU(3) symmetry[4] also referred to as Gell-Mann matrices. The three-component vector of spinors ψ has an implicit colour index, $i = r$ (red), b, (blue), g (green).

Each of the eight gauge or *gluon* fields G^a_μ has an associated conserved colour current $J^a_\mu = g_s \bar{\psi} \gamma_\mu \lambda^a \psi$. Analogously to the photon, these force carriers are also massless. However, contrary to QED, the defining feature of QCD is that it is a non-Abelian gauge theory. The non-commutativity of the gluon fields can be evinced from the additional term in the field strength tensor:

$$G^{\mu\nu}_a = \partial^\mu G^\nu_a - \partial^\nu G^\mu_a - g_s f^{bc}_a G^\mu_b G^\nu_c, \tag{1.11}$$

where the f^{abc} stucture constants of the $SU(3)$ group are responsible for the self-interactions of the gluon fields. The strong fine-structure constant $\alpha_s = 4\pi g_s^2$ varies with the momentum transfer Q as follows:

$$\alpha_s(Q^2) = \frac{12\pi}{(33 - 2N_f) \ln\left(\frac{Q^2}{\Lambda^2_{\mathrm{QCD}}}\right)}, \tag{1.12}$$

where Λ_{QCD} is the characteristic energy scale around 200 MeV, at which QCD processes enter the non-perturbative regime and N_f denotes the number of "active " quark flavours, i.e. for which $m_q^2 \ll Q^2$. This logarithmic dependence for α_S is reversed with respect to QED. In the large Q^2 limit, coloured particles can be regarded as free with respect to the strong interaction, a phenomenon referred to as *asymptotic freedom.* Furthermore, at distances of the order of few fm, the inter-quark potential increases approximately linearly with distance due to the gluon-self-interactions. Consequently, it is more energetically favourable for quarks to be confined into colour-neutral states, referred to as hadrons.

[4]In a SU(N) gauge group, consisting of $n \times n$ unitary matrices, the number of symmetry generators is given by $N^2 - 1$, one less degree of freedom with respect to the U(N) group, owing to the additional constraint on the unit determinant.

1.1.4 Weak interaction and EW unification

The first model of the weak interaction was proposed by E. Fermi [24] to describe the β decay of the neutron into a proton, via the emission of an electron and of an anti-neutrino, an electrically neutral particle, which is found to be extremely light. At low interaction energies, such radioactive decays are well-modelled by a four-fermion point interaction. However, above a certain energy scale, referred to as the electroweak scale ~ 100 GeV , the coupling strength of the weak force becomes comparable to that of electromagnetism, hence additional degrees of freedom, carried by massive mediators have to be introduced[5]. The force carriers are the charged $W^{\pm}$ bosons and the neutral Z boson, responsible for the charged and neutral currents respectively. Contrary to the electomagnetic current, the weak charged current violates parity, as observed in the fifties in the experiments conducted by Wu [25] on the β decays of cobalt ^{60}Co. This phenomenological feature is incorporated by introducing a vector-axial (V-A) form of the charged weak current:

$$J^{(\mathrm{CC})\mu} = \bar{\psi}\gamma^{\mu}\frac{1}{2}\left(1-\gamma^5\right)\psi, \tag{1.13}$$

where $P_{L,R} \equiv 1 \mp \gamma^5$ are the left- and right-handed projection operators. Equation 1.13 shows that the weak interaction couples exclusively to left-handed fermions (or right-handed anti-fermions). The weak interaction does not couple directly to the quark mass eigenstate, but rather to an admixture of the weak states. On the other hand, neutral weak currents mediated by the Z boson do not contribute to any flavour-changing currents:

$$J^{(\mathrm{NC})\mu} = \bar{\psi}\gamma^{\mu}\frac{1}{2}\left(g_V^f - g_A^f\gamma^5\right)\psi, \tag{1.14}$$

with g_V^f and g_A^f are the vector and axial fermionic couplings. The observation that photons also contribute to neutral currents as the Z boson paved the way to the proposition of unified *electroweak theory* by Glashow, Weinberg and Salam (GWS) [26–28].

Electroweak unification

The electromagnetic and weak interaction are unified into a single force in the GWS theory, which is encoded in the $SU(2)_L \times U(1)_Y$ gauge group structure. The conservation of the *weak isospin* quantum number I arises from the invariance of the EW Lagrangian under the left-chiral $SU(2)_L$ transformation, whilst the *weak hypercharge* Y conservation originates from the $U(1)_Y$ symmetry. The essence of the EW unification is succinctly defined in Glashow's observation, which relates the electromagnetic fermionic charge Q_f to the third component of the isospin I_3 and the weak hypercharge Y as follows:

$$Q_f = I_3 + Y/2. \tag{1.15}$$

[5] Fermi's β theory can be regarded as a low-energy effective theory of the gauge theory of the weak interactions.

The electroweak Lagrangian is rendered invariant under $SU(2)_L \times U(1)_Y$ transformations by replacing ∂_μ in the kinetic term by the covariant derivative D_μ:

$$D_\mu = \partial_\mu + i\frac{g}{2}\tau^i W_{\mu_i} + i\frac{g'}{2} Y B_\mu, \tag{1.16}$$

where τ^i denote the 2×2 generators of the $SU(2)$ symmetry, namely the Pauli matrices. Three non-Abelian weak isospin fields W^i_μ with $i = 1, 2, 3$ couple only to left-handed fermions with coupling strength g; the Abelian gauge field B_μ couples instead to both right and left-handed fermions via g'. The physical fields responsible for the charged $W^\pm$ bosons are expressed as the superposition of eigenstates below:

$$W^\pm_\mu = \frac{1}{\sqrt{2}}(W^1_\mu \mp iW^2_\mu), \tag{1.17}$$

Since the remaining neutral gauge fields B_μ and W^3_μ couple to neutrinos, both of them are not viable candidates as the electromagnetic mediator. However, these unphysical gauge fields mix, yielding the gauge field A_μ, which is conventionally assigned to the photon γ, and the orthogonal Z_μ eigenstate, accounting for the Z boson:

$$\begin{pmatrix} A_\mu \\ Z_\mu \end{pmatrix} = \begin{pmatrix} \cos\,\theta_W & \sin\,\theta_W \\ -\sin\,\theta_W & \cos\,\theta_W \end{pmatrix} \begin{pmatrix} B_\mu \\ W^3_\mu \end{pmatrix}, \tag{1.18}$$

where θ_W is the weak mixing angle. The prescription of gauge invariance for the SM Lagrangian under the electroweak symmetry group forces all EW gauge bosons to be massless. This is in deep contrast with the experimental observations of massive W and Z bosons. Furthermore, the Dirac fermionic mass term shown in Equation 1.3 is disallowed since it does not preserve electroweak gauge symmetry[6].

1.1.5 Phenomenological overview

The matter content of the SM comprises two types of elementary spin $\frac{1}{2}$ fermions, quarks and leptons. Leptons are sensitive only to the electroweak force, and are further categorised in electrically charged particles, the electron e^-, the muon μ and the tau τ and the corresponding type of neutrino. Quarks are colour-charged particles that interact also via the strong nuclear interaction. The flavour changing transitions are encoded in the CKM mixing matrix for quarks [29]. As in the case of leptons, they also come in three flavours, or families, namely up u, charm c, and top t quarks with a charge assignment of $+\frac{2}{3}e$, while the down d, strange s and bottom b quarks carry a negative charge $-\frac{1}{3}e$. All fermions of the first generation are the stable matter constituents of ordinary atoms. The

[6]The Dirac mass term for fermions can be explicitly decomposed into $m(\bar{\psi}_L\psi_R + \bar{\psi}_R\psi_L)$, which is evidently not invariant under $SU(2)_L$ transformations since left- and right-handed fermionic fields belong to different gauge representations.

second and third generations can be regarded as direct generalisations of the first one. Particles with higher generation index are exact replicas of the ones with lower index, albeit larger in mass. A summary of the particle content in the SM, including their basic properties, namely their mass and quantum numbers is shown in Table 1.1.

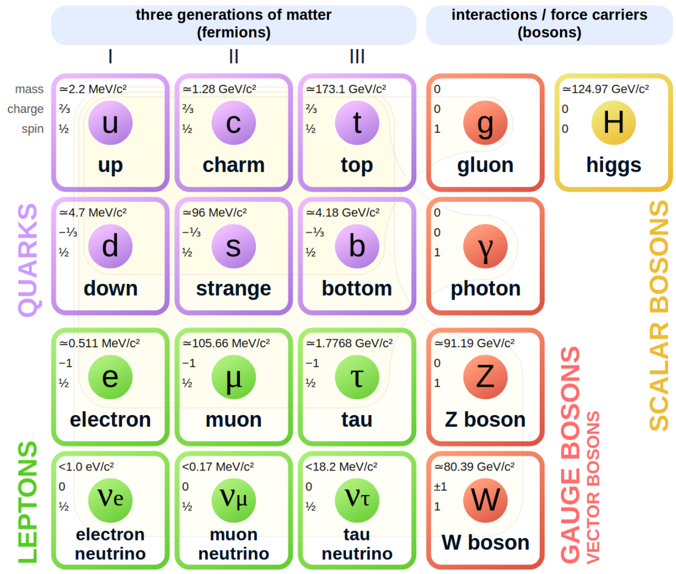

Figure 1.1: Elementary particles of the Standard Model including their masses and quantum numbers taken from [30].

All fundamental known interactions except gravity are encoded in a single gauge group structure satisfying an internal group symmetry, expressed as the direct product of Lie groups:

$$G_{SM} = SU(3)_C \times SU(2)_L \times U(1)_Y \tag{1.19}$$

where $SU(3)_C$ is the colour gauge group referring to chromodynamics, which commutes with the electroweak gauge group $SU(2)_L \times U(1)_Y$. The gauge particles are the vector spin-1 bosons massless photons γ and gluons accounting for electromagnetism and the nuclear strong interaction, respectively, and the massive vector $W^\pm$ and Z bosons responsible for the short-ranged, weak nuclear interactions. Parity violation in weak decays is incorporated in $SU(2)_L$ group structure. As a consequence, left-handed and right-handed particles are organised into different chiral mulitplets. All left-handed fermions transform as $SU(2)_L$ doublets. They are assigned a weak isospin of $I_3 = \frac{1}{2}$ for up-type quarks and neutrinos, and of $-\frac{1}{2}$ for down-type quarks and charged leptons. On the other hand, since right-handed fermions do not contribute to weak currents, they transform as singlets under $SU(2)_L$, and are subsequently assigned a weak isospin $I_3 = 0$[7].

In the low-energy limit, spontaneous symmetry breaking (SSB) of the electroweak symmetry occurs, also referred to as the *Higgs mechanism.* The resulting electromagnetic interaction is encoded in $U(1)_{em}$, a linear combination of $U(1)_Y$ and a $U(1)$ subgroup of the original $SU(2)$ group. Renormalisibility is a crucial ingredient for a finite, self-consistent theory that is scalable at different energy ranges. The Standard Model is renormalisable even after the occurrence of SSB as proven by t'Hooft [31]. This implies that the coupling parameters of the theory are *running*, i.e. they display a dependence on the energy scale μ, encoded in the corresponding beta function, $\beta(g)$, which depends implicitly on μ. The only scalar (spin-0) particle present in the SM is the Higgs boson. Its existence restores the unitarity bound of the tree-level amplitudes in the SM (for longitudinal W and Z bosons and also fermions) which would otherwise be violated at the scale $\Lambda_{EWSB} = \sqrt{8\pi v} \sim O(1\text{TeV})$[8].

1.1.6 Electroweak symmetry breaking and the Higgs mechanism

The generation of non-zero masses for vector gauge-bosons and the fermions can be achieved whilst maintaining electroweak gauge invariance via the *Higgs mechanism*, proposed independently by Higgs [32], Brout, and Englert [33]. In the context of a gauge field theory, the expression spontaneous symmetry breaking indicates that the Lagrangian remains invariant under the original hidden symmetry. On the other hand, the redundancy in description of the vacuum configuration (gauge symmetry of the ground state) is explicitly removed by a particular choice of gauge fixing[9]. In the Higgs mechanism, the scalar Lagrangian density of a non-Abelian gauge theory reads as:

$$\mathscr{L}_{Higgs} = (D^\mu\Phi)^\dagger(D_\mu\Phi) - V(\Phi^\dagger\Phi), \tag{1.20}$$

where D^μ is the covariant derivative of the EW Lagrangian shown in Eq.1.16 and Φ is the newly introduced complex scalar field, whose adjoint representation is the isospin doublet (and colour singlet):

$$\Phi = \begin{pmatrix} \phi^+ \\ \phi^0 \end{pmatrix}, \tag{1.21}$$

with hypercharge $Y_\Phi = 1$. The symbols ϕ^+ and ϕ^0 denote the positively charged and electrically neutral fields respectively. Invariance of the Lagrangian under the $SU(2)_L \times$

[7]The sole exception are right-handed neutrinos, which are absent in the SM.

[8]The alternative way to restore unitarity other than including extra degrees of freedom (carried for instance by the Higgs boson), would be to achieve spontaneous symmetry breaking by means a strongly-coupled interactions present in technicolour models.

[9]The gauge symmetry is actually preserved via the Stuckelberg extension of the SM [34], which provides a mechanism for a non-linear realisation of the gauge symmetry of the vacuum state.

$U(1)_Y$ gauge group as well as the renormalizability of the SM restrict the functional form of the potential of the *phi–to–the–fourth* theory to:

$$V(\Phi^\dagger\Phi) = -\mu^2\Phi^\dagger\Phi + \lambda(\Phi^\dagger\Phi)^2, \tag{1.22}$$

where μ^2 and λ are the parameters of the potential. The quartic coupling λ is responsible for the scalar fields self-interactions. The requirement of vacuum stability forces the Higgs potential to be bounded from below, which occurs for a positive definite value of λ[10]. On the other hand, the quadratic term μ^2 has its sign reversed with respect to the Lagrangian of a free complex scalar field with mass μ, with a zero-valued minimum of the potential. In fact, by imposing the condition $\mu^2 > 0$, the scalar field acquires a non-zero vacuum expectation value (VEV) of $v = \sqrt{-\mu^2/\lambda}$. Consequently, a continuum of degenerate minima fulfils the ground state condition $\Phi^\dagger\Phi = \frac{v}{2}$. In order to spontaneously break the vacuum symmetry, the *unitarity gauge* is conveniently chosen for gauge fixing:

$$\langle 0|\Phi|0\rangle = \frac{1}{\sqrt{2}}\begin{pmatrix} 0 \\ v \end{pmatrix}. \tag{1.23}$$

This ensures conservation of electric charge and hence that the photon remains massless. Since the electric charge operator still annihilates the vacuum state $|0\rangle$, it is by construction an unbroken symmetry generator. Therefore, the spontaneous symmetry breaking of the electroweak group $SU(2)_L \times U(1)_Y$ into the $U(1)_{EM}$ subgroup is realised. The value of the VEV of the Higgs field determines the electroweak scale, and it is fixed by the reduced Fermi constant G_F^0 as $v = (\sqrt{2}G_F^0)^{-1/2} \approx 246$ GeV [30]. By expanding the kinematic term in Equation 1.20 for small radial excitations of the Higgs field $h = h(x)$ in the vicinity of the VEV, viz:

$$\Phi = \frac{1}{\sqrt{2}}\begin{pmatrix} 0 \\ v+h \end{pmatrix}, \tag{1.24}$$

one can infer directly from the $O(v^2)$ terms in the Lagrangian density vector boson mass terms as follows:

$$m_W = \frac{1}{2}gv, \quad m_{Z^0} = \frac{1}{2}v\sqrt{g^2+g'^2} = \frac{m_W}{\cos\,\theta_W}, \tag{1.25}$$

while the $O(v)$ terms denote the coupling of the Higgs field to the weak vector bosons V:

$$g_V = 2\frac{m_V^2}{v}. \tag{1.26}$$

In the case of the massless gauge bosons, the Higgs coupling to photons and gluons can only be induced by vector boson and fermionic loops. In the unitary gauge adopted, three

[10]Since the λ parameter is also running with the interaction energy, this implies that $\lambda(\mu)$ should remain positive up to the energy cut-off Λ of the theory.

of the four degrees of freedom of the massless Goldstone bosons [35, 36] are manifestly absorbed after SSB into the longitudinal polarisation of the massive vector bosons. The remaining degree of freedom represents the Higgs boson H, whose mass $M_H = \sqrt{-2\mu^2}$ is a free parameter of the SM.

In addition, Weinberg noticed that the Higgs mechanism can be exploited also for the mass generation of all the fermions. By postulating a gauge invariant interaction term between the scalar Higgs field and the fermionic fields, namely the Yukawa term:

$$\mathscr{L}_{\text{Yukawa}} = -g_Y \bar{\psi} \Phi \psi, \tag{1.27}$$

a mass term for the fermion appears in the SM Lagrangian density after the occurrence of spontaneous symmetry breaking:

$$m_f = \frac{1}{\sqrt{2}} g_Y^f v, \tag{1.28}$$

where g_Y^f is the Yukawa coupling constant of a fermion, which is found to be directly proportional to the fermion mass. The recently discovered Higgs boson is the only fundamental scalar (spin-0) boson present in the SM. High precision measurements of the mass of the Higgs-like resonant state at 125 GeV [37–39], as well as its spin properties, [40, 41] and decay width [39, 42] have been found to agree with the predictions of the SM. The production and decay modes of the Standard Model Higgs boson are discussed thoroughly in the next section.

1.1.7 Search for the Standard Model Higgs boson at the LHC

Although the Higgs mechanism was formulated as early as in the sixties, the discovery of the Higgs boson came only after decades of experimental effort. At high-energy hadron colliders, there are several viable production mechanisms for the Higgs boson depicted in Figure 1.2. The four dominant ones are in the order *gluon fusion* (ggF), *vector boson fusion* (VBF), *higgstrahlung* (VH) and the *production in association with top* ($t\bar{t}H$) *and bottom quarks* ($b\bar{b}H$).

The gluon-gluon fusion process $gg \to H$ exemplified in Figure 1.2 (a) is the production mechanism with the highest cross section of 49 pb at $\sqrt{s} = 13$ TeV for a Higgs boson with a mass of $m_H = 125$ GeV. The coupling to the gluon is mediated through a virtual quark loop, induced mainly by top quark, whilst all other quark contributions are suppressed by a factor m_q^2.

The vector boson fusion process $qq \to Hqq$ shown in Figure 1.2 (b) is the second largest Higgs production mode at the LHC, albeit an order of magnitude lower in cross section with respect to ggF, as shown in Figure 1.3 (left). The weak bosons emitted by the quarks in the initial state fuse to form a Higgs boson. The scattered quarks of the

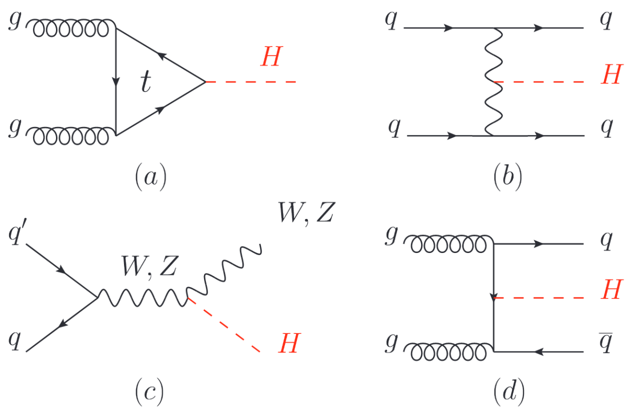

Figure 1.2: Diagrams exemplifying the main Standard Model Higgs boson production mechanisms by means of gluon-gluon fusion (a), vector boson fusion (b), associated production with vector boson (c) and with heavy-flavour quarks (d).

process initiate two hard jets with a large rapidity gap. This characteristic signature of the VBF process can be exploited to distinguish it from QCD background events.

The third dominant Higgs boson production mechanism at the LHC consists of the associated-production with a vector boson V, exemplified in Figure 1.2 (c). It is also referred to as the Higgstrahlung mechanism since an off-shell weak boson radiates a Higgs boson while decaying to its on-shell state. This process is characterised by leptonic decays of the vector boson and by the presence of missing transverse energy in the final state. The resulting peculiar signature of the one- and two- lepton channels can be exploited to reject efficiently background events already at trigger level.

The next most relevant production mechanism represented in Figure 1.2 (d) is the Higgs boson associated production with a heavy flavour quark pair. As shown in Figure 1.3 (left) the cross section for the $t\bar{t}$ and $b\bar{b}$ associate Higgs production are both approximately 0.5 pb at $\sqrt{s} = 13$ TeV. This channel provides a unique tool to probe directly the on-shell top-quark Yukawa coupling y_t, thereby breaking the assumed degeneracy with the off-shell coupling evinced from the ggF process. The $t\bar{t}H$ channel was recently observed by CMS and ATLAS [43, 44] at the LHC. The other production mechanism $b\bar{b}H$ is even more challenging to measure due to the presence of large irreducible QCD background.

In addition, the SM Higgs boson possesses a plethora of decay modes, resulting in a very rich phenomenology, which can be exploited to investigate its properties. The overall decay width for a Higgs boson with a mass close to the observed value of 125 GeV is not expected to be directly measurable at the LHC[11]. In the case of a SM-like Higgs boson the total width is predicted to be approximately 4 MeV for $m_H = 125$ GeV, which is a

[11]It can be inferred indirectly from the sum of the partial decay widths, assuming the coupling structure mimics the SM expectation.

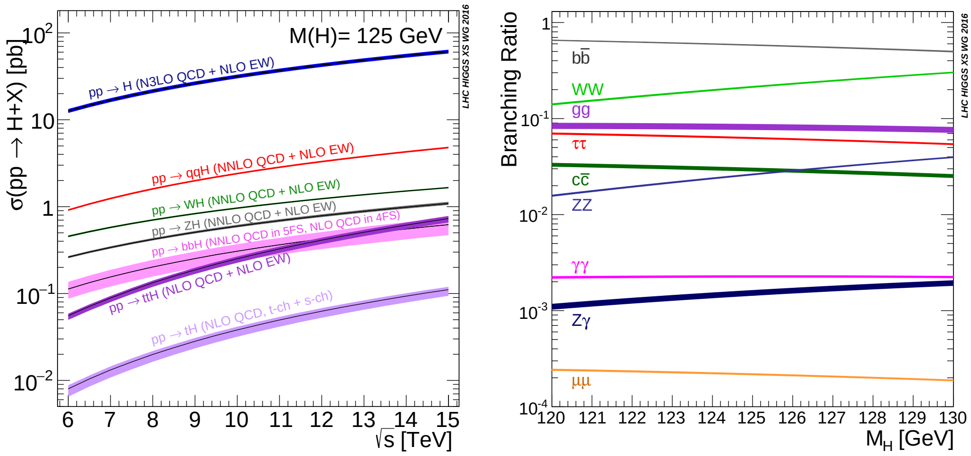

Figure 1.3: The SM Higgs boson production cross sections versus the center of mass energy, $\sqrt{s}$ (left). The branching ratios for the SM Higgs boson decay modes in the mass (right) for a mass range in the vicinity of $m_H = 125$ GeV [45]. The theoretical uncertainties are represented as bands.

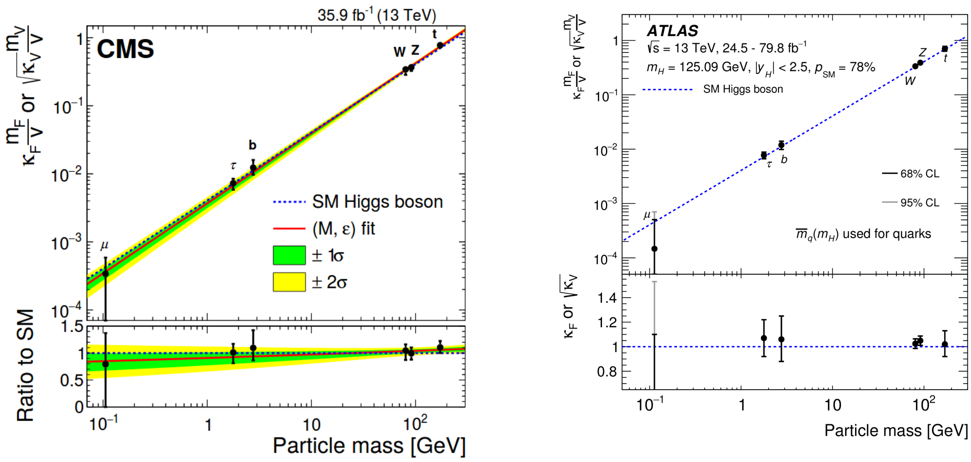

Figure 1.4: Best fit for deviations of the observed Higgs boson coupling from the Standard model versus the mass of the particle obtained with LHC Run 2 data collected by CMS [46] (left) and ATLAS [47] (right), respectively. The Higgs boson coupling is parameterised respectively as $\kappa_F \cdot m_F$ for fermions and as $\sqrt{\kappa_V} \cdot m_V/v$ for weak bosons.

thousand times lower than the achieved mass resolution at the LHC. Consequently, the observed Higgs boson has an extremely short lifetime $\tau_H \approx 1.6 \cdot 10^{-22}$s, and it decays preferentially to the heaviest decay products that are kinematically allowed owing to the coupling structure highlighted in Figure 1.4. The couplings of the recently discovered

Higgs-like resonance at the LHC to fermions and bosons [39, 48, 49] are consistent with a SM Higgs boson. In the case of fermionic decays, the partial decay width in the Born approximation can be written as follows [50] :

$$\sigma(H \to f\bar{f}) \propto N_c m_H m_f^2, \tag{1.29}$$

where $N_c = 3$ (1) is the colour factor for quarks, and leptons respectively, m_H is the Higgs boson mass, and m_f is the fermion mass. Analogously, in Higgs boson decays into a pair of vector bosons the tree-level decay amplitude can be written as in [51]:

$$\sigma(H \to VV) \propto \delta_V m_H^3 F(m_1^2, m_2^2, m_H), \tag{1.30}$$

with $\delta_V = 2(1)$ for the W and Z bosons respectively, while $F(m_1^2, m_2^2, m_H)$ stands for a kinematic contribution that depends on the mass of the Higgs bosons and of the vector bosons. Furthermore, decays into massless vector bosons such as $\gamma\gamma$, γZ and gg can also occur. The di-photon decay channel and $H \to \gamma Z$ are loop induced by either W bosons or electrically charged fermions, while $H \to gg$ is realised only through intermediate quark loops.

Since the SM Higgs boson mass is a free parameter, once its value is fixed, the profile of the Higgs branching fractions can be uniquely obtained. The most recent measurement of the Higgs mass $m_H = 125.38 \pm 0.14$ GeV [52] was performed at CMS exploiting the decay channels $H \to ZZ^* \to 4l$ and $H \to \gamma\gamma$ by combining the Run 1 and the 2016 Run 2 results. Despite their low branching ratios, these so-called "golden" channels achieve the best sensitivity because of the low background rates and the excellent lepton identification and momentum resolution of the CMS detector in the four-lepton final state; the di-photon channel benefits instead from the outstanding performance in the energy and momentum resolution. The $\tau\tau$ decay mode, which has the second largest fermionic decay mode, was observed at the LHC [53, 54]. It features the best sensitivity among the fermionic decay channels due to its relatively clean signature. On the other hand, Figure 1.3 demonstrates that the highest branching fraction around $BR(H \to b\bar{b}) \sim 57\%$ occurs for SM Higgs boson decays into a b-quark pair. The b- quark is the fermion with the largest mass meeting the kinematic condition $m_H > 2m_f$. This process is particularly challenging to detect due to the presence of the irreducible QCD background consisting of multiple hadronic jets in the final state. At the LHC, the $H \to b\bar{b}$ decay channel was observed in the VH process [55, 56], thus completing the picture of the third-generation fermion couplings to the SM Higgs boson. The final state with two charged leptons from the decay of the vector boson makes the largest contribution to the sensitivity of the decay channel. The third most relevant fermionic decay process is the Higgs boson decay to a pair of c-quarks, which occurs over 20 times less frequently than the dominant decay channel $H \to b\bar{b}$ in the SM. Because of the similar properties of heavy flavour c- and b- jets, this process is extremely difficult to disentangle from the more abundant $H \to b\bar{b}$ channel. The current observed (expected) upper limit at 95% confidence level on $\sigma(pp \to H + X)B(H \to \mu^+\mu^-)$ is a factor 3.0 (2.5) larger than the SM expectation. In this limit obtained from the combination of 7, 8 and 13 TeV CMS results [57] the SM production cross sections are assumed for a Higgs boson with a mass $m_H = 125.09$ GeV.

1.1.8 The shortcomings of the Standard Model

The Standard Model of elementary particles is regarded as one of the greatest triumphs of fundamental particle physics. However, it does not incorporate gravitational quantum effects that are expected to arise at the Planck scale $M_{Pl} \sim 10^{19}$ GeV. Attempts at quantising gravity in the framework of a perturbatively renormalisable QFT with 3+1 dimensions in a similar way to other SM force fields encounter several difficulties in mathematical consistency. Consequently, the SM must be an effective field theory valid up to a certain energy scale Λ, at which new physics phenomena should be observable. The large scale difference between the electroweak scale $O(100\text{GeV})$ and the Planck mass constitutes the notorious *hierarchy problem*. This is not, strictly speaking, a problem of the SM, since the latter is a renormalisable, UV-complete theory, i.e it is valid up to arbitrarily high energy scales. However, the introduction of a cut-off scale in the regularisation procedure below the Planck scale has important implications on the running masses of the scalar particle present in the model. This translates in the *naturalness problem* of the observed Higgs boson mass, the only fundamental scalar in the SM. The quadratic one-loop radiative corrections to the Higgs boson mass m_H are given by [58]:

$$\delta m_H^2 = \frac{3G_F}{4\sqrt{2}\pi^2}\left(4m_t^2 - 2m_W^2 - m_Z^2 - m_H^2\right)\Lambda^2, \tag{1.31}$$

where the top contribution has an opposite sign with respect to the bosonic induced loops, and Λ is sensitive to the largest mass scale in the model. Thus, the experimentally ascertained value of the Higgs boson mass of 125 GeV requires a large dose of *fine-tuning* over at least 15 orders of magnitude to be kept at the electroweak scale. Another theoretical issue of the SM that is inherently linked to the concept of naturalness[12] is the strong CP problem, where the CP-violating phase in QCD is unnaturally suppressed below $|\theta| \lesssim 10^{-10}$ [30]. Furthermore, the incontrovertible observation of neutrino oscillations, originally considered massless in the SM, may be a hint of the existence of new physics. The Standard Model also does not provide a dynamical mechanism to explain the number of generations, and the large fermion mass hierarchy. The latter spans several order of magnitudes, from the mass of the electron neutrino constrained below $\lesssim 1.0$ eV, according to the recent KATRIN result [60], to the top quark mass, comparable to that of a gold nucleus. Furthermore, the SM lacks a suitable matter candidate to account for

[12]The t'Hooft naturalness criterion [59] states that a parameter of the Lagrangian is naturally small only if the underlying theory acquires and additional symmetry when the parameter of interest is set to zero.

the cosmological observation of dark matter. Non-baryonic cold dark-matter candidates are instead present in supersymmetric theories, which are discussed in the next section.

1.2 Extensions of the Standard Model

Supersymmetry (SUSY) [61] is an attractive property of a large class of Beyond Standard Model (BSM) theories. The Minimal Supersymmetric extension of the SM features an enlarged Higgs sector, which is also prescribed by the more general Two-Higgs-Doublet Models. In this chapter, a brief overview of supersymmetry precedes an extensive discussion of the phenomenology of the Higgs sector in the MSSM and 2HDM models, with a particular emphasis on the neutral BSM Higgs boson production and decay modes.

1.2.1 Supersymmetry

The Standard Model is subject to the Coleman-Mandula theorem [62], stating that the allowed symmetries in a relativistic QFT are exclusively a non-trivial combination of the Poincare' group and the internal symmetry gauge group. However, Wess and Zumino demonstrated that this no-go theorem can be evaded by defining a new type of external "supergauge" symmetry, or supersymmetry, connecting the bosonic and fermionic degrees of freedom of the theory [63]. This is achieved by the introduction of an extended super-Lie algebra whose symmetry generators transform as spinors under the Lorentz group. In general, a SUSY generator Q_α transforms bosonic spinorial representations into fermionic ones and vice versa. In the simplest supersymmetric models, the maximum spin difference each particle and its supersymmetric counterpart, also referred to as superpartner, is $\frac{1}{2}$. The particle content in supersymmetric theories is organised into supermultiplets, containing both bosonic and fermionic components, while the spinors are decomposed in the left- and right-handed Weyl components, denoted with the indices α and $\dot{\beta}$ respectively. The quintessence of SUSY models is encoded in the anti-commutation relation :

$$\{Q_\alpha, \bar{Q}_{\dot{\beta}}\} = 2(\sigma^\mu)_{\alpha\dot{\beta}} P_\mu, \tag{1.32}$$

where $P_\mu = -i\partial_\mu$ is the space-time translation operator and σ^μ are the Pauli matrices. Equation 1.32 highlights the fact that supersymmetry is effectively a new space-time symmetry, since fermionic generators act as the "square root" of the four-dimensional space-time derivative ∂_μ[13]. Supersymmetric models are particularly appealing since they provide an elegant solution to the aforementioned gauge hierarchy problem. The cancellation of quadratic divergences to the Higgs boson mass is achieved by the introduction of two scalar superpartners for each fermion present in the SM. The coupling of the sfermions to the Higgs boson is forced to be identical to the SM partner, albeit it contributes an

[13] This is analogous to the Dirac equation being the square rooted version of the Klein-Gordon equation.

opposite correction in sign to the Higgs boson mass. Nonetheless, *exact supersymmetry* cannot be realised in Nature since degenerate super-partners of the SM particles have not been observed at colliders. Consequently, supersymmetry must be explicitly "softly" broken [64] such that Higgs mass radiative corrections are only logarithmically divergent[14].

R-parity conservation

The total baryon B and lepton L numbers are conserved quantum numbers of the SM Lagrangian density, respectively defined as :

$$B = (n_q - n_{\bar{q}})/3, \qquad L = n_l - n_{\bar{l}}, \tag{1.33}$$

where $n_q(n_{\bar{q}})$ is the number of (anti-)quarks and $n_l(n_{\bar{l}})$ is the number of (anti)-leptons. Differently from the SM, lepton and baryon number violating terms can appear in the SUSY Lagrangian density. However, current experimental bounds on the proton lifetime $\tau_p > 2.1 \times 10^{29}$ years at 90 % confidence level [30] pose stringent constraints on the simultaneous presence of L and B violating terms. A discrete multiplicative quantum number, namely $R-$parity, also referred to as *matter parity*, is introduced:

$$R_P = (-1)^{2S+3B+L}, \tag{1.34}$$

where S denotes the spin of the particle. By construction in R-parity conserving models, all SM particles possess even R-parity, whilst SUSY partners are characterised by odd-parity. Therefore, SUSY particles can only be produced (or annihilated) in pairs at colliders, since the initial state contains only particles with parity $R_P = +1$. If exact, R-parity also enforces the absence of mixing between supersymmetric and SM particles. The conservation of R-parity has interesting phenomenological implications for the lightest supersymmetric particle present in the model (LSP). The LSP particle must be the end-product of a SUSY particle decay chain, therefore it is stable. It is also likely to be colour- and electrically neutral, which would render it a plausible non-baryonic cold dark matter candidate [65].

1.2.2 Minimal Supersymmetric SM extension

The simplest supersymmetric extension of the SM characterised by the minimal particle content is the Minimal Supersymmetric Standard Model (MSSM). In this theoretical model, all SM field representations are promoted to the corresponding supermultiplet. In general, in renormalizable field theories only two classes of supermultiplets are allowed, *vector* and *chiral* supermultiplets. In the MSSM, the vector multiplets accomodate the SM vector gauge bosons and the corresponding fermionic superpartner, while each chiral

[14]This "soft SUSY breaking" mechanism is valid as long as new heavy particles are observed at the TeV scale.

multiplets comprise a SM fermion and its relative scalar superpartner. There are two classes of bosonic superpartners, squarks and sleptons conventionally named with the prefix "s" after their SM counterpart. Since the gauge structure $SU(3)_C \times SU(2)_L \times U(1)_Y$ of the SM is preserved, the vector superfield associated with each gauge group establishes the presence of spin $\frac{1}{2}$ partners of the gauge bosons, referred to as gauginos. Among the latter, the zino and the photino carry the same quantum number as the neutral higgsinos, the fermionic superpartners of the neutral Higgs bosons. Thus, these electroweak states should mix, yielding the four mass eigenstates called neutralinos, denoted as $\tilde{\chi}_1^0, ..., \tilde{\chi}_4^0$, while the charginos $\tilde{\chi}_1^\pm, \tilde{\chi}_2^\pm$ are a linear combination of the winos and the charged higgsinos. Since the LSP must be uncolored and uncharged to contribute to the observed relic dark-matter density, the only viable candidates are sneutrino and the neutralinos. However, the exclusion limits from direct sneutrino searches combined with indirect constraints on the Z boson invisible decay width [66] ruled out the first option in the MSSM. An overview of the extended Higgs sector in the MSSM model with R-parity conservation follows.

1.2.3 The Higgs sector in the MSSM

The MSSM features an extended Higgs sector with two chiral Higgs supermultiplets. The latter comprise two $SU(2)$ Higgs doublets with opposite hypercharge, responsible for the Yukawa interactions with the up-type and the down-type fermions and the corresponding higgsinos denoted as $\tilde{\Phi}_u$, $\tilde{\Phi}_d$. There is a two-fold motivation for the presence of two distinct Higgs doublets. On one hand, the superpotential of any supersymmetric theory must be a holomorphic function of the chiral supermultiplets [64]. Consequently, simple charge conjugation of the Higgs doublet coupling to up-type fermions to yield the down-type Yukawa terms is disallowed, unlike in the SM. Furthermore, the gauge anomaly-free character of theory, achieved in the SM due to the peculiar hypercharge pattern, must be enforced in the MSSM by inclusion of an additional, suitably defined Higgs doublet. The simplest form of the CP-preserving Higgs potential in the MSSM[15] can be derived, in analogy with Equation 1.22, as:

$$
\begin{aligned}
V_{MSSM}(\Phi_1, \Phi_2) = |\mu|^2|\Phi_1|^2 + |\mu|^2|\Phi_2|^2 + \frac{1}{4}(g^2 + g'^2)\left(|\Phi_1|^2 + |\Phi_2|^2\right) + \\
+\frac{1}{4}(g^2 - g'^2)|\Phi_1|^2|\Phi_2|^2 - \frac{1}{2}g^2\Phi_1^\dagger\Phi_2\Phi_2^\dagger\Phi_1,
\end{aligned}
\tag{1.35}
$$

where Φ_1 and Φ_2 denote the down- and up- type Higgs doublets, while μ is the supersymmetric Higgsino mass parameter. Differently from the SM, supersymmetry dictates that the quartic Higgs coupling must be defined as a function of the squared electroweak g^2 and g'^2 gauge couplings[16]. Minimising the MSSM potential, only the electrically neutral

[15]Soft SUSY breaking correction terms are omitted for simplicity.

[16]The scalar Higgs couplings are the cubic $\lambda_3 = \frac{1}{4}(g^2 - g'^2)$ and the quartic coupling $\lambda_4 = -\frac{1}{2}(g'^2)$, respectively.

components of the Higgs fields Φ_i^0 acquire non-zero VEVs in order to preserve $U(1)_{em}$ after electroweak symmetry breaking :

$$\langle 0|\Phi_1|0\rangle = \frac{1}{\sqrt{2}}\begin{pmatrix} v_1 \\ 0 \end{pmatrix}, \langle 0|\Phi_2|0\rangle = \frac{1}{\sqrt{2}}\begin{pmatrix} 0 \\ v_2 \end{pmatrix}, \tag{1.36}$$

where the vacuum expectation values v_1 and v_2 must satisfy $v = \sqrt{v_1^2 + v_2^2} \simeq 246$ GeV to correctly reproduce the vector gauge boson masses. The ratio of the vacuum expectation value is defined as $\tan\beta \equiv v_2/v_1$. Prior to symmetry breaking, the Higgs doublets contribute each four degrees of freedom, three of which are then absorbed by the three massive gauge bosons. Consequently, the remaining five physical degrees of freedom give rise to two charged Higgs bosons, $H^\pm$, and three neutral states, the h, H and A bosons, collectively denoted as $\phi = \{h, H, A\}$. The A boson is a CP-odd pseudo-scalar stemming from the rotation of the imaginary part of the neutral components of the Higgs doublets as follows:

$$A = \sqrt{2}(Im\phi_1^0 \sin\beta - Im\phi_2^0 \cos\beta), \tag{1.37}$$

while the CP-even states originate from the superposition of the real part of the Higgs doublets. Assuming that the h boson is the lightest state the mixing is given by:

$$\begin{pmatrix} h \\ H \end{pmatrix} = \begin{pmatrix} -\sin\alpha & \cos\alpha \\ \cos\alpha & \sin\alpha \end{pmatrix} \begin{pmatrix} \sqrt{2}Re\phi_1^0 - v_1 \\ \sqrt{2}Re\phi_2^0 - v_2 \end{pmatrix}, \tag{1.38}$$

with the mixing angle α defined as [67]:

$$\tan\alpha = \frac{-(m_Z^2 + m_A^2)\sin 2\beta}{(m_Z^2 - m_A^2)\cos 2\beta + \sqrt{(m_Z^2 + m_A^2)^2 - 4m_Z^2 m_A^2 \cos^2 2\beta}}, \tag{1.39}$$

to diagonalise the tree-level squared-mass matrix of the CP-even states[17]. The resulting tree-level mass eigenvalues of the CP-even states are:

$$m_{h,H}^2 = \frac{1}{2}\left(m_A^2 + m_Z^2 \mp \sqrt{(m_A^2 + m_Z^2)^2 - 4m_A^2 m_Z^2 \cos^2 2\beta}\right). \tag{1.41}$$

Furthermore, the charged Higgs boson masses are given to lowest order by the expression:

$$m_{H^\pm}^2 = m_A^2 + m_W^2. \tag{1.42}$$

[17]The tree-level mass-squared matrix of the CP-even states reads [67]:

$$M_{\text{tree}}^2 = \begin{pmatrix} m_A^2 \sin^2\beta + m_Z^2 \cos^2\beta & -(m_A^2 + m_Z^2)\sin\beta\cos\beta \\ -(m_A^2 + m_Z^2)\sin\beta\cos\beta & m_A^2\cos^2\beta + m_Z^2\sin^2\beta \end{pmatrix}. \tag{1.40}$$

Thus, the parameter space of the MSSM Higgs sector can be interpreted at tree level as a function of only two non-SM parameters, conventionally selected as tanβ and the mass of the A boson, as well as the vector boson masses. In the region of phase space where $m_A \gg m_Z$, referred to as the *decoupling limit*, Eq. 1.41 simplifies to :

$$m_h^2 \simeq m_Z^2 \cos^2 2\beta; \qquad m_H^2 \simeq m_A^2 + m_Z^2 \cos^2 2\beta. \tag{1.43}$$

As a consequence, the tree-level mass of the h boson is bounded from above by the Z boson mass, as illustrated in Figure 1.5. The other Higgs states form a high mass degenerate triplet since in this limit $m_A \simeq m_H \simeq m_{H^\pm}$.

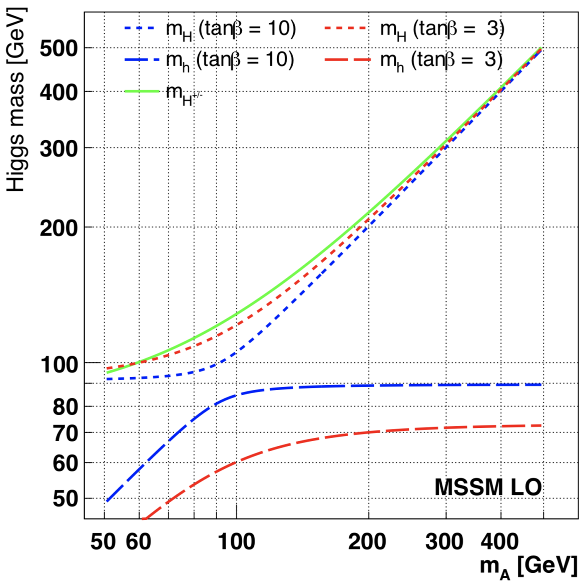

Figure 1.5: MSSM Higgs bosons tree-level masses against the pseudoscalar mass m_A for the values of $\tan\beta = 3; 10$ [67].

Searches for MSSM Higgs boson conducted at the Large Electron-Positron collider (LEP) established a lower bound on the Higgs boson mass of 114.4 GeV [68] at 95% confidence level. The latter is incompatible with the tree-level condition $m_h \leq m_Z|\cos 2\beta|$. Thus, substantial radiative corrections arising from the SUSY sector parameters to the Higgs sector were introduced to reconcile the MSSM prediction with LEP constraints. The leading loop-induced correction to the lightest CP-even Higgs state arises from the top/stop sector:

$$m_h^2 \leq m_Z^2 \cos^2 2\beta + \frac{3g^2 m_t^4}{8\pi^2 m_W^2} ln(\frac{m_{\tilde{t}}^2}{m_t^2}), \tag{1.44}$$

where $m_{\tilde{t}}$ is the stop mass parameter. The observation of a SM-like CP-even Higgs boson with a mass of 125 GeV at the LHC posed additional constraints on the MSSM parameter space.

This result is of particular phenomenological interest since the lightest CP-even state decouples entirely from the rest of the Higgs sector. In fact, in the decoupling region, the alignment limit, i.e. $\alpha \approx \beta - \pi/2$ is automatically verified[18]. The latter corresponds to the particular direction in field space, for which the lightest CP-even state is aligned with the SM Higgs boson [15], viz :

$$h_{\mathrm{SM}} = h\sin(\alpha-\beta) - H\cos(\alpha-\beta). \tag{1.45}$$

In this limit, the lightest CP-even Higgs boson possesses identical tree-level couplings as in the SM case. This is in agreement with the measured Higgs boson properties [42, 46, 47, 69], while the interpretation of the observed $h(125)$ resonance as the heavier CP-even state is disfavoured by data.

1.2.4 Production and decay modes

The production and decay modes of the MSSM Higgs bosons are mostly driven by the coupling structure. The coupling of the neutral MSSM Higgs bosons to up- (κ^u) and down-type quarks and charged leptons ($\kappa^{d,\ell}$) and to massive vector bosons (κ^V) with respect to the equivalent SM Higgs boson couplings are illustrated in Table 1.1.

	κ^u	$\kappa^{d,\ell}$	κ^V
h	$\cos\alpha/\sin\beta$	$-\sin\alpha/\cos\beta$	$\sin(\beta-\alpha)$
H	$\sin\alpha/\sin\beta$	$\cos\alpha/\cos\beta$	$\cos(\beta-\alpha)$
A	$\cot\beta$	$\tan\beta$	0

Table 1.1: The coupling of the neutral MSSM Higgs bosons to up- (κ^u) and down-type quarks and charged leptons ($\kappa^{d,l}$) SM fermions and to massive vector bosons (κ^V) with respect to the SM Higgs boson couplings [15].

The main production mechanism for the MSSM Higgs bosons at the LHC are the gluon fusion $gg \to \phi$ and the b-associated production $b\bar{b}\phi$. Gluon fusion prevails at tanβ $\lesssim$ 30 [70], while at leading order the bottom Yukawa coupling is enhanced by tanβ, leading to the b-associated production becoming dominant at high tanβ.

The partial decay widths of the CP-even MSSM Higgs bosons into a fermion or a vector boson pair are obtained directly from the SM equivalent width by rescaling the relevant Higgs boson couplings. The partial decay widths of h and H boson into massive weak bosons is significantly lower with respect to the SM equivalent process. The kinematic

[18]Exact alignment can also be obtained irrespective of the Higgs boson mass spectrum, albeit with an accidental cancellation between tree-level mixing parameters and the first-order loop corrections in the CP-even mass-squared matrix.

constraints account for this reduction in the case of the h boson, while the suppression of the coupling κ_H^V affects $H \to VV$ decays. Furthermore, the A boson tree-level decays to a massive gauge boson pair vanish owing to CP conservation.

1.2.5 SUSY radiative corrections on bottom Yukawa coupling

Beyond tree-level, the bottom Yukawa sector receives large radiative corrections involving additional SUSY parameters, with a sizable impact on the main MSSM Higgs boson production and decay processes. The coupling of the up-type Higgs doublet Φ_2 to down-type fermions is loop-suppressed, leading to an additional term, namely the *wrong-sign Higgs interaction* in the Lagrangian density:

$$\mathscr{L} \approx g_Y^b \Phi_1^0 b\bar{b} + \Delta g_Y^b \Phi_2^0 b\bar{b}, \tag{1.46}$$

where the second term is loop-induced by SUSY particles with a mass below the soft-SUSY breaking scale. As a consequence, the running b-quark mass m_b is subject to a modification Δ_b arising from SUSY radiative corrections:

$$m_b = g_Y^b v(1 + \Delta_b). \tag{1.47}$$

Among the latter, the dominant contribution stems from the SUSY parameters of the QCD sector, in particular the sbottom-gluino loops, hence Δ_b can be expressed as:

$$\Delta_b = \frac{\Delta g_Y^b}{g_Y^b} \tan\beta \approx \frac{2\alpha_s}{3\pi} \times \frac{\mu m_{\tilde{g}} \tan\beta}{\max(m_{\tilde{g}}, m_{\tilde{b}1}, m_{\tilde{b}2})}, \tag{1.48}$$

where $m_{\tilde{g}}$, $m_{\tilde{b}1}$, $m_{\tilde{b}2}$ are the gluino ans sbottom masses respectively. Therefore, the correction Δ_b yields an additional $\tan\beta$ dependence of the bottom Yukawa coupling with respect to the tree-level dependence on the angles α and β. As a consequence, the bottom Yukawa coupling modifier of the lightest CP-even boson with respect to the SM Higgs boson coupling becomes:

$$\kappa_h^b = -\frac{\sin\alpha}{\cos\beta}[1 - \frac{\Delta_b}{1+\Delta_b}(1 + \cot\alpha\cot\beta)], \tag{1.49}$$

which can generate a considerable shift in the partial decay width $h \to b\bar{b}$. In fact, the magnitude of this correction can attain a value of $\Delta_b \sim 0.5$ for large $\tan\beta \gg 1$. The sign of the correction is instead controlled by the Higgsino mass parameter μ. For negative values of Δ_b, the bottom Yukawa coupling may be strongly enhanced. In the limit where Δ_b approaches -1, the bottom Yukawa coupling may exceed the perturbative limit and enter in tension with unitarity constraints. As a consequence, from theoretical arguments the accessible range of $\tan\beta$ in the MSSM is expected to be restricted to:

$$1 \lesssim tan\beta \lesssim \frac{m_t}{m_b}, \tag{1.50}$$

where the upper (lower) bound is set by the requirement of a perturbative bottom (top) Yukawa coupling. In the alignment limit, the bottom Yukawa coupling modifiers of the remaining neutral MSSM bosons with respect to the SM Higgs boson become:

$$\kappa_A^b \approx \kappa_H^b \approx \frac{\tan\beta}{1+\Delta_b}. \tag{1.51}$$

In the context of this thesis, the process of interest is the b-associated production of neutral Higgs bosons $\phi = h, H, A$ that later decay into a b-quark pair, exemplified in Figure 1.6, which is controlled by the effective strength of the bottom Yukawa coupling of the MSSM Higgs boson.

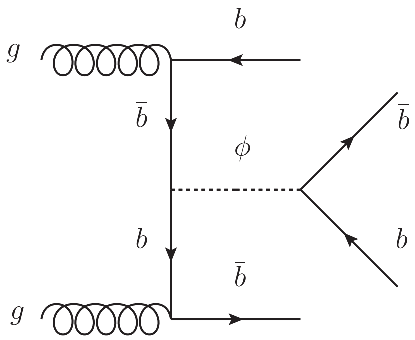

Figure 1.6: A Feynman diagram illustrating the ϕ boson production in association with b-quarks and its subsequent decay into a b-quark pair, realised with [71].

From Equations 1.49 and 1.51 it follows that, in the alignment limit, the $b\bar{b}(\phi \to b\bar{b})$ process is largely dominated by the A and H boson contribution. In fact even for moderate $\tan\beta \gtrsim 10$, the lightest CP-even boson accounts for a negligible contribution below the subpercent level. In the decoupling region, the branching fraction of the $A \to b\bar{b}$ decay approximately reads [72]:

$$B(A \to b\bar{b}) \simeq \frac{9}{(1+\Delta_b)^2 + 9}, \tag{1.52}$$

where the numerical factor of 9 corresponds to the squared colour factor $N_c = 3$. Therefore, the overall rate for the b-quark associated $A \to b\bar{b}$ production becomes :

$$\sigma(b\bar{b}A)B(A \to b\bar{b}) \simeq \sigma(b\bar{b}A)_{\mathrm{SM}} \frac{\tan^2\beta}{(1+\Delta_b)^2} \times \frac{9}{(1+\Delta_b)^2 + 9}, \tag{1.53}$$

where $\sigma(b\bar{b}A)_{SM}$ is defined as the production cross section for the SM Higgs boson at an same mass value as m_A. An analogous expression can be formulated for the H boson assuming near degeneracy in mass with the CP-odd Higgs state. The total cross section of the b-quark associated $\phi \to b\bar{b}$ production is subsequently given by:

$$\sigma(b\bar{b}\phi)B(\phi \to b\bar{b}) \simeq 2 \times \sigma(b\bar{b}A)B(A \to b\bar{b}). \tag{1.54}$$

The large number of free parameters present in the MSSM renders an exhaustive scan of the parameter space of the theory inconvenient for the purpose of this work, as well as of the majority of physics analyses. To this end, a series of benchmark scenarios have been devised to probe a particular configuration in MSSM parameter space consistent with the observation of a Higgs-like particle with a mass of 125 GeV. The number of free parameters is limited to the tree-level parameters m_A and $\tan\beta$ plus the vector gauge boson masses. An overview of the main MSSM benchmark scenarios is discussed below.

1.2.6 Benchmark scenarios

Several MSSM benchmark scenarios have been conceived and updated over time, incorporating the constraints deriving from the interpretation of Run 1 [67, 73] and Run 2 [74] data collected at the LHC. Most importantly, the major discovery of a SM-like Higgs boson whose mass and couplings are compatible with the lightest CP-even scalar present in the MSSM is included. Alternative assignments of the observed scalar particle to the heavier CP-even state are strongly disfavoured by data [75, 76]. In addition, the non-observation of additional Higgs states and of supersymmetric particles further constrains the parameter space of these models. Despite the high accuracy in the determination of the observed Higgs boson mass, a conservative uncertainty of ± 3 GeV is assumed in order to account for the unknown impact of the higher-order SUSY corrections. The predicted mass value for the lightest MSSM CP-even scalar state is set to 125 GeV [67].

The hMSSM benchmark scenario

The hMSSM ("habemus MSSM") phenomenological scenario follows a peculiar "model independent" approach. The theoretical predictions regarding the features of the MSSM Higgs sector are by construction independent from the SUSY parameter space.

This approach is based upon a series of simplifying assumptions relating the SUSY sector. Firstly, the discovered Higgs boson is identified as the lightest MSSM CP-even boson. Secondly, only the top/stop loop induced radiative corrections to the Higgs boson mass, succinctly formulated in Eq. 1.44, are taken into consideration. Lastly, because of the non-observation of supersymmetric particles at the LHC, their characteristic mass scale M_S is lifted to values well beyond the TeV scale, so that any other alteration of the Higgs sector properties is discarded.

Following these assumptions, the heavy CP-even scalar mass can be obtained from the stop sector radiative corrections as follows:

$$m_H^2 = \frac{(m_A^2 + m_Z^2 - m_h^2)(m_Z^2 \cos^2\beta + m_A^2 \sin^2\beta) - m_A^2 m_Z^2 \cos^2 2\beta)}{m_Z^2 \cos^2\beta + m_A^2 \sin^2\beta - m_h^2}, \tag{1.55}$$

whereas the formula for the $H^\pm$ boson masses is identical to the tree-level expression shown in Eq. 1.42. Under this simplified scenario, the Higgs sector can be parameterised solely in terms of $\tan\beta$ and m_A, without any further assumption regarding the SUSY parameters. Owing to the lack of SUSY radiative corrections to the bottom Yukawa coupling, the hMSSM scenario is only an approximate representation of the MSSM for intermediate $\tan\beta \gtrsim 10$. The most recent coupling measurements of the observed h(125) state performed with the full Run 2 data at ATLAS [47] exclude a rectangular region in the $[\tan\beta, m_\mathrm{A}]$ plane of this scenario, corresponding to an observed limit on $m_A < 520$ GeV for $\tan\beta < 25$ at 95% confidence level.

The $m_\mathrm{h}^\mathrm{mod}$ benchmark scenario

The $m_\mathrm{h}^\mathrm{mod}$ scenario [73] is an upgraded version of the $m_\mathrm{h}^\mathrm{max}$ scenario [77], initially conceived to maximise the lightest CP-even Higgs boson mass in the context of LEP Higgs searches [78]. Prior to the discovery of a Higgs-like resonance at the LHC, the higher order SUSY correction from the stop sector in the $m_\mathrm{h}^\mathrm{max}$ scenario were tuned to lift the mass of the lightest CP-even MSSM state m_h well above 130 GeV for $\tan\beta \gtrsim 10$ in the decoupling region. The $m_\mathrm{h}^\mathrm{max}$ scenario is compatible with the observed scalar state exclusively for low $\tan\beta$ values. Consequently, a new SUSY parameter configuration has been proposed in the modified $m_\mathrm{h}^\mathrm{mod}$ scenario. The agreement of the light h boson state with the observed SM-like Higgs boson over a large region of the $[\tan\beta, m_\mathrm{A}]$ plane is ensured by decreasing the contribution from the stop sector in the radiative corrections to the Higgs boson mass, achieved by requiring :

$$|X_t/M_\mathrm{SUSY}| \lesssim 2.0, \tag{1.56}$$

where the SUSY parameter M_SUSY denotes the squark mass for the third generation sfermions and X_t is the mixing parameter defined as $X_t = A_t - \mu\cot\beta$. Two possible variants of this scenario have been proposed, namely the $m_\mathrm{h}^\mathrm{mod+}$ and $m_\mathrm{h}^\mathrm{mod-}$ scenarios, based on the definition of the sign and absolute value of this ratio. On one hand, the positive sign of the quantity μM_2 is in good agreement with the anomalous muon magnetic moment $(g-2)_\mu$ measurement, whereas the product μA_t is in better agreement with the observed flavour anomalies in rare B-meson decays, particularly in the $BR(b \to \gamma s)$ observable. The parameter settings common to the $m_\mathrm{h}^\mathrm{mod+}$ and $m_\mathrm{h}^\mathrm{mod-}$ benchmark scenarios are summarised below:

$$\begin{aligned} &\mu = M_2 = 200\ \text{GeV}, && m_t = 173.2\ \text{GeV}, && M_\mathrm{SUSY} = 1000\ \text{GeV}, \\ &M_1/M_2 = 5/3\tan^2\theta_\mathrm{w}, && M_{\tilde{g}} = M_{\tilde{q}_{1,2}} = 1500\ \text{GeV}, && M_{\tilde{l}_{1,2}} = 500\ \text{GeV}, \\ &M_{\tilde{l}_3} = 1000\ \text{GeV}, && A_b = A_\tau = A_t = X_t + \mu\cot\beta, && A_{f\neq t,\ b,\ \tau} = 0. \end{aligned} \tag{1.57}$$

In comparison with the hMSSM scenario, this configuration of the MSSM parameter space implies the prediction of lighter SUSY particles, in particular in the case LSP candidates such as neutralinos and charginos. The subsequent reduction of the MSSM boson fermionic decay modes such as $b\bar{b}$ and $\tau^+\tau^-$ is significant for $\tan\beta \lesssim 20$. In this region of phase space, the decay of the MSSM Higgs bosons into a pair of charginos or neutralinos can attain a value up to $\sim 80\%$.

Other scenarios

Additional benchmark scenarios have been proposed that achieve consistency with the observed Higgs resonance. The light–stop scenario requires a large value of $|X_t|$ and a low value of M_{SUSY} to maximise the value of m_h. This leads to a value of $M_{\tilde{t}} \sim 324$ GeV, which is expected to make a sizeable impact on the effective rate of the gluon-fusion process. Differently from the light $\tilde{t}$ scenario, in the light–stau scenario the existence of relatively light $\tilde{\tau}$ with a mass around 250 GeV should yield a substantial alteration of the lightest CP-even boson decay $h \to \gamma\gamma$, which, however, has not been observed in data. Aside from the loop-induced modifications of the MSSM Higgs boson vertices, propagator-type corrections affecting the CP-even mixing angle α are taken into account in the τ-phobic scenario. The latter is also characterised by the presence of light stau particles. In addition, in this scenario, SUSY radiative corrections suppress the coupling of the lightest MSSM scalar to down-type fermions.

Recently, new benchmark scenarios have been proposed in [79] incorporating all constraints from negative BSM searches with Run 2 data. The $m_{\mathrm{h}}^{\mathrm{mod}}$ scenario has been replaced by a new vanilla benchmark scenario, referred to as the m_{h}^{125} scenario, which fixes all supersymmetric particles masses at an energy scale above the TeV level. Nevertheless, these scenarios have not been included in this work owing to their recent appearance.

1.2.7 The Two Higgs Doublet Model

Theoretical models comprising an enlarged Higgs sector provide a fertile ground for many BSM signatures due to their richer phenomenology. However, there are several experimental and theoretical constraints defining the possible extensions of the Higgs sector. One major restriction is posed by the ρ parameter, defined as the ratio $M_W^2/(M_Z^2 \cos\theta_W{}^2)$, which is experimentally measured very close to unity [30]. This condition is automatically realised at tree-level in the SM. The most natural minimal extension of the Standard Model satisfying this constraint is the addition of an extra gauge singlet or alternatively of another Higgs doublet. The Two-Higgs Doublet Models (2HDM) [15] feature two complex $SU(2)$ doublets and in general may introduce CP- and charge violating terms[19] in

[19] Additional sources of CP violation represent one of the three Sakarov conditions necessary to account for the baryon asymmetry in the universe.

Model	u_R^i	d_R^i	e_R^i
Type I	Φ_2	Φ_2	Φ_2
Type II	Φ_2	Φ_1	Φ_1
Lepton-specific	Φ_2	Φ_2	Φ_1
Flipped	Φ_2	Φ_1	Φ_2

Table 1.2: The four types 2HDM Models leading to natural flavour conservation. The coupling of the right-handed up- (u_R) and down- (d_R)-type quarks as well as of charged leptons (e_R) to either Higgs doublet Φ_1 is illustrated. The superscript i indicates the fermion family index.

the Higgs potential. Imposing CP conservation whilst preserving the SM gauge group structure, the 2HDM potential takes the following form:

$$\begin{aligned} V_{2HDM}(\Phi_1, \Phi_2) = m_{11}^2|\Phi_1|^2 + m_{22}^2|\Phi_2|^2 - m_{12}^2[\Phi_1^\dagger\Phi_2 + \Phi_2^\dagger\Phi_1] + \frac{\lambda_1}{2}|\Phi_1|^2 + \\ + \frac{\lambda_2}{2}|\Phi_2|^2 + \lambda_3|\Phi_1|^2|\Phi_2|^2 + \lambda_4\Phi_1^\dagger\Phi_2\Phi_2^\dagger\Phi_1 + \frac{\lambda_5}{2}\left[(\Phi_1^\dagger\Phi_2)^2 + (\Phi_2^\dagger\Phi_1)^2\right], \end{aligned} \tag{1.58}$$

where the quartic terms have been discarded. The symbols $m_{11},\ m_{22},\ m_{12}$, denote the mass matrix parameters while $\lambda_1,\ \lambda_2,\ \lambda_3,\ \lambda_4,\ \lambda_5$ represent the scalar Higgs self-couplings. Despite the increased number of free parameters with respect to the MSSM Higgs potential, two-Higgs-doublet models also acquire five physical Higgs bosons after the occurrence of electroweak symmetry breaking. The non-observation of flavour-changing-neutral-currents (FCNCs) at tree-level poses another stringent phenomenological constraint on the Yukawa sector of the 2HDM.
The Paschos-Glashow-Weinberg theorem [80, 81] dictates that a necessary and sufficient condition to forbid FCNCs at tree-level is that all fermions with a given charge and chirality must transform under the same $SU(2)$ irreducible representation. In the context of the 2HDM, this is guaranteed by the introduction of discrete global symmetries [15] relating the Yukawa interactions of fermions. This condition restricts the number of viable CP-preserving 2HDM models with natural flavour conservation to only four possibilities.

A Z_2 symmetry $\Phi_1 \to -\Phi_1$ is implemented in the Type I 2HDM to force all right-handed quarks to couple to a single Higgs doublet, conventionally chosen as Φ_2. In Type II 2HDM, the right-handed up-type quarks couple to one $SU(2)$ doublet, (usually chosen as Φ_2) whereas the down-type quarks must couple to the other (Φ_1). This is enforced by imposing an additional discrete symmetry $d_R^1 \to -d_R^1$ leading to the same Higgs sector structure as in the MSSM[20].

[20] In the case of the MSSM, however, this configuration of Yukawa couplings is obtained by the imposition of a continuous symmetry.

In Type I and II 2HDM models, the right-handed leptons couple to the same Higgs doublet as the down-type quarks as reported in Table 1.2. However, this is not a prerequisite of the Glashow-Weinberg theorem, hence two additional models are allowed: the Type III 2HDM, also referred to in the literature as the *lepton-specific model*, in which all right-handed leptons couple to one Higgs doublet (Φ_1), and the right-handed quarks to the other (Φ_2); the *flipped model*, or Type IV 2HDM, with the same Yukawa couplings for the quark sector as in Type-II, but with the right-handed leptons now coupling to Φ_1.

A summary of the Yukawa sector for the neutral 2HDM bosons, in terms of the Yukawa coupling to fermions relative to the corresponding SM Higgs boson coupling is illustrated in Table 1.3. The couplings of the gauge bosons to the neutral 2HDM Higgs bosons relative to their couplings to the SM Higgs boson, regardless of the 2HDM type are as follows:

$$\kappa_h^V = \sin(\beta - \alpha), \qquad \kappa_H^V = \cos(\beta - \alpha), \qquad \kappa_A^V = 0. \tag{1.59}$$

The CP-odd pseudoscalar decay into a pair of vector bosons is forbidden owing to the conservation of parity. The couplings of the lightest CP-even state to both fermions and bosons are identical to that of the H boson, when the mixing angle α is shifted by $\pi/2$, as expected from Eq. 1.38. In the case $\alpha = \beta(\beta + \pi/2)$, the gauge-phobic limit for the h (H) boson is reached, meaning that the decays of the CP-even bosons into a pair of vector bosons are suppressed at tree-level.

	type-I	type-II	lepton-specific	flipped
κ_h^u	$\cos\alpha/\sin\beta$	$\cos\alpha/\sin\beta$	$\cos\alpha/\sin\beta$	$\cos\alpha/\sin\beta$
κ_h^d	$\cos\alpha/\sin\beta$	$-\sin\alpha/\cos\beta$	$\cos\alpha/\sin\beta$	$-\sin\alpha/\cos\beta$
κ_h^ℓ	$\cos\alpha/\sin\beta$	$-\sin\alpha/\cos\beta$	$-\sin\alpha/\cos\beta$	$\cos\alpha/\sin\beta$
κ_H^u	$\sin\alpha/\sin\beta$	$\sin\alpha/\sin\beta$	$\sin\alpha/\sin\beta$	$\sin\alpha/\sin\beta$
κ_H^d	$\sin\alpha/\sin\beta$	$\cos\alpha/\cos\beta$	$\sin\alpha/\sin\beta$	$\cos\alpha/\cos\beta$
κ_H^ℓ	$\sin\alpha/\sin\beta$	$\cos\alpha/\cos\beta$	$\cos\alpha/\cos\beta$	$\sin\alpha/\sin\beta$
κ_A^u	$\cot\beta$	$\cot\beta$	$\cot\beta$	$\cot\beta$
κ_A^d	$-\cot\beta$	$\tan\beta$	$-\cot\beta$	$\tan\beta$
κ_A^ℓ	$-\cot\beta$	$\tan\beta$	$\tan\beta$	$-\cot\beta$

Table 1.3: Yukawa couplings to right-handed up(u)- and down(d)-type quarks as well as charged leptons (ℓ) of the neutral Higgs bosons in 2HDM relative to the analogous SM Higgs boson coupling [15].

1.2.8 Comparison with the MSSM

The 2HDM Type-II model is a generalisation of the MSSM without supersymmetric constraints, featuring the same Higgs sector. There are however some distinctive differences between the two models with important phenomenological consequences:

- the type-II 2HDM does not pose a stringent constraint on the lightest CP-even Higgs boson mass;
- the scalar Higgs self-couplings and the mass; mixing m_{12} are free parameters in the 2HDM models;
- the mixing angle α between the CP-even bosons, which in the MSSM is a function of the masses of the Z and the A bosons, is also unconstrained; thus it can vanish at the $b-$phobic point, unlike in the MSSM, where a value of $\alpha = 0$ is disallowed at tree-level;
- in all 2HDM types, a lower (upper) bound on $\tan\beta$ of approximately 0.3 (100) can be derived by enforcing perturbativity on the top (bottom) Yukawa coupling. The allowed parameter space in the MSSM is restricted to $1 \lesssim \tan\beta \lesssim 60$ owing to the different β functions for the Yukawa coupling, which receive additional supersymmetric constraints.

MSSM-like benchmark scenario

Several benchmark scenarios have been proposed by Haber and Stal [82]. Among them the benchmark "Scenario G" is particularly interesting for it resembles MSSM, yet it is not restricted to 2HDM Type-II. This scenario prescribes the following settings for the parameters of the 2HDM Higgs potential:

$$\lambda_5 = 0, \quad m_h = 125 \text{ GeV}, \quad m_{\mathrm{H}} = m_{\mathrm{A}} = m_{\mathrm{H}^\pm}, \quad m_{12}^2 = 0.5 \cdot m_{\mathrm{A}}^2 \sin 2\beta. \tag{1.60}$$

In this configuration of the 2HDM parameter space, three free parameters can be identified, namely m_{A}, $\tan\beta$ and $\cos(\beta-\alpha)$. The latter substitutes without loss of generality the CP-even mixing angle α, which is an additional parameter with respect to the MSSM tree-level parameter space. Consequently, three-dimensional scans of the 2HDM parameter space have been performed to interpret the results in the light of the 2HDM Type-II and flipped model, where the sensitivity of the analysis is prominent. The values of the 2HDM cross sections and branching fractions have been computed with next-to-next-to-leading order precision utilising SusHi v. 1.6.1 [83], 2HDMC v. 1.7.0 [84] and LHAPDF v. 6.1.6 [85] to achieve a fine mesh of the 2HDM parameters m_{A}, $\tan\beta$ and $\cos(\beta-\alpha)$.

1.2.9 Production and decay modes

Owing to the large number of 2HDM models and parameters, it is customary to pursue a strategy in which the parameter space of the 2HDM models under scrutiny is relevant for the physical process being probed. In the 2HDM Type-II and in the flipped model, the bottom Yukawa coupling of the CP-even H and CP-odd A bosons exhibits a tanβ dependence:

$$\kappa_H^d \approx \kappa_A^d = \tan\beta, \tag{1.61}$$

with respect to the SM Higgs boson Yukawa coupling. The relation for κ_H^d holds in the alignment limit[21]. On the other hand, at low values of $|\cos(\beta-\alpha)|$, the bottom Yukawa coupling of the lightest CP-even state tends to the corresponding value of the SM Higgs boson coupling. The dominant neutral Higgs boson production modes in the 2HDM Type-II and flipped model are gluon fusion and b-associated production. The other production modes involving the presence of a weak gauge boson are highly suppressed for analogous reasons as in the MSSM. Because of the enhacement of the Yukawa coupling to down-type quarks, the b-associated production dominates at large tanβ in both 2HDM Type-II and flipped models.

Fermionic decays

The branching fractions of the mass degenerate H and A bosons for a Higgs boson mass value of $m_{\mathrm{A/H}} = 300$ GeV at a moderate value of $\tan\beta = 30$ are displayed in Figure 1.7 for the Type-II 2HDM and the flipped model, respectively. In both models, the tanβ-enhancement of the bottom Yukawa coupling of the A and H bosons renders the $b\bar{b}$ decay mode the dominant fermionic contribution over the full $\cos(\beta-\alpha)$ range for $\tan\beta \gg 1$. In the Type-II 2HDM model, the second most relevant fermionic decay channel $A/H \to \tau^+\tau^-$ is lower in branching fraction by $m_\tau^2/3m_h^2$. This fixed factor is approximately 10% of $B(A/H \to b\bar{b})$, using the running b-quark mass value in the computation. In the case of the flipped model, because of the dependence of the down-type quark (charged lepton) Yukawa coupling on $\tan\beta$ ($\cot\beta$) highlighted in Table 1.3, the $A \to \tau^+\tau^-$ decay mode is suppressed by a factor $\tan^4\beta$ with respect to the $b\bar{b}$ decay mode. In the case of the analogous decay for the H boson, the reduction is maximal near the alignment limit. The slight asymmetry in the $H \to \tau^+\tau^-$ branching fraction is caused by the presence of the tau-phobic point at $\sin\alpha = 0$, as it can be evinced from the Yukawa coupling modifiers listed in Table 1.3. The plots shown in Appendix A highlight that the fermiophobic point of the H boson drifts towards the alignment limit when $\tan\beta$ is increased.

[21] The H boson coupling $\kappa_H^d = \cos\alpha/\cos\beta = \cos(\beta-\alpha) + \tan\beta\sin(\beta-\alpha)$ approaches tanβ in the low $|\cos(\beta-\alpha)|$ region.

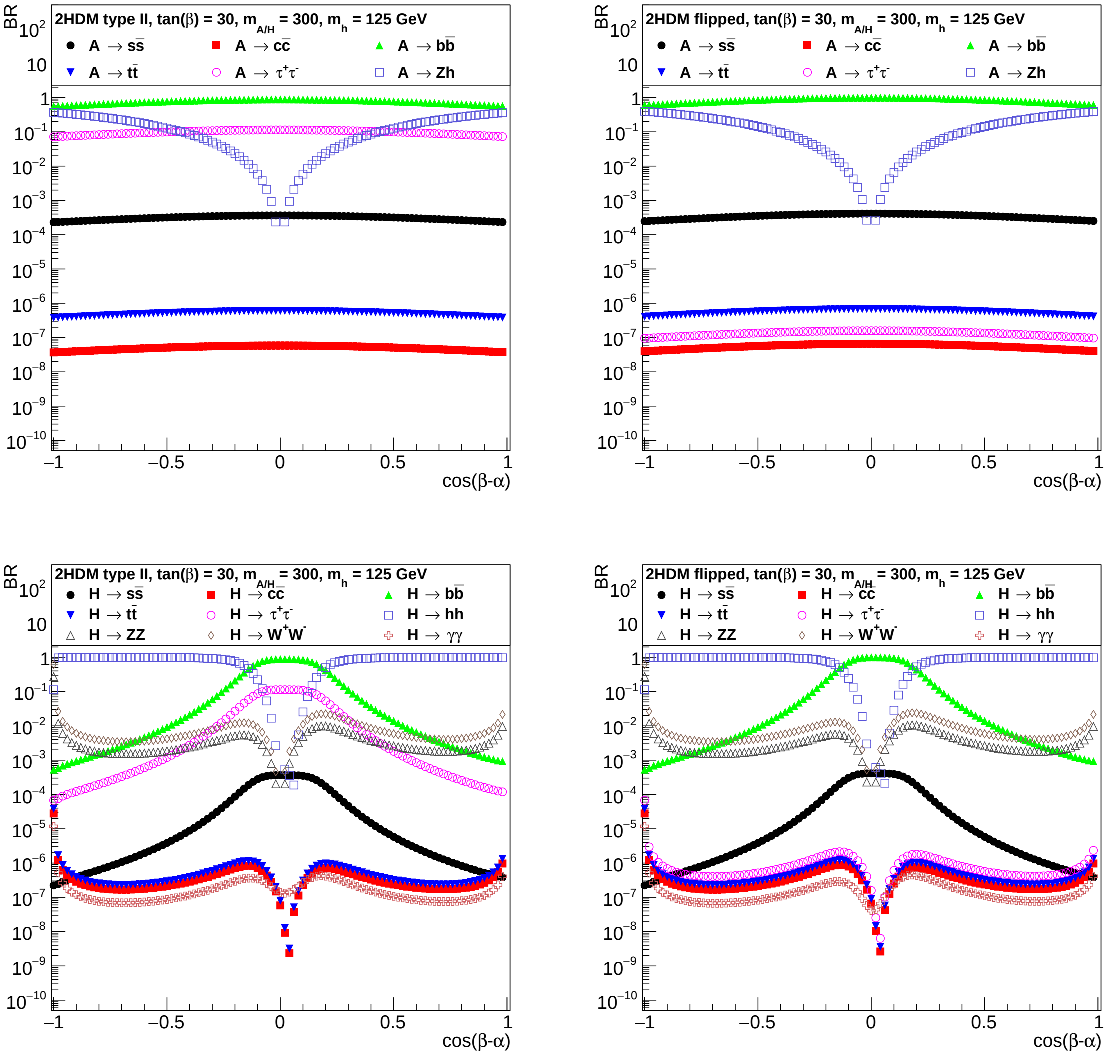

Figure 1.7: Branching fractions of the CP-odd A boson (top row) and of the CP-even H boson (bottom row) computed in the type II 2HDM (left column) and in the flipped model (right column) as a function of $\cos(\beta - \alpha)$ for the benchmark masspoint $m_{\mathrm{A/H}} = 300$ GeV at a moderate value of $\tan\beta = 30$.

Bosonic decays

Inspecting the bosonic decay modes in both models, it can be noted that the $A \to Zh$ partial width becomes comparable to that of $A \to b\bar{b}$ only as $|\cos(\beta-\alpha)| \to 1$ and it vanishes in the alignment limit. The analogous Zh decay channel for the H boson is disallowed as a result of CP invariance. The decay channels into a di-boson pair, in particular the $H \to hh$, make a leading contribution as $|\cos(\beta-\alpha)|$ approaches unity, while the gauge-phobic point for the H boson is reached at zero. Nevertheless, the $H \to b\bar{b}$ process is the prevailing decay mode in the central $|\cos(\beta-\alpha)|$ region.
The alignment limit is of particular interest since all Higgs boson couplings acquire the corresponding Standard Model values. Constraints from the rates of the observed Higgs boson production and decays obtained by Higgs boson coupling measurements performed with Run 2 data collected by CMS [46] and ATLAS [47] exclude a large portion of the $[\tan\beta, \cos(\beta-\alpha)]$ plane. Only the central $|\cos(\beta-\alpha)|$ region is allowed as well as a narrow portion of phase space arising from the possible negative sign of the down-type Yukawa couplings with respect to the SM prediction.

Total production rate of the main process

Overall, the $A/H \to b\bar{b}$ partial decay width in the type-II 2HDM and the flipped model are comparable due to the identical Yukawa structure for quarks. As it will be discussed later, a unique sensitivity for the $b\bar{b}\phi$ production mode in the $\phi \to b\bar{b}$ channel is achieved in the central $|\cos(\beta-\alpha)|$ region for the flipped model. The overall production rate of the process $\sigma(b\bar{b}\phi)B(\phi \to b\bar{b})$ assuming a fixed mass value of $m_h = 125$ GeV for the lightest CP-even state (as required by the MSSM-like parameterisation) is illustrated in Figure 1.8 in the 2HDM Type-II and flipped models. As expected from the $\tan\beta$ dependence of the A/H coupling to b-quarks, the rate of the process is greatly enhanced in the vicinity of the alignment limit. The lightest CP-even Higgs boson contribution to the total production rate is limited to the first mass-point and it is found to be at the sub-percent level for $\tan\beta \gtrsim 10$.

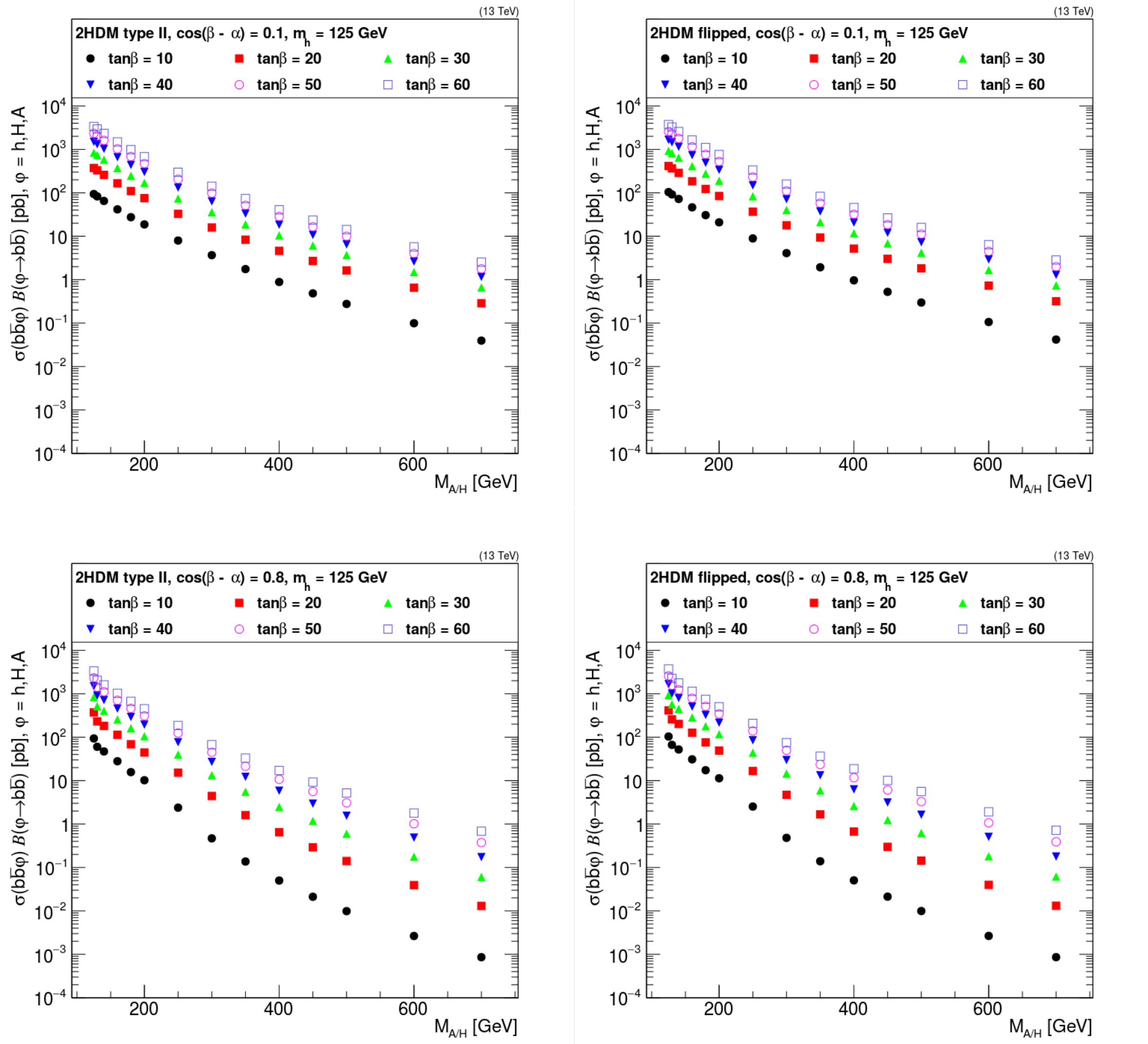

Figure 1.8: Overall production rate of the process $\sigma(b\bar{b}\phi)B(\phi \to b\bar{b})$, versus m_ϕ for a fixed value of the mass of the lightest CP-even boson $m_h = 125$ GeV. The results are shown in the type-II 2HDM model (left column), and the flipped model (right column) for two values of $|\cos(\beta - \alpha)| = 0.1$ (top row) and 0.8 (bottom row) for several values of tanβ.

CHAPTER 2

The Compact Muon Solenoid experiment at the Large Hadron Collider

The Large Hadron Collider (LHC) [86] is the world's largest particle collider operating at an unprecedented center-of-mass energy of 13 TeV. It outperforms in instantaneous luminosity by over twenty times the former largest collider Tevatron, whose collaborations CDF and DØ [12, 87] were credited with the discovery of the top quark in 1995. After that, the Higgs boson was regarded as the last unobserved particle of the Standard Model. The experiments conducted at the Large Electron-Positron collider (LEP) established a lower bound on the Higgs boson mass of 114.4 GeV [68] at the 95% confidence level. The LHC was designed specifically to perform searches for Higgs bosons over a large mass range and to potentially target BSM signatures. The discovery of a SM-like Higgs boson state announced by LHC in 2012 may represent a portal to an unexplored extended scalar sector. The measurements of the present BSM Higgs boson search are based on the proton-proton collision data collected with the Compact Muon Solenoid (CMS) detector [88] in 2017. Following a brief introduction regarding the LHC, an overview of the CMS experimental apparatus is given, with a particular emphasis on the subdetector components relevant for this analysis.

2.1 The Large Hadron Collider

The LHC is located at the European Organisation for Nuclear Research (CERN) in Geneva. It was installed in a circular underground tunnel with a circumference of 26.7 km, originally excavated to host the LEP electron-positron experiment operating between 1989 to 2000. The LHC machine can collide two counter-rotating beams constituted of proton (p) bunches at a center of mass energy of 13 TeV, heavy nuclei such as lead (Pb) at 5 TeV, and also perform Pb-p collisions at 8 TeV.

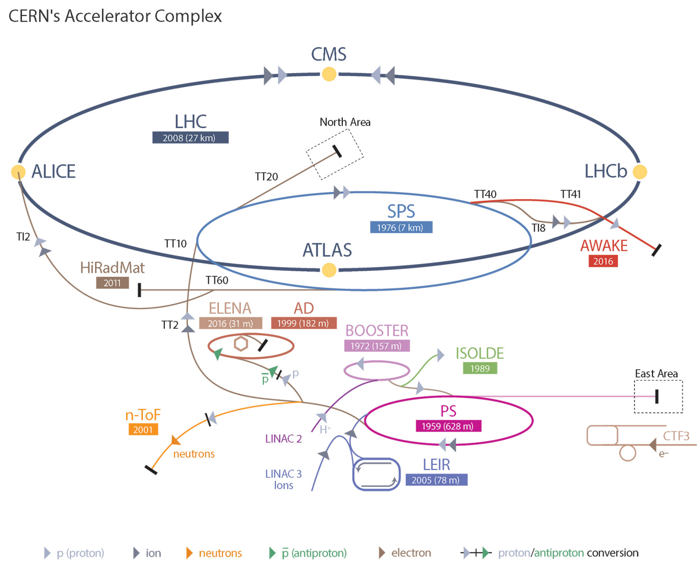

Figure 2.1: Schematic drawing of the LHC accelerator complex at CERN [88].

Protons are initially isolated from a duoplasmatron source by means of strong ionising fields and are subsequently accelerated into a sequence of linear pre-accelerators. The protons are first injected into Linac2, where they are accelerated to an energy of 50 MeV. Then they enter the Proton Syncrotron Booster (PSB), where they are pushed to 1.4 GeV, followed by the Proton Synchrotron (PS), where they reach an energy of 25 GeV. After the last step of this chain, the Super Proton Synchrotron (SPS), the proton beams with an energy of 450 GeV enter into the LHC rings via two tunnels, where they acquire the collision energy of 13 TeV. The acceleration of the protons beams in this last step is performed by means of eight radio-frequency cavities per beam operating at a frequency of 400 MHz, which compensate for the large synchrotron radiation losses.

Under optimal machine operating conditions, the minimum time required to ramp-up the energy of the protons to 6.5 TeV is approximately twenty minutes. The maximum beam energy that can be reached at the LHC is limited by the peak magnetic dipole field in the storage ring, needed to retain the protons in their circular orbit. This field is produced by the 1232 LHC superconducting dipole magnets operating at 1.3 K leading to a magnetic field of 8.33 T. The LHC beams cross in four interaction points (IP) corresponding to the location of the four large-scale detectors, CMS, ATLAS, LHCb and ALICE.

In the case of heavy ion collisions, vaporised ions of the heavy nuclei are injected into LINAC3 and pre-accelerated in the Low Energy Ion Ring (LEIR) before entering the same accelerator chain complex as protons. The ALICE collaboration focuses on the study of the heavy ion collisions reproducing the extremely high temperature and density conditions of the primordial quark-gluon plasma.

The two general-purpose detectors, ATLAS and CMS experiments cover a broad range of precision tests of the Standard Model with a particular emphasis on Higgs boson physics as well as on beyond Standard Model searches in events arising from pp collisions. Both experiments benefit from an excellent jet momentum resolution and flavour tagging, an essential ingredient of the present physics analysis. In addition, ATLAS provides high precision measurements of standalone muon tracks in the muon spectrometer, whilst the CMS detector achieves a unique precision at the LHC of charged particles' momentum.

Finally, the LHCb apparatus consisting of a single forward spectrometer is a large b-hadron factory dedicated to the study of rare heavy flavour decays. Such studies may shed some light on the existence of additional CP-violating mechanisms, which needed to account for the observed baryon asymmetry in the universe. In addition to these four large collaborations, there are two small scale experiments, LHCf whose objective is to investigate forward physics, and the TOTEM detector, dedicated to the study of elastic and diffractive processes originating from pp collisions.

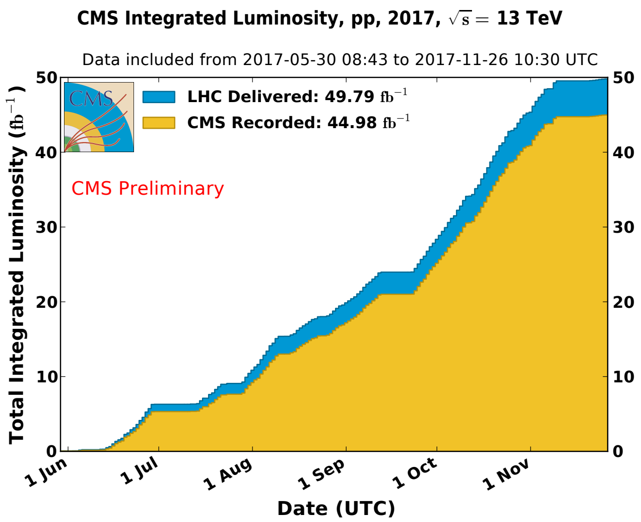

Figure 2.2: Cumulative plot of the per-day luminosity recorded by CMS (yellow) with respect to the total luminosity delivered by LHC (blue) in the 2017 data-taking period [89].

The primary quantity of interest in a measurement at a particle collider is the cross

Beam parameter	Design	2012	2016	2017	2018
beam energy [TeV]	7	4	6.5	6.5	6.5
bunch spacing [ns]	25	50	25	25	25
N_p [10^{11} ppb]	1.15	1.65	1.1	1.15	1.15
N_b	2808	1374	2220	2556	2556
$\mathscr{L}_{peak}$ [10^{34} cm^{-2}s^{-1}]	1	0.75	1.4	2.06	2.01
$<\mu>$	20	21	27	38	37

Table 2.1: The main LHC machine parameters for the data production years 2012 in Run 1, and 2016, 2017, 2018 in Run 2 compared to the design beam configuration [90]. The mean number of interactions per bunch crossing (pile-up) denoted with $<\mu>$ is taken from [89]. To compare the pile-up conditions at different values of the center-of-mass-energy, the theoretical prediction of the pp inelastic cross-section derived with PYTHIA [91] is used, i.e. $\sigma_{in}^{pp}(8\text{ TeV}) = 73.0$ mb and $\sigma_{in}^{pp}(13\text{ TeV}) = 80.0$ mb.

section (σ) of a physical process. The total number of measured events (N_{ev}) is given by the product by $N_{ev} = \sigma \times \mathscr{L}_{int}$ where $\mathscr{L}_{int}$ is the total luminosity delivered over the beam-interaction time. This corresponds to the time integral of the instantaneous luminosity $\mathscr{L}(t)$ generated by the collider, which affects the statistical precision of any physical measurement. It is defined as a function of the LHC beam parameters as :

$$\mathscr{L} = \frac{f N_b N_p^2}{A}, \tag{2.1}$$

which are the bunch revolution frequency f, the maximum number of proton bunches per beam N_b, the bunch population N_p, and the geometric parameter A representing the bunch transverse size. The main limitation to the bunch proton density is coming from the non-linearities in the beam-beam interactions. A summary of the main LHC machine beam parameters is illustrated in Table 2.1 and compared to the design beam configuration for the data production years 2012, during Run 1, and 2016, 2017 and 2018 during Run 2. In the case of ATLAS and CMS, which are designed to operate in a high luminosity regime, the instantaneous luminosity reached an unprecedented peak value of 2.06×10^{34} cm^{-2}s^{-1} for the pp collisions in 2017.

The progressive increase in the instantaneous luminosity from 2012 to 2017 is mostly driven by the stepwise raise in the number of proton bunches, yielding a larger number of inelastic pp collisions. The subsequent high-occupancy environment in the track and vertex reconstruction is referred to as pile-up (PU). The mean number of pile-up interactions $<\mu>$ was found to be 32 during the 2017 data-taking period, as illustrated in the pile-up profile distribution shown in Figure 2.3. Two types of pile-up interactions can be distinguished, namely in-time (IT) and out-of-time (OOT) pile-up. The former occurs within the same bunch crossing as the hard scattering vertex, whereas the latter arises from soft particles produced in previous collisions, reaching the detector during subsequent collisions. The presence of a high pile-up environment poses a serious challenge for many physics analyses. A large pile-up contamination can have an adversarial effect on the accurate identification of the true hard scattering vertex, and also affect the reconstruction of kinematic quantities, such as the missing transverse energy.

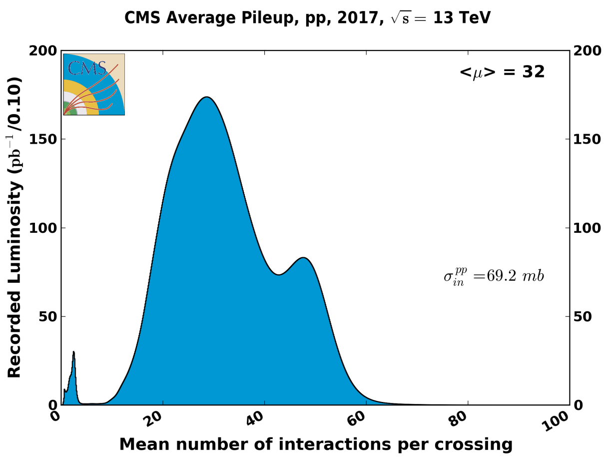

Figure 2.3: Mean number of interactions per bunch crossing (pile-up) for the 2017 proton-proton run at 13 TeV [92]. The value of the pp inelastic cross-section $\sigma_{in}^{pp} = 69.2$ mb provides the best agreement with the 2017 data collected with the CMS detector.

2.2 The Compact Muon Solenoid

The Compact Muon Solenoid (CMS) experiment is one of the two general purpose detectors operating at the LHC. It is installed in a 100-meter deep cavern situated in the proximity of the French village of Cessy. The detector was designed to cover a broad scope of physics analyses at the TeV scale, ranging from precision measurements of the electroweak observables to beyond standard model Higgs boson searches. Its main design feature is the highly homogeneous magnetic field of 3.8 T provided by a superconducting solenoid, which renders it more compact in size with respect to the other general purpose detector, ATLAS[1]. The solenoidal field provides a large bending power needed to measure accurately the momentum and charge of particles with energies up to 1 TeV. The fine granularity of the CMS detector over a large geometrical coverage allows achieving excellent muon identification and momentum resolution. The other detector design goals are

[1]In contrast with CMS, the ATLAS detector comprises both a central solenoid magnet and toroidal magnet system.

high resolution of the electromagnetic and hadronic energy deposition, as well as excellent tracking and vertexing. Owing to the large particles' flux originating from the interaction region, all detector components including front-end electronics must be able to withstand a large dose of radiation harnessing.

In order to distinguish more efficiently between different particle signatures, the CMS detector was built with an onion-like structure, where each subdetector targets a particular particle response. A schematic diagram of the CMS detector and its main components discussed in detail later in this chapter are illustrated in Figure 2.4. The innermost subdetector is the silicon tracker, which is surrounded by a crystal-scintillator hadronic calorimeter (ECAL); the brass-scintillator electromagnetic calorimeter (HCAL); both the tracker and the calorimeters are accomodated within the magnetic field volume; a steel return yoke is utilised to measure the energy of the muons by means of gas-ionising muon chambers inserted between the iron plates. The CMS apparatus possesses an overall cylindrical symmetry, with a diameter of 15 m, a length of 21.6 m and it weighs approximately 14000 tonnes.

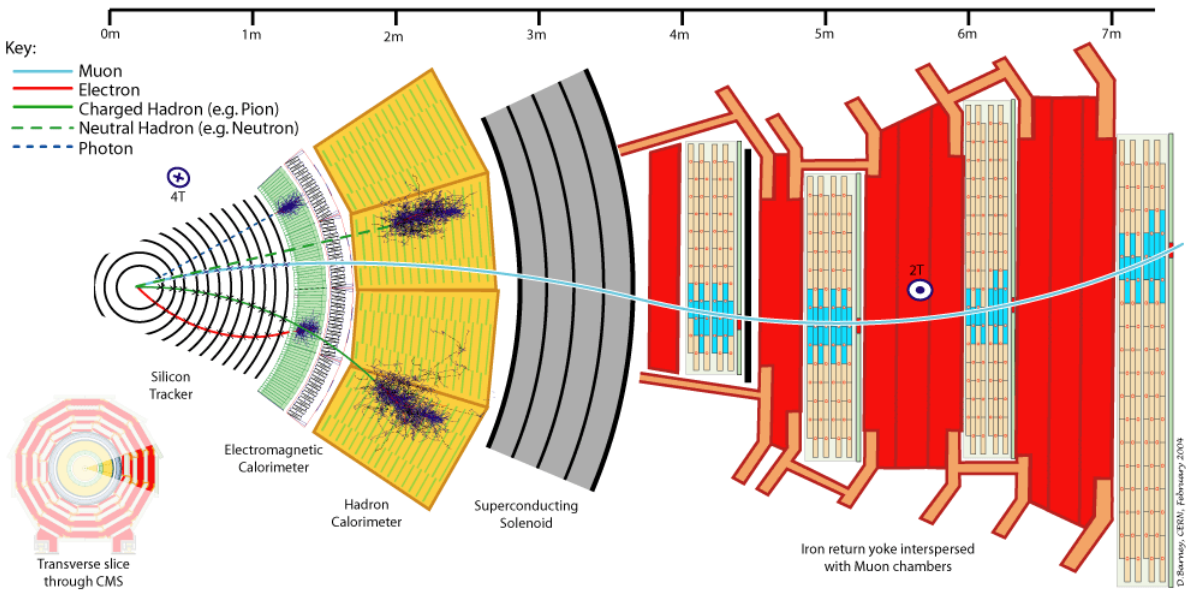

Figure 2.4: A simplified transverse view of the CMS detector cross section [93]. The typical signatures of the five particle collections detected are shown.

It is convenient to adopt a right-handed coordinate system to describe the CMS detector. Its origin is defined as the interaction point located at the center of the detector. The Cartesian axes are oriented such that the x-axis points towards the center of the detector, the y-axis is orthogonal to the LHC plane, while the z-axis is directed along the anticlockwise beam direction.

Kinematic variables

In high energy-physics, particles are often described by their rapidity, defined as follows:

$$y = \frac{1}{2} \ln \frac{E + p_z}{E - p_z}. \tag{2.2}$$

Differences in rapidity are invariant under Lorentz boosts along the z-axis. The rapidity goes to zero for a particle travelling perpendicular to the beam axis, whereas it tends to infinity for a particle parallel to the beam line. A convenient, equivalent kinematic quantity used in several physics analyses is the pseudo-rapidity, which coincides with the rapidity in the ultra-relativistic limit :

$$\eta = -\ln \left(\tan \frac{\theta}{2} \right), \tag{2.3}$$

where θ represents the polar angle with respect to the z-axis, while the ϕ is the azimuthal angle measured in the x-y plane. The alternative parameterisation in terms of the coordinates $r = \sqrt{x^2 + y^2}$ and the azimuthal angle ϕ can also prove insightful since it exploits the cylindrical symmetry of the detector components. The difference in rapidity is used to define the angular distance between two physical objects i and j in the $\eta - \phi$ plane:

$$\Delta R(i,j) = \sqrt{(\Delta\eta(i,j))^2 + (\Delta\phi(i,j))^2}, \tag{2.4}$$

which is also invariant under Lorentz boosts in the z-direction. The transverse momentum p_T of a particle, i.e. its projection in the x-y plane, is extremely useful to distinguish the partons produced in the hard scattering vertex from the beam remnants of the underlying event, which are usually associated with much lower transverse momentum transfer. Some particles, such as neutrinos and those predicted in several BSM scenarios, can escape detection since they barely interact with matter. By exploiting momentum conservation in the transverse plane, the *missing transverse energy* (MET) of any undetected particles can be obtained from the total p_T imbalance

$$\not{E}_T = -\left| \sum_{measured} \vec{p_T} \right|, \tag{2.5}$$

computed from the negative vectorial sum of all detected particles in the event.

2.2.1 The CMS tracker

The CMS inner silicon tracker provides an excellent measurement of the charged particles trajectory, conventionally referred to as *tracks*. The latter are reconstructed by combining the electrical signal (hits) of the outgoing charged particle as it propagates through the different layers of the tracker, which is composed of silicon modules. The bending of the tracks trajectory operated by the homogeneous magnetic field B allows performing a measurement of the charged particle transverse momentum p_T. The sign of the curved track permits to identify the electric charge of the particle. The reconstruction of primary and secondary vertices position relies on the accuracy in the track reconstruction[2]. The tracking detector also enables the measurement of the lifetime of several particles, such as b-hadrons and tau leptons, and to measure efficiently the track impact parameters of intermediate states, which cannot be matched to any primary vertex. The active area of the inner silicon tracker corresponds to a total surface of 200 m^2, covering a pseudorapidity range extending up to $|\eta| < 2.5$.

The usage of silicon as a material offers several benefits for precision tracking. Firstly, the high mobility in the charge carriers implies a low charge collection time, around 20 ns, yielding a significantly faster signal processing with respect to gaseous detectors, at the μs level. Owing to its high density, a large amount of electron-hole pairs, approximately 110 pairs per micron, are generated when a minimum ionising particle propagates through silicon. Furthermore, its low ionisation energy threshold of 3.6 eV provides a large sensitivity to energy deposition, which is needed to achieve optimal energy resolution. Another advantage of using silicon as a tracking material is that it can be conveniently segmented into multiple, independent, tiny sensing structures, thus achieving good spatial resolution. The reduced geometrical area lowers the initial noise levels as well as the relative occupancy per channel.

The local hit reconstruction starts from the digitised raw electric signal of the readout system. First, the signals from close-by channels fulfilling a certain signal-to-noise threshold are clustered together taking into consideration the noise calibration. After that, the local cluster charges are converted into hit candidates. A local set of coordinates defining the silicon module is used to provide hit positional information. The final output of the local hit reconstruction consists of the cluster charge profiles as well as the hit position.

The CMS tracker is composed of two subdetectors: a high-granularity pixel detector situated in the innermost region of the detector, in close proximity with respect to the beam pipe, and a silicon strip tracker with a radial distance from the interaction point comprised between 0.2 and 1.2 m. A transverse cross-section of the inner tracker detector is shown in Figure 2.5.

[2] Only track candidates emerging from a common interaction point are used for vertexing.

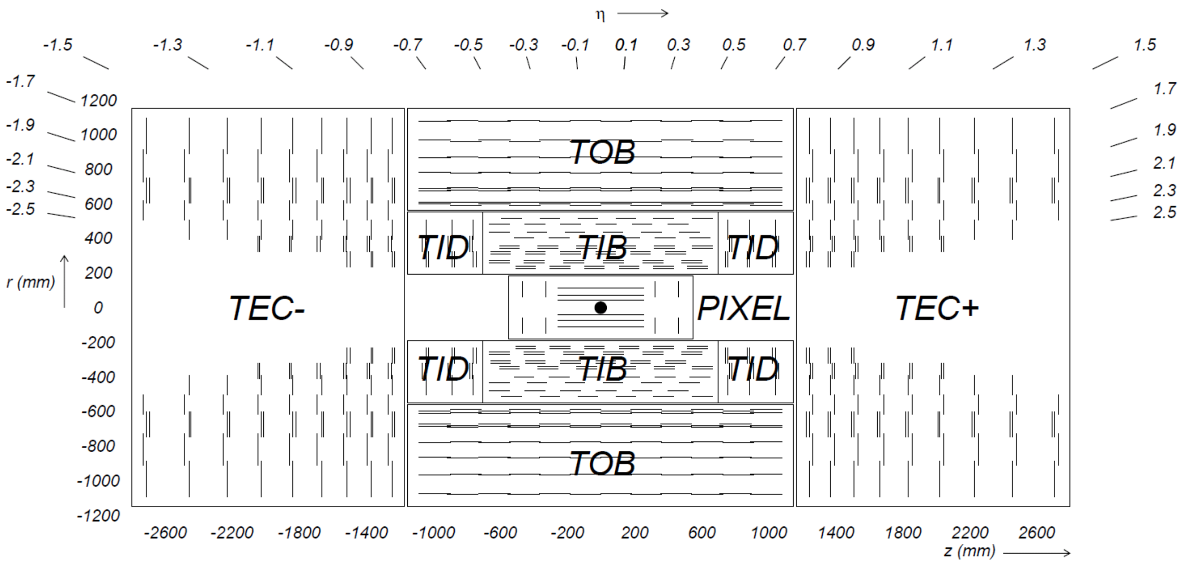

Figure 2.5: Sketch of the CMS inner tracker detector geometry in the $r-z$ plane in 2016. The expected position of the interaction point is highlighted with a black dot. Each line-element denotes individual detector modules, whilst double lines represent modules that are arranged back-to-back for stereo angle interpolation. [94].

The Silicon Pixel Detector

The high-occupancy environment of the inner tracking system is the primary cause of the radiation ageing of the detector, which can result in an increase in the leakage currents and subsequent loss of data. To counteract these issues, the CMS pixel was upgraded during the end-of-year technical shutdown, which took place in the 2016/2017 winter, referred to as the *CMS Phase-I Pixel Upgrade*. The aim of the upgrade was to preserve the excellent tracking performance under conditions of increased peak luminosity, i.e. with a mean number of 50 primary vertices.

The Phase I pixel detector is the innermost tracking subsystem and it consists of two parts, the Barrel Pixel (BPIX) and the Forward Pixel (FPIX) detectors. The BPIX is composed of four coaxial barrel layers located at a radial distance of 2.9, 6.8, 10.9 and 16.0 cm. The FPIX consists of three end cap disks per side constituted by several blades positioned at a distance of 29.1, 39.6 and 51.6 cm from the nominal interaction point (IP). Unlike the BPIX modules which are parallel to the beamline, the FPIX sensors are arranged into blades, oriented with a tilt of 20° with respect to normal incidence in order to exploit the Lorentz drift effect[3]. Figure 2.6 shows the geometry of the newly

[3]The non-parallel arrangement of the blades causes the deflection of the particle trajectory by a small Lorentz angle θ_{LA}. This *Lorentz drift* effect induces additional charge-sharing in the neighbouring silicon

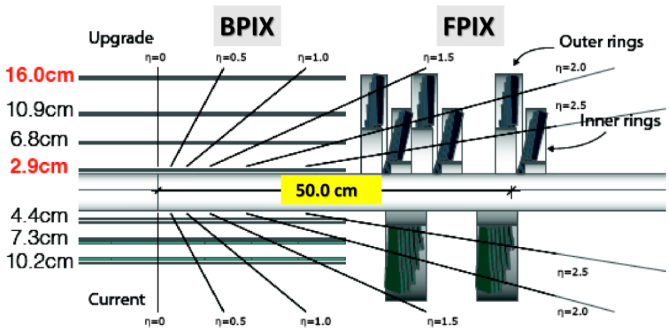

Figure 2.6: Geometrical scheme of the Phase-I pixel detector (top) compared with the 2016 legacy system (bottom) [95].

installed pixel detector with respect to the 2016 legacy system. The improvement in vertex resolution and b-tagging performance is driven by the increased redundancy and finer granularity of the pixel system, and by the innermost barrel layer location closer to the IP.

The Phase I pixel detector features almost 124 million silicon sensors, with an individual pitch of 100 μm$\times$ 150 μm. The doubling of the amount of pixel channels with respect to the previous geometry permits to resolve four single hits per trajectory over the full $|\eta| < 2.5$ coverage. A new power conversion scheme based on 1200 DC-DC converters was installed using the Phase-I Upgrade to cope with the increased power consumption. The latter is due to the doubling in the number of readout channels, whilst keeping the pre-existing cabling system [96]. These converters are able to deliver the necessary voltage in the range 2.4-3.3 V to the pixel front-end modules of the data acquisition (DAQ) system reducing the initial input voltage of 10V. During the last 2017 data-taking period, referred to as era F, a design problem was aggravated by the sub-optimal operation of the pixel detector. Approximately 5% of such converters located in the innermost barrel pixel layer failed and another 35% were found to be damaged due to irradiation and were subsequently successfully replaced during the end-of-year 2017/2018 technical stop [97].

The Silicon Strip Detector

The strip silicon tracker is located outside of the pixel detector at a radial distance comprised between 20 and 116 cm. It consists of 15148 silicon modules, with approximately 9.3 million strips and it extends over a pseudorapidity range up to $|\eta| < 2.5$. The strip subsystem features an analogous barrel-endcap partition as in the case of the pixel detector. The barrel region is subdivided into the Tracker Inner Barrel (TIB) and the Tracker Outer Barrel (TOB), while the end-cap system is partitioned into the Tracker Inner Disks

sensors, thereby improving the hit resolution.

(TID) and the Tracker End Cap (TEC).

The inside of the tracker barrel is occupied by the four cylindrical layers of the TIB subdetector, extending up to ±65 cm along the z axis, and the three TID disks covering up to a radius of 55 cm. The double-sided modules arranged back-to-back present in the first two TIB layers allow for a hit measurement both in cylindrical coordinates with a 23-34 μm spatial resolution in the $r - \phi$ plane and of 530 μm in the z-direction. The TIB/TID system is enclosed by the six barrel layers of the TOB, which extends to a radius of 116 cm and up to ±118 cm in the direction of the proton beam. The TOB sensors are almost a factor two wider than the TIB due to the expected lower fluence. Coverage in the z region $124 \leq |z| \leq 282$ cm is ensured by the TEC subdetector, composed of nine disks of various sizes, providing hit positional information in the $r - \phi$ plane with a resolution in the range $18 - 47$ μm.

2.2.2 Calorimeters

Complementary to the tracker, which provides information on charged particles trajectories and their transverse momenta, the purpose of the calorimeters is to measure the total energy of both electrically charged and neutral particles by complete absorption. The detection principle relies on the detection of the shower of secondary particles induced by cascading effects within the calorimeter volume. Two main classes of calorimeters have been designed based on the type of *sensitive* material used to collect the signal, and the *passive* medium needed to induce the shower in the calorimeter. A *homogeneous* calorimeter is built from a sensitive material, and its energy resolution is limited exclusively by sampling fluctuations, such as shower leakage and detector effects. On the contrary, a *sampling* calorimeter alternates layers of a high-density, passive medium needed to induce cascading effects, with layers of an active material. Furthermore, calorimeters can be further categorised into electromagnetic and hadronic ones, measuring showers induced respectively by electromagnetically charged and neutral particles.

The distinctive properties of the detecting material can be used to parameterise the size of showers. The Molière radius R_M, defined as the radius of a cylinder containing on average 90% of the total energy deposition of a shower, sets the scale of its typical transverse size. The depth of electromagnetic showers is measured in terms of the radiation length X_0, i.e. the mean distance travelled by an electron in the detecting material over which its total energy is decreased by a factor e^{-1}. In the case of hadronic showers, it is customary to use as a reference the *nuclear interaction length* λ_I, i.e. the average distance covered by a hadron prior to the occurrence of an inelastic nuclear interaction.

The CMS calorimeter was designed to have a compact size in order to be fully embedded within the CMS solenoidal magnetic field. As a result, the particles traversing

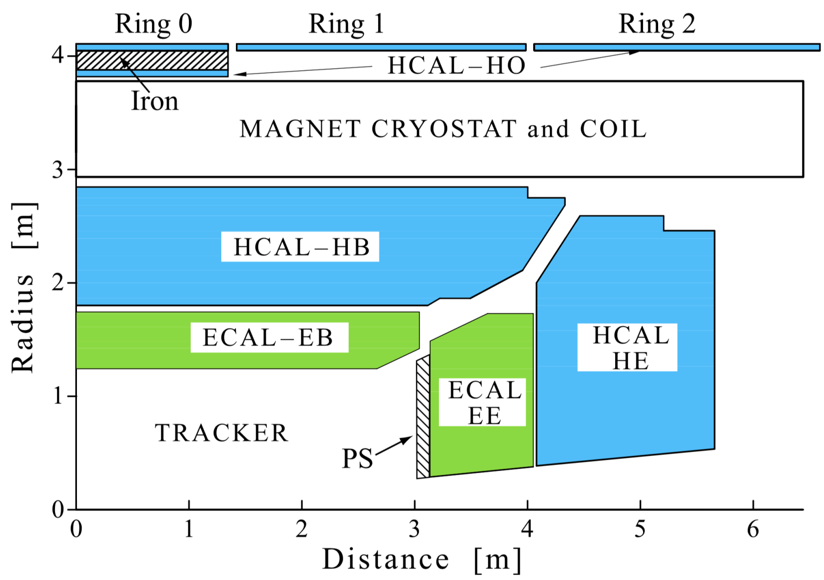

Figure 2.7: A quarter of the longitudinal cross section of the CMS calorimeter. The electromagnetic and hadronic calarimeter are highlighted as the green and blue areas respectively. The magnet cryostat, coil and three ring structures are also shown [98].

the tracker retain most of their initial energy before the measurement of their energy deposits in the calorimeter. It is composed of two separate subsystems, the electromagnetic calorimeter (ECAL) and the hadronic calorimeter (HCAL). Showers induced by photons, electrons and other charged particles, commonly referred to as electromagnetic showers, are detected in the ECAL. Energy deposits from hadrons and from the associated hadronic showers are instead measured in the HCAL system. Since such showers are more extended than the electromagnetic ones, the HCAL has a larger geometric size and it is placed outside the ECAL. A simplified view of the CMS calorimeter system is illustrated in Figure 2.7. The fine granularity of the calorimetry allows discriminating between different types of particles on the basis of the characteristic shape of the shower, and it also provides relevant information about its direction.

The CMS Electromagnetic Calorimeter

The ECAL calorimeter surrounds the inner tracking system and it covers the pseudorapidity region up to $|\eta| < 3.0$. It is composed of a total of 75848 lead tungstate ($PbWO_4$) crystals, organised into a barrel geometry (EB) covering up to $|\eta| < 1.479$, and an endcap region (EE) extending up to $1.479 < |\eta| < 3.0$ comprising 7324 crystal per side. The $PbWO_4$ crystals are characterised by a high-density of 8.28 g/cm^{-3} and they possess a short Molière radius $R_M \sim 22$ mm and a small radiation length X_0 of 8.9 mm. These unique properties of the detecting material permit a compact design and fine granularity of the crystals, whose dimensions are of $\Delta\eta \times \Delta\phi = 0.0174 \times 0.0174$. The crystals act as scintillators and are equipped with avalanche photo-diodes (APD) in the EB and vacuum photo-triodes in the EE regions respectively. These photodetectors collect the scintillating light emitted by the EM interacting particles. The measurement of the light yield is largely affected by thermodynamic processes, hence a water cooling system was designed to keep the ECAL at a constant temperature of 18°C. A pre-shower subdetector (ES) consisting of two additional layers of lead absorbers equipped with silicon strip sensors is used to increase the identification efficiency of unconverted photons, whilst rejecting photons from neutral pion decays.

The ECAL energy resolution σ_E/E for electrons was obtained in a test beam measurement [99]:

$$\frac{\sigma_E}{E} = \frac{2.8\%}{\sqrt{E(\mathrm{GeV})}} \oplus \frac{12\%}{E(\mathrm{GeV})} \oplus 0.3\%, \tag{2.6}$$

where the $\oplus$ symbol denotes the addition in quadrature of the individual uncertainty contributions. The first term represents the stochastic part which dominates for energy deposits of photoelectrons below 100 GeV; the second term stands for the noise contribution; the constant accounts predominantly for calibration inaccuracies and additionally for the non-uniform response of the photodetectors.

The CMS Hadron Calorimeter

The HCAL calorimeter is a sampling detector employed for the measurement of the energy deposits of hadrons. The central part of the HCAL covers a pseudorapidity range up to $|\eta| < 1.3$ and it consists of two distinct subdetectors: the inner barrel part with brass absorbing layers and plastic scintillator tiles (HB) and the outer hadronic calorimeter entirely composed of plastic scintillators (HO) installed outside the solenoid. Because of the limitations in size of the CMS calorimeter, some of the most-energetic hadronic tails may leak outside the full volume of the HB detector. Thus, the HO subdetector has been installed to extend the depth of the HCAL to 11.8 hadronic interaction lengths in order to catch the most energetic hadronic shower tails, utilising the magnet coil as an absorber. The hadron forward calorimeter extends the pseudorapidity range to $|\eta| = 5.0$ and it is located at a distance of 11 m from the beamspot. Since it is affected by hadronic energy depositions seven times more intense than in the rest of the HCAL, it is composed of a more radiation-hard active material, composed of iron absorbers and quartz fibers. It is further equipped with a set of photomultipiers, which detect the cone of Cherenkov light emitted by charged particles passing through the material. The relative HCAL energy response curve for isolated charged pions is illustrated in Figure 2.8. A broader response curve is an indicator of a larger pile-up contamination. Out-of-time pile-up mitigation helps reduce the latter, thereby improving the quality of pion isolation. Aside from

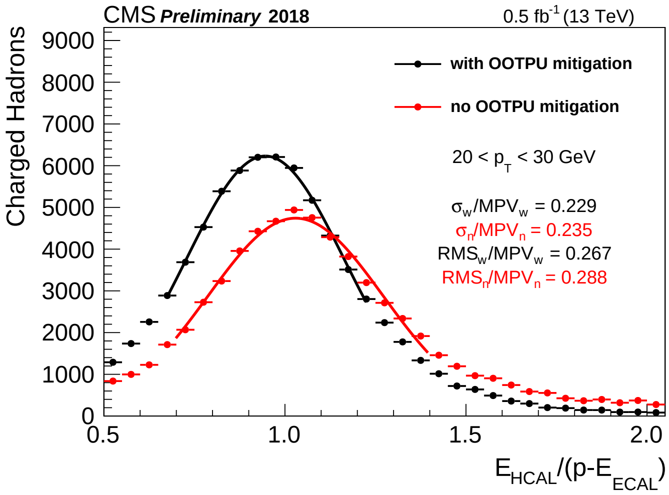

Figure 2.8: Energy response of the HCAL system with respect to the track momentum of the isolated charged pion candidates within the range of $20 < p_{\mathrm{T}} < 30$ GeV [100]. Two different response curves are shown, both with and in the absence of out-of-time pile-up mitigation denoted in black and red dots, respectively.

recognising hadrons and their decay products, the HCAL provides a crucial measurement of the missing transverse energy exploiting its extensive coverage in η, a property referred to as *hermiticity*.

2.2.3 Muon system

Gaseous detectors

In gaseous detectors, a charged primary particle ionises the atoms composing the gas, which are freely moving within the detector volume. An external electric field makes the resulting charge carriers drift, inducing a signal in the readout electrodes. In contrast with solid-state detectors, which have an ionisation energy lower by an order of magnitude, the Equivalent Noise Charge (ENC)[4] is as low as 80 e/cm in gaseous chambers. Thus, a crucial operational principle of such detectors is the internal amplification of the primary particle charge obtained by means of electron avalanches generated by the electric field. The overall gain in charge multiplication can attain a factor 10^{4-6} in the ionisation regime. In general, the fundamental parameters governing the tracking performance are the large detector volume, the high multiplicity of measurement points, the single point resolution and the low amount of multiple scattering. To determine the position of the primary particle with high precision, cathode metal plates can be segmented into strips with high

[4]This quantity is defined as the minimum charge threshold needed to register a signal equal to the noise level.

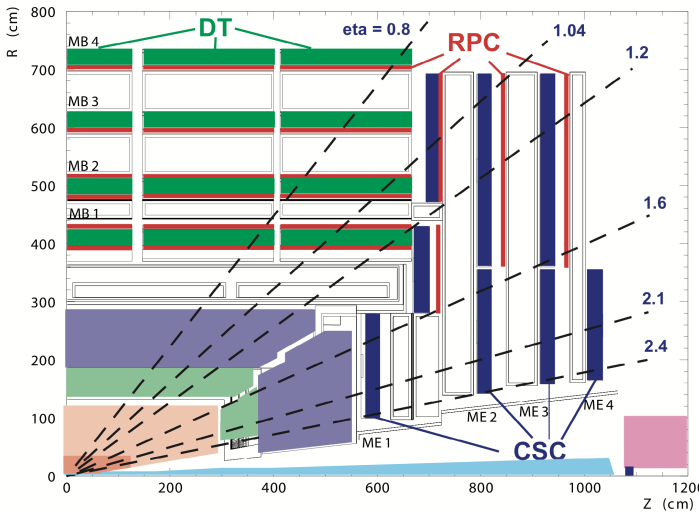

Figure 2.9: A quadrant of the CMS muon system displayed in the $r - z$ plane. [88].

granularity. In order to measure accurately the drift time of charge carrier, cylindrical gas tubes with a large volume are instead used. A description of the CMS muon system which is entirely based on gaseous detectors, follows.

2.2.4 The CMS Muon system

A fundamental design goal of the CMS detector is the efficient identification of muons. These minimum-ionising particles are present in the final state of the "golden" channel used for the Higgs boson discovery $H \to ZZ \to 4\mu$ as well as of several BSM signatures. Because of their lower Bremsstrahlung radiation losses compared to electrons, muons can be reconstructed with a large identification efficiency, whilst achieving a high degree of purity.

The first measurement of the muon p_{T} is performed in the inner tracker exploiting the 3.8 T solenoidal magnetic flux. A complementary second measurement is obtained independently in the muon system, utilising a magnetic flux of 2 T returned by the iron yoke. The latter is also employed as a hadron absorber for the muon flux. The performance of the muon system in the measurement of the muon p_{T} is compared to that of the inner tracker in Figure 2.10 both in the barrel and the endcap regions. In general, the amount of multiple scattering in the tracking material decreases for higher muon p_{T}. As a consequence, the muon system provides a substantial contribution to the momentum resolution for muons with a p_{T} larger than 200 GeV, owing to its large spatial resolution.

The detection planes in the muon chamber cover a total surface amounting to 25000

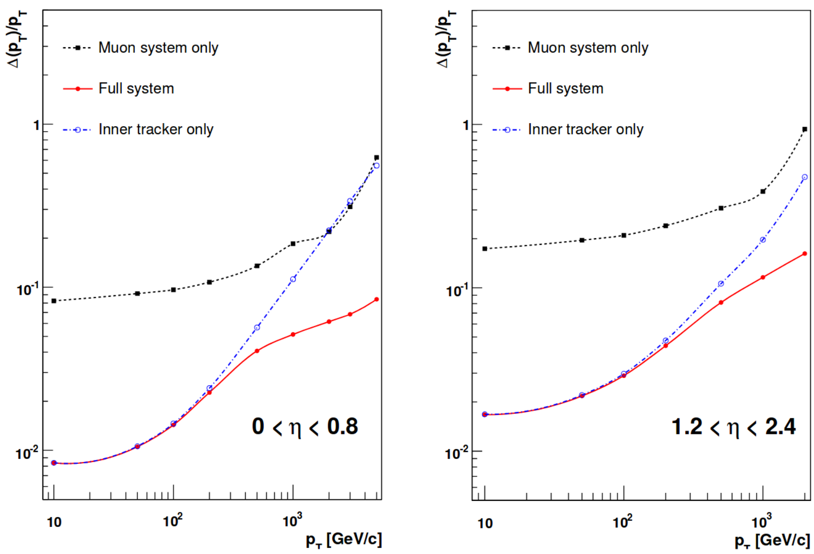

Figure 2.10: Transverse momentum resolution against the p_{T} of a muon identified using information from the muon system , the inner tracking or their combination, respectively in the barrel-only (left) and in the endcap-only (right) regions [94].

m^2 and are composed of a resistant and inexpensive material. The muon system combines three kinds of gaseous detectors, referred to as *muon chambers*, which are portrayed in Figure 2.9: the drift tube stations (DT), covering a pseudorapidity range up to $|\eta| = 1.2$, the cathode strip chambers (CSC) located in the range $0.9 \leq |\eta| \leq 2.4$ and the resistive plate chambers (RPC) probing muons with $|\eta| < 1.6$. The CMS barrel muon system is interested by the least intense muon flux and by the lowest neutron-induced background. Therefore, a drift chamber system with coarse granularity consisting of 12 gaseous tubes is used. In the endcap region, because of the larger signal and background rates [101], a set of 468 cathode strip chambers, with finer granularity and faster response is installed. The precise determination of the muon position in the $r - \phi$ plane is obtained utilising the hits in the CSC, with a spatial resolution in the range 40-150 μm. Analogous information is provided by the double-gap RPC chambers, albeit with a coarser spatial resolution, approximately at the level O(1cm). The resistive plate chambers are well-suited as an independent source for triggering owing to their fast response and optimal timing resolution. Robust standalone muon identification constitutes an essential ingredient of the CMS trigger capability, as discussed in the next section.

2.2.5 Trigger System

The enormous LHC proton-proton collision rate of 40 MHz with a characteristic event size of approximately 1MB poses a serious challenge to the CMS data acquisition system. On

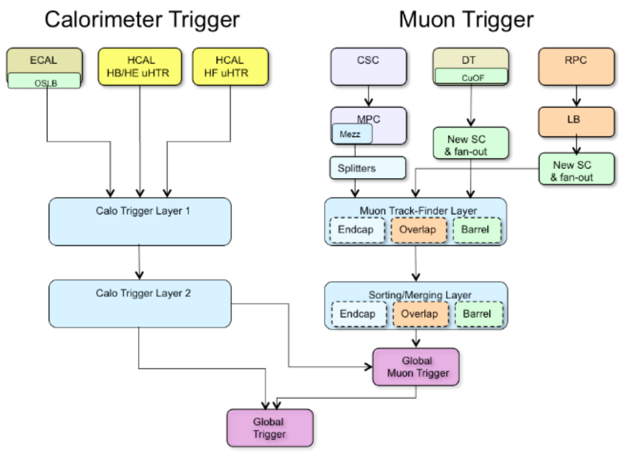

Figure 2.11: Principal block diagram for the CMS Level-1 trigger upgrade [102].

the other hand, the large majority of these data comprises low-energy transfer interactions, rather than the expected hard scattering collisions and rare processes. Consequently, a system that is able to reduce the huge data flow to a manageable rate prior to storage on disk, whilst selecting efficiently the interesting events is necessary. These requirements are met by the so-called CMS triggering system, which reduces the initial bandwidth by over three orders of magnitude. The CMS triggering system adopts a sophisticated two-stage approach, consisting of a Level-1 trigger (L1) fully implemented in hardware logic and a high-level trigger (HLT) software farm. The L1 trigger achieves a rate reduction down to the level of 100 kHz, which is subsequently downscaled to around 1 kHz at HLT level.

Level-1 Trigger

The L1 trigger is the first step of the CMS trigger, which must filter events with a latency time no longer than $4\mu s$. It is implemented exclusively at hardware level using two sets of logic boards: Field Programmable Gate Arrays (FPGAs) which are generic and easily customisable, in contrast with the Application Specific Integrated Circuits (ASICs), which are more resilient to high pile-up conditions, albeit not easily reconfigurable. The L1 trigger processes basic information in a coarse granular format provided by the muon systems and the calorimeters. A simplified view of the L1 trigger system is illustrated in Figure 2.11. The logic of the L1 trigger is based upon the inputs from local, regional and global trigger components, referred to as *trigger primitives*.

The L1 trigger calorimeter is a two-layered procedure consisting of a regional calorimeter trigger (RCT) and a global calorimeter trigger (GCT). In the first step, the trigger primitives from the ECAL and HCAL towers regarding the transverse energy deposits and the quality flags are calibrated and subsequently preprocessed. The GCT receives this kinematic information from the RCT and it builds the actual calorimeter objects such as jets, tau leptons, electrons and photons by means of clustering. Furthermore, global observables such as missing transverse energy are reconstructed using E_T sums. Lepton identification and isolation algorithms are also subsequently applied.

A novel geometry-based approach has been implemented for the L1 muon trigger system during the end-of-year technical shutdown in 2016, upgrading the original detector-based scheme [103]. Instead of processing directly the trigger primitives associated with the DT, RPC and CSC sub-detectors, three complementary track finders targeting the barrel, overlap and endcap regions are used. The hit information is recorded efficiently with complementary measurements and sent via fast optical connections to the regional track finders. The global muon trigger (GMT) combines and correlates the information from different systems and removes duplicate muon candidates. The installation of the new L1 muon trigger successfully halved the total trigger muon bandwidth, whilst yielding a slight increase in the overall muon trigger efficiency. The rate reduction for a single muon trigger with respect to the legacy 2015 muon trigger system is illustrated in Fig 2.12. The improvement is mostly concentrated for low p_T muons in the range $20 - 80\%$ over the full coverage in pseudorapidity.

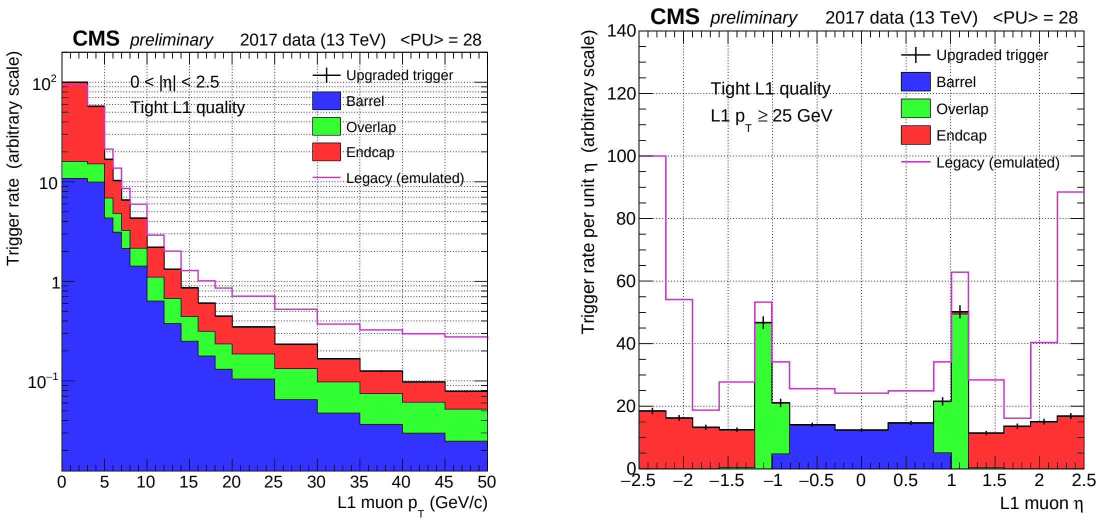

Figure 2.12: Single muon trigger rates passing different p_{T} thresholds of the upgraded L1 muon trigger system (2017) with respect to the emulated legacy trigger system in 2015 (purple line) for the three muon track finders for the barrel (blue), overlap (green) and endcap (red) regions. The decrease in the trigger rates in 2017 is shown as a function of the muon transverse momentum threshold (left) and in pseudorapidity bins for muons with transverse momentum larger than 25 GeV (right) [103].

The combined kinematic and topological information on the event configuration is then transmitted to the global L1 trigger processor for the final decision on whether to accept or reject the event. The L1 acceptance data is subsequently merged and processed by the event builder in the DAQ system for the next triggering step.

High-level Trigger

The high-level trigger (HLT) is a sophisticated, completely software-based triggering system, exploiting tens of thousands of CPUs running multiple analysis algorithms simultaneously. This array of commercial computers elaborate the full event reconstruction according to a series of sequential algorithms, targeting a particular signature of interest, referred to as trigger path. The selection of the events should be as inclusive as possible, while keeping the corresponding rate below $O(100\text{Hz})$. This threshold represents the current level enabled by the recording technology, which has to be met even under conditions of large pile-up.

For all the trigger paths that would exceed the allocated bandwidth, such as the triggers selecting a single physical object, a pre-scaling of the recorded events is conventionally applied to obtain a sustainable output trigger rate. This consists of a random reset of the events passing a sequential step, commonly at Level-1 or prior to the HLT selection, which are subsequently discarded in successive, algorithmic steps.

Another major constraint of the HLT system is that the maximum processing time or *timing* associated with each trigger cannot exceed 50 ms, owing to limitations in the latency of the software farm. In order to optimise the timing, the HLT reconstruction modules that are more computationally intensive are run only at the end of the filtering sequence. These modules perform a streamlined, simplified version of the algorithms exploited in the standard offline reconstruction. A description of the techniques used in the offline physics object identification and reconstruction is provided in the next chapter.

CHAPTER 3

Physics objects reconstruction in CMS

In this chapter, the reconstruction of physics objects by means of the standard CMS algorithms is discussed. In this analysis, the physics objects of interest are tracks, primary vertices, muons and b-tagged jets. A particular emphasis is dedicated to the b-tagging algorithm and muon identification criteria. They are particularly relevant in the selection of $b\bar{b}\mu$ events that characterise both signal and background processes. The initial step in the identification and reconstruction of the fundamental physics objects in this work is performed with the CMS Particle Flow algorithm.

3.1 Particle Flow algorithm

The Particle Flow algorithm [104] was originally implemented in the context of the ALEPH experiment at LEP. It has been successfully adopted by the CMS experiment to provide an unprecedented precision in the global event reconstruction of the final state particles at any hadron collider. The key features of the CMS detector that ensure excellent performance of the PF algorithm are the high granularity of the electromagnetic calorimeter, the hermiticity of the hadron calorimeter, and the large magnetic field integral. The algorithm is based upon an accurate track reconstruction, a precise clustering technique, able to distinguish efficiently between overlapping showers. In addition, a robust linking procedure is needed to combine information regarding the energy deposits associated to a single particle measured in different sub-detectors. The first step of the PF sequence is the identification of charged particles' tracks, followed by the extrapolation of these tracks to the compatible calorimeter energy deposits. In order to avoid double counting of leptons both as individual particles and jet constituents, the isolated leptons are preventively excluded from the jet clustering sequence. Furthermore, charged hadrons, which are identified by linking track momentum to energy calorimeter deposits, are also discarded in the reconstruction sequence, a step denoted as *Charged Hadron Subtraction*. In the absence of associated tracks, the residual calorimeter hadrons are attributed to neutral hadrons and photons. This identification occurs provided that the cluster energies of the neutral hadron candidates exceed their track momentum taking into account detector resolution effects.

3.2 Track reconstruction

The reconstruction of charged particles' trajectory with high precision at the CMS detector is a complex task because of the large combinatorics from the high multiplicity of particles and the large number of readout channels. Additional systematic effects having an impact on the track reconstruction may arise from possible distortions in the tracking material and inhomegeneities in the magnetic field. Prior to the global track reconstruction, the conversion of local charge clusters into hits takes place using the digitised output of the tracking system. The local track reconstruction output is then buffered to the global track reconstruction, whose aim is to identify hit combination that match to possible trajectories of the charged particles present in the event. All steps of the reconstruction are performed using an iterative pattern recognition technique, a Kalman-like fitting procedure adapted for the CMS framework in the *Combinatorial Track Finder* [105] (CTF) algorithm. At each iteration of CTF, positional information from the hits used in the previous step is discarded and the set of requirements are gradually relaxed. The tracking algorithm carries out three main substasks;

1. **seed finding**, involving the generation of the starting points of the iterative sequence, namely pairs or triplets of hits ;

2. **pattern recognition**, in which at least five track candidates must satisfy a series of quality criteria, based on cuts on the track impact parameter significance with respect to the beamspot, the number of hits in the inner tracking system and the normalised χ^2 of the track trajectory;

3. **final fitting**, in which the best-fit value of the track parameters and the covariance matrix are determined by means of a least-squares fit;

Figure 3.1 illustrates the expected improvement in the tracking performance in 2017 with respect to the legacy system, arising from the new tracker geometry. The actual improvement is partially adversely compensated in data by the end-of-year degradation of the pixel performance. A dynamic inefficiency in the innermost barrel pixel layer was caused by the so-called *DCDC converter problem*, described in Section 2.2.1. However, this issue affects only Era F accounting for approximately one fourth of the total integrated luminosity recorded in the 2017 data-taking period. The subsequent loss of tracking

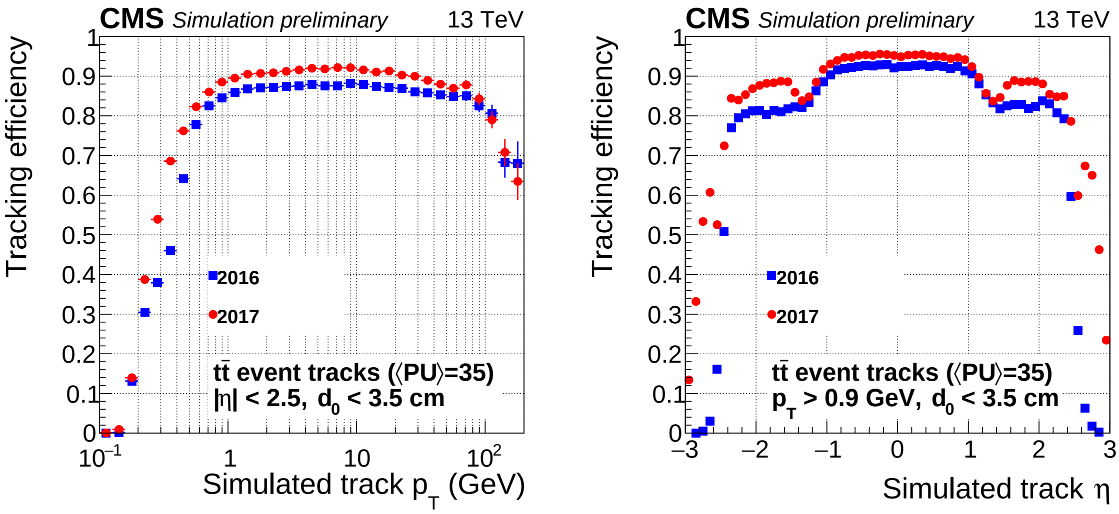

Figure 3.1: Track reconstruction efficiency as a function of simulated track kinematic variables p_T (left) and η (right) for the CMS 2016 and 2017 detector geometries. The performance of CMS detector is expected to improve in 2017 the full p_T and η spectra [89].

efficiency up to 10% is mostly concentrated for $|\eta| > 2.4$, which lies outside the acceptance of the present analysis.

3.3 Primary Vertex

Probing the hadronic activity in the vicinity of the interaction points, the most energetic scattering vertex is selected as the primary vertex (PV) of the interaction. The PV reconstruction aims at measuring the position of the primary production interaction vertex. It consists of a two-step procedure performed on top of track reconstruction by the CTF algorithm. The tracks matched to a single primary vertex candidate are clustered by means of the *Deterministic Annealing* (DA) algorithm [107]. The DA algorithm determines the assignments of each track to a primary vertex candidate based on the transverse position of the track with respect to the interaction point. The algorithm then decides probabilistically whether each primary vertex candidate should be further split into two vertices. The presence of outlier tracks, often associated with lower fit quality, can generate fake primary vertices. For this reason, they are preventively down-weighted in the calculation of the total number of primary vertices.

After that, the selected clustered vertex candidates with at least two associated tracks are fitted with the *Adaptive Vertex Filter* [108]. At this step, the vertex position and the covariance matrix are calculated. The adaptive vertex reconstruction assigns a certain

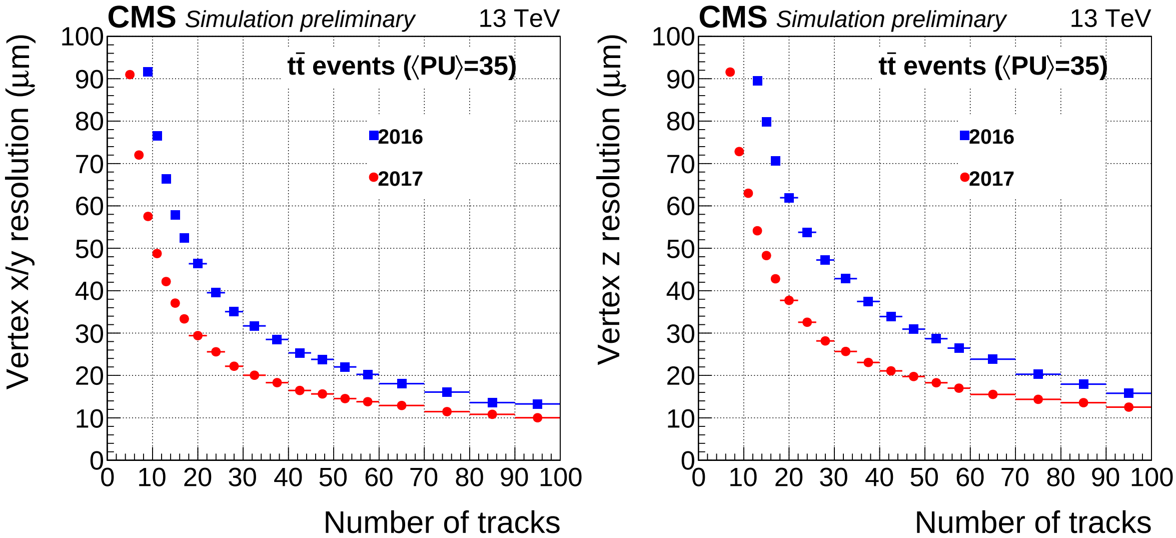

Figure 3.2: Comparison of primary vertex spatial resolution in the along the x/y axes (left) and the z axis (right) in simulated samples of $t\bar{t}$ events with current and legacy detector geometry [106].

probability and a corresponding weight w_i to quantify the degree of compatibility of the track to the fitted vertex. The resulting quality of the vertex fit is defined in terms of the number of degrees of freedom:

$$n_{dof} = -3 + 2\sum_{i=1}^{N_{tr}} w_i, \tag{3.1}$$

where N_{tr} is the number of tracks associated to a particular vertex candidate. The vertices must have a z position within 24 cm of the beamspot, a radial position within 2 cm from the interaction point and the vertex fit must have at least four degrees of freedom. The vertex with the highest p_T^2 sum of the associated tracks is selected as the primary vertex of the interaction. Other reconstructed vertices can be identified as secondary vertices or interpreted as a pile-up contribution. Figure 3.2 highlights the expected increase in the PV spatial resolution in the 2017 data-taking period with respect to 2016 arising from the new pixel geometry. This improvement mirrors the better track reconstruction efficiency, which also has a positive impact on b-tagging performance.

3.4 Muon

The CMS detector was designed specifically to achieve high precision in the measurement of momentum and charge of muons for a wide range of kinematic parameters. The target momentum resolution at a center-of-mass-energy of 13 TeV is of the order of $\sigma(p_T)/p_T \sim 1\%$ for single muons with a p_{T} of 100 GeV and approximately 10% for 1 TeV [109]. The actual performance, as measured in *pp* collisions in 2015 from cosmic muon data, was found to be comparable with expectation for low and moderate muon transverse momentum. In the case of muons with a harder p_{T} spectrum, the achieved momentum resolution largely exceeds design, attaining a value of 6% for $p_{\mathrm{T}} > 400$ GeV. Because of their long lifetimes and low energy deposits in the calorimeter muons can propagate through the whole CMS apparatus and reach the muon system located outside the superconducting solenoid.

Muon track reconstruction

In the standard muon track reconstruction sequence, a track fitting is first performed independently for muon hits in the inner tracker to form *tracker tracks*, and for hits in the muon chamber to obtain *standalone muon tracks*. Two different reconstruction algorithms with complementary approaches are exploited to identify and reconstruct *Global* and *Tracker muons*, respectively. The former type is reconstructed with an "outside-in" approach by matching the track of a standalone muon to a tracker track. Prior to this extrapolation, both tracks are propagated to a common surface using a Kalman-filter technique [110]. Following a complementary "inside-out" approach, Tracker muon tracks are built using less stringent requirements starting from the tracker track candidates. Each track candidate with a total momentum $p > 2.5$ GeV and transverse momentum $p_T > 0.5$ GeV is propagated to the muon system taking into account the mean expected energy losses, the magnetic field strength and the amount of Coulomb scattering in the tracking material. The extrapolated track must also successfully match at least a muon segment in the CSC or DT system of the muon spectrometer. Owing to the excellent performance of the the inner tracker and of the muon system, approximately 99% of the muons detected within the fiducial tracker volume are reconstructed as either tracker or global muons.

Muon identification

Following the muon track reconstruction, potential muon candidates are identified with the PF algorithm combining muon track information as well as the energy deposits in the calorimeter. The PF muon reconstruction allows suppressing most of hadronic punch-through, i.e. when highly-energetic charged hadrons, such as pions, induce electromagnetic showers leaking in the muon system. Muon identification (ID) criteria are imposed in parallel to the muon reconstruction sequence, exploiting several variables, such as the number of hits per track, the track fit quality, and the track impact parameter. Another important discriminating variable is the muon segment compatibility between tracker tracks and standalone muon tracks, defined as a probability estimate comprised between 0 and 1. A kink-finding algorithm separates sequentially each tracker track into two disjoint tracks to evaluate their degree of compatibility with a single track at several points along the trajectory. The definition of *muon identification* working points (WP) permits to refine the balance between the selection efficiency and the purity of the reconstructed muons, according to the specific needs of each physics analysis.

The loose working point aims at maximising the selection efficiency, approximately 99%, for all muons reconstructed by the PF algorithm, taking into account both tracker and global muons. The medium working point is designed to achieve high efficiency, around 98%, both for prompt muons and for those stemming from cascade decays of heavy flavoured hadrons. The muons passing loose identification requirements that are associated with a large fraction of valid tracker hits (above 80 %) are considered as *good* muon candidates. In addition, only global muons that satisfy a low normalised track fit parameter $\chi^2 < 3$, a position match between the tracker track and the standalone muon track of $\chi^2 < 12$, as well as high track-segment compatibility are further selected with the medium WP.

The *tight* working point, introduced to suppress the rate of muons from in–flight decays, requires PF muon candidates to be also identified as global muons. The tracker track candidate is built from valid hits in at least six different tracker layers, including a pixel layer. In order to suppress cosmic muons, the associated tracker track must have a transverse impact parameter of $|d_{xy}| < 2$ mm with respect to the beamspot, and a longitudinal distance of $|d_z| < 5$ mm from the primary vertex to reduce pile-up contamination. Moreover, the global muon fit must also satisfy normalised track $\chi^2 < 10$ to suppress the hadronic punch-through, and at least one hit must be present in the muon chamber. The resulting probability for pions to be mis-labelled as muons is as low as 0.1% for muons passing tight identification.

Tight muon identification efficiency

The measurement of the tight muon identification efficiency, based on a tag-and-probe method was performed centrally [111]. Events with a J/ψ di-muon topology are selected to measure the reconstruction efficiency of low p_T muons. A Drell-Yan sample is used for muons with a harder p_T spectrum up to 120 GeV. The J/ψ dimuon channel event selection is reported in detail in Section 4.5.5 since it is also used to derive the muon kinematic trigger efficiency. The main difference in the two methods consists of the trigger selection: a muon-plus-track trigger is used for the measurement of the tight identification efficiency; a single-muon trigger is used for the kinematic efficiency of the dedicated semi-leptonic trigger. The adoption of a muon-plus-track trigger introduces a net positive bias on the tight muon identification sequence, which relies on the aforementioned tracker muon quality cuts. The procedure for the extraction of the tight muon ID efficiency is discussed extensively in [109]. Muons passing the tight working point are associated with the largest identification efficiency, above 95% at the efficiency plateau, as illustrated in Figure 3.3 both in data and simulation.

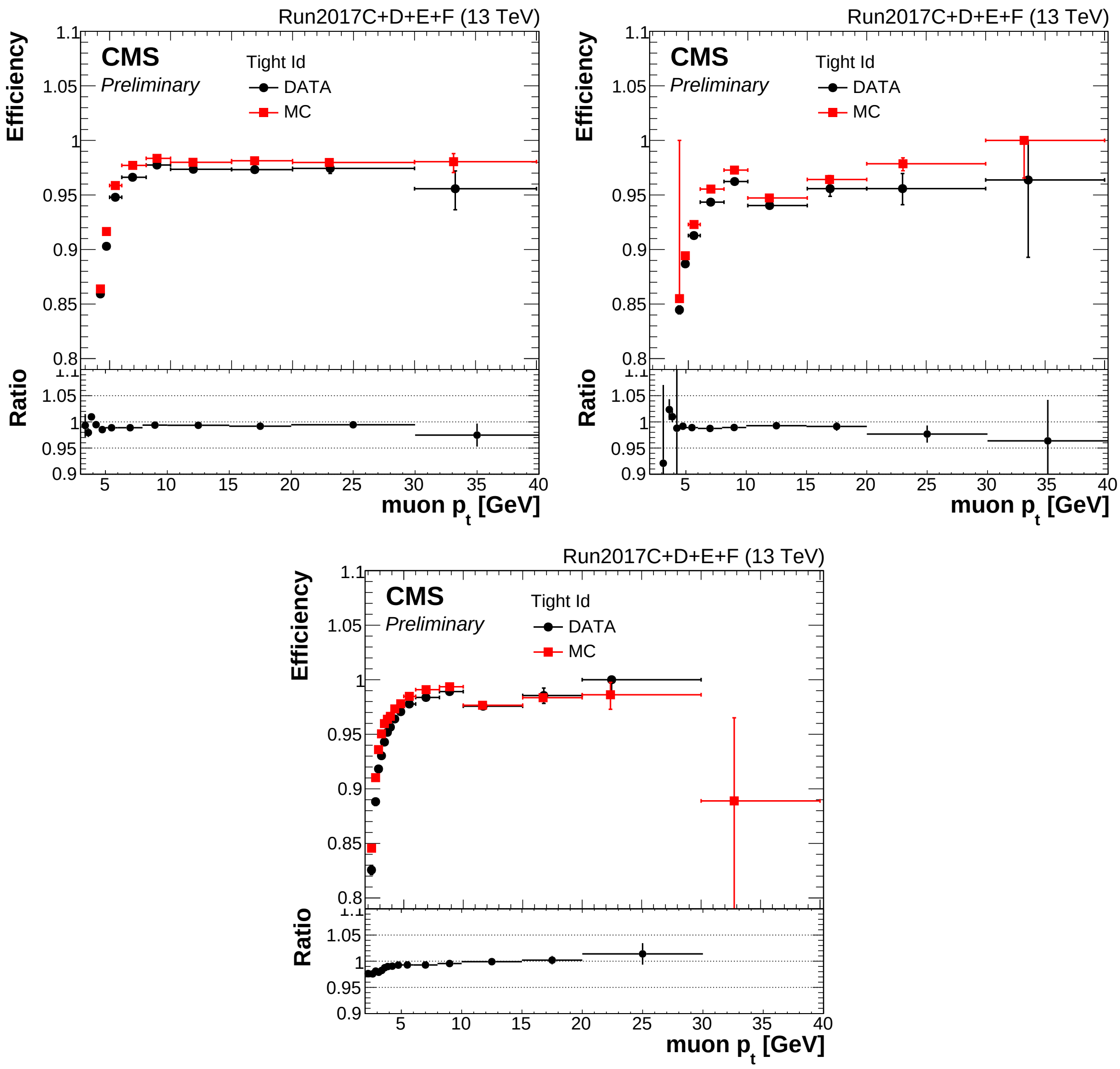

Figure 3.3: Muon tight identification efficiency measurements for low muon p_{T} obtained in J/ψ di-muon channel in three different pseudorapidity bins $|\eta| < 0.9$ (top left), $0.9 < |\eta| < 1.2$ (top right) and $1.2 < |\eta| < 2.1$ (bottom) respectively [111]. Black dots denote measurements in data for the 2017 data-taking eras C to F, corresponding to the data-taking period of the main semi-leptonic trigger used in this analysis. Red dots indicate the results obtained in the $J/\psi \to \mu^+\mu^-$ with the simulated Monte Carlo sample.

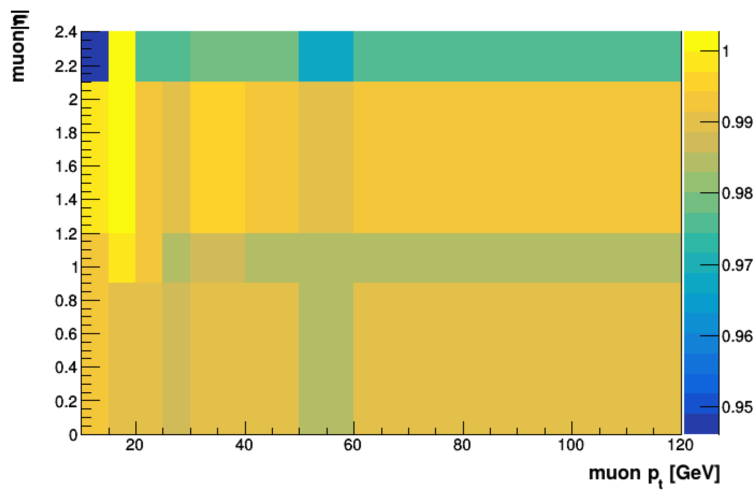

Figure 3.4: Scale factor for tracker muons passing the tight identification requirements plotted in bins of muon p_T and $|\eta|$. The correction factors were obtained with two separate tag-and-probe methods, respectively in the $J/\Psi \to \mu^+\mu^-$ channel for $p_T^{(\mu)} < 20$ GeV, and in the $Z \to \mu^+\mu^-$ channel for $p_T^{(\mu)} > 20$ GeV [111].

The resulting efficiency scale factors shown in Figure 3.4 were obtained separately for tight muons with $p_T^{(\mu)} < 20$ GeV in the $J/\Psi \to \mu^+\mu^-$ channel and $p_T^{(\mu)} > 20$ GeV in the $Z \to \mu^+\mu^-$ channel. Aside from the transition at this p_T threshold, little dependence of the correction factor on the p_T spectrum of the muon is observed. The tight muons in the endcap-only region with $|\eta| > 2.1$ are identified on average less efficiently in data than in simulation. This is due to some mis-modelling in the MC samples of the detector accuracy of the tracker muon reconstruction in the very forward region. The statistical error is derived from the fitting uncertainty, while the systematic uncertainty was obtained varying the signal plus background fitting functions. In the $J/\Psi \to \mu^+\mu^-$ channel, the systematic uncertainty was estimated to be in the range $1-3\%$.The systematic error in the background estimation of $Z \to \mu^+\mu^-$ channel was found to be approximately $0.2 - 0.4\%$ by recalculating the efficiencies with a pure sample of isolated probe tracks and comparing it with the results obtained with the inclusive sample.

3.5 Jet

Hadronisation and fragmentation of quarks and gluons, collectively referred to as coloured partons, are a direct consequence of colour confinement prescribed by QCD. As a consequence, the hard processes of the most energetic partons in pp collisions lead to a huge rate of hadron production at the LHC. The dynamics of this process favours the collimation of these QCD bound states along the direction of the mother parton into a narrow cone. The resulting spray of particles is reconstructed as a single composite object, referred to as a *jet*, which is needed to infer the properties of the original mother parton.

3.5.1 Jet Algorithms

Jet algorithms codify the relationship between the original parton and the jet observable. The main properties of jet clustering algorithms are *infrared* and *collinear safety* (IRC), which must be simultaneously satisfied to avoid divergences in perturbative QCD calculations of the jet shape. Collinear safety requires that splitting a single particle over a set of co-moving particles each carrying a fraction of the initial momentum should not alter the jet observable. Infrared safety enforces that the latter is also preserved under the addition of an arbitrary number of ultra-soft particles. Furthermore, the measured offset in the p_{T} spectrum prior to the pile-up correction scales with radius parameter R adopted for the clustering. In this analysis, the optimal size of the jet cone parameter is $R = 0.4$ (AK4 jets), whereas during Run 1 a distance parameter of $R = 0.5$ was utilised, owing to the lower pile-up conditions.

Two types of jet clustering techniques are distinguished: *cone algorithms*, defining the jet as a hadronisation cone centered around the direction of the energy flow and *sequential recombination* algorithms clustering the jet constituents by embedding them in a particular metric. The majority of such algorithms adopts the following metric:

$$d_{ij} = \min\left(k_{T,i}^{2p}, k_{T,j}^{2p}\right)\frac{\Delta_{ij}^2}{R^2}, \qquad \text{where} \qquad \Delta_{ij}^2 = (y_i - y_j)^2 + (\phi_i - \phi_j)^2, \tag{3.2}$$

with the cluster variables $k_{T,i}$, ϕ_i, y_i representing respectively the transverse momentum, the azimuthal angle and the rapidity of the entity i, which can be identified either as a pseudo-jet or a particle. The exponent p sets the energy power law with respect to the metric. It also enters the definition of the distance between the proton beam axis and the object i:

$$d_{iB} = k_{T,i}^{2p}. \tag{3.3}$$

The first step of the clustering method is the calculation of all possible d_{ij} and d_{iB} combinations. The smallest distance is then used as the starting point of the iterative sequence. If the minimum distance is of type d_{iB}, then the cluster i is identified as a jet, otherwise the entities i and j are merged into a single cluster and the algorithm proceeds with the next iteration. This sequence terminates only when all the constituents are clustered into jets. The parameter p determines the order in which the jet components are clustered and is set to $p = -1$ in the case of the anti–k_T algorithm [112] adopted in the present work. This algorithm starts the jet clustering sequence from the most energetic partons, thereby reducing a possible bias in the jet substructure from the emission of soft particles. On the experimental side, this results in a cone-like shape of the anti–k_T jets, as illustrated in Figure 3.5, which eases their calibration as well as their pile-up handling.

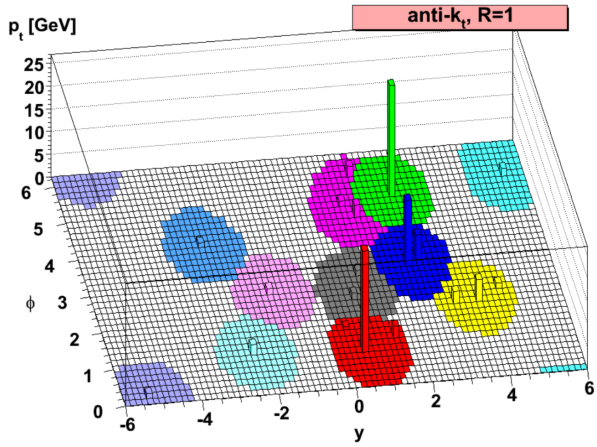

Figure 3.5: A sample parton-level event with several random soft "ghosts" clustered with the anti–k_T jet algorithm highlighting the active catchment areas of the clustered hard jets [112].

Jet clustering algorithms have a high degree of generality and can be applied to any object with an associated four-momentum. In simulation, for instance, *particle-level jets* are formed by clustering all generated visible particles, except for neutrinos. The stable, final state particles, i.e. with a decay length larger than 1 cm, represent viable candidates as jet constituents. At the CMS experiment, the latter are reconstructed as individual particle flow candidates with a precision of approximately 90%. Within the tracker acceptance, a similar reconstruction accuracy is achieved also for the *calorimeter jets* constituents. The latter are reconstructed from the energy deposits measured in the calorimeters towers. On the other hand, both inner tracker and calorimeter information is used in the reconstruction of *jet-plus-track jets* (JPT) components. Particle-flow jets benefit consistently from a better energy resolution and a lower jet energy scale uncertainty with respect to the other jet collections. The corrections to the initial jet energy measurement in data and simulation are discussed thoroughly in the following section.

3.5.2 Jet Energy Corrections

The mismatch between the measured jet energy and the original parton energy must be corrected at reconstruction level, both in data and simulation. In data, these deviations are driven by the non-uniformity and non-linearity of the calorimeter response, while in Monte Carlo simulation, the corrections ensure *a posteriori* the agreement with the observed data. Furthermore, contributions from pile-up events or detector noise may bias the measurement of the jet energy. To this end, a calibration of the reconstructed jet is performed by applying a series of corrections on the measured jet energy, collectively referred to as *Jet Energy Scale* corrections (JES). This class of corrections represents an important source of systematic uncertainty in the analyses with a multi-jet final state.

Jet Energy Scale

The JES corrections are calculated in the form of a multiplicative factor on the four-momentum of the measured jet, in order to match the measured energy of each jet to its true energy at the generator level. The measured jet transverse momentum response is defined as the ratio of the measured jet p_T at the reconstruction step to the generated jet p_T^{ptcl} at particle level. These corrections and the corresponding uncertainties are provided centrally by the CMS JetMet group [113]. A factorised approach is followed for the calibration of the jets and the single corrections are applied sequentially in the order exemplified in Figure 3.6:

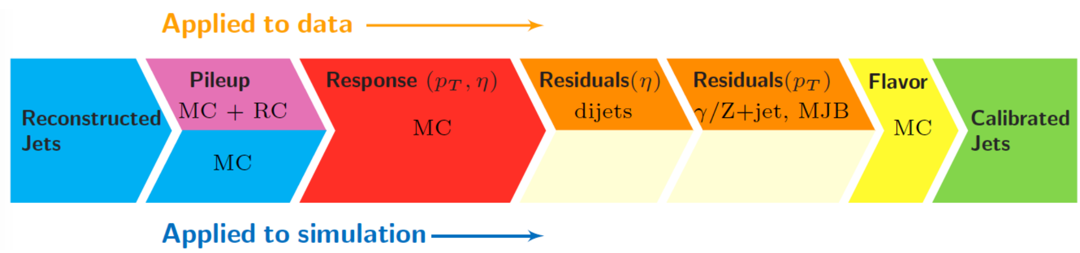

Figure 3.6: Overview of the jet energy calibration procedure follwed in data and simulation taken from [114].

- *pile-up offset* corrections account for the measured energy of the jet in excess due to the presence of in-time (IT) and out-of-time (OOT) pileup. They are derived from the simulation of QCD multi-jet events processed with or without pile-up overlay and they are applied to both data and MC samples.
- *simulated response* corrections compensate for the non-linear response in p_T from the calorimeters and the non-uniform angular response in the tracker transition region and they are parameterised as a function of these jet kinematic variables.

- *residual data to Monte Carlo* corrections must be applied to improve the data to simulation agreement as a function of the jet η and p_T. The absolute scale of the measured jet p_T response is corrected in data using multi-jet and Drell-Yan plus jets events, which benefit from the high precision measurement of the Z-boson and the photon energy in the ECAL. The residual η correction is derived in di-jet events exploiting the p_T imbalance of the di-jet system.

- additional flavour corrections can be applied since the typical p_T response differs for light and heavy flavour jets. In the case of jets initiated by b-quarks, flavour corrections are extracted from data with Z+b events.

Besides generic jet energy corrections, b-jet energy corrections are applied in this analysis to recover partially missing transverse momentum caused by neutrino emission in semi-leptonic b-hadron decays. Such corrections are discussed in detail in Section 4.7.2.

Jet Energy Resolution

Jet Energy Resolution (JER) corrections introduce a dose of smearing in the simulated jet p_T spectrum to compensate for data-to-simulation differences due to detector resolution effects. This alteration of the jet p_T distribution can ultimately bias the steeply falling mass spectra which is the main observable in di-jet resonant searches. In order to determine JER corrections, an extension of the method used to measure the relative η-dependent corrections to the jet p_T response in $\gamma/Z + jets$ events is adopted [114]. The main difference is that one needs to assess the detector effects with an impact solely on the width, (and not producing an overall shift as in the case of JES), on the residual Δ of the p_T response distribution:

$$\Delta = \frac{p_T - p_T^{\mathrm{ptcl}}}{p_T}. \tag{3.4}$$

The simulated p_T response resolution is modelled accurately by a double-sided Crystal-Ball functions since the spectrum has a Gaussian core accompanied by non-gaussian tail. The low p_T response tail can be caused by detector effects, such as inactive areas of the calorimeter or hadronic punch-through, and neutrino emission in semi-leptonic decays of heavy-flavour hadrons. The JER corrections are also provided centrally by the CMS collaboration [115]. Two methods are utilised to match the measured p_T spectra in simulation to the accuracy observed in data. The first method, the *scaling method*, is applied when the simulated reconstructed jet can be matched to particle-level generated jet according to the following criteria:

- the phase-space distance between the particle-level object and the reconstructed jet $\Delta R < 0.5R$, where R is the jet radius parameter;

- the residual p_T response in simulation $\Delta < 3\Delta_{data}$, where Δ_{data} is the relative p_{T} resolution measured in data.

Consequently, the four-momentum of a reconstructed jet is rescaled by the following correction factor:

$$C_{JER} = 1 + (S_{JER} - 1) \times \Delta, \tag{3.5}$$

where $S_{JER} = \Delta_{data}/\Delta$ indicates the data-to-simulation scale factor.
In the absence of a matching particle-level jet fulfilling the aforementioned criteria, the *stochastic smearing* method is utilised. In this case, the reconstructed jet four-momentum is multiplied by a factor

$$C_{JER} = 1 + N(0, \Delta_{\mathrm{data}}) \times \sqrt{\max(S_{JER} - 1, 0)}, \tag{3.6}$$

where $N(0, \Delta_{\mathrm{data}})$ denotes a random number sampled from a Gaussian distribution centered at zero and having a width of Δ_{data}.

3.6 B-tagged jet

Heavy bottom-quarks arise from many interesting processes, such as the decays of the top quark and of the Higgs boson, as well as in several BSM signatures. Owing to the relatively long lifetime of b-hadrons[1], of the order of few ps, the decay topology of b-jets involves the presence of secondary vertices displaced typically a few mm with respect to the primary vertex. Because of the large b-hadron mass generally around 5 GeV, its decay products tend to have higher transverse momentum than those in light flavoured jets. This causes b-jets to have a wider jet area and a larger charged particle multiplicity with on average five charged particles per decay. Furthermore, the large fraction of semi-leptonic decays in the muon channel of b-hadrons ($BR(b \to \mu\nu X) \approx 11\%$) and c-hadrons stemming from b-hadron decays ($BR(b \to c \to \mu\nu X) \approx 10\%$) [116] enhance the presence of muons in b-jets. The topology of b-jets production and decay is shown in Figure 3.7.

To distinguish b-jets from light ($udsg$-) and charmed (c-) jets, various b-tagging algorithms have been developed at CMS [117]. They exploit a combination of the kinematic and topological features of b-jets, such as the transverse impact parameters of the charged-particle tracks, the emission of soft leptons, and the properties of secondary vertices.

Secondary vertex reconstruction

The architecture of the SV reconstruction makes use of the Inclusive Vertex Finder (IVF), which is able to resolve at least one vertex located within a jet without requiring any jet

[1] Some light flavour hadrons also feature relatively long lifetimes, e.g. K^0_S, Λ. However their signatures are easily identifiable, hence they are suppressed efficiently by b-tagging algorithms.

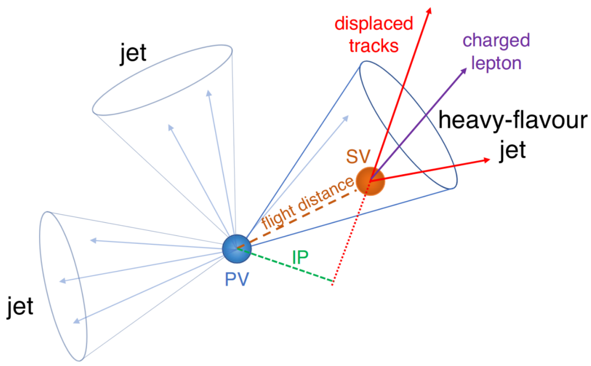

Figure 3.7: Simplified view of heavy-flavour jets formation in a *pp* collision environment.

information. The algorithm first performs a pre-clustering of the tracks present in the event using displaced tracks as seeds and in parallel a clustering of the residual tracks on the basis of the pairwise separation. All reconstructed tracks in the event are used as an input to the IVF[2]. The SV candidates must fulfill several criteria in order to be classified as a *RecoVertex*. The transverse distance between the primary and secondary vertex must be comprised between 0.1 and 25 mm. The invariant mass of any charged particle associated to the vertex must be lower than 6.5 GeV. Furthermore, secondary vertex candidates compatible with a K^0_S meson decay are rejected.

B-tagging algorithms

The IVF represents the standard vertex finder used for all b-taggers in CMS. The performance of different b-tagging algorithms is described by two quantities; the *b-tagging efficiency*, which is the probability of a real b-jet to be identified correctly by the b-tagger and the *mis-identification rate*, which accounts for the probability of a light-flavoured jet being incorrectly identified as a b-jet. Three operational *working points* (WP) are defined centrally by the CMS B-tagging and Vertexing group (BTV) [118] to characterise different levels of accuracy of the b-tagger :

- **tight** (T) for mis-identification probability of 0.1% of non b-jets;
- **medium** (M) for mis-identification probability of 1% of non b-jets;
- **loose** (L) for mis-identification probability of 10% of non b-jets;

Several b-taggers have been utilised in this analysis to conduct optimisation studies. The CSVv2 tagger is based on the CSV algorithm employed in Run 1, combining

[2]This differs from the AVF algorithm used in primary vertex reconstruction, which takes assumes that vertices are located along the jet axis.

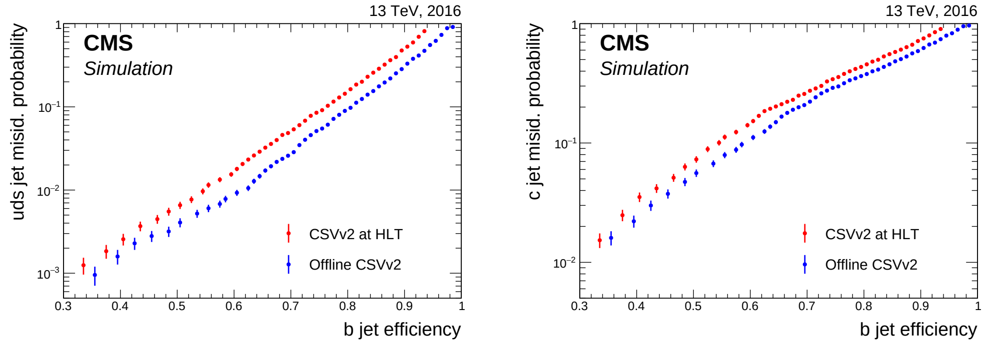

Figure 3.8: b-tagging performance of the HLT level (red dots) and offline versions of the CSVv2 algorithm (blue dots) demonstrating the mis-identification rate of udsg- (left) and c- jets (right) as b-jets versus the efficiency for correct b-jet identification measured in simulated $t\bar{t}$ events before the PhaseI Pixel upgrade [119].

secondary vertex (SV) information with track-based lifetime information into a multivariate technique. The discriminating variables are subsequently fed to an artificial neural network, namely a feedforward multilayer perceptron with a single hidden layer [117].

A streamlined version of the CSVv2 algorithm is implemented for the online b-tagging. This simplification is necessary due to the latency constraints of the tracking reconstruction sequence imposed at HLT level. The Fast Primary Vertex Finder (FPVF) locates the primary vertex along the beamline as the region with the largest number of pixel hits projected on the z-axis that are compatible with a jet signature. It achieves a spatial resolution of O(mm) under standard pile-up conditions and is further complemented by a regional track reconstruction. A comparison of the performance of the online and the offline versions of the CSVv2 algorithms is illustrated in Figure 3.8 for a simulated sample of $t\bar{t}$ events with a mean PU of 35. From these plots, it can be evinced that the offline CSVv2 b-tagger is consistently more accurate than the equivalent online b-tagger. The impact of the online b-tagging sequence on the final selection efficiency is addressed by the calculation of b-tag efficiency scale factors, discussed in Section 4.7.2.

The offline b-tagging performance of the CSVv2 is further improved by means of deep machine learning techniques, collectively denoted as *deep learning*. The DeepCSV b-tagger is an extension of the CSVv2 tagger, utilising a deep neural network approach with five hidden layers, each with a width of a hundred nodes. The same input tracks and secondary vertices reconstructed with the Inclusive Vertex Finder (IVF) algorithm are used. The initial set of observables fed to the fully connected dense network is extended by the addition of extra track-based variables.

Further advances in deep learning techniques can be exploited to improve the performance of flavour taggers [120]. Convolutional Neural Networks (CNNs), originally developed for image processing and pattern recognition, can be adapted to process directly low-level LHC data for flavour tagging. The main application is the analysis of energy deposits from calorimeters which are naturally pixelised. The logical structure of the DeepJet, a.k.a. DeepFlavour tagger, relies on a hierarchical tile ordering architecture for each collection of reconstructed PF objects. A subset of the properties for the particle-flow candidates is processed in a heterogeneous, multi-dimensional phase-space, including sixteen features for charged particles, eight for neutral ones and seventeen for secondary vertices.

A summary of the b-tagging efficiencies and mis-identification rates for the various b-taggers tested in the analysis is shown in Table 3.1. The improvement in the discrimination power of the DeepCSV algorithm in the 2017 tracker geometry is estimated to be around $5 - 7\%$ for the tight working point. It is driven by the increased redundancy of the tracking subdetectors, with the innermost barrel layer located closer to the beamline. The DeepFlavour algorithm outperforms the DeepCSV tagger particularly in the case of jets with a hard p_T spectrum, as shown in Figure 3.9. This improvement arises from the absence of a strong kinematic pre-selection in the training phase. This effect leads to a significant sensitivity improvement for the $H \to b\bar{b}$ search at high values of the di-jet invariant mass.

The main systematic uncertainty in the derivation of the b-tagging efficiency is the fraction of heavy-flavour jets estimated from the multi-jet samples in simulation, followed by other flavour contributions. These include the observed number of K_S^0 and Λ hadrons, affecting the precision of the secondary vertex reconstruction, and the estimated gluon fraction. The contribution to the uncertainty from mis-measured tracks, reconstructed from wrong hit combinations, prevails only for b-tagged jets with a soft p_{T} spectrum. The extraction of the heavy-flavour tagging efficiencies is needed to improve the agreement between data and simulation. It is the preliminary step to the derivation of the *b-tag* scale factors, obtained as the ratio of the offline b-tag efficiencies in data and simulation.

3.6.1 Offline b-tagging scale factors

The aim of the calibration procedure for b-tagging is to correct for the potential differences in the flavour composition of the b-tagged jets in simulation with respect to the observed data. For a simple multi-jet event topology with a small number of b-tagged jets, the calibration procedure can be performed operating an event-wise re-weighting procedure, using the offline b-tag scale factors, viz:

$$w_{entry}(p_T, \eta, f) = \prod_{i=\text{tagged}} \mathrm{SF}(p_T,\eta,\mathrm{f})_i \prod_{j=\text{not tagged}} (1 - \mathrm{SF}(p_T,\eta,\mathrm{f})_j), \tag{3.7}$$

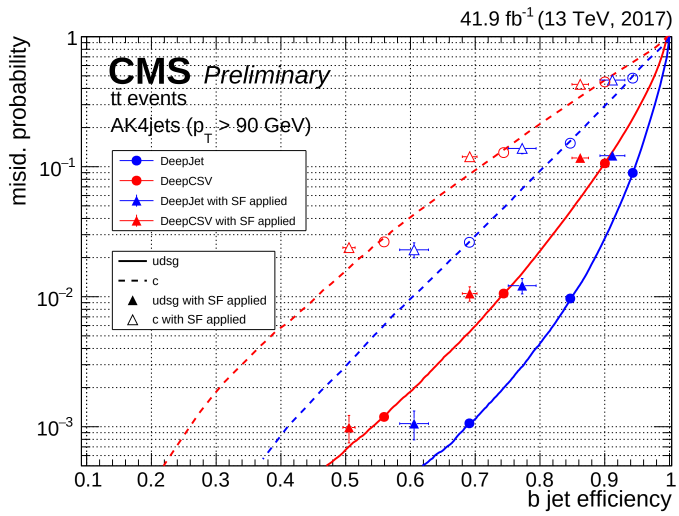

Figure 3.9: Performance of the b-tagging algorithms DeepJet and DeepCSV. The mis-identification rate of udsg- and c- jets versus the efficiency for correct b-jet identification was measured in simulated $t\bar{t}$ events for jets with $p_T > 90$ GeV and $|\eta| < 2.5$. The cross-hairs illustrate the impact of the data-to-simulation scale factors on the loose, medium and tight b-tag working points [118].

Tagger	Working point	ε_b (%)	ε_c (%)	ε_{udsg} (%)	d
	loose	81	37	8.9	0.58
CSVv2	medium	63	12	0.9	0.88
	tight	41	2.2	0.1	0.97
	loose	84	41	11	0.15
DeepCSV	medium	68	12	1.1	0.49
	tight	50	2.4	0.1	0.80
	loose	90	46	12	0.052
DeepJet	medium	77	12	1.2	0.30
	tight	60	2.2	0.1	0.75

Table 3.1: The b-jet identification efficiency and the corresponding mis-identification rates for c- and $udsg$-jets and values of the discriminant d for the CSVv2 and DeepCSV taggers for the three standard working points. The values of the identification efficiencies are integrated over the full jet p_T and η spectrum.

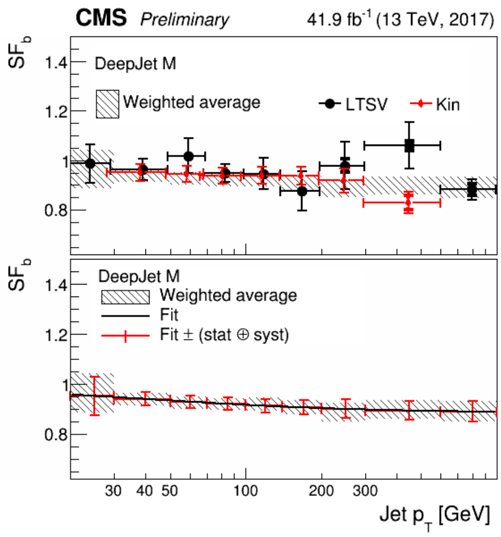

Figure 3.10: Data-to-simulation b-tag scale factors as a function of the jet transverse momentum for the medium WP of the DeepJet tagger computed separately with the LTSV and Kin methods respectively (top panel) and their combination (bottom panel) taken from [118].

where the indices i and j run over the number of b-tagged and non-tagged jets respectively, and the offline b-tag scale factor SF is computed as a function of the jet flavour, and the kinematic variables p_{T} and η. In the triple b-tag signal topology of the analysis, Equation 3.7 simply translates into the product of the individual b-tag scale factors of the three leading jets in p_{T}:

$$w_{entry}(N_b = 3) = \mathrm{SF}_1 \times \mathrm{SF}_2 \times \mathrm{SF}_3. \tag{3.8}$$

The offline b-tag scale factors used in this analysis were derived centrally by the BTV group. The correction factors for the medium working point of the DeepJet algorithm are shown in Figure 3.10. They were obtained with two different methods, the *Kinematic* (Kin) method and the *Lifetime Tagging Secondary Vertex* (LTSV) method. In the former case, a boosted decision tree (BDT) discriminant with kinematic observables is used to distinguish between real b-jets from those originating from initial and final state radiation using di-lepton top pair MC events. In the latter, the Jet Probability Tagger is adopted to evaluate the secondary vertex identification efficiency in multi-jet events. Thus, the correction factors are extracted by means of a template fit to either the BDT discriminant or to the secondary vertex mass distribution, depending on the method. The weighted average of the two measurements is fitted to obtain the offline b-tag scale factors that are used in the present analysis. The uncertainties in the scale factors are obtained as shape variations of the corresponding template fits.

CHAPTER 4

Search for neutral Higgs bosons produced in final states with b-quarks

Since the discovery of a new resonance at a mass of 125 GeV by the CMS and ATLAS collaborations [11, 121, 122] a monumental effort has been put forward to pin down the properties of the newly discovered boson. The current experimental evidence points towards the compatibility of the observed h(125) state with the predicted coupling structure, CP properties and the other features of a Standard Model (SM) Higgs boson of this mass. The latter has a large coupling to b-quarks, and the $b\bar{b}$ channel is the predominant decay mode. Despite its large branching fraction, this decay channel was experimentally confirmed at the LHC only recently [55, 56]. In fact, the sensitivity is limited by the large background consisting of heavy-flavour multi-jet production, and by the effective detector resolution. In SUSY models, the running bottom mass is sensitive to higher order corrections from the unexplored SUSY sector. Thus, a precise measurement of the bottom Yukawa coupling is needed to look for possible deviations from the SM prediction that may point indirectly to the existence of BSM physics.

The observed Higgs boson may be further interpreted as the first discovered scalar state of an enlarged Higgs boson sector, foreseen by several BSM models such as the Minimal Supersymmetric Standard Model (MSSM) and the general Two Higgs Doublet Model (2HDM) discussed thoroughly in Sections 1.2 and 1.2.7. Furthermore, based on the ATLAS searches at 13 TeV for invisible decays of the Higgs boson [47] an indirect upper limit on $B(H \to BSM)$ below 0.47 is obtained at 95% confidence level[1]. Therefore the existence of undetected Higgs boson decays into BSM particles remains an interesting

[1] In the SM only the $H \to ZZ \to 4\nu$ channel contributes to invisible decays, with a branching fraction of only 10^{-3}.

possibility, which motivates the need for direct BSM searches. Due to the absence of a "golden" search channel, the latter must probe a large Higgs boson mass window, complementing the indirect constraints on 2HDM from the h(125) coupling measurements [47] and from rare B meson decays [123]. Both the 2HDM and the MSSM feature two scalar Higgs doublets, yielding five physical Higgs bosons after electroweak symmetry breaking. These comprise the neutral Higgs states $\phi = \{h, H, A\}$, of which the first member is conventionally identified with the observed h(125) state, while the latter are the nearly mass degenerate higher mass Higgs bosons A/H, differing by their CP properties. An overview of the recent results of searches for BSM neutral Higgs bosons in fermionic decays with CMS Run 2 data is reported in Appendix D. In this work, additional neutral Higgs boson decays are searched for in the b-associated production mechanism exemplified in Figure 1.6. This production channel is chosen over the gluon-gluon fusion because of the lower QCD multi-jet background. In this chapter, a search for the b-associated production with the neutral Higgs boson decays into a b-quark pair in the semi-leptonic channel with 2017 data collected with the CMS detector is presented.

4.1 Overview of previous results

Searches for neutral Higgs bosons in the context of the MSSM model were first conducted at the Large Electron-Positron Collider (LEP) at CERN [124]. Comprising the four experiments ALEPH, DELPHI, OPAL and L3, LEP was the largest electron-positron collider ever built, operating at a centre of mass energy of up to 209 GeV in the pre-LHC era. The most relevant Higgs production mechanisms at LEP are the *Higgsstrahlung* process $e^+e^- \to Z \to h/HZ$, which prevails at low values of tanβ, and the *Higgs pair production* $e^+e^- \to Z \to h/HA$, dominating at large tanβ. Searches at LEP for Higgs boson decays in the $b\bar{b}$ channel did not find any significant deviation from the background-only expectation. The largest excess found in the mass region in the vicinity of $m_\phi = 100$ GeV corresponds to a 2.5 σ deviation from expectation [77].

Searches for Higgs boson decays to b-quark pairs were also performed by the experiments CDF and DØ at the Tevatron [125] located at the Fermilab National Accelerator Laboratory. This proton anti-proton collider operated at a center of mass energy of 1.96 TeV. Due to the large multi-jet production rate, typical of any hadron collider, an inclusive search in the $b\bar{b}$ decay mode is extremely challenging. Consequently, only the b-associated production mechanism has been exploited at Tevatron and in subsequent LHC searches for MSSM Higgs bosons. Both the CDF and DØ experiments collected a significant amount of data during the Tevatron Run 2, corresponding to an integrated luminosity of 2.6 fb^{-1} and 5.2 fb^{-1} respectively. The Tevatron results were derived for the $gb \to \phi b$ production mode in the $\phi \to b\bar{b}$ decay channel. While no significant signal was identified, excesses at the level of $\sim 2\sigma$ with respect to expectation have been observed by both experiments [126, 127] for $m_\phi = 120$ GeV and 140 GeV. The LEP and Tevatron exclusion limits in the tanβ-m_A parameter space of the $m_{\mathrm{h}}^{\mathrm{max}}$ benchmark scenario complement each other, as illustrated in the left plot of Figure 4.1.

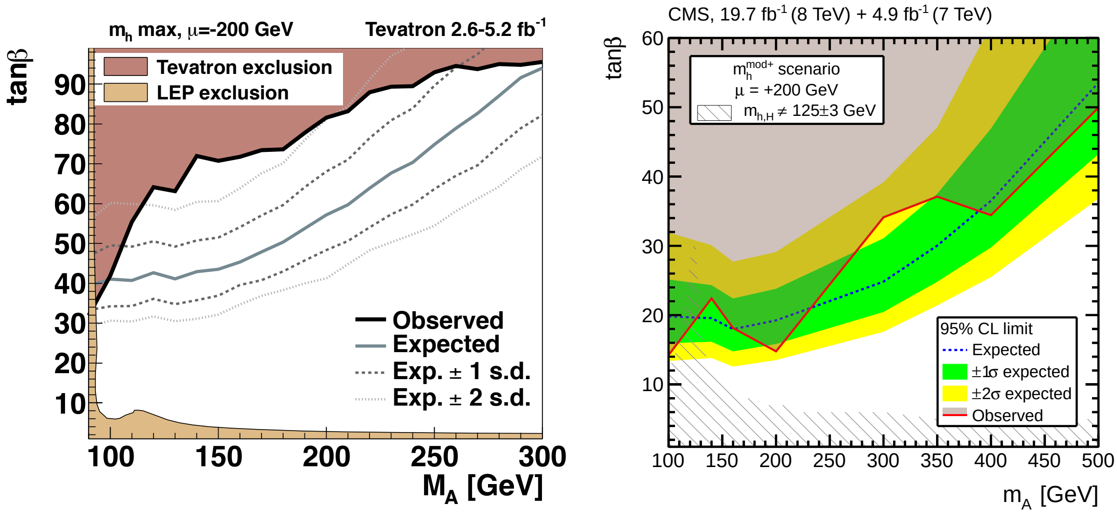

Figure 4.1: Upper limits for the parameter tanβ on the b-associated production of the ϕ boson times the branching fraction of the $\phi \to b\bar{b}$ decay in the low m_A region at 95 % confidence level. The results are obtained with Run 2 combination of Tevatron results [128] in the $m_{\mathrm{h}}^{\mathrm{max}}$ scenario and compared with the LEP combined measurements [77] (left). The Run 1 combination of analogous searches with CMS data [129] for the updated $m_{\mathrm{h}}^{\mathrm{mod+}}$ scenario is also shown (right). In the latter case, the theoretical uncertainty on the mass of the observed CP-even boson [73] arising from the unknown higher-order SUSY corrections is estimated in a conservative way by assigning a $\pm$ 3 GeV uncertainty band.

Analogous searches have also been performed in pp collisions at the LHC by the CMS collaboration at $\sqrt{s} = 7$ TeV [130], 8 TeV [129], whose results are combined in the right plot of Figure 4.1, and 13 TeV [17], shown on the left of Figure 4.2, with integrated luminosities of 4.9 fb^{-1}, 19.7 fb^{-1} and 35.7 fb^{-1}, respectively. The ATLAS results obtained at $\sqrt{s} = 13$ TeV [131] using data corresponding to an integrated luminosity of 27.8 fb^{-1} are illustrated in the right plot of Figure 4.2.

The common event category addressed by all these searches is the all-hadronic channel, with the exception of the CMS analysis at 7 TeV, which employs also the semi-leptonic channel. Both these categories make use of a triple b-tagged jet event selection conventionally denoted as the bbb search region. Thus, the signal is usually searched in this region as an excess in the invariant mass spectrum of the di-jet system of the two most energetic b-tagged jets. The CMS Run 1 results $\sqrt{s} = 7$ TeV and 8 TeV have been com-

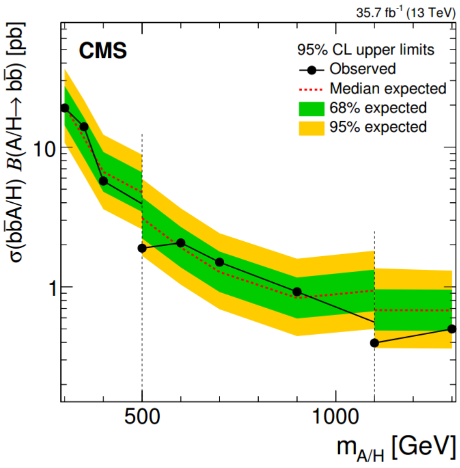

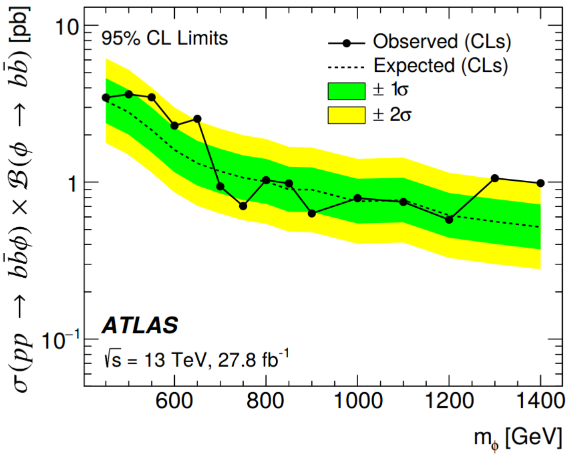

Figure 4.2: Model-independent upper limits on $\sigma(b\bar{b}\phi)B(\phi \to b\bar{b})$ at 95 % confidence level as a function of the Higgs boson mass obtained using 35.7 and 27.8 fb^{-1} of pp collision data at $\sqrt{s}$ =13 TeV collected with the CMS [17] (left) and ATLAS [131] (right) detector, respectively.

bined for the updated MSSM benchmark scenario $m_{\mathrm{h}}^{\mathrm{mod+}}$. This scenario incorporates the constraints of the discovered CP-even SM-like h(125) state, as discussed in Section 1.2.6. At the time, these results posed the most stringent constraints in the $b\bar{b}$ decay mode in the low m_A region of the MSSM parameter space. The increase in center-of mass-energy up to 13 TeV allowed probing higher values of the pseudoscalar boson mass, with an upper bound at m_{A} = 1200 GeV and 1400 GeV for the CMS and ATLAS searches, illustrated in Figure 4.2. On the other hand, because of the larger trigger rates, tighter jet kinematic thresholds were adopted, thus restricting significantly the sensitivity reach in the low-mass region down to 300 GeV and 450 GeV for CMS and ATLAS results, respectively.

This thesis work is based on a novel search at $\sqrt{s}$ = 13 TeV, the semi-leptonic channel. The additional requirement of a muon within any of the two most energetic b-tagged jets in the final state is introduced. This type of muon selection acts as a soft b-tagging requirement since it targets the semi-leptonic decays of b-hadrons contained in heavy flavour jets. This enables the reduction of the transverse momentum thresholds of the selected jets at trigger level. Consequently, additional Higgs bosons decaying to a $b\bar{b}$ pair with masses as low as 125 GeV can be probed at the LHC.

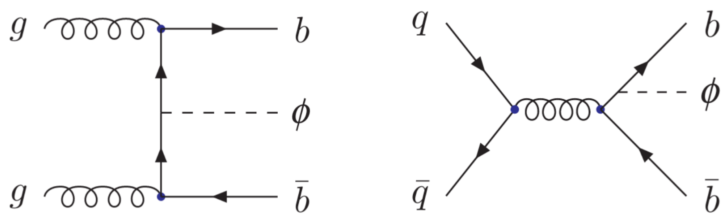

Figure 4.3: A selection of Feynman diagrams of the leading-order processes in the 4-flavour scheme (4FS) concurring to the ϕ production in association with two b-quarks [131].

4.2 Signal and background processes

The search presented in this thesis uses CMS data collected in 2017 corresponding to an integrated luminosity of 36.5 fb^{-1}. It complements and extends the sensitivity reach of the search exploiting the fully-hadronic category using the CMS data collected in 2016 [17]. Despite the similar parametric approach for the modelling of the signal and background processes, several substantial changes to the analysis strategy have been implemented: the selection of the b-tagged jets is performed with more sophisticated multivariate algorithms; the improvement in the signal resolution and scale by means of corrections to the b-tagged jet energy; the development of an advanced data-driven approach exploiting a tag-and-probe technique to factorise the individual contributions of the trigger systematic uncertainties affecting the di-jet plus muon system.

The main process of interest is the b-associated production of the neutral Higgs boson ϕ, which subsequently decays into a $b\bar{b}$ pair. In several theories comprising an enlarged Higgs sector, the $b\bar{b}\phi$ process can become the dominant production mode due to the tanβ enhancement of the bottom Yukawa coupling. Depending on the assumptions regarding the mass of the b-quark, different flavour schemes can be adopted to calculate the total inclusive cross section of the process.

The four-flavour scheme (4FS) is valid provided that the characteristic scale of the process is much lower than the b-quark mass. In this case, the bottom quark parton density vanishes [132], hence mostly gluons participate in the initial state, as exemplified by the leading order Feynman diagrams shown in Figure 4.3. On the other hand, if the interaction energy reaches a value of $Q = m_\phi/4 \gg m_b$,[2] where m_ϕ is the mass of the searched Higgs boson, then the bottom parton density must be taken into account. In the latter case, the calculation is performed within the five flavour scheme (5FS). The value

[2]At this value of the characteristic scale of the process, the collinear limit is reached. The logarithmic terms present at all orders in the 4FS describing the soft $g \to b\bar{b}$ splitting spoil the perturbativity of the calculation provided that $Q \gg m_b$.

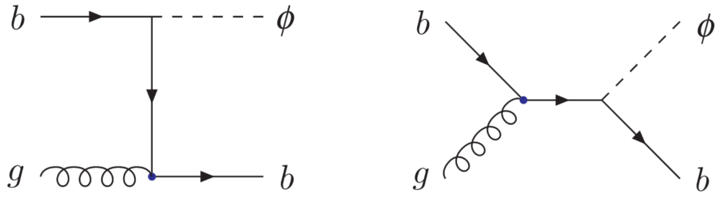

Figure 4.4: A subset of Feynman diagrams of the leading-order ϕ production in association with a single b-quark contributing exclusively in the 5-flavour scheme (5FS) [131].

of the b-quark mass is set to zero in the leading order Feynman diagrams portrayed in Figure 4.4.

At finite order, the computation of the total inclusive cross section is obtained by combining the predictions of the four- and five-flavour schemes by means of an empirical approach, namely the Santander matching scheme. The latter was introduced to reconcile the numerical predictions of the total inclusive cross section of the signal process with leading order accuracy in the 4FS and 5FS, which differ by a factor ~ 5 at a characteristic scale of $Q = m_{\phi}$[3]. Next-to-leading order signal processes can also be calculated in both flavour schemes including initial and final state radiation.

The characteristic signature of the $b\bar{b}(\phi \to b\bar{b})$ signal process is the presence in the final state of two highly energetic b-tagged jets, initiated from the decay products of the Higgs boson, and at least one additional associated b-tagged jet, denominated as the *spectator* jet. Despite the frequent presence of two spectator jets in the signal process, the requirement of a well-reconstructed fourth b-tagged jet would limit both the signal acceptance and rate exceedingly. Unlike the fully-hadronic channel, the statistical power of the channel is already constrained by the requirement of a muon within a jet , which accounts for a reduction of the signal rate by approximately an order of magnitude. Therefore, only three b-tagged jets and a muon within a jet are required in the event selection.

Background contributions arise from Standard Model events with the same triple b-tagged jet signature as the signal process and from multi-jet events, in which at least a

[3]This technique combines 4FS and 5FS predictions for the $b\bar{b}\phi$ cross section using a weighted mean based on the Higgs boson mass [132], viz:

$$\sigma^{matched} = \frac{\sigma^{4FS} + w\sigma^{5FS}}{1+w}, \qquad \text{where} \qquad w = ln\frac{m_H}{m_b} - 2, \tag{4.1}$$

where σ^{4FS} and σ^{5FS} indicate the total inclusive cross section in the 4FS and the 5FS. As the mass ratio w tends to unity (infinity) the four (five-) flavour scheme predictions become unique in the asymptotic limit.

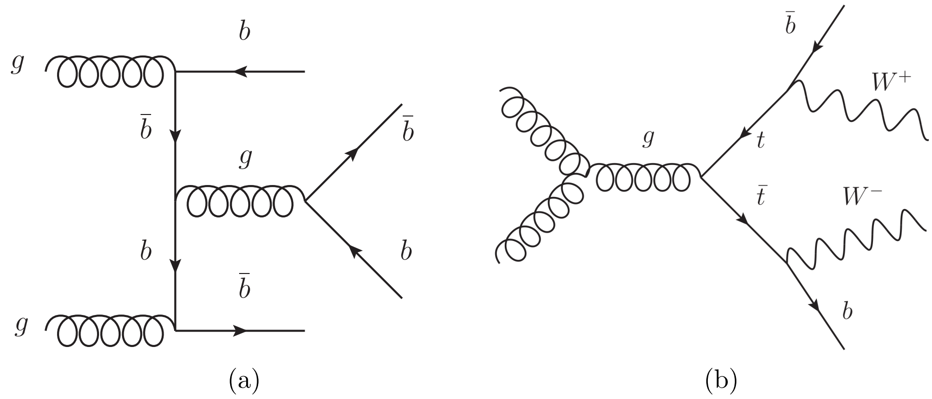

Figure 4.5: Feynman diagrams with at least three b-quarks in the final state produced in a QCD process (left) and in $t\bar{t}$ decay (right). The diagrams have been realised with [71].

light-flavoured jet is misidentified as b-quark initiated jet. The predominant background source is the irreducible QCD multi-jet production. The QCD production cross-section for at least two b-tagged jets lies in the range $\sigma_{QCD}(n_{jets} > 2) = 10^{3-6}$ pb depending on the jet activity, defined as the scalar p_{T} sum of all the jets in the event with a transverse momentum larger than 20 GeV. A representative Feynman diagram of a QCD process with four bottom quarks in the final state is shown in Figure 4.5 a.

A second background contribution originates from the $t\bar{t}$ + jets production. Such events always contain at least two b-quarks in the final state because of the almost exclusive $t \to b$ decay, as illustrated in Figure 4.5 (b). Nevertheless, the production cross section $\sigma_{t\bar{t}} = 888$ pb [133] of the $t\bar{t}$ process is significantly lower than most QCD subprocesses. The total contribution was estimated in Monte-Carlo simulation studies to account for less than 6% of the events selected in data with the signal topology, as discussed in Section 4.8.1. A data-driven approach is adopted in this work to estimate all background processes inclusively, and to simplify the modelling of the background shape using a single analytical description.

4.3 Analysis strategy

The analysis strategy is to search for an excess of events in the observed dijet mass distribution of the jet candidates stemming from the Higgs boson decay. In this type of selection of the signal process, the two leading jets in p_{T} are initiated by the Higgs boson decay products. The main observable of the analysis is the di-jet invariant mass M_{12} of the leading two b-tagged jets. Signal events are selected with at least three b-tagged jets in the final state, thus defining the triple b-tag bbb signal region. In addition, a muon

Run-period	Run-range	Integrated luminosity, fb^{-1}
Era 2017C	299337-302029	9.6
Era 2017D	302030-303434	4.2
Era 2017E	303435-304826	9.3
Era 2017F	304911-306462	13.5
Total		36.5

Table 4.1: Amount of data collected in each 2017 data-taking period with the semi-leptonic trigger used in the analysis with the CMS detector.

candidate stemming from the b-hadron decay of one of the two highest-p_T jets must be identified.

The background is evaluated by means of a suitably defined control region. A signal depleted region, denoted as *bbnb*, is obtained by requiring that the spectator jet does not satisfy the b-tag requirement. Since the background estimation is completely data-driven, a breakdown of individual background components is not necessary for the purpose of the background modelling. In order to prevent any bias in the analysis optimisation, a conventional *blinding policy* is adopted, requiring that the M_{12} spectrum in the signal region is not inspected prior to the definition and validation of the analysis methods in the control region. As the final step, the M_{12} distribution in the *bbb* region is used together with the background model to perform a global signal plus background fit to evaluate the signal production cross section.

4.4 Data and Monte Carlo simulated samples

The present analysis is based on the data collected with the CMS detector at a centre-of-mass energy of 13 TeV in 2017. The data-taking period in which the main semi-leptonic trigger were deployed spans several run periods, or *eras*, C to F, and the corresponding recorded luminosity per era is displayed in Table 4.1.

The signal samples listed in Table 4.2 for the simulation of the MSSM Higgs boson production and subsequent decay were produced centrally. The leading-order signal process is simulated with the Pythia8 generator [91] $pp \to b\bar{b}A/H \to b\bar{b}$. Pythia is a parton-shower generator that calculates $2 \to 2$ matrix elements at tree level, which is widely used to simulate hadronisation and parton showering. The next-to-leading corrections, including the gluon emission responsible for initial and final state radiation, are instead computed with the event generator Madgraph5_aMC@NLO [134]. Madgraph is an event generator used to compute the hard-scattering process at matrix element level with

Process	Generator	Mass point, [GeV]	Events	Fraction of negative weights
$b\bar{b}A/H \to b\bar{b}$, LO	PYTHIA8	120	1000000	–
		350	1000000	
		600	1000000	
		1200	1000000	
$b\bar{b}A/H \to b\bar{b}$, NLO	MADGRAPH5	120	9543000	36%
		125	24934500	
		130	7277000	
		140	9774000	
		160	9644000	
		180	9757000	
		200	8513000	
		250	7257396	
		300	18972000	
		350	9177000	
		400	9936000	
		450	9857000	
		500	8385000	
		600	10000000	
		700	9144903	

Table 4.2: Summary of the simulated signal samples utilised in this analysis. In each Monte Carlo sample the mass of the hypothetical Higgs boson is indicated, as well as the the total number of generated events and the relative fraction of negative weights from the interference terms in the cross section computation.

a maximum of two (four) additional partons with (next-to)-leading order accuracy. In this analysis, MADGRAPH5_aMC@NLO is interfaced with PYTHIA8 for the parton shower computation. Interference terms in the NLO cross-section calculation of the signal process lead to a sizable fraction of events, around 36%, carrying a negative weight. The leading order signal samples have been used for a quantitative comparison with the samples with next-to-leading order accuracy.

Furthermore, centrally-produced Monte Carlo samples listed in Table 4.3 simulating the prevailing background source, the QCD multi-jet production, have been used in the trigger efficiency studies described in Section 4.5. Due to the requirement of a muon within a jet in the event selection, the statistical power of the inclusive QCD samples is excessively reduced. Consequently, QCD samples enriched in muons have been generated to study the online muon kinematic efficiency.

Sample	Generator	$\hat{p}_T/H_T$, [GeV]	Events	Cross section, pb
QCD μ-Enriched	PYTHIA8	$\hat{p}_T = 30 - 50$	29030324	1362000
		$50 - 80$	24068613	376600
		$80 - 120$	23248995	88930
		$120 - 170$	20774848	21230
		$170 - 300$	46170668	7055
		$300 - 470$	17744779	797.3
		$470 - 600$	24243589	59.24
		$600 - 800$	16390713	25.25
QCD b-Enriched	MADGRAPH5	$H_T = 100 - 200$	8894908	1260274
		$200 - 300$	9952918	80430
		$300 - 500$	3547725	16620
		$500 - 700$	2010208	1487
		$700 - 1000$	891925	296.5
QCD b-gen filter	MADGRAPH5	$H_T = 100 - 200$	9417440	1282000
		$200 - 300$	8611681	111800
		$300 - 500$	5529691	28070
		$500 - 700$	7621842	3082
		$700 - 1000$	1816716	724.2
$t\bar{t}$	PYTHIA8	-	10139950	831.76

Table 4.3: Summary of the QCD and $t\bar{t}$ simulated samples utilised in this analysis. In the QCD μ-enriched sample, the selected muon must satisfy a kinematic cut of $p_{\mathrm{T}}^{(\mu)} > 5$ GeV at generator level. For each sample, binned in terms of either the parton transverse momentum $\hat{p}_T$ or in the event activity H_T, the total number of generated events and the production cross section is indicated.

4.5 Triggers

One of the main challenges of the present analysis is the development of a set of dedicated triggers used to collect the data for the analysis and to perform the studies required to determine the trigger efficiencies. As outlined in Section 2.2.5, the CMS trigger system consists of a two-step procedure adopting *level one triggers* (L1) for a fast event selection performed with custom-built logic boards, followed by further processing in a *high level trigger* (HLT) computer farm, which executes a simplified version of the offline CMS reconstruction software. The key objective of any physics trigger is to retain as many signal events as possible, whilst keeping the output rate at an acceptable level at each step of the triggering sequence.

4.5.1 The semileptonic L1 trigger

The semileptonic L1 trigger used in the 2017 data-taking period selects events with at least two jets and it also requires the presence of a muon lying within the hadronisation cone of either the two jets passing the p_{T} selection. The requirement of a L1 muon in the semileptonic trigger drives down the overall rates by an order of magnitude. This rate reduction allows retaining jets with lower p_{T} compared to those from the all hadronic analysis.
The L1 selection implemented in the semileptonic trigger is summarised below :

- at least two calorimeter jets are present with $p_T^{(1,2)} \geq 40$GeV located within a pseudo-rapidity window $\left|\eta^{(1,2)}\right| \leq 2.3$. A tight $|\eta|$ selection is possible without compromising the sensitivity, as signal jets are produced more centrally than in background events;

- any jet pair fulfilling the kinematic requirements must have an angular separation $\Delta\eta \leq 1.6$, which reduces the overall L1 rate by approximately 15%. This cut improves the purity of the signal sample by rejecting a large fraction of background processes. The QCD multi-jet events tend to have a broader $\Delta\eta$ separation between the most energetic jets, when compared to signal events;

- one Level-1 muon is selected with a $p_T^{(\mu)} \geq 12$ GeV and $\left|\eta^{(\mu)}\right| \leq 2.3$ and with a maximal distance from the jet axis of any of the two most energetic b-tagged jets of $\Delta R(\mu, j_i) \leq 0.4$, where the index $i = 1, 2$ denotes the jet rank in p_{T}.

All the kinematic thresholds of the L1 sequence have been optimised to keep the output rates under control. The methodology followed for the preliminary L1 rate study prior to the inclusion of the semileptonic trigger in the 2017 trigger menu is described extensively in Appendix B.1. The starting point of the L1 sequence, the *L1 seed*, was emulated using 2016 data. The observed L1 rate at a peak pile-up $\langle\mu\rangle = 56$ is around 1.7 kHz, which agrees well with the predicted value from simulation. The achieved high precision of the rate estimates is in line with expectations since the CMS calorimeter and muon system in 2017 are unvaried with respect to the 2016 legacy system.

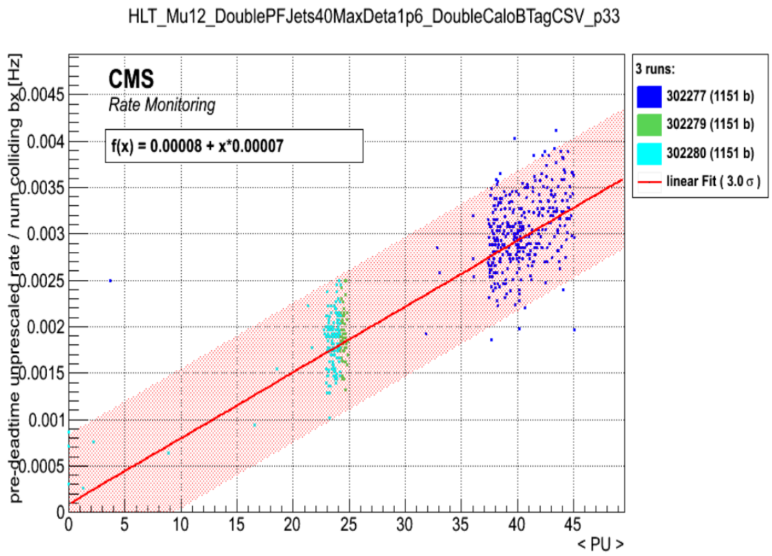

Figure 4.6: Linear dependence of the HLT rate on the mean number of pile-up interactions for the main semi-leptonic trigger of the analysis for a representative 2017 LHC fill 6165 with $N_b = 1151$ circulating bunches per beam. The HLT rate was found to be 10.2 ± 2.3 Hz at an instantaneous luminosity of $\mathscr{L} = 2.06 \times 10^{34} cm^{-2} s^{-1}$.

4.5.2 HLT trigger

The events passing the L1 requirement are further processed at the HLT level. This trigger step consists of a sequential workflow, where the most computationally expensive sequences are placed at the end in order to minimise the processing time, or *timing*, of the trigger. A detailed description of the HLT timing study is reported in Appendix B.2. The architecture of the HLT trigger sequence is structured as follows:

- at least two anti–k_T calorimeter jets, corrected for the pile-up offset, pass the kinematic cuts of $p_T^{(1,2)} > 30$ GeV and $\left|\eta^{(1,2)}\right| < 2.3$;
- one particle flow muon with a $p_T^{(\mu)} > 12$ GeV and in the same η window as the two leading jets in p_{T};
- at least two calorimeter jets out of a maximum of eight candidates are processed in the online b-tagging sequence based on the CSVv2 b-tagger described in Section 4.5.6. This involves a series of quality cuts on the primary and secondary vertex

reconstruction, which are crucial for accurate b-jet identification. The value of the online b-tagging CSVv2 discriminant is set to 0.92, which corresponds to a 0.33% fake rate rejection for light-flavoured jets. This requirement is more stringent than the 1% mis-identification (medium) working-point imposed in the offline event selection;

- at least two particle-flow jets with a tighter p_{T} threshold of 40 GeV with respect to calorimeter jets and the other kinematic cuts unvaried with respect to previous steps[4];

- as in the L1 seed, any pair of jets passing the kinematic requirements must have an angular separation in $\Delta\eta \leq 1.6$;

This HLT sequence was designed to meet the total rate budget of 15 Hz allocated by CMS for any physics triggers, without the application of any random pre-scaling of the triggered events. However, the actual observed rate in data was found to be on average around 10 Hz, as shown in Figure 4.6. The latter is lower than expectation owing to the large uncertainties in the rate estimation, coming from Monte Carlo samples with the upgraded 2017 geometry. Besides keeping the trigger rates under control, this complex sequence of online cuts maximises the sensitivity of the analysis. The last sequential step involves the full PF reconstruction sequence, which is the most computationally expensive part. The timing of the trigger is reduced by performing the baseline selection of the dijet-plus-muon system already at Level-1. The mean total timing of the semi-leptonic trigger path was found to be ~ 2.8 ms at peak pile-up $\langle\mu\rangle = 56$ in simulation, which is well below the acceptable maximum of 10 ms.

In general, the difference in precision between reconstruction algorithms can lead to trigger inefficiencies. For instance, the decision to reject events based on the jet p_{T} is much faster at Level-1 than for particle-flow jets selected at HLT because of the different complexity of the reconstruction sequence. This leads to an underestimation of the fraction of triggered events with a very soft p_{T} spectrum, which can be parameterised in terms of a kinematic *turn-on* behaviour. Trigger efficiencies are determined for all PF analysis objects selected at trigger level, following a factorised approach. The trigger efficiency for the di-jet system is split between the *kinematic* part, which describes the performance of the triggered jet transverse momentum and angular response, and the *online b-tag* factor, which accounts for the trigger response of the b-jet filtering sequence. An independent measurement is performed for the kinematic trigger efficiency of the selected muon within-a-jet as a function of its transverse momentum.

[4]Applying a looser p_{T} threshold to calorimeter jets with respect to the PF jets is useful to keep the HLT rate sustainable. This is due to the lower reconstruction efficiency, and faster processing time, for calorimeter jets with a soft p_{T} spectrum with respect to the corresponding PF objects.

Run-period	Run-range	Integrated luminosity, pb^{-1}		
		JetHT		DoubleMuon
		PFJet40	PFJet60	Mu8
Era 2017C	299337-302029	58.3	232	0.716
Era 2017D	302030-303434	193.3	357	0.499
Era 2017E	303435-304826	66.2	277	0.553
Era 2017F	304911-306462	72.6	259	0.754
Total		390.7	1108	2.52

Table 4.4: Summary of the primary datasets run ranges and of the corresponding luminosity the single-jet PF triggers in the JetHT dataset and the single-muon trigger in the DoubleMuon dataset after prescale.

4.5.3 Kinematic trigger efficiency

The aim of the study on kinematic trigger efficiency for the physics objects of interest, namely muons and jets, is twofold. On one hand, one needs to determine the efficiency dependence on the object selection arising from the difference in scale and resolution between the online and offline versions of the variable used in the selection. Another effect, which can be partially correlated with the former, is the efficiency dependence on data-taking conditions and on the detector geometry.

Primary datasets are inclusive subsets of the event stream recorded by the CMS experiment. They contain similar physical objects present in the final state of the event that are reconstructed by the HLT sequence. An overview of the primary datasets used to evaluate the kinematic trigger efficiency is shown in Table 4.4. The *JetHT* and *DoubleMuon* dataset contain single jet (muon) triggers with different p_{T} thresholds, respectively. The total integrated luminosity corresponding to each data-taking period for the certified data, satisfying the required quality criteria is also indicated. Owing to their high trigger rate, the inclusive single-object triggers are prescaled according to their kinematic thresholds. This leads to a substantially lower integrated luminosity with respect to the main analysis trigger, which is unprescaled.

Tag-and-probe method

A *tag–and–probe* method was adopted to compute the kinematic efficiency of both jet and muon objects. This is a powerful technique that can be exploited to obtain the reconstruction efficiency of a generic physics object. The key advantage consists in the selection of a pure, unbiased sample of one of such objects in a pair, which by construction removes potential mis-reconstruction effects ascribable to the selection of a single object. The tag–and–probe method usually exploits some known physical process, such as resonant production. The object that effectively *probes* the reconstruction efficiency is left unbiased by the selection applied on the tag object side. The efficiency is then simply extracted as:

$$\epsilon_T = \frac{N(passing\ probes)}{N(probes)}, \tag{4.2}$$

where all events whose probe pass the selection of interest contribute to the numerator, whereas all events with probes identified by the tag selection are included in the denominator.

4.5.4 Jet kinematic trigger efficiency

The jet kinematic efficiency is determined as a function of the offline kinematic variables, namely the offline jet p_T and η. Neglecting the kinematic cross-correlation between the two most energetic jets, the total kinematic trigger efficiency can be expressed as the following product:

$$\epsilon_{\mathrm{kin.}} = f(p_T^{(1)}, p_T^{(2)}, \eta^{(1)}, \eta^{(2)}) = f(p_T^{(1)}, \eta^{(1)}) \cdot f(p_T^{(2)}, \eta^{(2)}), \tag{4.3}$$

where $f(p_T^{(1)}, \eta^{(1)})$ and $f(p_T^{(2)}, \eta^{(2)})$ are the individual kinematic trigger efficiencies of the first and the second leading jet in p_T, respectively.

The jet kinematic trigger efficiency was obtained using a sample of back-to-back di-jet events. Pre-scaled single-jet triggers denoted as `HLT_PFJetX` with p_T thresholds `X= 40, 60` GeV listed in Table 4.5 have been used in this study to probe different offline p_T ranges. The more inclusive trigger has the same p_T threshold as the semileptonic trigger used in the analysis. Owing to its lower pre-scale, the PF trigger with the tighter threshold has been used to overcome the statistical limitations of the former at high p_T. Previous studies have shown that the `HLT_PFJet60` becomes fully efficient at 85 GeV [135]. Therefore, this trigger was used to extend the efficiency measurement in p_T from a value of 110 GeV up to 300 GeV. Moreover, the Level-1 and calorimeter jet kinematic thresholds are emulated by applying the same kinematic cut as in the PF object to the corresponding trigger object. The most energetic jet is identified as the tag, while the second leading one as the probe. The following baseline double-jet selection is applied:

- both leading jets in p_T passing tight identification requirements are forced to be back-to back by requiring $\Delta\phi_{12} > 2.4$;
- they must satisfy $p_T^{(1,2)} > 30$ GeV and $\left|\eta^{(1,2)}\right| < 2.3$;
- if a third jet is present in the event, it must have a significantly lower p_T than the mean transverse momentum of the two leading jets, i.e. $p_T^{(3)} < 0.3 \times \frac{p_T^{(1)}+p_T^{(2)}}{2}$. The

Trigger name	N_{jets}	N_{b-tags}	$p_{T,jet}$ (GeV)	$\lvert\eta_{jet}\rvert$	$\lvert\Delta\eta_{jet-ij}\rvert$	d_{CSVv2}	N_{μ}	$p_{T,\mu}$ (GeV)	$\lvert\eta_{\mu}\rvert$
Main trigger									
`HLT_Mu12_DoublePFJets40 MaxDeta1p6_Double CaloBTagCSV_p33`	2	2	40	2.3	1.6	0.92	1	12	2.3
Control triggers									
`HLT_SingleJet30_Mu12_ SinglePFJet40_p33`	1	0	40	5	—	—	1	12	5
`HLT_PFJet40`	1	0	40	5	—	—	—	—	—
`HLT_PFJet60`	1	0	60	5	—	—	—	—	—
`HLT_Mu8`	—	—	—	—	—	—	1	8	5

Table 4.5: Summary of the triggers adopted in this work. The main semi-leptonic trigger is used to collect the data for the analysis, while the control triggers are used for the determination of the kinematic trigger efficiencies.

suppression of additional jet activity in the event serves the purpose of improving the purity of the di-jet sample. Furthermore, it is desirable to suppress soft jet radiation since soft QCD processes are generally more prone to mis-modelling in simulation;

- the matching condition between offline jets and the online objects at all reconstruction levels requires an angular separation of $\Delta R < 0.5$.

Thus, the efficiency is calculated as the fraction of events in which both leading jets in p_{T} fire the single jet trigger over the total number of events in which the first leading one fires the trigger. Since the single jet trigger pre-scale are not constant, in order to combine correctly different eras in a single efficiency curve, the following luminosity event-by-event weight was applied:

$$w = \frac{\mathscr{L}^{era}_{total}}{\mathscr{L}^{era}_{trigger}}, \tag{4.4}$$

where $\mathscr{L}^{era}_{total}$ is the total luminosity collected per era, and $\mathscr{L}^{era}_{trigger}$ corresponds to the luminosity collected by the single jet trigger in the same era, taking prescales into account. This reweighting allows addressing time-dependent shifts in the position of the kinematic turn-on points. The same procedure was followed to determine the kinematic trigger efficiency in simulation using PYTHIA8 QCD samples listed in Table 4.3. The pile-up profile of the simulated events was corrected with a standard re-weighting procedure. In order to obtain a fair comparison with data, corrections to the leading jets energy and p_{T} resolution, described in Section 3.5.2, have also been applied prior to the efficiency computation.

Kinematic trigger scale factor

In order to correct the efficiency in simulation to the observed one in data, it is convenient to derive a correction commonly referred to as *scale factor*. In this context, the kinematic scale factor is computed from the ratio of the kinematic efficiency curves obtained from data and simulation for each of the two leading jets which are selected by the trigger:

$$SF_{\mathrm{kin}}(p_T^{(i)}, \eta^{(i)}) = \frac{\epsilon^{\mathrm{data}}_{\mathrm{kin.}}(p_T^{(i)}, \eta^{(i)})}{\epsilon^{\mathrm{MC}}_{\mathrm{kin.}}(p_T^{(i)}, \eta^{(i)})}, \;\; with \;\; i = 1, 2, \tag{4.5}$$

where the index i stands for the jet ranking according to its transverse momentum. The overall scale factor of the event can be factorised as the product of the individual scale factors of the two most energetic jets under the assumption that the jet-jet kinematic correlations are well-modelled in the simulation.

$$SF_{\mathrm{kin,\ event}} = SF_{\mathrm{kin}}(p_T^{(1)}, \eta^{(1)}) \times SF_{\mathrm{kin}}(p_T^{(2)}, \eta^{(2)}). \tag{4.6}$$

In order to smoothen out the statistical fluctuations, the correction is fitted with a *Gauss error function*, the cumulative distribution of a Gaussian function, defined as:

$$erf(x) = \frac{2}{\sqrt{\pi}} \int_0^x e^{-t^2} dt. \tag{4.7}$$

The resulting efficiency curves and the scale factors are illustrated in Figure 4.7. This study shows that turn-on point differs significantly between data and Monte Carlo in the endcap region, which is characterised by a higher occupancy and more intense jet activity. The uncertainty of the scale factor is estimated from the covariance matrix of the fit and it is used to obtain the analytical form of the up and down two-sigma variations of the jet trigger kinematic scale factor, discussed in detail in Section 4.7.4.

4.5.5 Muon kinematic trigger efficiency

The measurement of the overall online and offline muon reconstruction efficiency is a crucial aspect of this analysis since it impacts the signal efficiency of the di-jet plus muon system. In the most general case, the overall selection efficiency of an offline reconstructed muon can be factorised as follows:

$$\epsilon^{\mu}_{total} = \epsilon^{\mu}_{Tracker} \times \epsilon^{\mu}_{ID} \times \epsilon^{\mu}_{Trigger}, \tag{4.8}$$

where $\epsilon^{\mu}_{Tracker}$ is the muon tracking efficiency for global muons, ϵ^{μ}_{ID} is the muon identification efficiency, $\epsilon_{Trigger}$ is the muon trigger efficiency. The muon tracking efficiency was measured and found to be very close to unity, therefore it can be neglected in the efficiency computation. Thus, the overall muon selection efficiency in this analysis can be factorised solely in terms of two contributions :

$$\epsilon^{\mu}_{total} = \epsilon^{\mu}_{ID} \times \epsilon^{\mu}_{Trigger}. \tag{4.9}$$

These efficiency measurements are performed independently using a sample of muon passing the previous selection step in the sequence $tracker \rightarrow ID \rightarrow trigger$.

A tag-and-probe method was also used to evaluate the muon kinematic trigger efficiency using the $J/\psi \rightarrow \mu^+\mu^-$ decay channel. Events selected in the J/ψ mass window are used to obtain a pure sample of muons with a soft p_{T} spectrum. The J/ψ resonance peaking at 3.096 ± 0.006 GeV possesses the ideal decay topology to probe the kinematic turn-on region of the semi-leptonic trigger used in the analysis. The data samples used in the muon kinematic efficiency measurement in data correspond to the *DoubleMuon* dataset listed in Table 4.4. The kinematic leg in the HLT sequence of the main trigger was emulated by imposing the same set of kinematic cuts as in the semileptonic trigger on the online trigger muon objects of the more inclusive single-muon trigger `HLT_Mu8`.

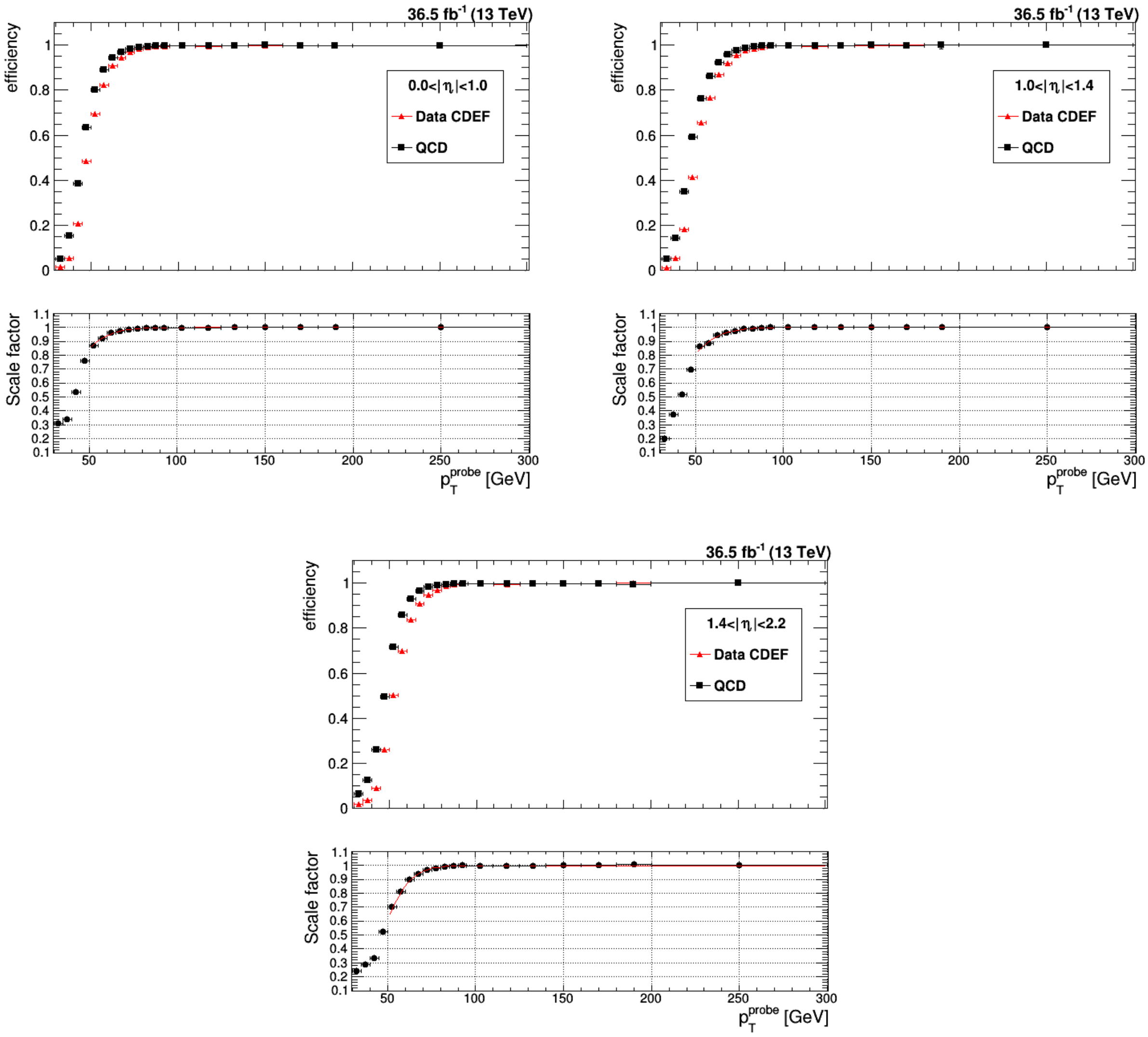

Figure 4.7: Kinematic trigger efficiency as a function of the jet p_T as determined from data (red) and simulated QCD samples (black) in three non-overlapping pseudorapidity bins, namely from top left to bottom: $0 < |\eta| < 1.0$, $1.0 < |\eta| < 1.4$, and $1.4 < |\eta| < 2.2$, corresponding to the barrel, overlap and endcap regions, respectively. In the bottom panel of each plot, the scale factors obtained from the ratio of the corresponding efficiency curves are fitted with the Gauss error function.

A p_{T} threshold of 12 GeV and a pseudorapidity restriction to $|\eta| < 2.3$ is imposed for both Level-1 and PF muons. An analogous procedure was followed for the determination of the efficiencies in simulation using QCD muon-enriched samples. Owing to statistical limitations of the data samples, the kinematic efficiency was evaluated exclusively in bins of the offline muon p_{T}. The following selection criteria are applied on the tag-and-probe muon pair:

- two oppositely-charged muons passing tight identification;
- di-muon pairs within the mass window of $\left|m_{\mu\mu} - m_{J/\psi}\right| < 0.15$ GeV are selected;
- $5 < p_T^{(\mu)} < 30$ GeV; $\left|\eta^{(\mu)}\right| < 2.3$;
- $p_T(\mu_{tag}) > 10$ GeV;
- $\Delta R(\mu_{probe}; \mu_{tag}) > 0.1$.

The tag muon tests whether the event has fired the emulated single-muon trigger. The matching condition to the online trigger objects of the probe consists of a spatial separation of $\Delta R(\mu_{probe}, \mu_{L1}) < 0.4$ and $\Delta R(\mu_{probe}, \mu_{L3}) < 0.005$. This matching requirement is identical for the tag muon.

This probe matching condition splits the events into two disjoint event categories, distinguishing between the *passing* and the *failing probes*. The combinatorial background from additional muon tracks makes a substantial contribution, especially in the low p_{T} region of the di-muon mass spectrum. The cuts on the angular separation ΔR between the online trigger objects and the offline reconstructed muons, as well as the separation between the tag and probe pair were optimised to suppress the background events from mis-matched muon pairs. The overall background rejection is approximately 90% in the lowest p_{T} bins. The residual background is subtracted from the efficiency computation by means of a simultaneous signal plus background fit with identical shape parameters to the di-muon invariant mass spectrum in both categories:

$$f(x) = \{A \exp\left(-\frac{(x-m_0)^2}{2\sigma^2}\right) + k\} \times \begin{cases} \epsilon & : passing\ probe \\ (1-\epsilon) & : failing\ probe \end{cases} , \tag{4.10}$$

where A, m_0 and σ are respectively the normalisation, mean and width of the gaussian fit used for the signal parameterisation, whereas the parameter k is an offset which accounts for the background contribution. Thus, the trigger efficiency ϵ is derived from the overall normalisation factor of the simultaneous invariant mass fit categories for every p_{T} bin. The statistical uncertainty on the efficiency is extracted from the Poissonian-likelihood function since this estimator is more accurate than the χ^2 test in the case of samples with low statistics, as verified for the higher p_{T} bins.

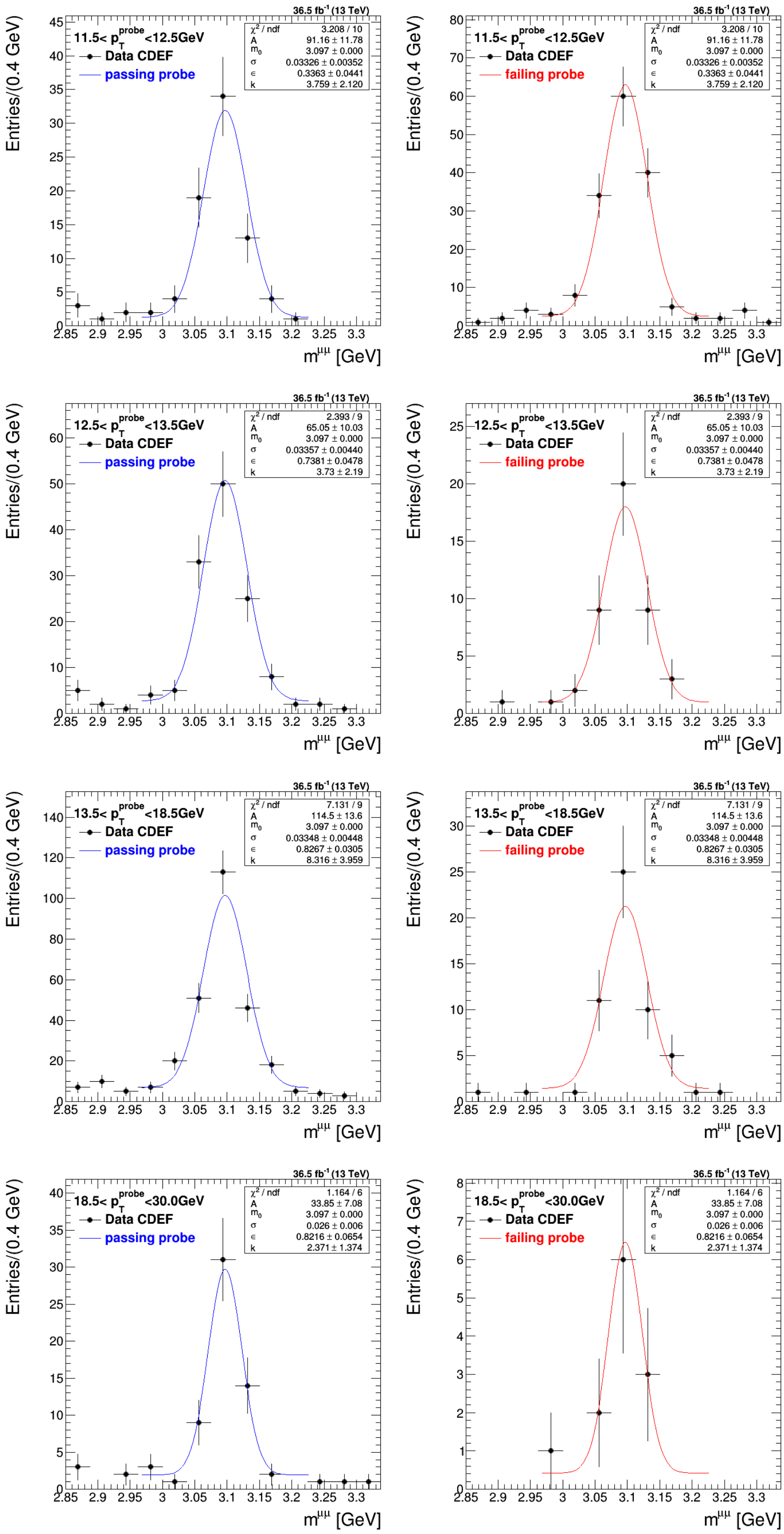

Figure 4.8: Simultaneous fit of the invariant mass di-muon spectra in the two event categories of failing and passing probes in data for the probe p_{T} in data.

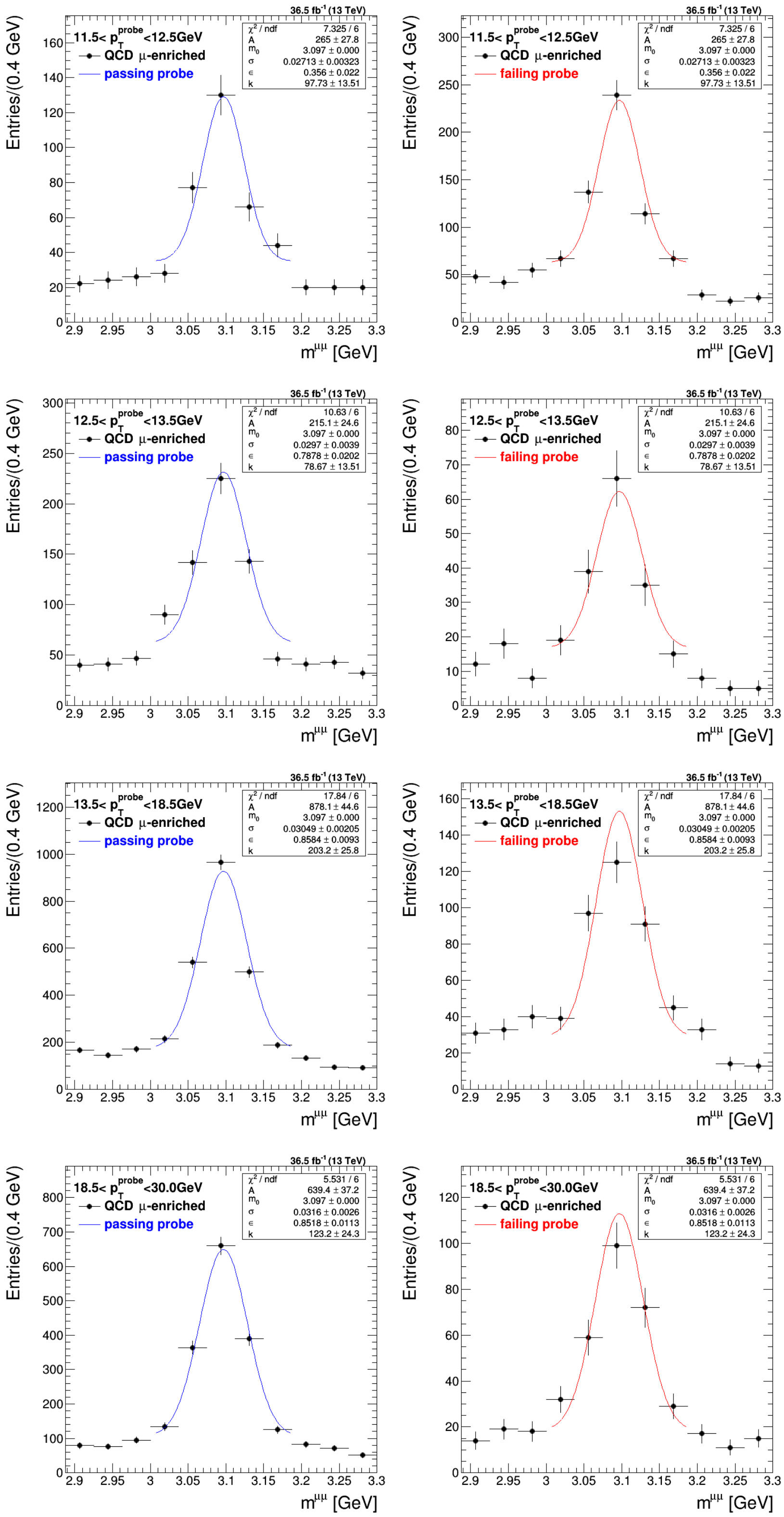

Figure 4.9: Simultaneous fit of the invariant mass di-muon spectra in the two event categories of failing and passing probes in data for the probe p_{T} in simulation.

Since all the shape parameters of the signal plus background fit are correlated, this fitting uncertainty on the efficiency takes already into account the background subtraction procedure. The parameter m_0 is fixed to the known value of the J/ψ resonance in order to reduce the overall uncertainty of the fit. The results of the simultaneous fit are shown in Figure 4.8.

The same procedure is followed to obtain the trigger p_{T} turn-on in simulation using QCD muon-enriched samples, exemplified in Figure 4.9. The muon trigger involves some quality selection, which despite the offline tight identification, yields some inefficiency that is reflected on a plateau below 100% of the efficiency curves both in data and simulation, as illustrated in Figure 4.10. The resulting muon p_{T} scale factor has been found to be slightly below unity, with a central value ~ 0.96 at the efficiency plateau, which is verified for $p_{\mathrm{T}}^{(\mu)} > 13$ GeV.

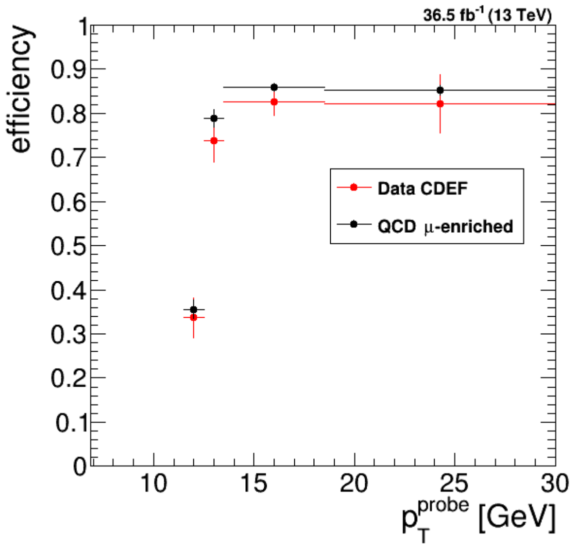

Figure 4.10: Trigger efficiency p_{T} turn-on curve of the muon measured in data (red) and in simulation (black).

4.5.6 Online b tag efficiency

The online b-tag efficiency dependence on kinematic variables is determined relative to the offline b-tagging discriminant. The prescaled single jet triggers with a b-tag requirement used in this study are listed in Table 4.6. This efficiency estimate is also achieved in a fully data-driven way by means of a tag-and-probe method. The aim of this study is to select events arising from the $pp \rightarrow q\bar{q}$ process to obtain a pure sample of b-jet candidates, by applying tight offline b-tagging requirements on the "tag" jet. For the background processes, such as $pp \rightarrow gb, gg$, the same scale factors determined for the online b-tag efficiency are assumed to be valid. Most of the background events in which the probe jet originates from a merged jet initiated by two b-quarks are removed by topological cut on the jet pair angular separation. In analogy with the event selection used in the extraction of the kinematic jet scale factors, the leading jets in the selected double b-jet sample are forced to be in a back-to-back topology. Additional background rejection is performed by cutting on the merged b-jet probability of the tag jet. The selected events must fire at least one of the control triggers. In addition, the two most energetic jets present in the event must satisfy the following criteria:

- $p_T^{(1,2)} > 40; 100; 200; 350$ GeV depending on the p_T threshold of the trigger fired. The optimised p_T bin ranges adopted are defined in Table 4.6;
- restriction in $|\eta^{(1,2)}| < 2.2$ and in $\Delta\phi_{12} > 2.5$;
- offline DeepJet b-tagging with medium (tight) working point for the leading (sub-leading) jet;
- ΔR matching with the Level-1, calorimeter and particle-flow trigger objects.

The sub-leading jet, identified as the "tag" jet, must also match the appropriate b tag trigger object. The "probe" condition is passed by events in which the first leading jet matches the relevant b tag trigger object. The fraction of events fulfilling the "probe" condition with respect to the total number of probes provides a measurement of the online b tag efficiency.

Path name	L3 $p_\mathrm{T}^\mathrm{min}$ [GeV]	tag d_CSVv2
HLT_DoublePFJets40_CaloBTagCSV_p033	40	0.84
HLT_DoublePFJets100_CaloBTagCSV_p033	100	0.84
HLT_DoublePFJets200_CaloBTagCSV_p033	200	0.84
HLT_DoublePFJets350_CaloBTagCSV_p033	350	0.84

Table 4.6: Control triggers deployed for the determination of the online b tag efficiency and the cut on the tag jet b-tag score d_CSVv2.

The best discriminant variable to suppress background events was found to be the merged b-jet probability of the tag jet. This cut is optimised as a function of the probe p_T to reduce the contamination from background events in which the probe jet is initiated by a light-flavoured parton, as illustrated in Table 4.7.

The maximal reduction in the light-flavour contamination from soft gluons splitting is approximately 80%, which is achieved for the highest probe p_T bin. The PU profile observed in the last data-taking period (Era F) is significantly different with respect to previous eras, owing to the different LHC bunch injection scheme adopted, as shown in

probe $p_{\mathrm{T}}^{\mathrm{min}}$–$p_{\mathrm{T}}^{\mathrm{max}}$ [GeV]	tag merged bb prob d_{min}	probe $udsg$- prob
40 - 160	0.0200	-25 %
160 - 220	0.0020	-40 %
220 - 400	0.0022	-66 %
400 - 800	0.0020	-80 %

Table 4.7: Optimised cuts on the DeepJet merged b-jet probability d_{min} as a function of the probe p_{T}. The subsequent decrease in the light flavour contamination of the probe evaluated in simulated samples is also shown.

Figure 2.3. Since the b-tagging performance may be affected by the different pile-up conditions, the simulated Monte Carlo samples were splitted into independent sub-samples to match the pile-up profile observed in data, and later recombined according to the era luminosity. The kinematic and b-tag distributions for the tag-and-probe datasets are determined separately for the data-taking periods in the 2017 eras C to E, and era F, respectively.

The ratios of the kinematic distributions for passing probes to the total number of probes was used to estimate the relative online b tag efficiency. The same procedure has been applied to events from PYTHIA QCD simulation. The top panel of Figure 4.11 illustrates the b-tag efficiency dependence on the offline probe p_{T} in data and simulation. In both cases, a decreasing trend of the online b tag efficiency is observed, as expected from the degradation in the performance of online b-tagging with increasing p_{T}.

Thus, the online b tag efficiencies scale factors are extracted as the ratio of the efficiency obtained in data with respect to simulation. The resulting scale factors are shown in the bottom panel of Figure 4.11, for 2017 eras C-E, for era F alone, and for all eras combined. The correction factor is parameterised linearly to smoothen out statistical fluctuations and to ease the derivation of the scale-factor uncertainty variations. The $|\eta|$ dependence is well modeled in simulation in all cases, hence only the p_T dependence of the online b tag scale factor is considered in the analysis.

4.6 Offline Event selection

The signature of the event is the presence of three b-tagged jets and of a muon within one of the two leading jets in p_{T}. The first step of the event selection is applied at trigger level. In this section, the criteria adopted for the full event selection and reconstruction are discussed with a particular emphasis on the b-jet energy corrections.

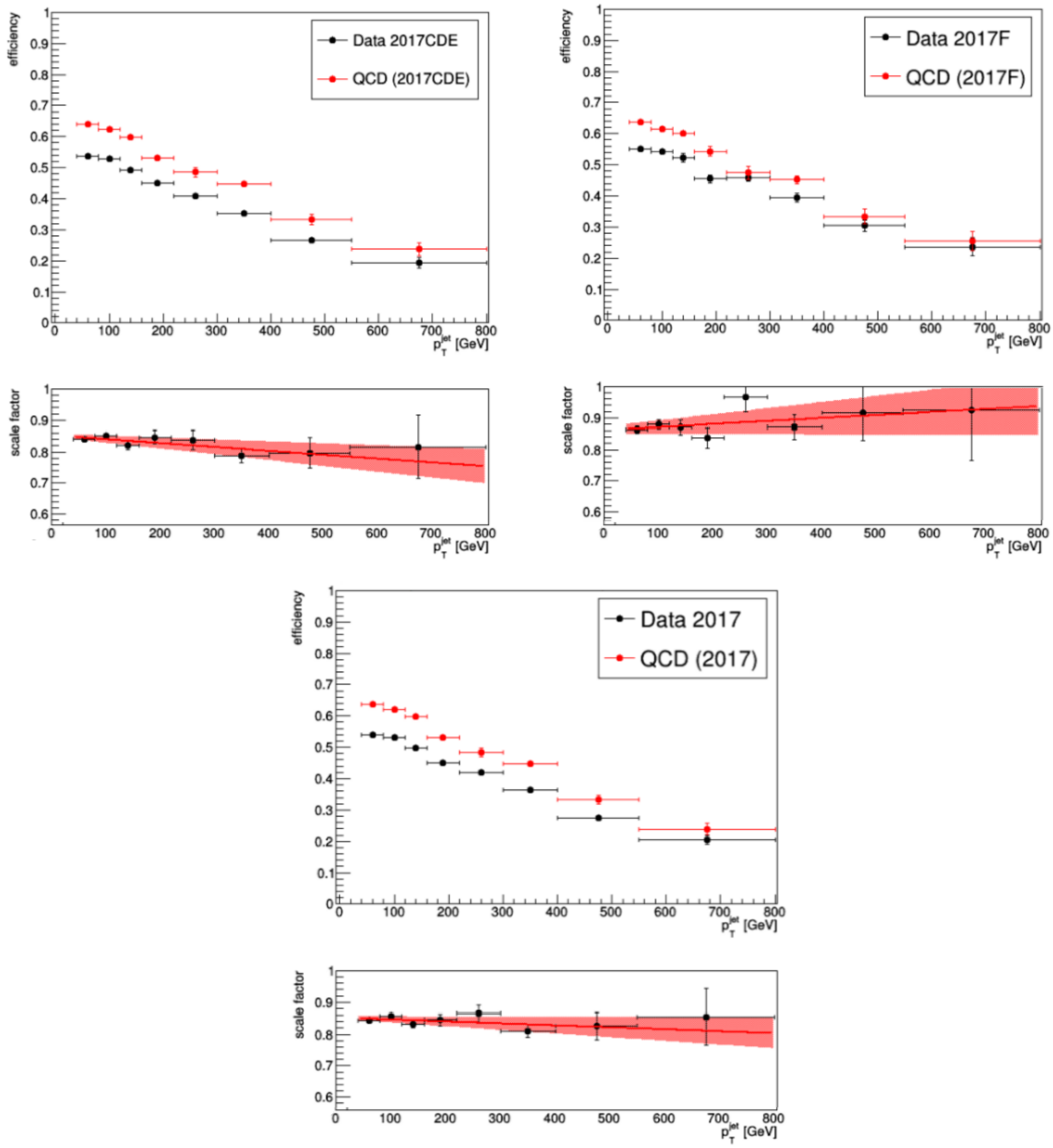

Figure 4.11: Online b-tag efficiency curves for both data and Monte Carlo (top panel) for eras C to E, era F and all 2017 eras from top left to bottom. In the bottom, the ratio of the efficiency curves is fitted with a linear function to obtain the scale factor dependence on the jet p_{T}.

4.6.1 Primary vertex selection

The starting point of the offline selection is the identification of a well-reconstructed primary vertex of the hard interaction. The requirements for the identification of a high-quality PV are summarised in Section 3.3.

4.6.2 Jet selection

The offline selection of jet objects is performed in three successive steps: jet identification, kinematic selection and b-tagging. Several identification working points have been devised for PF jets based on their reconstruction accuracy. The tight WP is characterised by a 98% fake rejection for a selection efficiency above 99% in the pseudorapidity region $|\eta| < 3.0$ [136].

Jet identification

In this work, the tight identification (ID) working point is applied on all the selected jets in the event to maximise the purity of the sample. This requirement translates into forcing each jet to possess at least two constituents, with a fraction of neutral and electromagnetic components below 90%. Each jet must also contain at least one charged hadron. In addition, the three most energetic jets in the event must satisfy a certain pile-up ID requirement, which is based on several discriminating variables, such as the jet cone profile, the charged neutral multiplicities and the β beam size parameter. The loose pile-up ID is adopted to suppress the contamination from pile-up events, whilst retaining as many signal events as possible.

Kinematic selection

An asymmetric transverse momentum threshold of 60 (50) GeV is applied for the two leading jets in p_{T} with (without) a muon in the jet cone to improve background rejection. A looser p_{T} threshold of 30 GeV is imposed on the third leading jet. In addition, the three leading jets in p_{T} must also fulfil the requirement $|\eta| < 2.2$. Furthermore, an offline cut $\Delta\eta^{12} < 1.5$ between the leading jets in p_{T} is imposed to improve background suppression. A spatial separation $\Delta R > 1.0$ between any pair of the three leading jets is also enforced to reduce the contribution from events with gluon splitting into a collimated b-quark pair. This cut was originally introduced in the 8 TeV analysis to remove the bias in the application of offline b-tag efficiencies scale factors arising from the probed multi-jet topology. The latter is slightly different with respect to the topology of the $t\bar{t}$ sample used to extract the b-tag correction factors, as explained in Section 3.6.

B-tag selection

The most sophisticated b-tagging algorithm currently available, the so-called DeepJet algorithm, described in Section 3.6, has been adopted as offline tagger. The choice of the b-tag working point relies on the overall gain in the analysis sensitivity and the statistical power of the final samples. An optimisation study has been realised by testing the discovery ratio $N_S/\sqrt{N_B}$, where N_S and N_B are the total number of signal and background events passing a simplified triple b-tag selection. Following this study, the triple b-tag tight working point ($d_{DeepJet} > 0.30$) was chosen. The background model is performed in the *bbnb* control region, obtained by means of a b-tag veto on the third leading jet. This is achieved by flipping the third b-tag requirement of the loose WP ($d_{DeepJet} < 0.052$). Furthermore, corrections to the b-jet energy, namely b-jet energy regression and final state radiation recovery (FSR), are employed to improve the shape of the di-jet invariant mass spectrum.

B-jet energy regression

The goal of b-jet energy regression is to improve the reconstructed b-jet energy resolution using a multi-dimensional correction based on a Deep Neural Network technique [137], which accounts for the missing energy of neutrinos emitted in semi-leptonic decays of b-hadrons. This multivariate approach exploits several variables as classifiers, such as the jet kinematic and track-based variables, primary and secondary vertex information as well as the presence of soft leptons in the vicinity of the jet axis. The b-jet energy regression correction is provided centrally in the form of a multiplicative factor to be applied to the transverse momentum of each selected jet [138]. The training of the algorithm has been performed in $t\bar{t}$ events for jets with a minimum p_{T} of 20 GeV. The expected improvement in the shape of the p_{T} spectrum is concentrated for a jet transverse momentum below 400 GeV. The impact on the signal yield and shape in this analysis of the application of b-jet energy regression as well as FSR recovery is discussed in detail in Section 4.7.2.

Final State Radiation recovery

A method to partially recover FSR emitted by the two leading jets as a function of p_{T} has been developed for this analysis. It consists of identifying additional reconstructed *soft jets* other than the three leading jets in p_{T}. The soft jet candidate is selected provided that it is located in the vicinity of any of the two most energetic b-tagged jets. The following criteria for the soft jet selection were optimised to maximise the sensitivity of the analysis:

- jet tight identification and loose pile-up identification ;
- spatial separation of $\Delta R(j_{soft}, j_i) < 0.8$ from b-jet with p_{T} rank $i = 1, 2$;

- $p_T > 20$ GeV; $|\eta| < 2.3$.

The four-momentum of the selected soft jet is then added in a vectorial sum to that of the close-by b-tagged jet.

4.6.3 Muon selection

The final step of the offline selection is the requirement of a muon within a distance $\Delta R < 0.4$ from the axis of any of the two leading jets. It must also fulfil the kinematic cuts $p_{\mathrm{T}}^{(\mu)} > 13$ GeV and $\left|\eta^{(\mu)}\right| < 2.2$. In this analysis, the tight muon identification requirement has been chosen since it provides the highest purity with little signal efficiency reduction. The categorisation of the leading b-jets into (non-) muon containing b-jets allows refining further the offline selection cuts in the analysis. The muon-containing b-jet tends to have a harder p_{T} spectrum than the other leading jet, because of the muon p_{T} cut imposed already at trigger level biasing the overall jet transverse momentum. For this reason, asymmetric p_{T} cuts on the two most energetic b-jets can be introduced, yielding a slight improvement of the signal-to-background ratio.

Cut	#events	ϵ_{abs}	ϵ_{rel}
Trigger	17465231	1.000	1.000
Jet identification	17255642	0.988	0.988
Jet kinematics	7632300	0.437	0.442
$\Delta R_{i;j}$	5571404	0.319	0.730
$\Delta\eta_{12}$	4156723	0.238	0.746
Double b-tag	1956105	0.112	0.469
Muon-in-jet	1641731	0.094	0.837
Trigger match	1449614	0.083	0.889
Signal region (*bbb*)			
3^{rd} jet b-tag	160010	0.009	0.107
Reverse b tag control region (*bbnb*)			
3^{rd} jet non b-tag	1130031	0.063	0.758

Table 4.8: Summary of the event selection steps with the corresponding filtering of events in the signal ("bbb") and in the reverse b tag control region ("bbnb"). The number of events passing each set of cuts is shown, as well as the fraction of residual events with respect to the total amount firing the trigger (ϵ_{abs}), and to the previous selection step (ϵ_{rel}).

4.6.4 Cutflow

The number of events retained after each selection step are shown in Table 4.8 for both the signal and the control regions. The cutflow among these event categories differs exclusively on the basis of the b-tag requirement on the third leading jet, which is required to be light flavoured in the control region. Consequently, in the latter the overall event population after the full selection is approximately seven times larger than in the signal region.

4.7 Signal modelling

The signal model is based on a simulation of the production and subsequent decay of the MSSM neutral CP-odd Higgs boson. The simulation of the $b\bar{b}(A \to b\bar{b})$ process is used in a quasi-model-independent way, as it is further exploited in the 2HDM Type-II and flipped model interpretation. This is motivated by the common tree-level Yukawa coupling structure to down-type fermions across these BSM models. As discussed in Section 1.2.3, the MSSM neutral Higgs boson coupling to fermions can be derived from the equivalent in the SM simply by rescaling of the coupling strength, hence this simulation was also used as a template to model the equivalent processes involving the CP-even Higgs bosons. Fifteen signal samples listed in Table 4.2 with next-to-leading order (NLO) accuracy have been used in the statistical inference. A comparative study of the LO and NLO signal samples listed in Section 4.4 was performed to determine the impact of higher order corrections on the signal shape and efficiency. A description of the modelling of the signal invariant mass spectra, their parameterisation with analytical functions and the impact of the shape-altering sources of systematic uncertainties is also presented in this section.

In general, the natural intrinsic width of the BSM Higgs boson may be model dependent, e.g. as a function of tanβ in the MSSM. Within the accessible parameter range of typical models, the largest width is smaller than the achieved di-jet mass resolution. In comparison, the Higgs boson mass has a relatively narrow natural width, whose dependence on model parameters may therefore be neglected. The resulting shape of the di-jet invariant mass distributions, or *signal templates* is affected by jet energy resolution effects, the potential mis-reconstruction of the Higgs boson decay products, as well as the identification of the correct associated b-jet candidate. There are four main factors with a substantial impact on the signal shape:

1. **neutrino emission**: semi-leptonic decays are largely affected by incomplete mass reconstruction due to the missing momentum carried by undetectable neutrinos. This has a visible impact particularly on the low-mass tails of the signal mass distribution peaking at low values $m_{A/H} < 300$ GeV;

2. **final state radiation**: gluon emission in the final state also contributes to shifting the reconstructed mass peak to lower values than the nominal mass peak;

3. **selection bias**: the left shoulder of the invariant mass spectrum of the lowest mass samples is steepened by the rising edge of the jet p_T trigger turn-on; the shape of the mass spectrum is also affected by the kinematic cuts, and by the p_{T} dependence of the b-tagging performance;

4. **wrong pairing**: the high-mass tails, which are particularly prominent for the low-mass signal samples originate from the combinatorial background caused by the wrong pairing of the Higgs boson daughters. This occurs when at least one of the two selected leading b-tagged jets is not stemming from the Higgs boson decay.

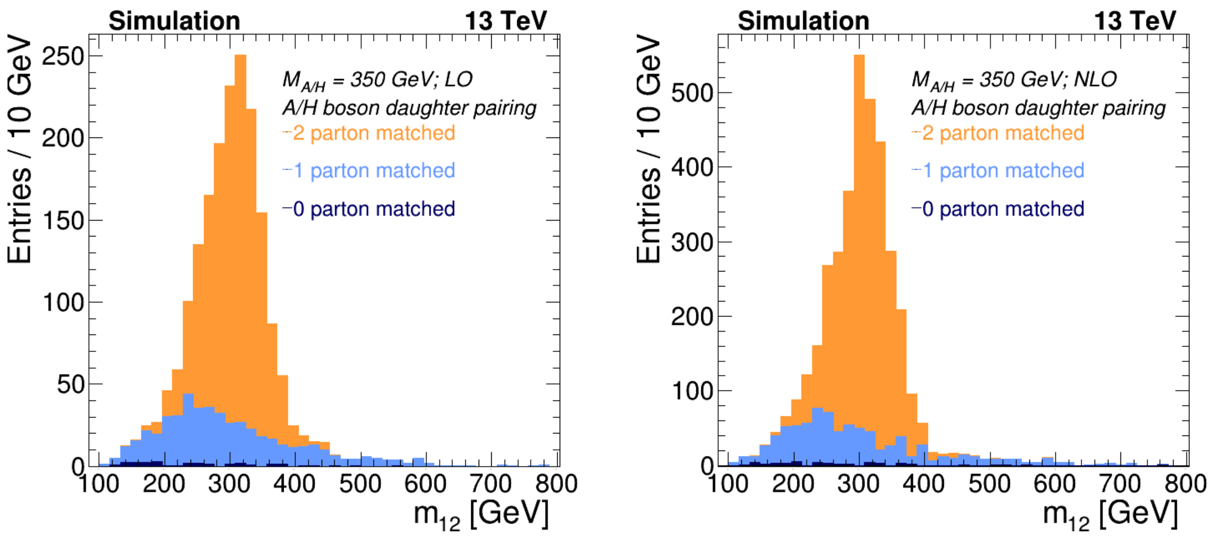

Figure 4.12: The pairing of the MSSM Higgs boson daughter candidates at generator level in the leading order (left) and next-to-leading order sample (right) for the intermediate 350 GeV signal mass-point.

4.7.1 NLO versus LO comparison

A dedicated study in simulation is performed to assess the impact of the next-to-leading order processes on the signal yield and on the invariant mass spectrum shape. Within statistical uncertainty, the shape of the signal peaks in both NLO and LO samples are found to be equivalent, as illustrated in Figure 4.12 for the benchmark mass-point at 350 GeV. Inspection of the kinematic distributions at the generator level indicates that

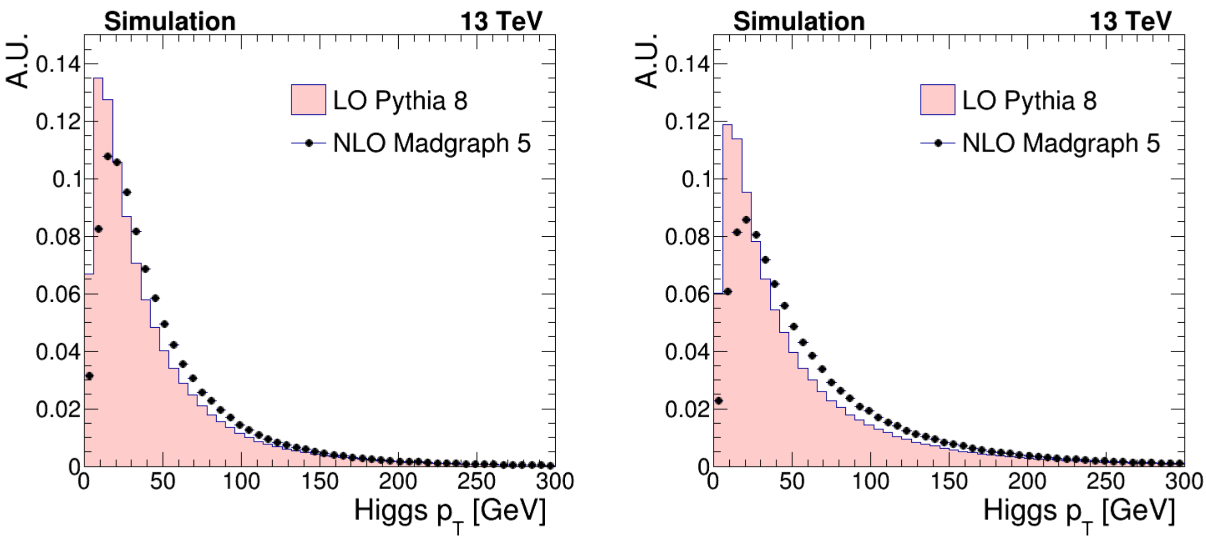

Figure 4.13: Comparison of the Higgs p_T spectrum at generator level in NLO and LO samples for different Higgs mass points, 350 GeV (left), 600 GeV (right).

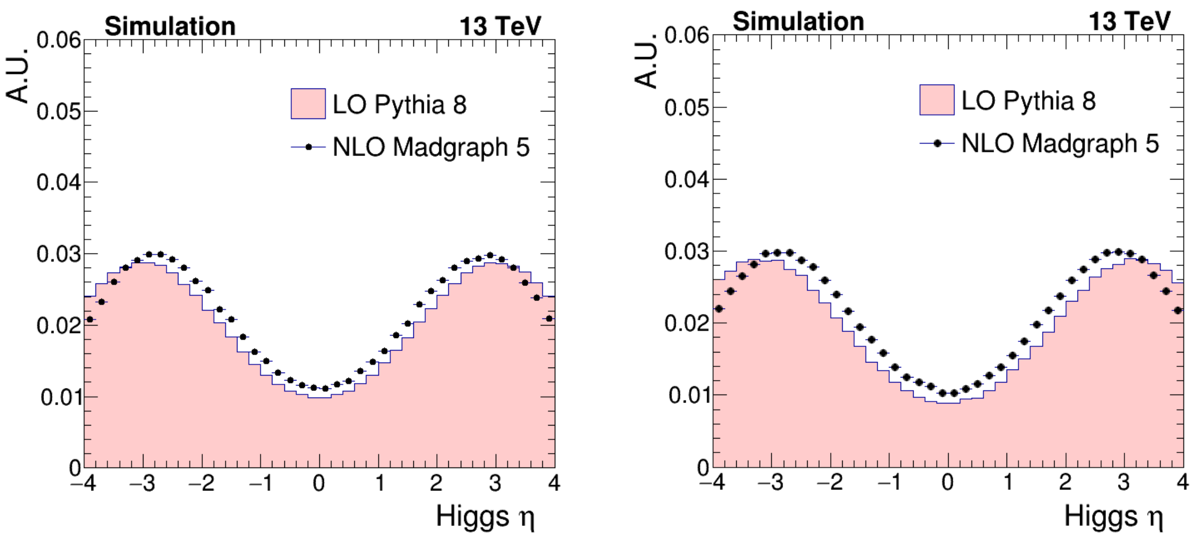

Figure 4.14: Comparison of the Higgs η distribution at generator level in NLO and LO samples for different Higgs mass points, 350 GeV (left), 600 GeV (right).

the NLO Higgs has a more central η distribution and a harder p_T spectrum with respect to the LO case as demonstrated in Figure 4.13 and Figure 4.14, respectively. This is expected to have a net positive contribution to the signal acceptance and hence the overall efficiency. Higher order corrections from final state radiation are modelled exclusively in NLO samples at matrix element level. This may explain the increased probability by up to 30 %, for the third leading jet to be initiated by a gluon instead of a real b-quark parton. The subsequent increase in the mis-identification rate of the true b-associated jet is expected to lower the overall signal efficiency in the NLO sample with respect to the leading-order sample. Overall, these two effects seem to cancel each other since the signal efficiency after the full offline selection is essentially equivalent between LO and NLO samples, as shown in Figure 4.15.

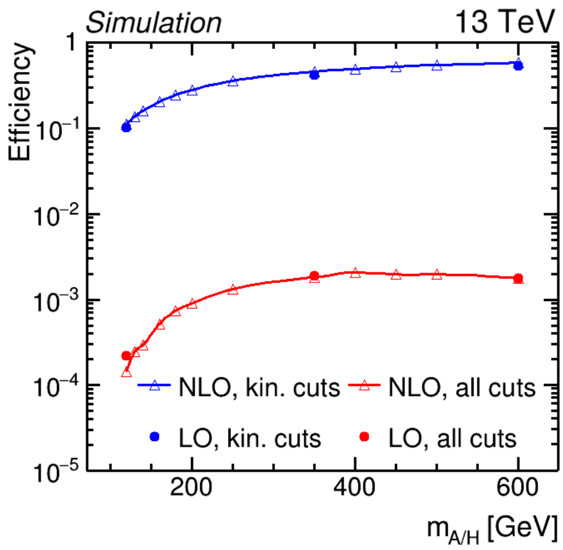

Figure 4.15: Signal efficiency as a function of the Higgs boson mass, after the kinematic selection (blue) and including the full online and offline selection (red) in leading order signal samples simulated with Pythia8, indicated with a solid circle, and in next-to-leading order samples generated with Madgraph5_aMC@NLO, denoted with empty triangles. This preliminary study was performed prior to the application of the b-jet energy corrections.

The maximum signal efficiency is reached for the mass-point at 400 GeV at a value of approximately 0.2%. The signal efficiency for the lower Higgs boson masses is reduced by the imposed kinematic thresholds on the di-jet plus muon system. On the other hand, at Higgs boson masses above 500 GeV the main limiting factor to the signal yield is the b-tagging selection.

$m_{A/H} = 350$ GeV			
Correction	peak x_p [GeV]	width σ_P [GeV]	asymmetry ϵ
uncorrected	313 ± 1	43 ± 1	-0.20 ± 0.01
regression	330 ± 2	40 ± 1	-0.19 ± 0.01
FSR recovery	316 ± 2	42 ± 1	-0.17 ± 0.01
combined	333 ± 2	39 ± 1	-0.16 ± 0.01
$m_{A/H} = 600$ GeV			
Correction	peak x_p [GeV]	width σ_P [GeV]	asymmetry ϵ
uncorrected	551 ± 3	63 ± 1	-0.30 ± 0.01
regression	569 ± 2	58 ± 1	-0.29 ± 0.01
FSR recovery	555 ± 2	63 ± 1	-0.29 ± 0.01
combined	574 ± 3	57 ± 1	-0.29 ± 0.01

Table 4.9: Impact of the b-jet energy corrections, namely regression and FSR recovery on the scale (parameterised with the peak position x_p), the resolution (width σ_P) and the symmetry (asymmetry parameter ϵ) of the di-jet mass distribution for two signal mass hypotheses, i.e. $m_{A/H} = 350; 600$ GeV.

4.7.2 Impact of b-jet energy corrections on signal

Aside from maximising the signal yield, the sensitivity of the analysis can also be improved by obtaining the best possible resolution of the di-jet invariant mass. The resolution of the invariant mass m_{12} is approximately 10% of the nominal mass peak and the bias on the scale is up to 10% for the lower signal masses. In order to improve the signal mass shape, resolution and scale two *ad-hoc* b-jet energy corrections have been included: b-jet energy regression and final state radiation recovery, introduced in Section 4.6.

The improvement on the mass resolution and scale by using regressed b-jets is illustrated in Table 4.9 for the benchmark signal mass-points at 350 and 600 GeV. The application of the b-jet energy regression before the implementation of the kinematic cuts enhances significantly the signal efficiency, up to 15%, for the lowest signal mass-point due to the recovery of signal events in which one of the leading jets p_{T} is just below the imposed kinematic threshold. As expected, the improvement of the mass resolution is approximately 10% for all the probed signal mass-points, as quantified by the fitted values of the width σ_P of the mass peak. In addition, the mass scale is also improved since the peak position x_p is shifted for all mass-points closer to the nominal mass peak value.

The method used for FSR recovery yields an overall improvement at the percent level $(1-2\%)$ on the mass resolution of the probed signal mass-points. In addition, the trend of the asymmetry parameter ϵ highlights that the application of FSR corrections symmetrises the shape of the di-jet mass spectrum, which has a positive impact on the sensitivity by lowering the fitting penalty of the final signal plus background fit. The individual and combined impact of these b-jet energy corrections is illustrated in Figure 4.16 for a selection of signal mass-points in the mass range between 120 and 1200 GeV. The net improvement from the application of b-jet energy regression and FSR recovery on the signal scale and resolution is more prominent than the individual corrections.

4.7.3 Systematic effects

Two classes of systematic effects can be distinguished in the modelling of the signal, those affecting the shape of the mass spectra and those altering the signal yield, and thus the normalisation. The sources of systematic effects relevant to this analysis are :

- the jet energy corrections affecting the energy scale (JES) and resolution (JER) of the leading b-jets;
- the b-tagging corrections impacting the heavy-flavour identification efficiency relative to the simulation both at trigger level (online b-tag scale factors) and in the offline selection (offline b-tag scale factors);
- the muon identification scale factor for the tight identification;
- the kinematic trigger corrections for the di-jet plus muon system, comprising the muon p_{T} trigger and the jet kinematic scale factor;
- the pile-up re-weighting correction.

The effect of the aforementioned systematic uncertainties is illustrated in Figures 4.17 to 4.20. Only the jet energy corrections JES and JER were found to have a significant impact on the signal shape. The remaining signal systematic effects have been shown to affect exclusively the overall normalisation of the signal. The adoption of DeepJet as the b-tagger enhances the signal yield by $10 - 30\%$ with respect to the DeepCSV algorithm, resulting in a flatter efficiency plateau for $m_{A/H} > 400$ GeV, as illustrated in Figure 4.21. This improvement in b-tagging performance arises from the less stringent kinematic jet pre-selection used in the training of the DeepJet algorithm.

4.7.4 Signal parameterisation

A parametric approach for the signal modelling by means of analytical functions is adopted. A robust signal parameterisation is needed to provide a stable set of signal parameters to the global signal plus background fit used in the statistical inference of the data. It is important to evaluate the shape-altering signal systematic sources with a substantial impact on the parameters of signal fit. The signal shapes differ markedly in the tail distribution between the low and the high masses, hence three different types of parameterisations are utilised for the signal templates:

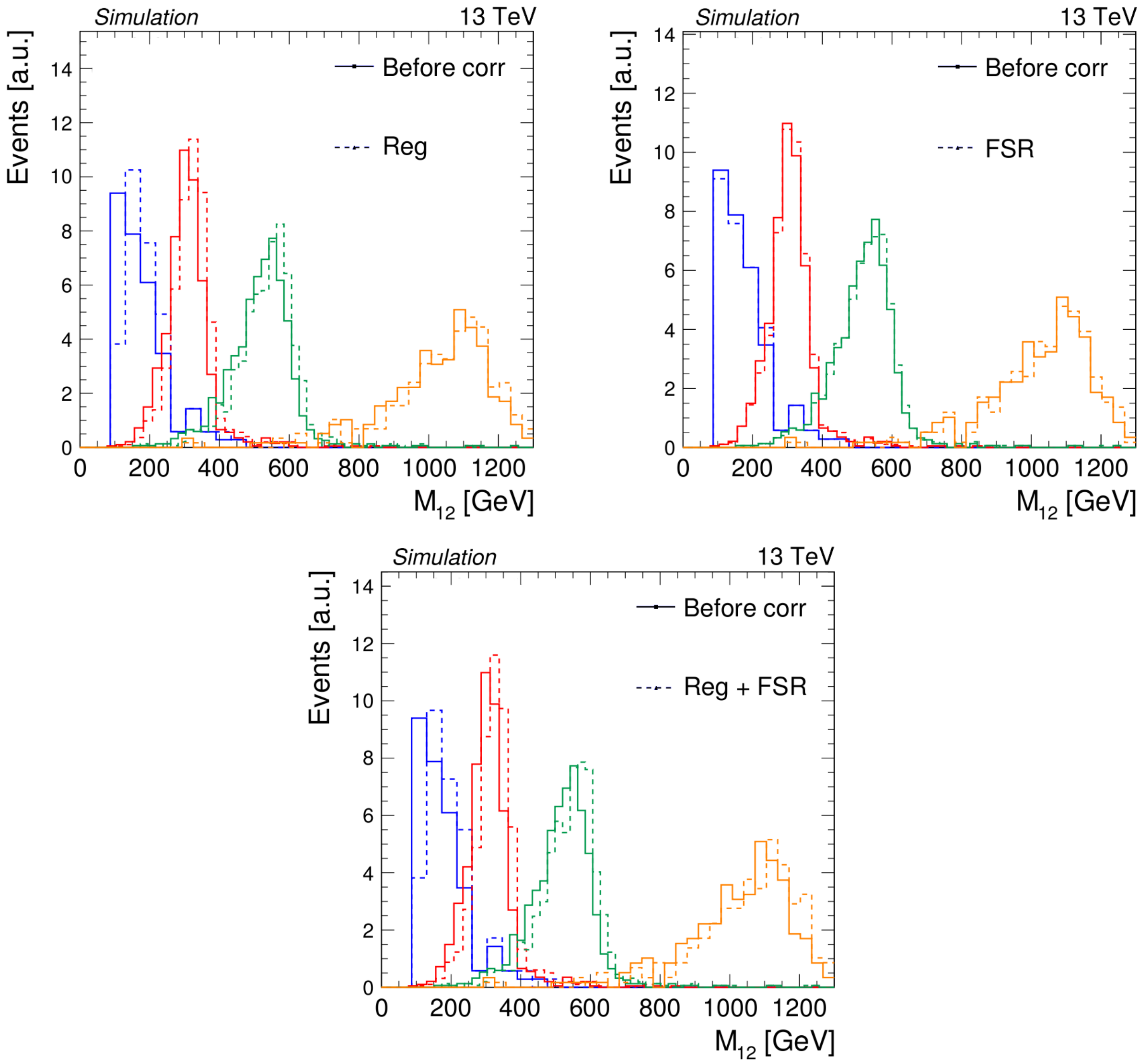

Figure 4.16: Impact on the di-jet invariant mass resolution and shape of the b-jet energy corrections, respectively FSR recovery (top left), b-jet energy regression (top right) and combination (bottom) for the signal mass peaks at 120 (blue), 350 (red), 600 (green) and 1200 GeV (orange) in samples generated with Pythia8.

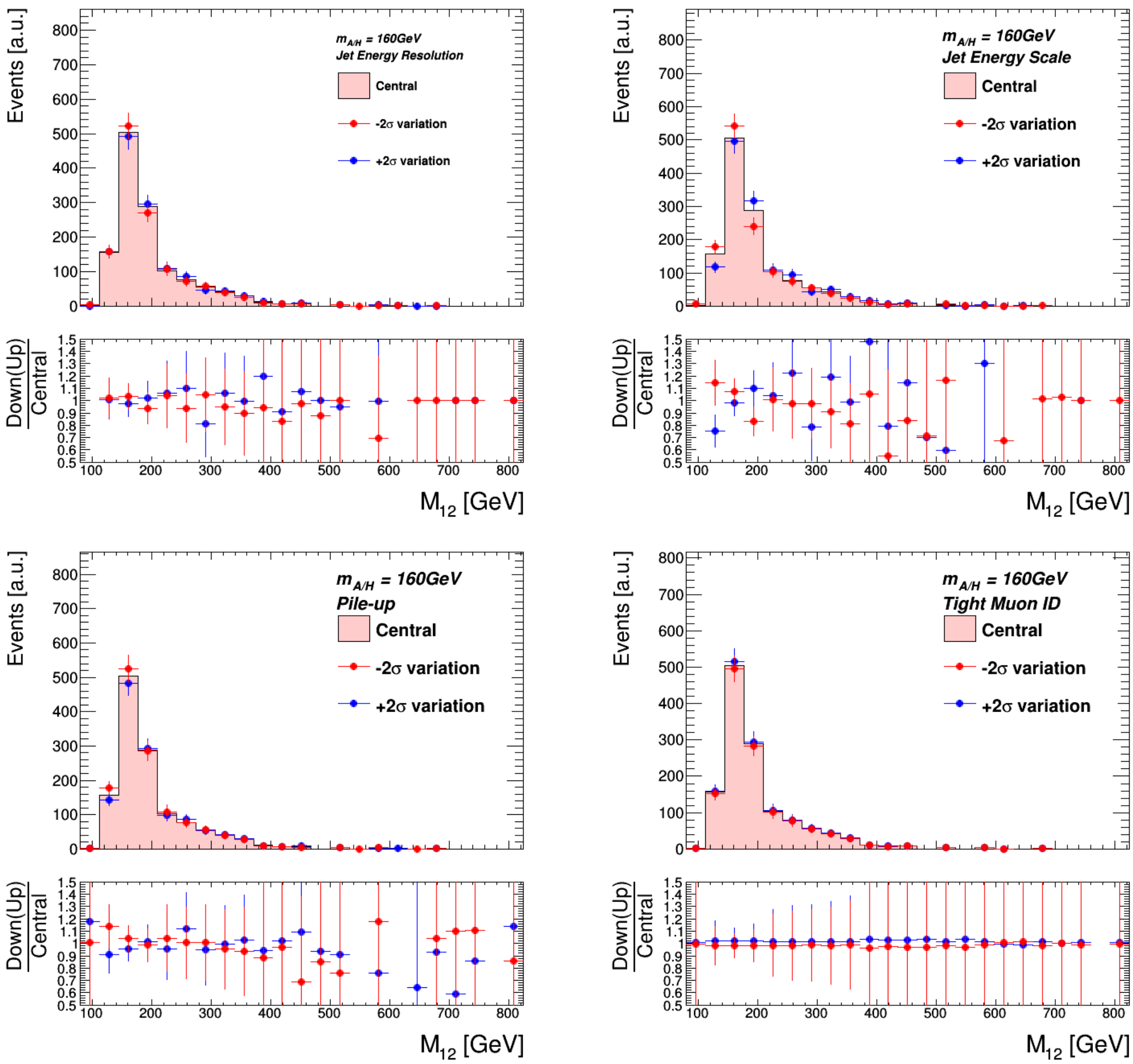

Figure 4.17: Impact of potentially shape-altering systematic uncertainties on the signal shape, for the signal 160 GeV masspoint. From top left to bottom right the signal systematic uncertainties under consideration are respectively the jet energy resolution, the jet energy scale, the pileup correction and the muon identification scale factor. The central signal template and the templates obtained varying by $\pm 2\sigma$ the systematic uncertainty of interest are shown in the top panel. In each bottom panel, the ratio of the up(down) variation with respect to the central signal template is shown.

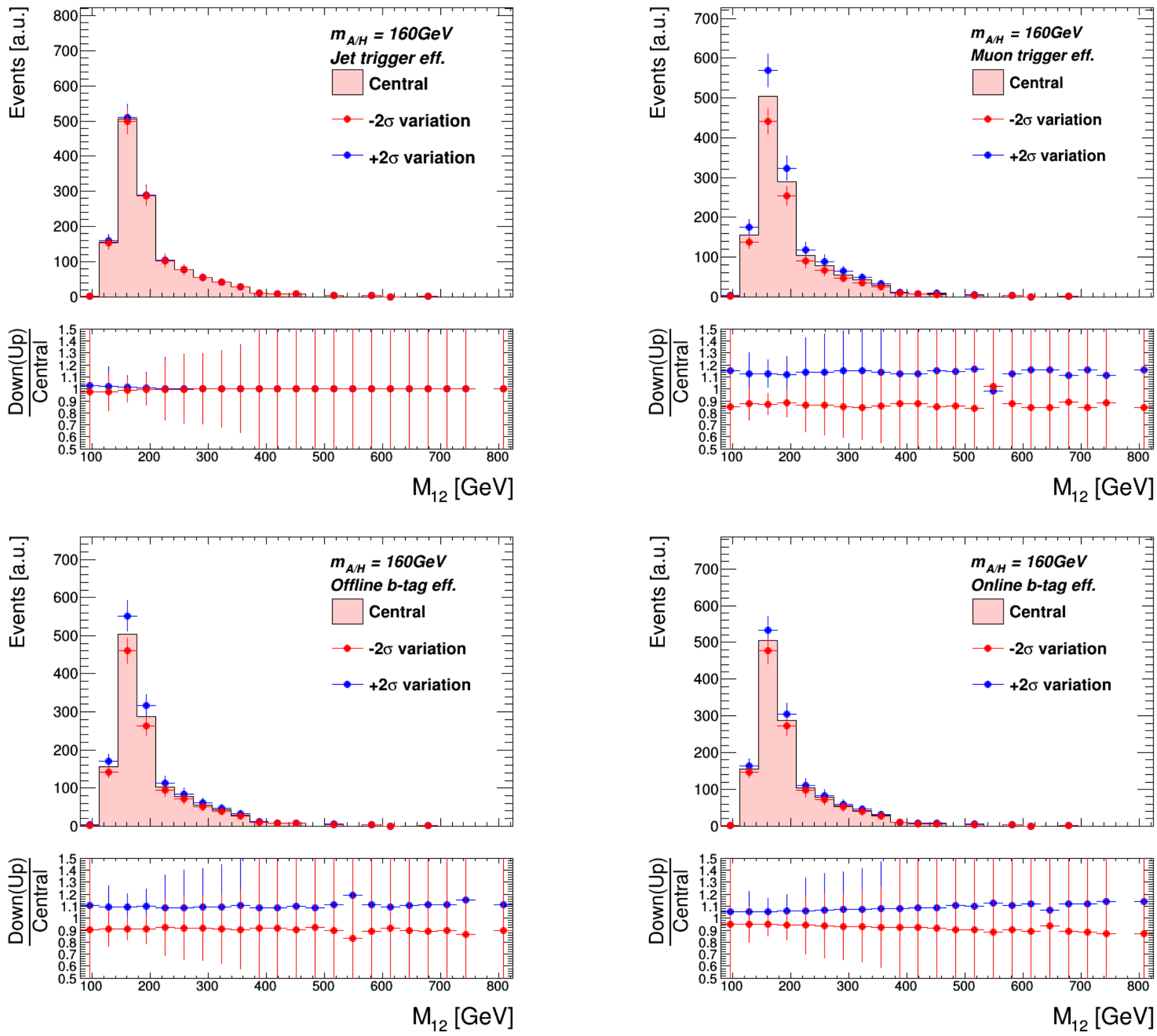

Figure 4.18: Impact of potentially shape-altering systematic uncertainties on the signal shape, for the signal 160 GeV masspoint. From top left to bottom right the signal systematic uncertainties under consideration are respectively the jet trigger kinematic efficiency scale factors (bottom left), the muon p_T trigger efficiency scale factor, the offline b-tag scale factors for heavy flavour (left) and online b-tagging scale factor. The central signal template and the templates obtained varying by $\pm 2\sigma$ the systematic uncertainty of interest are shown in the top panel. In each bottom panel, the ratio of the up(down) variation with respect to the central signal template is shown.

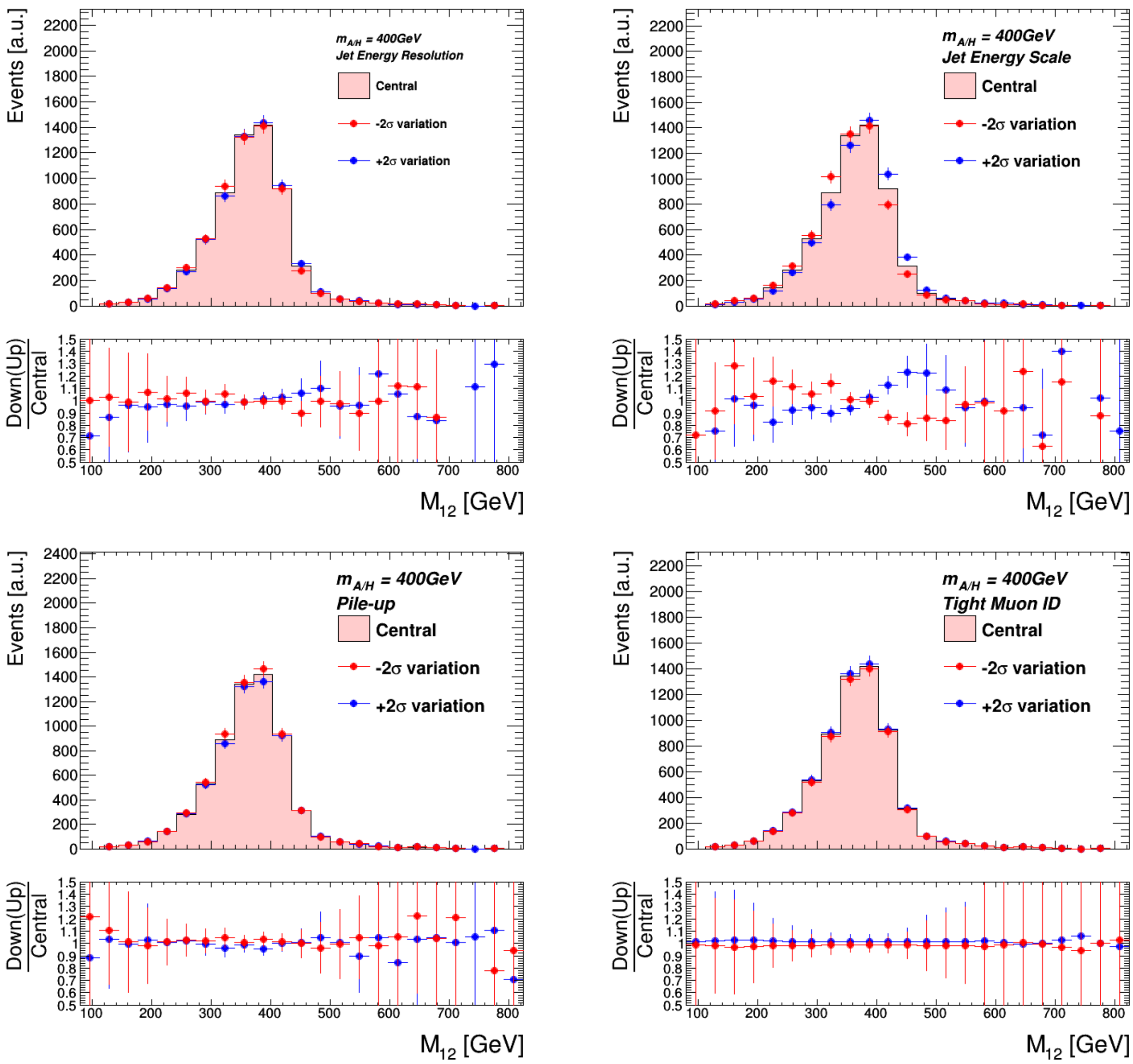

Figure 4.19: Impact of potentially shape-altering systematic uncertainties on the signal shape, for the signal 400 GeV masspoint. From top left to bottom right the signal systematic uncertainties under consideration are respectively the jet energy resolution, the jet energy scale, the pileup correction and the muon identification scale factor. The central signal template and the templates obtained varying by $\pm 2\sigma$ the systematic uncertainty of interest are shown in the top panel. In each bottom panel, the ratio of the up(down) variation with respect to the central signal template is shown.

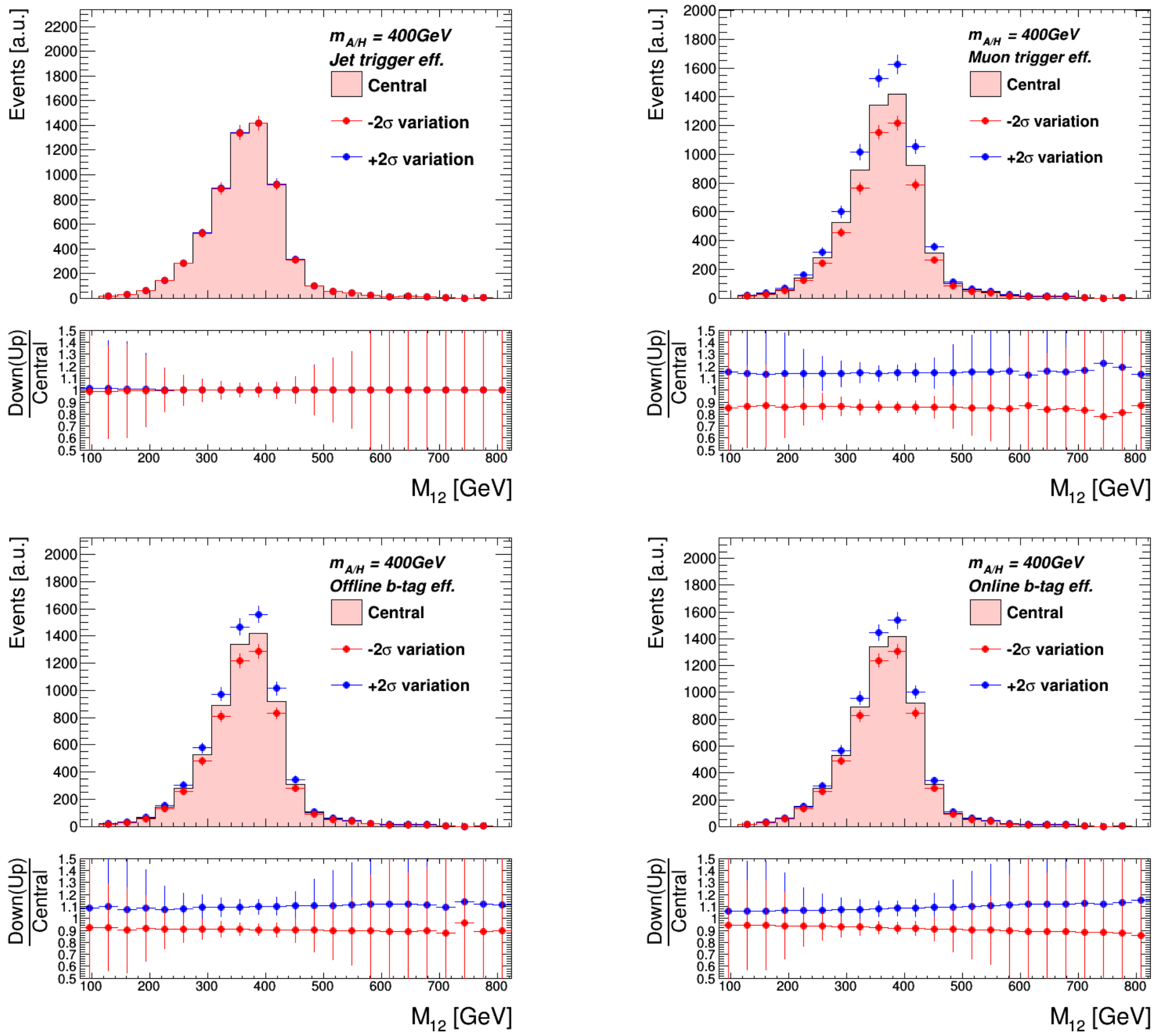

Figure 4.20: Impact of potentially shape-altering systematic uncertainties on the signal shape, for the signal 400 GeV masspoint. From top left to bottom right the signal systematic uncertainties under consideration are respectively the jet trigger kinematic efficiency scale factors (bottom left), the muon p_T trigger efficiency scale factor, the offline b-tag scale factors for heavy flavour (left) and online b-tagging scale factor. The central signal template and the templates obtained varying by $\pm 2\sigma$ the systematic uncertainty of interest are shown in the top panel. In each bottom panel, the ratio of the up(down) variation with respect to the central signal template is shown.

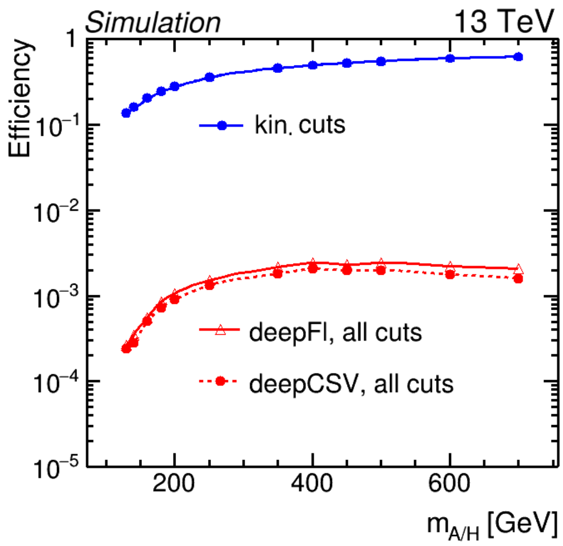

Figure 4.21: Impact of the two best performing b-taggers on the signal yield. The signal efficiency is plotted at two stages of the signal selection, after the offline kinematic selection (blue) and after the full selection including the offline b-tagging (red). The impact of the DeepFlavour a.k.a. DeepJet as a b-tagger (empty triangles) versus the deepCSV algorithm (solid circles) is also shown.

- for the mass points in the range 125-200 GeV, a bifurcated Gaussian function with asymmetric left and right sides continued by an exponential tail at larger invariant mass values is used. The analytical form of this function with five parameters is the following:

$$f(x) = \begin{cases} \exp\left(-\frac{(x-\mu)^2}{2\sigma_{\mathrm{L}}^2}\right), & x \leq \mu \\ \exp\left(-\frac{(x-\mu)^2}{2\sigma_{\mathrm{R}}^2}\right), & \mu < x \leq \mu_{\mathrm{tail}} \\ w_1 \cdot \exp\left(-\frac{(x-\mu_{\mathrm{tail}})}{\sigma_{\mathrm{tail}}}\right), & x > \mu_{\mathrm{tail}} \end{cases}, \tag{4.11}$$

  where

$$w_1 = \exp\left(-\frac{(\mu_{\mathrm{tail}} - \mu)^2}{2\sigma_{\mathrm{R}}^2}\right), \tag{4.12}$$

  and μ is the peak position, σ_L and σ_R are the widths of the left and right sided Gaussian functions respectively, μ_{tail} is the point of transition between the right-sided Gaussian and the exponential function and σ_{tail} is the standard deviation of the exponential tail.

- for the mass points in the range 250-350 GeV, a superposition of two left- and right-sided Gaussian distributions connected at the peak position and constrained by the overall left and right side normalisations continued by an exponential tail at higher masses is utilised. The function has a total of nine parameters, four additional ones with respect to the simpler function used for lower signal mass-points:

$$f(x) = \begin{cases} n_{\mathrm{L}} \cdot \exp\left(-\frac{(x-\mu)^2}{2\sigma_{\mathrm{L1}}^2}\right) + (1-n_{\mathrm{L}}) \cdot \exp\left(-\frac{(x-\mu)^2}{2\sigma_{\mathrm{L2}}^2}\right), \ x \leq \mu \\ n_{\mathrm{R}} \cdot \exp\left(-\frac{(x-\mu)^2}{2\sigma_{\mathrm{R1}}^2}\right) + (1-n_{\mathrm{R}}) \cdot \exp\left(-\frac{(x-\mu)^2}{2\sigma_{\mathrm{R2}}^2}\right), \ \mu < x \leq \mu_{\mathrm{tail}} \\ w_2 \cdot \exp\left(-\frac{(x-\mu_{\mathrm{tail}})}{\sigma_{\mathrm{tail}}}\right), \ x > \mu_{\mathrm{tail}} \end{cases}, \tag{4.13}$$

with

$$w_2 = n_{\mathrm{R}} \cdot \exp\left(-\frac{(\mu_{\mathrm{tail}}-\mu)^2}{2\sigma_{\mathrm{R1}}^2}\right) + (1-n_{\mathrm{R}}) \cdot \exp\left(-\frac{(\mu_{\mathrm{tail}}-\mu)^2}{2\sigma_{\mathrm{R2}}^2}\right), \tag{4.14}$$

where μ denotes the peak position, the parameters $\sigma_{\mathrm{L1}}, \sigma_{\mathrm{L2}}$, $(\sigma_{\mathrm{R1}}, \sigma_{\mathrm{R2}})$ are the widths of the each pair of the Gaussian components of the function on the left(right) side of the peak, n_{L} (n_{R}) represents the relative normalisation of the L1 (R1) Gaussian functions to the L2 (R2) Gaussian contributions, μ_{tail} controls the transition point to the exponential part of the function and σ_{tail} fixes the variance of the exponential function.

- for the mass points in the range 400-700 GeV, the Bukin function, a complex modification of the Novosibirsk function introduced in the next section, is adopted. Its functional form contains five parameters:

$$f(x) = A_p \exp\left[-\ln 2 \frac{\ln^2\left(1+\sqrt{2}\xi\sqrt{\xi^2+1}\frac{(x-x_p)}{\sqrt{\ln 2}\sigma_p}\right)}{\ln^2\left(1+2\xi(\xi-\sqrt{\xi^2+1})\right)}\right], \ x_1 < x < x_2 \tag{4.15}$$

$$f(x) = A_p \exp\left[\pm\frac{\xi\sqrt{\xi^2+1}(x-x_i)\sqrt{2\ln 2}}{\sigma_p \ln\left(\sqrt{\xi^2+1}+\xi\right)(\sqrt{\xi^2+1}\mp\xi)^2} + \rho_i\left(\frac{x-x_i}{x_p-x_i}\right)^2 - \ln 2\right],$$
$$x \leq x_1 \text{ or } x \geq x_2,$$

where $\rho_i = \rho_1$ and $x_i = x_1$ for $x \leq x_1$, $\rho_i = \rho_2$ and $x_i = x_2$ when $x \geq x_2$, and:

$$x_{1,2} = x_p + \sigma_p\sqrt{2\ln 2}\left(\frac{\xi}{\sqrt{\xi^2+1}} \mp 1\right). \tag{4.16}$$

where the parameters x_p and σ_p set the peak position and width respectively, while the parameter ϵ defined in the interval [0;1] controls the asymmetry of the distribution.

The final fits obtained for each signal template are illustrated in Figures 4.22 to 4.24. A good description of the signal shapes has been achieved for all signal mass-points of interest. The signal shape variations of the m_{12} invariant mass distribution have been studied by fitting the signal template with a $\pm 2\sigma$ variation for each systematic source under scrutiny. The offline and online b-tag variations, as well as the kinematic trigger efficiency of the dijet-plus-muon system were found to affect exclusively the normalisation and have no net effect on the shape parameters. The jet energy corrections in scale and resolution make instead a sizable impact on a subset of the signal shape parameters, as illustrated in the signal fits shown in Figures 4.26 and 4.27 for the representative mass points at 160 and 400 GeV, respectively. Thus, the parameters that need to be modified in the final signal extraction fit are the mean of the peak μ and the tail position μ_{tail}, in the case of a fit with the Bifurcated (Quadratic) Gaussian plus Exponential, and the mean peak position μ, for the Bukin function fit. The remaining parameters are fixed to the values obtained with the nominal fit of the central signal template. All shape systematic variations are well modelled by the same analytical functions that are used in the nominal fit of the central template.

4.8 Modelling of the background

An accurate description of the background process is an essential aspect of any analysis since it affects the extraction of signal yields. The predominant background component in this analysis is the QCD multi-jet production where two of the selected jets stem from real b-quarks, whereas the remaining selected jet is either a real b- jet or it is initiated by a non-b parton misidentified by the b-tag algorithm. Top quark-antiquark plus jets production is the second most relevant background contribution. This process has been found in simulation to account for only 6% of the events in the signal topology over the full mass range of interest. Since it is challenging to reproduce accurately in simulation all QCD background processes, a completely data-driven description of the background is adopted. The key advantage of the data-driven approach is that a precise knowledge of the yields of the individual background contributions is not required. The shape of the background spectrum is parameterised with an analytical function. The choice of the function is to some extent arbitrary since several alternative functions can achieve similar results. This arbitrariness can bias the measurement of the signal yield, hence tests are performed to address quantitatively this systematic effect.

4.8.1 The bbnb reverse b-tag control region

There are two main requirements for the definition of an appropriate control region. Firstly, the signal contamination should be minimal in the control region. In addition, a good agreement of the shape of the invariant mass M_{12} spectrum of the signal and in the background region is also required. The *bbnb* reverse b-tag control region satisfies these criteria. It is obtained from the double b-tag data with at least three jets by applying a

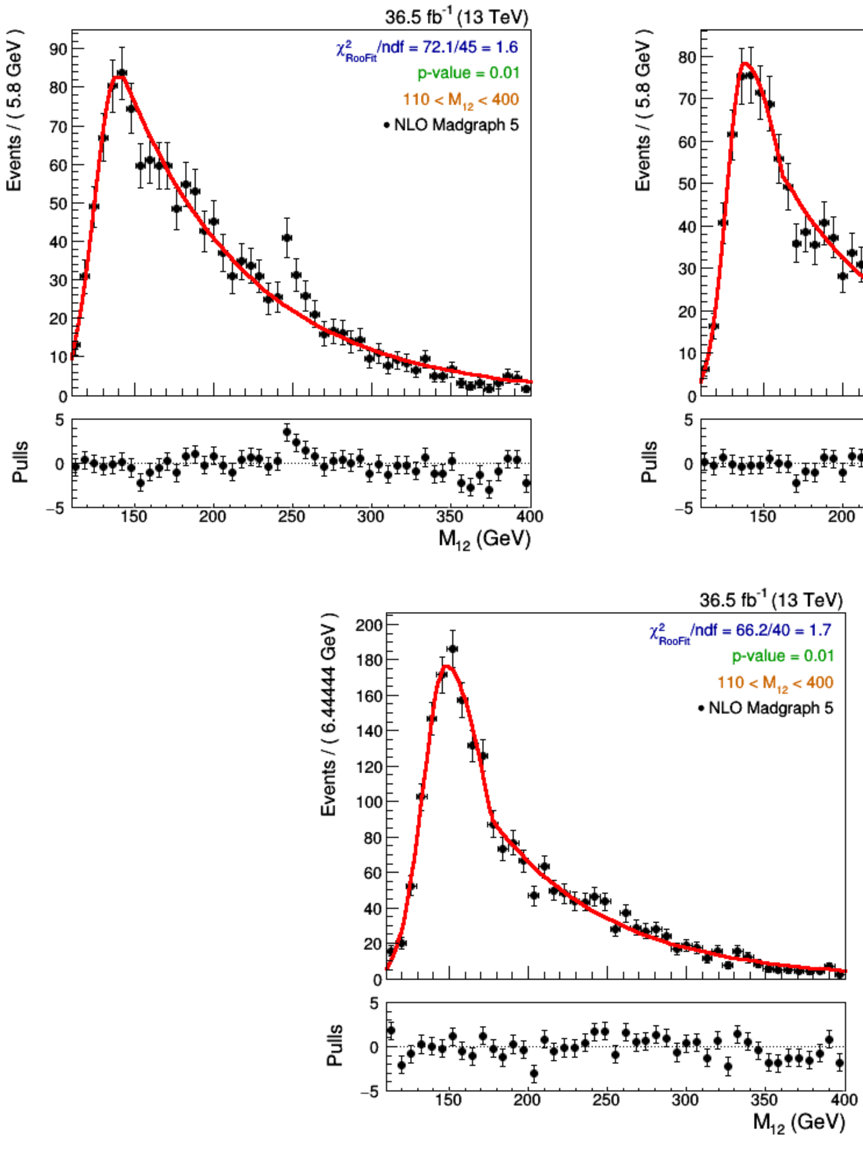

Figure 4.22: Fits of the signal shapes for the 125,130,140 GeV masspoints with the Bifurcated Gaussian plus Exponential function.

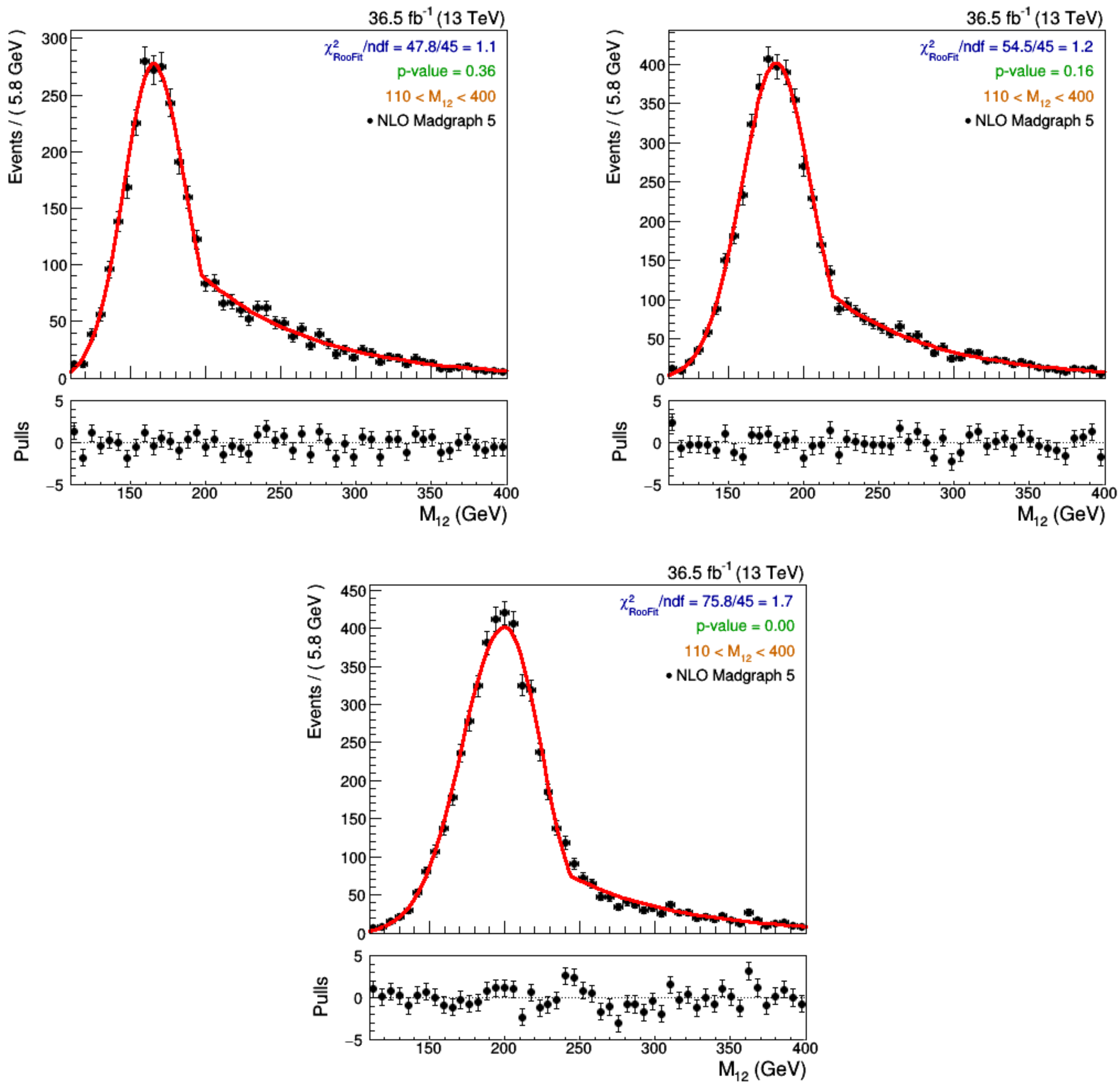

Figure 4.23: Fits of the signal shapes for the 160,180,200 GeV masspoints with the Bifurcated Gaussian plus Exponential function.

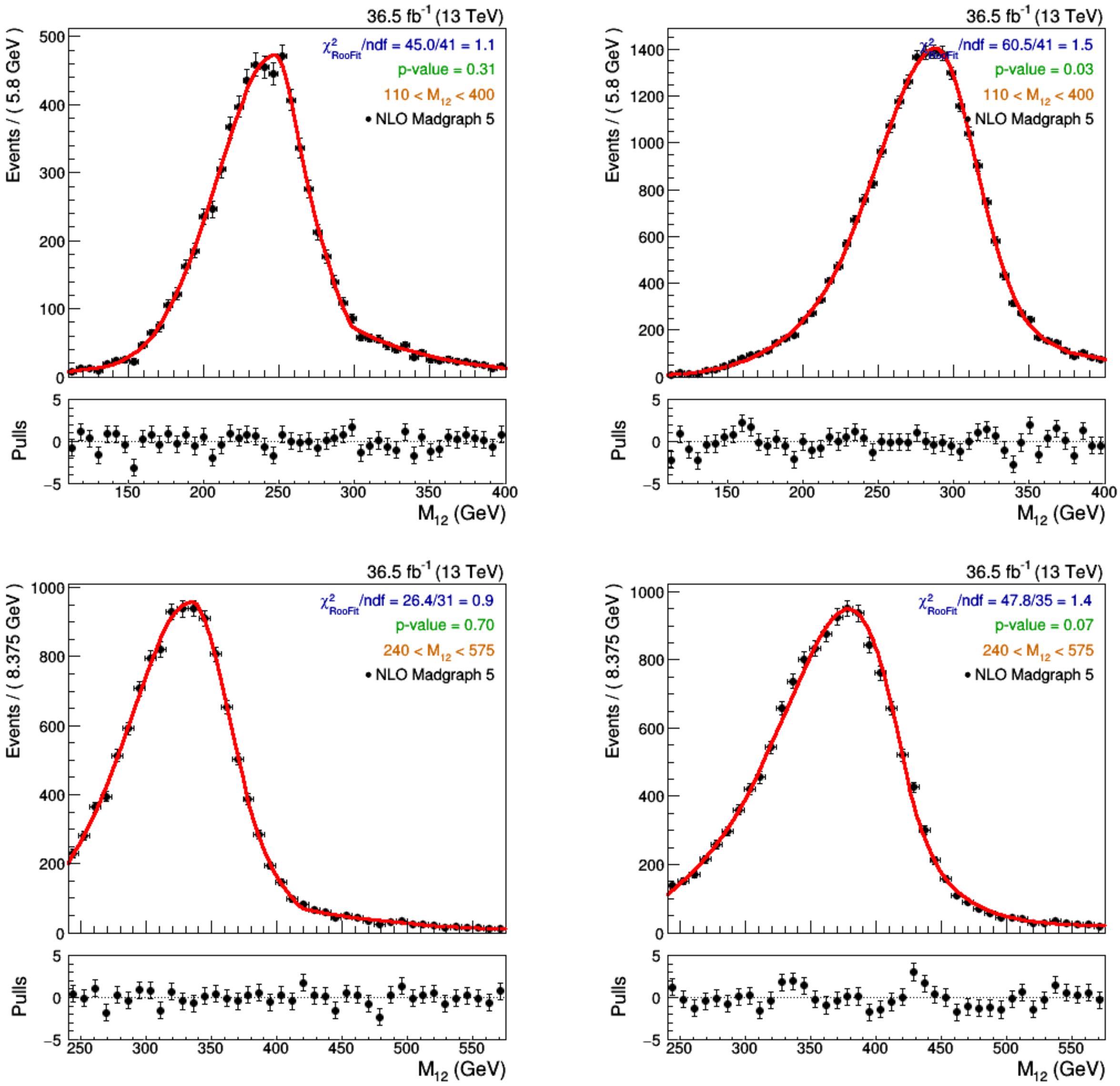

Figure 4.24: Fits of the signal shapes for 250,300,350 GeV masspoints with the Quadratic Gaussian plus Exponential function and the 400 GeV masspoint with the Bukin function.

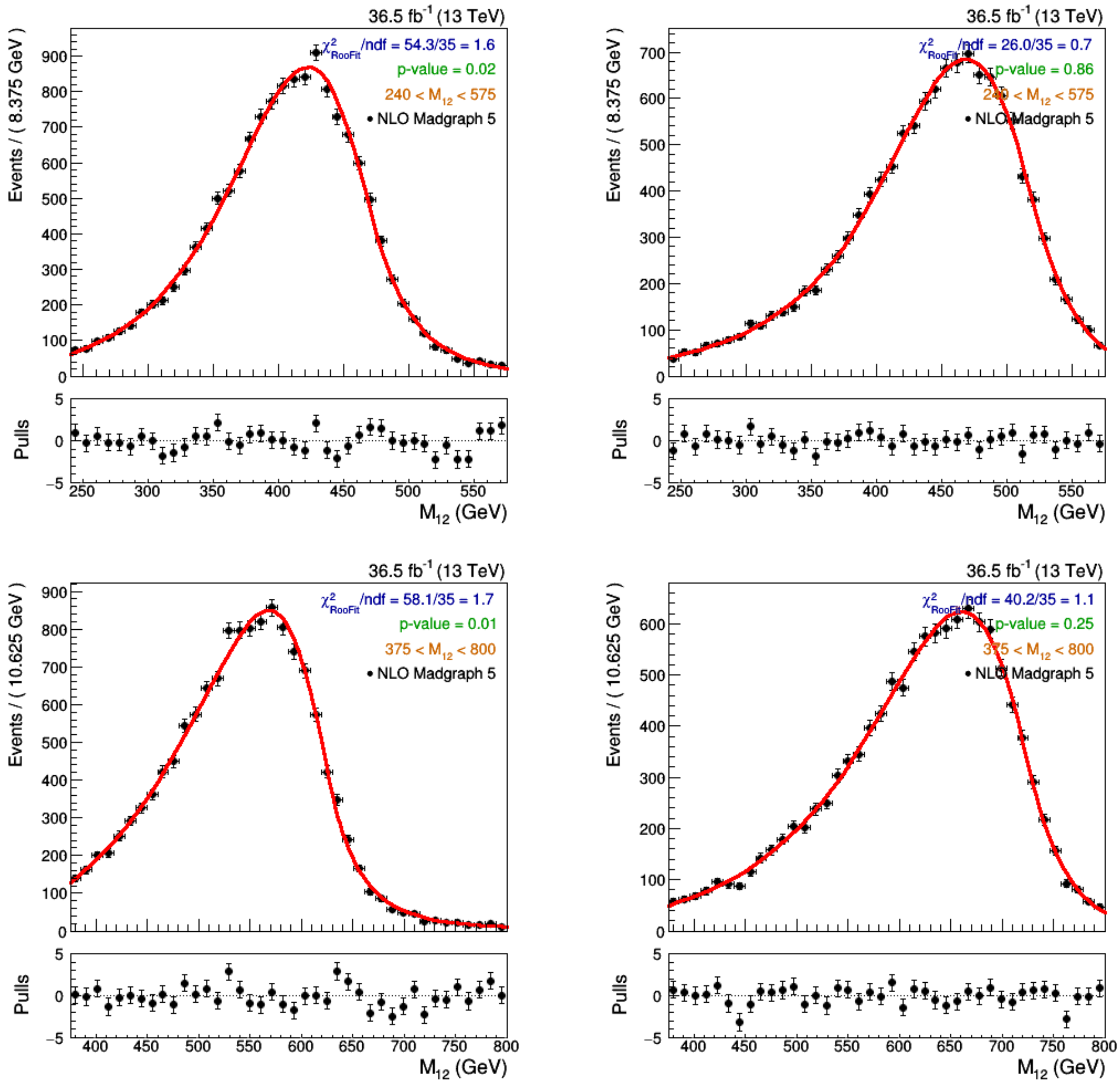

Figure 4.25: Fits of the signal shapes for the 450,500,600,700 GeV masspoints with the Bukin function.

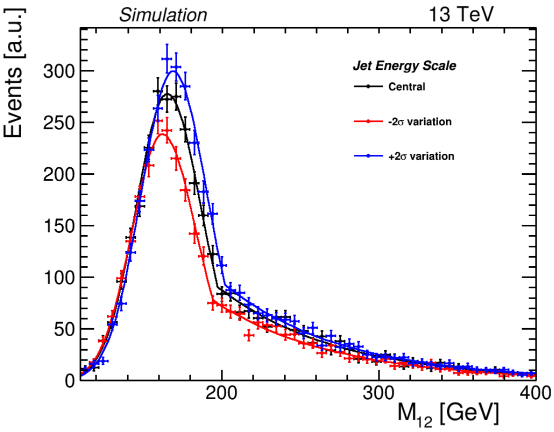

Figure 4.26: Fits of the signal templates for the up(down) two-sigma variations of the shape-altering systematic sources, the corrections to the jet energy scale (left), and resolution (right) respectively for the representative mass-points peaking at 160 GeV.

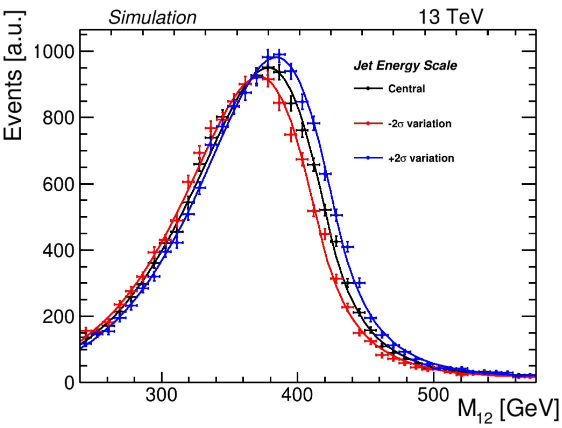

Figure 4.27: Fits of the signal templates for the up(down) two-sigma variations of the shape-altering systematic sources, the corrections to the jet energy scale (left), and resolution (right) respectively for the representative mass-points peaking at 400 GeV.

reverse b-tag requirement on the third leading jet using the loose working point. Thus, signal events are highly suppressed, with a S/B ratio reduced by a factor hundred in the control region sample. The application of b-jet energy corrections discussed in Section 4.6 was found not to bias the background shape derived in the control region.

A possible implementation of a veto on the fourth leading jet in p_{T} has been considered to reduce the $t\bar{t}$ contamination in the signal region, but it was discarded due to the little improvement in sensitivity. In principle, the $t\bar{t}$ background may potentially alter the results of the final signal extraction fit in the case of a substantial shape difference in the mass spectrum between the control and signal regions. Thus, a dedicated study was performed to confirm that shape of the spectrum of the $t\bar{t}$ background is very similar in both regions.

A sub-sample of the nominal background sample has been used in the background modelling to achieve similar statistical precision as the full sample obtained in the signal region. This down-scaling of the nominal control region sample has been performed randomly on a event-by-event basis exploiting a Mersenne Twister random number generator [139].

4.8.2 Background parameterisation

In this analysis, the expected shape according to Monte Carlo of the QCD di-jet background is generally that of a continuously falling spectrum for the reconstructed invariant mass M_{12}. However, the kinematic selection already implemented at trigger level induces a turn-on behaviour of mass spectrum, leading to a peak at low values of the di-jet invariant mass. In addition, the p_{T} dependence of b-tagging performance also affects the observed background shape. The formulation of an appropriate description with a single analytical function fitting simultaneously the continuous falling spectrum and the peak region represents one of the main challenges of this analysis.

In order to parameterise the full invariant mass spectrum, a function with a Gaussian-like behaviour in the bulk of the distribution and an exponential-like tail should be used. A suitable candidate is the Novosibirisk function, originally introduced to parameterise a Compton spectrum affected by detector resolution effects [140]. An extension of this function, the SuperNovosibirsk function, was first established in the 2016 version of this analysis in the fully-hadronic channel [17]. The Novosibirsk function is extended by addition of higher order polynomial terms :

$$\begin{aligned} F(M_{12}) = N \cdot \exp\left(-\frac{1}{2\sigma_0^2} ln^2(1 - \frac{\eta}{\sigma_E} \cdot (\sum_{i=1}^{n} p_{(i-1)} \cdot (M_{12} - x_p)^i) - \frac{\sigma_0^2}{2}) \right), \\ \sigma_0 = (2/\epsilon) \sinh^{-1}(\eta\epsilon/2), \\ \epsilon = 2\sqrt{(\ln 4)} = 2.36, \end{aligned} \tag{4.17}$$

where N is the normalisation parameter, σ_E and η are related to the asymmetry of the spectrum, x_p sets the peak position and the $p_{(i-1)}$ terms are the higher order coefficients, which provide additional degrees of freedom needed to model the falling part of the spectrum. It is useful to multiply the SuperNovosibirsk function by a so-called *Turn-on* function to model the rising edge of the background peak:

$$f(M_{12}) = 0.5 \cdot (\mathrm{erf}(p_0(M_{12} - p_1)) + 1)\,, \tag{4.18}$$

where the Gauss Error function has been previously defined in Equation 4.7. The Super-Novosibirsk function of degree one multiplied by a Turn-on function can provide an accurate description of the full mass range as illustrated in Figure 4.28. Nevertheless, it is convenient to split the M_{12} mass spectrum in three overlapping sub-ranges in order to reduce the bias in the signal extraction from the choice of the background model.

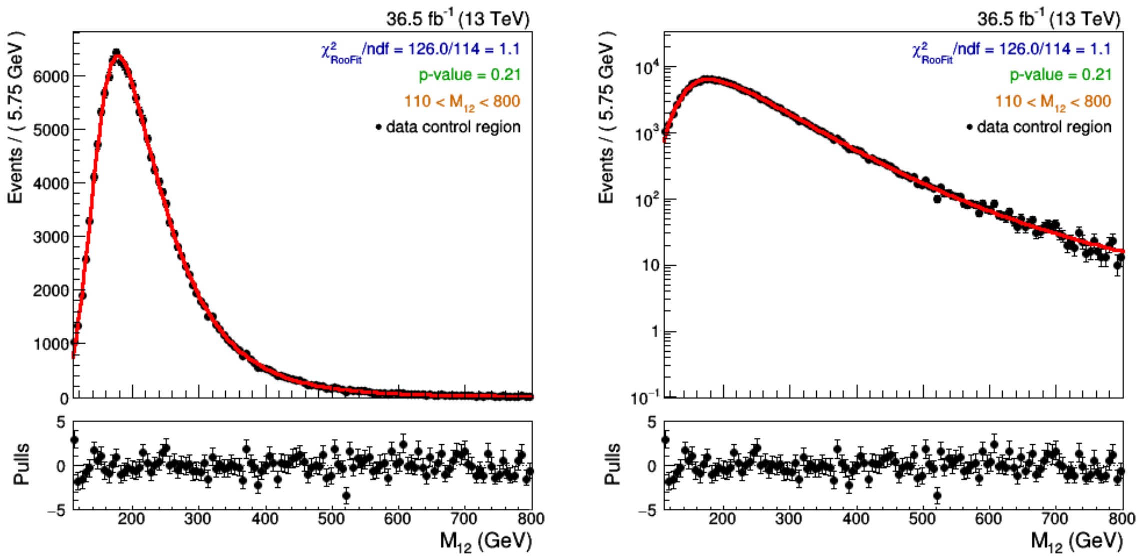

Figure 4.28: Invariant mass distribution of the two leading jets in the reverse b tag control region (solid black dots), both in linear (left) and logarithmic view (right). The result of a fit with the extended Novosibirsk function multiplied by the Gaussian error function is superimposed in the red curve. In the bottom panel, the normalised residuals $(\frac{\mathrm{data-fit}}{\sqrt{\mathrm{data}}})$ are shown.

4.8.3 Sub-range optimisation

This partition of the di-jet mass distribution into sub-ranges has been optimised to maximise the sensitivity of the analysis. The sub-range optimisation is also motivated by the

	Sub-range 1	Sub-range 2	Sub-range 3
M_{12} range, GeV	110 - 400	240 - 575	375 - 800

Table 4.10: Optimised di-jet invariant mass M_{12} sub-ranges.

search of a simpler analytical function to fit the full mass range than the SuperNovisibirsk of degree one multiplied by the Turn-on function, which has a total of six shape parameters. The first sub-range contains the background peak region, while the second and third sub-ranges cover different parts of the continuously falling mass spectrum. The final version of the sub-range division is summarised in Table 4.10. Besides the reduction of the bias effect, sub-range boundaries are also determined taking into account the resulting sensitivity and signal efficiency for the different signal mass hypotheses.

The turn-on effect arises from kinematic selection of the di-jet system, which is identical for the control and signal region. Thus, the number of free parameters in the final signal extraction fit is reduced by fixing the shape parameters of the Turn-on function to the fitted values in the control region. The Super-Novosibirsk of degree zero, referred to as the nominal Novosibirsk, multiplied by the Turn-On function fits well the mass spectrum in the first sub-range, as illustrated in Figure 4.29. In both the second and third sub-range, the nominal Novosibirsk function provides an optimal description of the falling spectrum of the background shape, using only three parameters.

4.8.4 Bias study

The aim of the bias study is to estimate the systematic effect on the extracted signal yield from the choice of the background function. In beyond Standard Model searches, the expected total number of signal events depends on the choice of the BSM model. Thus, it is natural to define the signal strength modifier μ as the ratio of observed signal events to the signal yield predicted by a particular model. Values of μ equal to zero and unity correspond to the number of signal events predicted by the background-only hypothesis, and by the BSM model under scrutiny, respectively.

There are several families of functions that can provide an appropriate description of the background. The Novosibirsk family is regarded as the main background function since it provides consistently the best description of the data in the full mass range of interest. Owing to the lack of a theoretical argument motivating a particular choice, the background function is decided exclusively on the basis of the goodness of fit achieved. However, the choice of a specific analytical model may introduce a potential bias in the

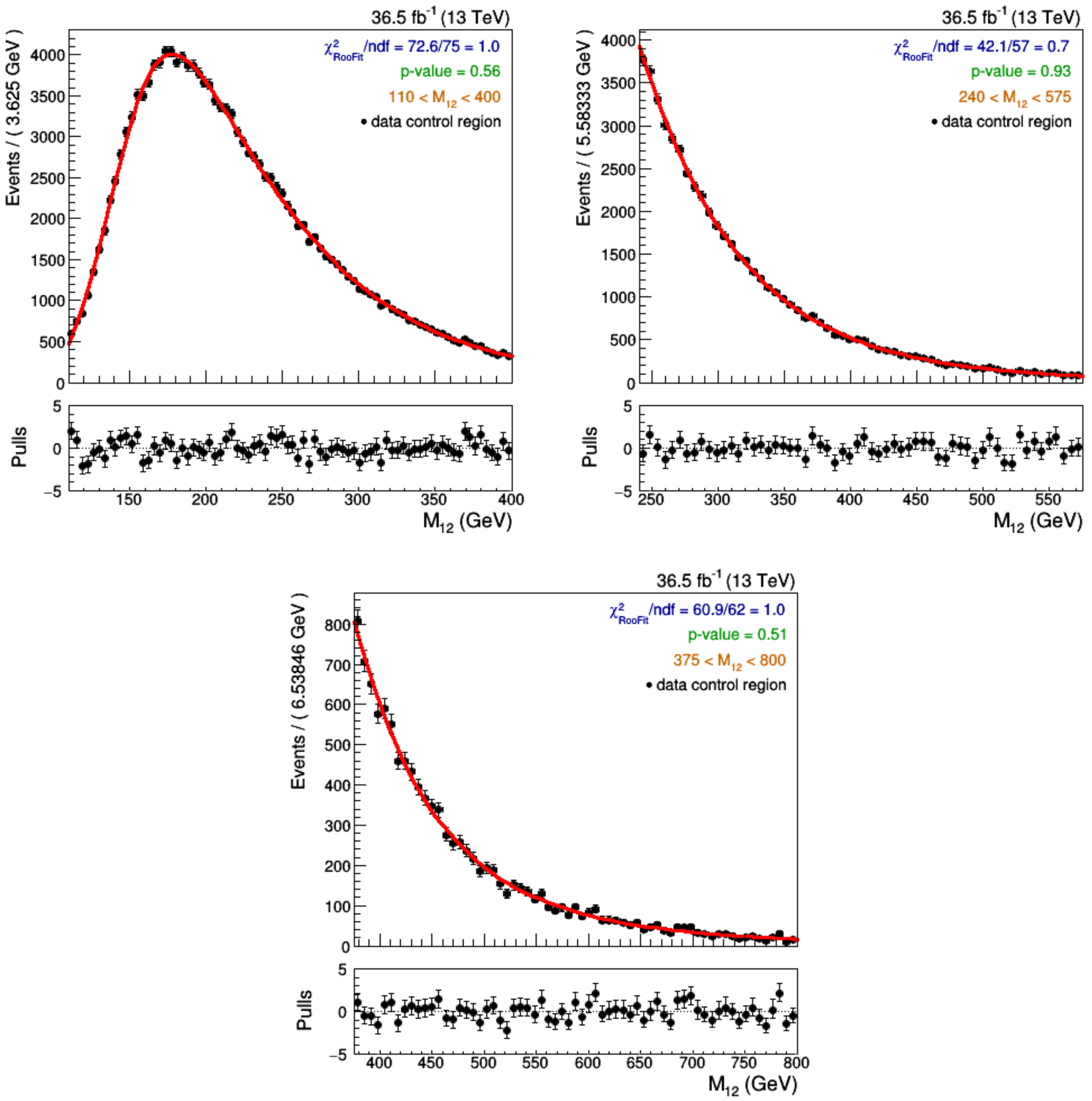

Figure 4.29: Di-jet invariant mass spectrum for the two leading b-tagged jets in the reverse b-tag control region (denoted with black dots) in the three sub-ranges: $M_{12} = [110; 400]$ GeV (top left), $M_{12} = [240; 575]$ GeV (top right) and $M_{12} = [375; 800]$ GeV (bottom). Red curves indicate the background-only fit performed in the relevant sub-range. In the first sub-range the Novosibirsk function multiplied by the Turn-on function is used as an analytical model. In the second and third sub-ranges respectively, the simple Novosibirsk function is instead adopted for the fit to the data. In the bottom panel the normalised residuals $(\frac{\mathrm{Data-Fit}}{\sqrt{\mathrm{Fit}}})$ are shown.

signal extraction. A Fisher test [141] is conducted in each sub-range to determine the optimal degree of the function under scrutiny for a satisfactorily accurate description of the data. The following families of analytical functions have been used in the bias study:

- Crystal Ball, originally introduced to model lossy physical processes such as radiative decays in charmonium spectroscopy [142].

$$f(M_{12};\alpha,n,x_p,\sigma) = N\cdot\begin{cases}\exp\left(-\frac{(M_{12}-x_p)^2}{2\sigma^2}\right), & \text{for } \frac{M_{12}-x_p}{\sigma} > -\alpha\\ A\cdot(B-\frac{M_{12}-x_p}{\sigma})^{-n}, & \text{for } \frac{M_{12}-x_p}{\sigma} \leqslant -\alpha\end{cases}, \tag{4.19}$$

  where

$$A = \left(\frac{n}{|\alpha|}\right)^n \cdot \exp\left(-\frac{|\alpha|^2}{2}\right);\;\; B = \frac{n}{|\alpha|} - |\alpha|\,;\;\; N = \frac{1}{\sigma(C+D)};$$
$$C = \frac{n}{|\alpha|}\cdot\frac{1}{n-1}\cdot\exp\left(-\frac{|\alpha|^2}{2}\right);\;\; D = \sqrt{\frac{\pi}{2}}\left(1+\mathrm{erf}\left(\frac{|\alpha|}{\sqrt{2}}\right)\right).$$

  This function with the four parameters (α, n, x_p, σ) multiplied by Turn-On function has been used as an alternative model in sub-range 1, as exemplified in Figure 4.30. In the remaining mass sub-ranges, the nominal Crystal Ball function has been adopted. The goodness of fit achieved is equivalent to that of the Novosibirsk of degree zero, albeit at the cost of introducing an additional parameter.

- Exponential-Polynomial, defined as the exponential function of a polynomial multiplied by a linear term as follows:

$$f(M_{12}) = (1 - p_a\cdot\frac{M_{12}}{\sqrt{s}})\cdot\exp\left[-\sum_{i=0}^{n} p_i\cdot\left(\frac{M_{12}}{\sqrt{s}}\right)^i\right], \tag{4.20}$$

  where p_a is a shift parameter and p_i are the coefficients of the polynomial terms in the exponent. The Fisher test shows that a polynomial of the third order can be used to describe equally accurately the data in the control region in both the second and third sub-range, as illustrated in the bottom plots of Figure 4.31.

- SuperDijet, which was also introduced in the 2016 analysis as a generalisation of the original di-jet function:

$$\begin{aligned} f(M_{12}) = \exp\left(-A\cdot\log X\cdot(1+B\cdot\log X+\sum_{i=1}^{n} p_i\cdot\log^{i+1} X)\right),\\ X = \frac{M_{12}-x_p}{\sqrt{s}}, \end{aligned} \tag{4.21}$$

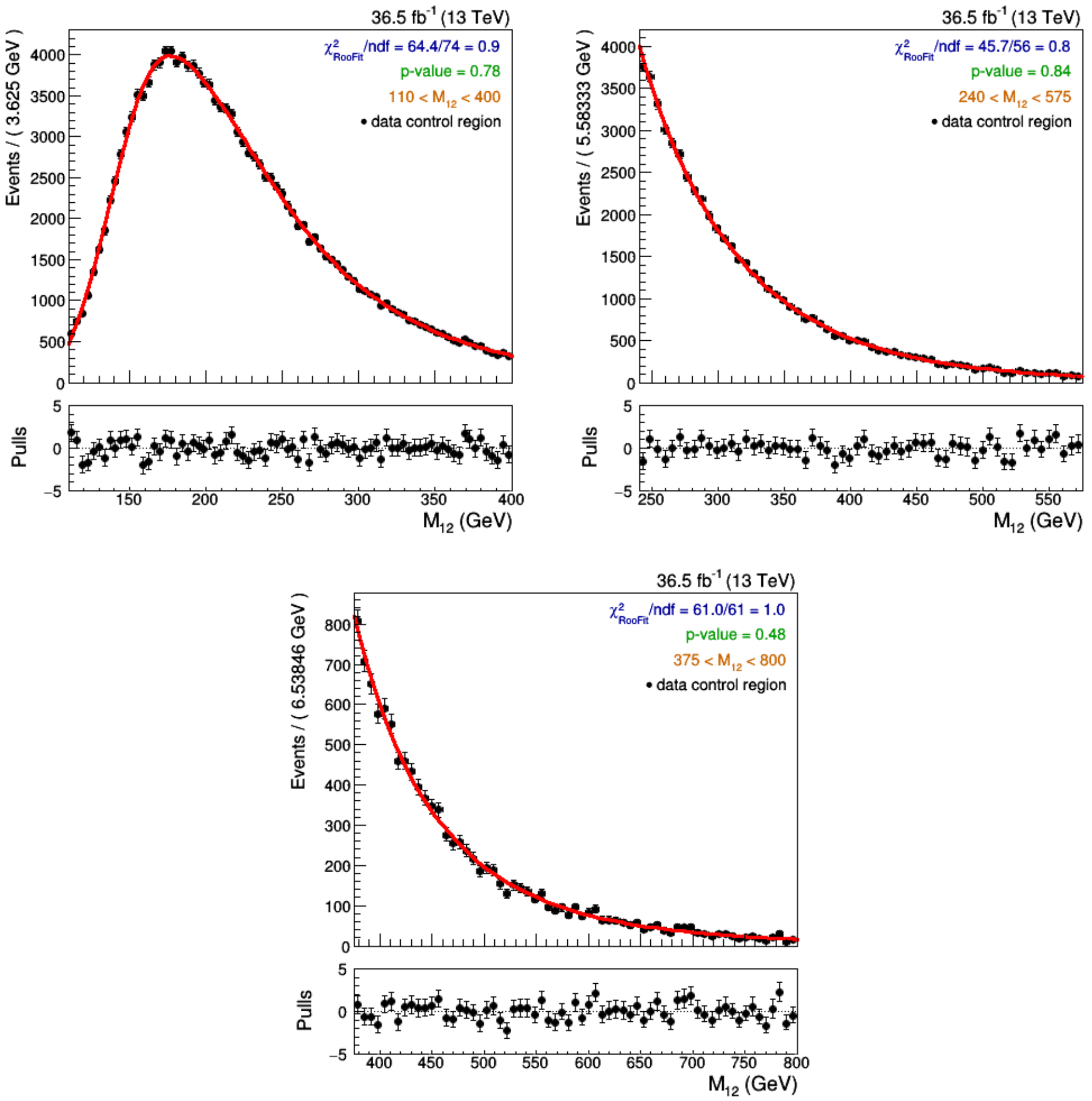

Figure 4.30: Di-jet invariant mass spectrum for the two leading b-tagged jets in the reverse b-tag control region (denoted with black dots) in the three sub-ranges: $M_{12} = [110; 400]$ GeV (top left), $M_{12} = [240; 575]$ GeV (top right) and $M_{12} = [375; 800]$ GeV (bottom). Red curves indicate the background-only fit performed in the relevant sub-range. In the first sub-range the Crystal-Ball function multiplied by the Turn-on function is used as an alternative analytical model. In the second and third sub-ranges respectively, the simple Crystal-Ball function is instead adopted as an alternative function for the fit to the data. In the bottom panel the normalised residuals ($\frac{\text{Data}-\text{Fit}}{\sqrt{\text{Fit}}}$) are shown.

with A and B are the parameters of the linear and quadratic logarithmic terms respectively, x_p sets the peak position and p_i are the coefficients of the higher order polynomial terms. The Fisher test confirms that the nominal Dijet function (degree zero) multiplied by the Turn-on function can describe with the same degree of accuracy as the main function the M_{12} distribution in the first sub-range as shown in the top left plot of Fig 4.31.

In the bias study, an *Asimov* dataset is used as a representative test-statistic [143]. It is defined as an artificial dataset, generated in such a way that the estimators for the parameters of interest are identical to their true value. The following procedure is applied to evaluate the bias effect for each individual mass point located in the relevant sub-range:

- A total of 5000 pseudo-experiments, also referred to as *toys*, are generated using the COMBINE TOOL package[5] [145] on the basis of the best-fit value of the alternative function under scrutiny. A certain amount of signal referred to as μ_{in} is also injected.

- The fit of the resulting signal plus background Asimov dataset is subsequently performed using the nominal background function and the signal function. The simultaneous $S+B$ fit maximises the binned log-likelihood function below:

$$-\mathrm{log}L = -\mathrm{log}\left(\prod_i e^{-\lambda_i}\frac{\lambda_i^n}{n_i!}\right) = \sum_i\left(\lambda_i - n_i\mathrm{log}\lambda_i + \mathrm{log}n_i!\right), \tag{4.22}$$

  with

$$\lambda_i = N\left[r_\mathrm{S} f_\mathrm{S}(x_i) + (1-r_\mathrm{S}) f_\mathrm{B}(x_i)\right], \tag{4.23}$$

  where i is the bin number, n_i is the total number of entries per bin, λ_i is the theoretical content assigned in each bin by the likelihood function, N is the total number of events in the given fit range, r is the fraction of signal, f_s and f_b are the functions used for the signal and background modelling respectively, while x_i is the central value of the i-th bin of the di-jet invariant mass.

- The total signal strength extracted from the fit, $\mu_{fit} = N \times r_s$ is compared to the injected signal strength μ_{in} for each toy, by considering the uncertainty of the fitted signal strength, σ_{fit}. The resulting pull distribution is interpreted as the systematic bias uncertainty from the choice of the background function, viz:

$$\mathbf{B}_{M_{A/H}} = \langle\frac{\mu_{fit} - \mu_{in}}{\sigma_{fit}}\rangle. \tag{4.24}$$

[5] This software package was originally implemented in the context of the combination of CMS and ATLAS results on the Higgs boson searches [144].

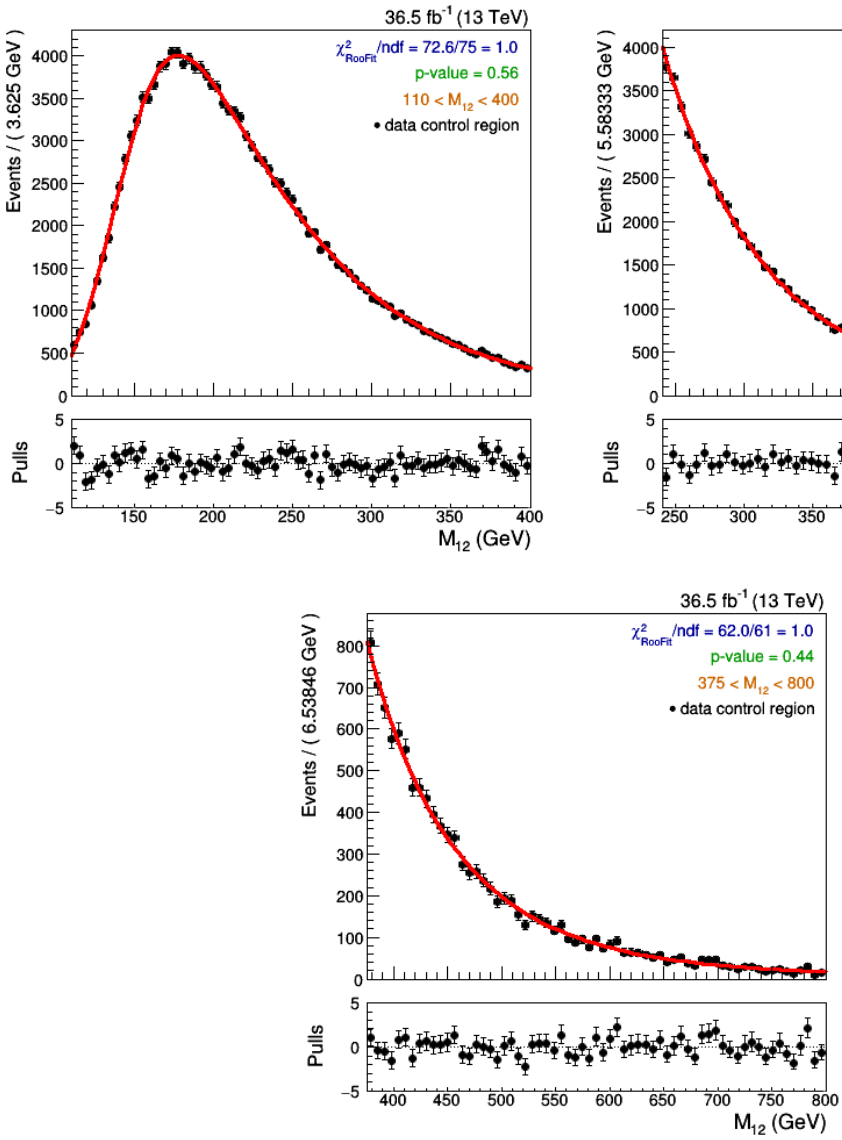

Figure 4.31: Di-jet invariant mass spectrum for the two leading b-tagged jets in the reverse b-tag control region (denoted with black dots) in the three sub-ranges: $M_{12} = [110; 400]$ GeV (top left), $M_{12} = [240; 575]$ GeV (top right) and $M_{12} = [375; 800]$ GeV (bottom). Red curves indicate the background-only fit performed in the relevant sub-range. In the first sub-range the nominal Dijet function multiplied by the Turn-on function is used as an alternative analytical model. In the second and third sub-ranges respectively, the Exponential-polynomial function of third degree is instead adopted as an alternative function for the fit to the data. In the bottom panel the normalised residuals ($\frac{\text{Data}-\text{Fit}}{\sqrt{\text{Fit}}}$) are shown.

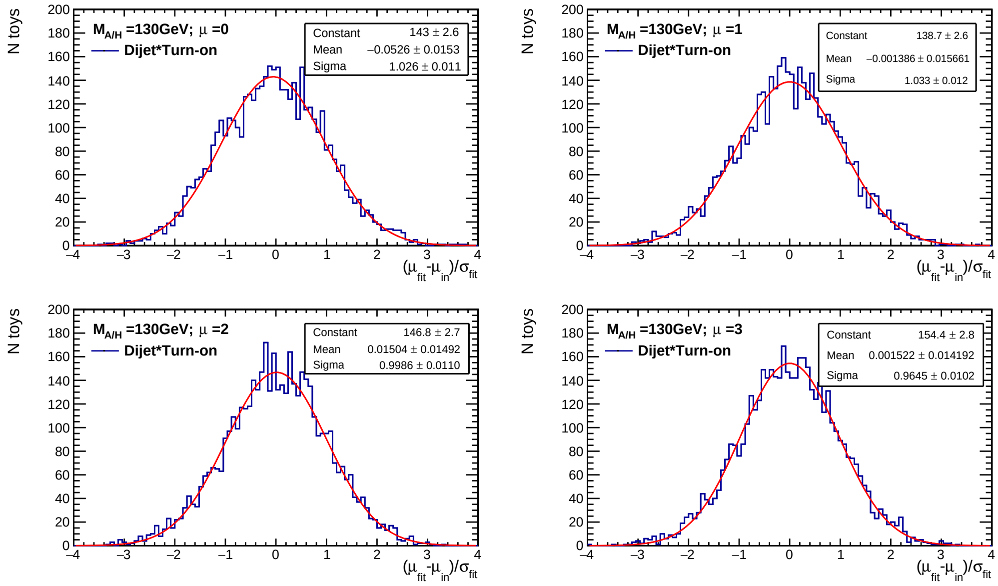

Figure 4.32: Measured bias from the background model for the signal mass-point $m_{A/H} =$ 130 GeV. The toys have been generated with the alternative background function, the Dijet multipled by the Turn-On function and several values of signal strength have been injected μ_{in} =0,1,2,3.

The bias studies are conducted separately for each signal mass point in its corresponding sub-range using the background alternative functions selected according to the Fisher test. As an illustration, the bias results for the alternative function Dijet multiplied by the Turn-On function are shown in Figure 4.32 for the $M_{A/H} = 130$ GeV signal mass-point. The pull distribution of the signal strength is fitted with a Gaussian function, and the mean and variance of the fit are used to determine the amount bias and its statistical error. The bias results are obtained for several injected signal strengths, namely $\mu_{in} = 0, 1, 2, 3$, where $\mu_{in} = 1$ corresponds to the expected signal yield predicted in the hMSSM benchmark scenario, introduced in Section 1.2.6, for a moderate value of $\tan\beta = 20$. This particular choice is motivated by the need to test a plausible range of initial signal strengths accessible by this analysis in the full mass range of interest. Nevertheless, the injected signal strength has a negligible impact on the results, and the measured bias is independent of μ_{in} in each sub-range, for all the signal mass hypotheses probed, as shown in Figures 4.33 and 4.34.

The background modelling bias effect is found to be maximal for the signal mass-points peaking in the bulk of *bbnb* control region at a di-jet mass value of $\sim$ 160 GeV. This is expected from the observed similarity of the background and the signal shapes in the first sub-range. For the final background systematic uncertainty, a conservative estimate of the bias uncertainty is applied for each sub-range. A bias of 100% is assigned to the first sub-range, while values of 50% and 35% are assigned to the second and third sub-range, respectively. The signal mass points peaking in the overlap region of adjacent sub-ranges are assigned to the sub-range with the best sensitivity. Following this criterion, the signal mass-point at 350 GeV and 500 GeV have been included in the second and the third sub-range, respectively.

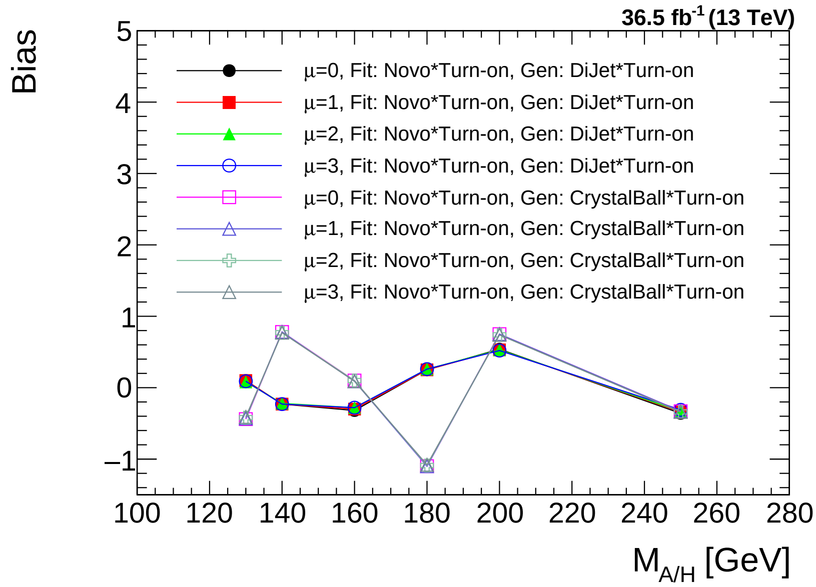

Figure 4.33: Bias results from the background model choice in the first sub-range versus $M_{\mathrm{A/H}}$ for several injected signal strengths (μ). The nominal Novosibirsk function multiplied by the Turn-on function is used as the main background function in the signal-plus-background fit of the toys. The latter are generated independently with two alternative background functions, respectively the Dijet and the Crystal Ball, both multiplied by the Turn-on function.

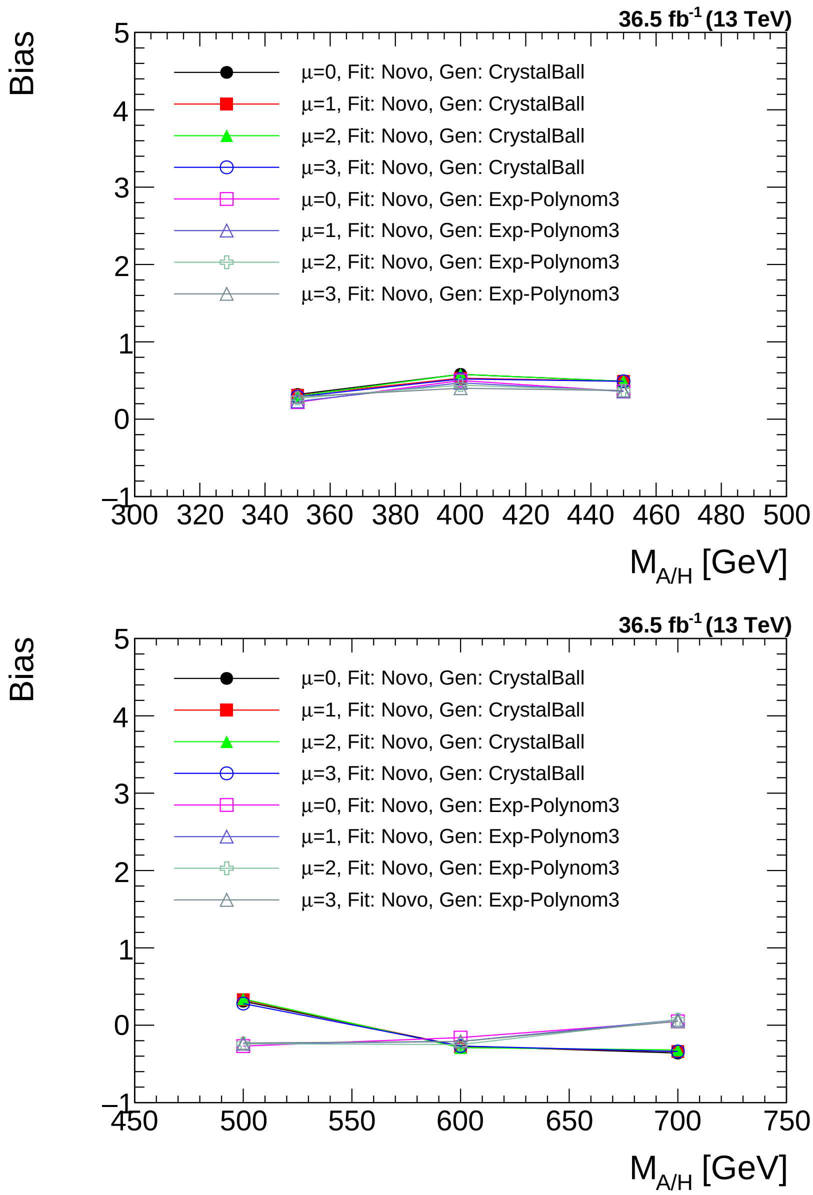

Figure 4.34: Bias results from the background model choice in the second (top row) and third sub-range (bottom row) versus $M_{\mathrm{A/H}}$ for several injected signal strengths (μ). The nominal Novosibirsk function is used as the main background function in the signal-plus-background fit of the toys. The latter are generated independently with two alternative background functions, respectively the Crystal Ball and the Exponential-Polynomial function of degree 3.

4.9 Statistical inference

The purpose of this search is to test a certain signal hypothesis by performing statistical inferences on the observed data. In case no significant signal is found, exclusion limits are derived both in a model-independent way and in the parameter space of the theoretical models under scrutiny. In this work, a modified frequentist procedure is adopted, namely the "Asymptotic CLs method" [143, 146], a criterion based on an asymptotic approximation of the likelihood-based test statistic. The statistical inference has been performed with the COMBINE TOOL software package [144], which enables the treatment of systematic effects as nuisance parameters.

4.9.1 Likelihood function

The likelihood function is defined as the probability density function (pdf) quantifying the agreement of an experimental observation with a theoretical model of reference. It is expressed as a function of several parameters, including the observable physical quantities $\vec{x}$ and the vector of nuisance parameters $\theta = (\theta_1, ..., \theta_m)$. The latter are introduced to account for the systematic uncertainties affecting the measurement, such as detector effects and theoretical uncertainties. In the case of a series of N independent measurements of the variables $\vec{x} = (x_1, ..., x_n)$, it is straightforward to obtain the overall likelihood as the product of the individual contributions:

$$L(\vec{x}, \theta) = \prod_{i=1}^{N} f(x_1^i, ..., x_n^i; \theta_1, ..., \theta_m), \tag{4.25}$$

where the index i indicates a particular measurement. In the context of a Poissonian counting experiment, the expected outcome of the total event yield can be parameterised as:

$$\nu = \mu \cdot s(\theta) + b(\theta), \tag{4.26}$$

where μ indicates the signal strength of the signal model and it represents one of the main parameters of interest. The expected signal s and background b yields are affected by specific sources of systematic uncertainty. The likelihood function estimate can be factorised in two independent terms:

$$L(\vec{x}, s, b, \theta) = L_x(\vec{x}, s, b, \theta) \cdot \prod_j \rho_j(\theta|\tilde{\theta}), \tag{4.27}$$

where the index j spans over all systematic sources of uncertainty. The first expression $L_x(\vec{x}, s, b, \vec{\theta})$ denotes the likelihood of the observed data, while the $\rho_j(\theta|\tilde{\theta})$ term indicates likelihood of obtaining the true value θ_j for a specific nuisance parameter from its initial estimate $\tilde{\theta}_j$. Since the latter cannot be determined *a priori*, a Bayesian interpretation is exploited to incorporate *a posteriori* the knowledge of the estimated value of each systematic source:

$$\rho(\theta|\tilde{\theta}) \sim p(\tilde{\theta}|\theta) \cdot \pi(\theta), \tag{4.28}$$

where $p(\tilde{\theta}|\theta)$ is the pdf of a nuisance parameter obtained in a separate, auxiliary measurement under similar conditions as the main problem of interest, e.g. the derivation of the kinematic trigger efficiency scale factors; $\pi(\theta)$ is the prior distribution of the nuisance parameter, is chosen to be flat to avoid biasing the overall likelihood.

4.9.2 Treatment of nuisance parameters

In general, systematic uncertainties can be categorised into two main classes, the ones affecting exclusively the event yield, referred to as the normalisation-only uncertainties, and those with an impact also on the shape of the predicted distribution.
The log-normal distribution is used to parameterise the signal normalisation-only systematic uncertainties:

$$p(\tilde{\theta}|\theta) = \frac{1}{\sqrt{2\pi}\ln K} \cdot \frac{1}{\tilde{\theta}} \cdot \exp\left(-\frac{(\ln\tilde{\theta}/\theta_m)^2}{2\ln^2 K}\right), \tag{4.29}$$

whose defining parameters $\kappa = e^{\tilde{\sigma}}$ and $\theta_m = e^{\tilde{\theta}}$ are related to the gaussian distribution width $\tilde{\sigma}$ and mean $\tilde{\theta}$, respectively. This functional form is more convenient than the normal distribution since it enforces the positive-definite character of the nuisance parameter of interest. This is a desirable feature since negative signal yields are regarded as unphysical, as in the case of the measured luminosity.
The shape-altering systematic uncertainties make a sizable impact exclusively on a subset of the shape parameters of the signal fit. A parametric approach is implemented to account for the systematic shift of the affected shape parameters α:

$$\alpha = \alpha_{ctrl} + \sum_k \frac{(\alpha_{up}^{\theta_k} - \alpha_{down}^{\theta_k})}{2n} \cdot \theta_k, \tag{4.30}$$

where the index k runs over all the shape-altering systematic uncertainties, n indicates the systematic variation in units of standard deviation, α_{ctrl} is the fitted value of the shape parameter for the central template fit, whereas $\alpha_{up}^{\theta_k}$ ($\alpha_{down}^{\theta_k}$) are extracted in the systematic up- (down) variations of the signal template associated with the θ_k nuisance. An arbitrary value of two standard deviations from the central signal template is employed to interpolate between the up- and down systematic shape variations.

4.9.3 Maximum likelihood fit

In this search, an unbinned shape analysis of the main observable x, the dijet invariant mass, is performed for the statistical inference. Assuming Poissonian distribution of the signal and background shapes, parameterised with the corresponding pdfs denoted as f_s and f_b, the first term in Eq.4.27 can be cast into the form:

$$L_x(x|\mu,\theta) = \frac{e^{-\mu s+b}}{N!}\prod_{i=1}^{N}(\mu s f_s(x^i,\theta) + b f_b(x^i,\theta)), \tag{4.31}$$

where s and b correspond to the predicted signal and background yields, x^i denotes the value of the main observable evaluated at the i-th event. In this work, the signal cross-section extraction procedure is based upon a *maximum likelihood* fit. As a general practice, it is customary to minimise the negative logarithmic likelihood (NLL), which is equivalent to maximising the likelihood function. This algorithm is computationally more efficient since it operates on a sum of terms rather than a product. The minimisation is performed with MINUIT [147], and the value of all the parameters concurring to the fit, including the signal strength, is floated in the vicinity of the NLL function minimum to derive their best-fit estimate. The statistical criterion adopted to determine the consistency of the experimental data with the hypothesis under consideration is referred to as *test statistic* [148].

4.9.4 Definition of the test statistic

According to the Neyman-Pearson lemma, the test statistic q yielding the most efficient discrimination for hypothesis testing is the profile likelihood ratio, defined as:

$$\tilde{q}_\mu = -2\ln\frac{L(\text{data}|\mu,\hat{\theta}_\mu)}{L(\text{data}|\hat{\mu},\hat{\theta})}, \qquad \text{with a constraint } 0 \le \hat{\mu} \le \mu, \tag{4.32}$$

where $\hat{\theta}_\mu$ in the numerator denote the *conditional* maximum likelihood (ML) estimators of the nuisance parameters, which maximise the likelihood given the data and the tested value of μ, while $\hat{\mu}$ and $\hat{\theta}$ represent the *unconstrained* ML estimators, evaluating the global maximum of the likelihood function in the data. The value of the estimator for the signal strength $\hat{\mu}$ is positive-definite to avoid unphysical negative signal yields, which may occur as a result of an upward background fluctuation. On the other hand, the upper bound on $\hat{\mu}$ enforces one sided-confidence intervals, and it prevents potential fluctuations in the signal strength above unity, which would disfavour the signal hypothesis under consideration.

Therefore, it is possible to compute separately the test-statistic for the background-only and the signal-plus-background $(s+b)$ hypothesis being tested as a function of μ. The maximum-likelihood estimators θ_μ^{obs} and θ_0^{obs} have to be evaluated independently in relation to the tested value of signal strength. Following the frequentist approach, the probability density functions $f(\tilde{q}_\mu|\mu,\tilde{\theta}_\mu^{\text{obs}})$ and $f(\tilde{q}_\mu|0,\tilde{\theta}_0^{\text{obs}})$ are then computed via a Monte Carlo method, which involves the generation of a substantial number of toys. A large sample size is a necessary requirement to ensure the validity of the *asymptotic approximation* for the test-statistic, as dictated by Wilks' theorem [149]. Consequently, two distinct probability p-values are computed:

$$p_\mu = P(\tilde{q}_\mu \geq \tilde{q_\mu^{\text{obs}}} | \hat{\mu} = \mu) = \int_{\tilde{q}_\mu^{\text{obs}}}^{\infty} f(\tilde{q}_\mu | \mu, \tilde{\theta}_\mu^{\text{obs}}) d\tilde{q}_\mu,$$
$$p_0 = 1 - p_b = P(\tilde{q}_\mu \geq \tilde{q}_0^{\text{obs}} | \hat{\mu} = 0) = \int_{\tilde{q}_0^{\text{obs}}}^{\infty} f(\tilde{q}_\mu | 0, \tilde{\theta}_0^{\text{obs}}) d\tilde{q}_\mu. \quad (4.33)$$

where p_μ quantifies the probability of obtaining a value for the test statistic larger than the observed one in the signal-plus-background hypothesis, while p_0 corresponds to the probability of rejection of the background-only hypothesis.

4.9.5 Limits setting

In the absence of a significant signal excess, the compatibility of the tested signal hypothesis with the observed data can be exploited to set upper limit on the signal cross-section and to exclude a region of the parameter space of the model under scrutiny. To this end the modified confidence level is commonly used at the LHC, defined as the dimensionless ratio:

$$CL_s(\mu) = \frac{p_{s+b}}{1 - p_b}, \quad (4.34)$$

which can be used to reject a certain signal strength hypothesis with a $1 - CL_s(\mu)$ confidence level. In this work, the upper limits on the observed signal strength μ are set by requiring the 95% confidence level (C.L.) , i.e. $CL_s \leq 0.05$. As for the expected upper limits, the same criterion applies to an Asimov dataset generated with a Montecarlo method from the background pdf. In addition, the one and two-sigma uncertainties are promptly derived from the cumulative distribution of the background pdf with the nuisance parameters fixed to their central value.

CHAPTER 5

Results

In this chapter, the results of the search for BSM Higgs bosons produced in association with b-quarks and decaying into a $b\bar{b}$ pair in the semi-leptonic channel are presented. This analysis uses the data collected with the CMS detector in 2017 at a center-of-mass energy of 13 TeV. A signal-depleted control region with background features similar to the signal region is exploited for the background modelling. Prior to unblinding, the expected limits obtained in the control region are used to test and optimise the sensitivity of the analysis. In the final signal extraction fit of the M_{12} invariant mass distribution, the systematic effects are treated as nuisance parameters, as described in Section 4.9.1. The impacts of the main groups of nuisances on the signal yields is evaluated prior to the extraction of the limits on the cross-section times branching fraction in the signal region. The results are further interpreted within the parameter space of several models featuring an enlarged Higgs sector, namely the Two-Higgs-Doublet-Model (2HDM) and the Minimal Supersymmetric extension of the Standard Model (MSSM).

5.1 Results before unblinding

The dominant sources of systematic uncertainty are parameterised as nuisance parameter groups, and their impact on the expected signal strength has to be studied prior to unblinding. The definition of meaningful nuisance parameter groups for the signal systematic uncertainties is to some extent arbitrary. The criterion adopted is to assign the nuisance parameters featuring the largest degree of correlation to the same group.

5.1.1 Systematic uncertainties

Systematic uncertainties have an impact on the cross-section measurement of the searched process by affecting the observed signal and background yields as well as their shapes. A brief summary of each systematic source of uncertainty and its impact on the signal and background estimation is quantified. The signal yields are sensitive to the normalisation uncertainties:

- of the luminosity estimate in the data as determined centrally by the CMS collaboration [150];
- of the minimum-bias cross section assumed in the pile-up profile re-weighting procedure;
- of the online b-tagging efficiency scale factors estimated from data using control triggers as described in Section 4.5.6;
- of the offline b-tagging efficiency scale factors for heavy flavour identification and light-flavour fake rate as explained in Section 3.6.1;
- of the kinematic efficiency, estimated separately for the leading jets and the selected muon using dedicated tag-and-probe methods illustrated in Section 4.5.3;
- of the selected muon identification scale factor as explained in Section 3.4;
- the model-dependent theoretical uncertainty of the normalisation and factorisation scale of QCD evaluated by the LHC cross section working group (LHCXSWG) [151];
- the model-dependent uncertainty due to the value of α_S and the choice of the parton distribution functions (PDFs) following the prescriptions of the LHCXSWG,

which are propagated as multiplicative factors in the final maximum likelihood fit. The impact of all signal systematic uncertainties on the signal yield is illustrated in Table 5.1. The jet energy corrections are treated as shape-altering systematic uncertainties, since they cause a percent level shift of the shape parameters controlling the signal peak and tail position.

Furthermore, since the background modelling is estimated with a data-driven technique, the background normalisation is allowed to float almost freely in the final fit. The shape parameters of the background function are unconstrained, with the exception of the turn-on parameters that are fixed to their fitted value in the control region. The bias effect from the choice of the analytical function used for the background modelling is evaluated in each sub-range in dedicated bias studies, described in Section 4.8.4. The corresponding systematic uncertainty is treated as a spurious signal in the final fit using a linear morphing technique. This bias normalisation uncertainty is modelled with a log-normal distribution with an initial estimate for the width $\tilde{\sigma} = \mathbf{B}\Delta\mu$, where $\mathbf{B}$ is the bias obtained for a certain Higgs boson mass hypothesis, and $\Delta\mu$ is the expected uncertainty on the signal strength. A conservative value of the bias uncertainty is assigned, i.e. 100%

Uncertainty source	type	Impact on normalisation
Jet energy scale	shape	4.5 – 0.9%
Jet energy resolution	shape	1.0 – 0.25%
Muon kinematic trigger efficiency	rate	6.7 – 7.9%
Jet kinematic trigger efficiency	rate	0.5 – 0.06%
Online b-tagging efficiency	rate	3.0 – 5.7%
Offline b-tagging efficiency	rate	4.6 – 5.8%
Muon identification efficiency	rate	1.0 – 0.5%
Pileup re-weighting	rate	1.4 – 0.17%
Luminosity	rate	2.3%
pdf + α_S, mssm/2hdm cross-section	rate	1.9 – 5.6%
QCD scale, mssm/2hdm cross-section	rate	7.2 – 1.8%

Table 5.1: List of signal systematic uncertainties classified either as normalisation-only (rate) or shape altering systematic uncertainties (shape). The impact on the signal strength is assessed by varying the uncertainty source by $\pm 1\sigma$. Each range indicates a monotonous variation with respect to the increasing Higgs boson mass.

for the mass-points in the first mass sub-range, 50% and 35% for those in the second and third sub-range, respectively.

A crucial aspect of any physics analysis is to quantify and mitigate the main systematic effects affecting the measurement. The p_{T} thresholds of the dijet-plus-muon system have been optimised to minimise the impact on the signal yield of the corresponding kinematic trigger efficiency scale factors uncertainty, which is found to be larger at low jet and muon p_{T}, respectively. In addition, the muon identification and the b-tagging working points have been chosen to achieve the best compromise between signal efficiency and purity.

5.1.2 Impacts of nuisance parameters

The contributions of the main nuisance parameters groups to the signal strength have been tested using a background-only Asimov dataset. The statistical uncertainty is quantified by setting simultaneously all nuisance parameters to their corresponding post-fit values. The contribution of a nuisance parameter group to the overall uncertainty in the signal strength ($\Delta\mu$) is instead addressed in two steps. First, the signal extraction fit is performed fixing all parameters in the nuisance parameter group of interest to their post-fit values. The resulting uncertainty is then subtracted in quadrature from the overall uncertainty of the global fit with all the nuisance parameters unconstrained. As an illustration, the impacts are shown for three representative mass-points assigned to different mass sub-ranges, namely $m_{A/H} = 130$ GeV, 350 GeV and 700 GeV. The individual contribution of each group of nuisances to the total uncertainty on the signal strength is illustrated in Table 5.2. The overall uncertainty in the global fit differs from the

	$\pm\Delta\mu$ (expected)		
Uncertainty source	$m_{H/A} = 130$ GeV	$m_{H/A} = 350$ GeV	$m_{H/A} = 700$ GeV
Total	$\pm$ 44	$\pm$ 3.10	$\pm$ 1.16
Statistical	$\pm$ 39	$\pm$ 2.64	$\pm$ 0.72
Total Systematic	$\pm$ 20	$\pm$ 1.64	$\pm$ 0.91
Background shape	$\pm$ 20	$\pm$ 1.61	$\pm$ 0.91
background bias	$\pm$ 0.8	$\pm$ 0.08	$\pm$ 0.04
Total signal	$\pm$ 3.9	$\pm$ 0.34	$\pm$ 0.13
trigger kinematics	$\pm$ 2.8	$\pm$ 0.23	$\pm$ 0.09
b tagging	$\pm$ 2.3	$\pm$ 0.23	$\pm$ 0.09
jet energy corrections	$\pm$ 0.90	$\pm$ 0.03	$\pm$ 0.04

Table 5.2: Contributions of the most relevant uncertainties to the estimated signal strength in simulation using an Asimov background-only (b) pseudo-dataset for three representative signal mass hypothesis assigned to different mass sub-ranges, i.e. $m_{H/A} =$ 130, 350, 700 GeV. The uncertainties are obtained by fixing the listed sources of uncertainties to their post-fit values in the fit and subtracting the obtained result in quadrature from the result of the full fit. They are found to be symmetric within the quoted precision. The statistical uncertainty is assessed by setting simultaneously all nuisance parameters to their post-fit values. The quadratic sum of the contributions differs with respect to the overall uncertainty due to cross-correlations between different nuisance parameter groups.

quadratic sum of the individual systematic contributions due to the correlations between different nuisance parameter groups. The signal strength uncertainty is dominated by the statistical component for all the signal mass hypotheses, highlighting that this analysis is statistically limited. The prevailing contribution to $\Delta\mu$ comes from background modelling, and it is dominated by the shape parameters. The total background uncertainty is over a factor five larger than the main signal nuisance parameter groups, b-tagging and trigger kinematic efficiency, which have similar contributions to $\Delta\mu$.

The impact and the pull distributions of the individual nuisance parameters have been studied with a signal-plus-background $(s + b)$ Asimov dataset. Each nuisance parameter is allowed to float freely in the global fit, with the others set to their best fit values. The resulting pulls and impacts are shown in Figure 5.1 for three representative signal mass-points. The ranking of the nuisance parameter confirms that the background shape parameters have the largest impact on the overall uncertainty of the signal strength in all the considered sub-ranges. The effect of the signal-related nuisances, including the bias, is factorised as a multiplicative factor on the overall signal strength, hence the individual contribution to the signal strength is not constrained in the final fit. This is visible in the pull distribution of all signal-related nuisances, for which the pre-fit and post-fit values coincide.

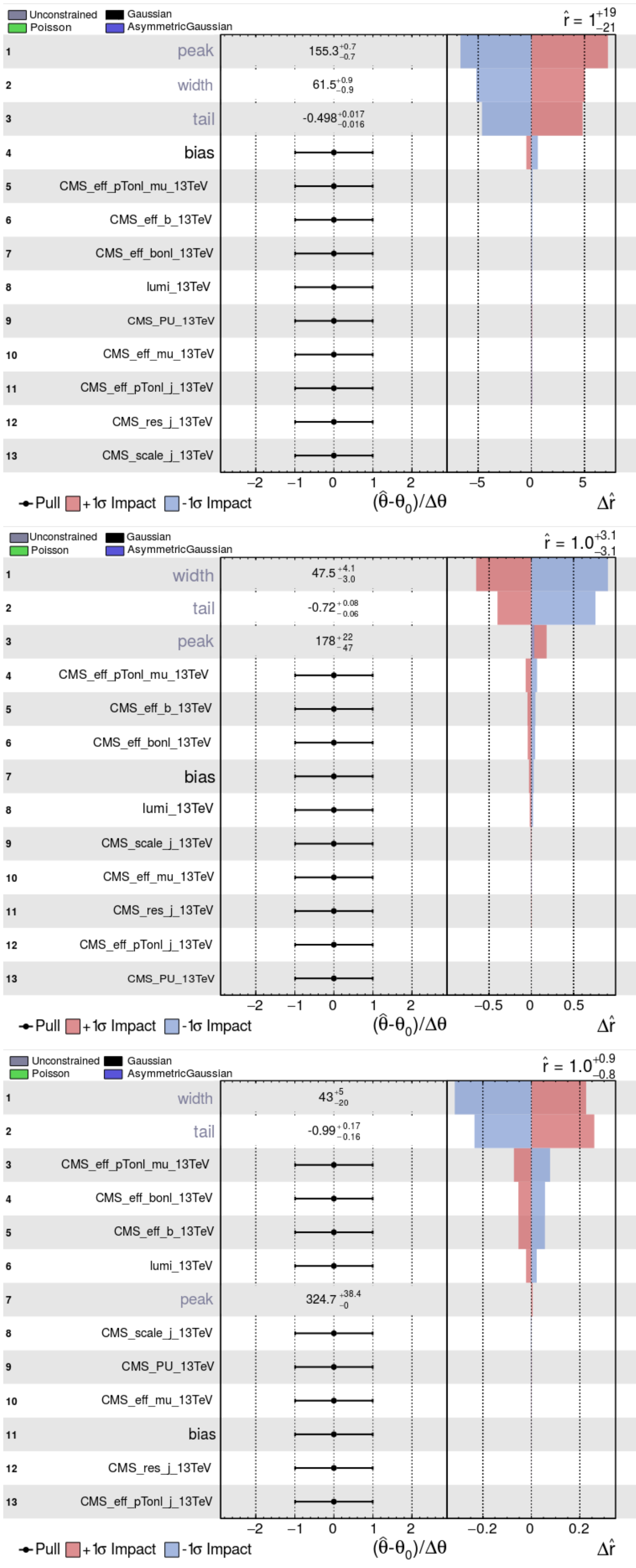

Figure 5.1: Pulls and impacts of each nuisance parameter in a Asimov s+b dataset for representative of signals in each sub-range: 140 GeV (top), 350 GeV (middle) and 700 GeV (bottom).

5.1.3 Expected limits

An optimisation study of the M_{12} subrange division is performed with the expected limits derived in the control region to maximise the sensitivity. The signal hypotheses whose mass peaks lie in the overlap region between adjacent sub-ranges have been tested in both regions prior to the final decision on their sub-range assignment. The resulting upper limits on the signal cross-section times branching fraction shown in Figure 5.2 incorporate the impact of all the nuisance parameter groups.

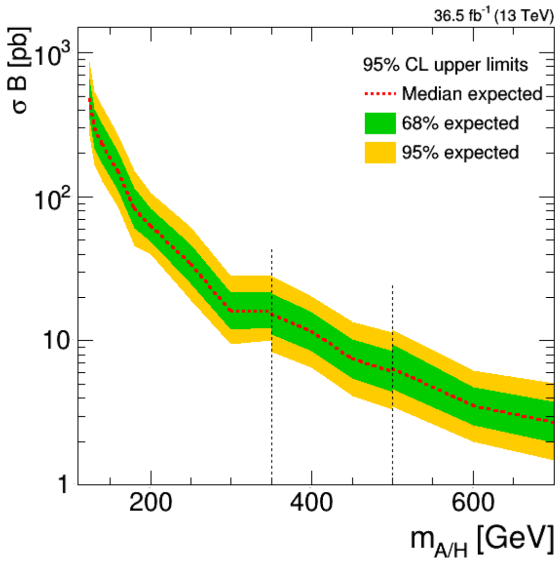

Figure 5.2: Model-dependent expected upper limits on Higgs cross section times branching fraction as a function of the Higgs boson mass, as determined from an Asimov background-only pseudo-dataset derived from the data in the control region. The expected upper limits for the 350 and 500 GeV signal hypotheses whose mass peaks lie in the overlap region between adjacent sub-ranges are displayed in both sub-ranges.

The shape of the upper limits mirrors the observed monotonous decrease of the M_{12} spectrum. At the sub-range boundaries, the discontinuities in the median of the limit for the 350 GeV and 500 GeV mass-point evaluated in adjacent mass-points reflect the corresponding differences in signal efficiency. At high masses, the lowering in sensitivity is caused by the progressive degradation of the di-jet mass resolution, due to the lower jet p_{T} resolution at high transverse momentum. Another effect is the increased fraction of missing energy carried away by neutrinos in semi-leptonic decays of b-hadrons.

5.2 Results after unblinding

Following the validation of the methods for the statistical inference and the detailed study of the impact of the nuisance parameters on the maximum likelihood fit, the mass spectrum of the M_{12} distribution is unblinded in the triple b-tag signal region.

5.2.1 Background-only fit of data in the signal region

The main background function selected in each mass sub-range in the reverse b-tag control region is also used to perform the background-only fit in the corresponding signal region sub-range. All the shape parameters are freely floating, with the exception of the Turn-on function parameters for the first sub-range. The background-only fits to the observed data in the signal region are displayed separately for each sub-range in Figure 5.3. A good agreement of the data with the background-only hypothesis is observed.

5.2.2 Model-independent results

A signal extraction fit in the signal region is performed independently for every signal mass-point in each mass sub-range. No significant excess is observed for any of the signal hypotheses. The resulting signal yields are used to obtain the 95 % C.L. upper limits on the Higgs boson cross section times branching fraction, following the procedure outlined in Section 4.9. The unblinded results portrayed in Figure 5.4 span several Higgs boson mass hypotheses between 125 GeV and 700 GeV. The upper limits on the signal cross-section within the range from 541 pb to 2.54 pb are listed in Table 5.3. The discontinuities in the median of the upper limit in correspondence of the 350 GeV and 500 GeV mass-points encode the impact of the mass sub-range optimisation. In order to set the observed limit for these signal mass-points peaking at sub-range boundaries, the sub-range associated with the lowest expected limit is selected. The observed and expected upper limits are compatible within two standard deviations.

One of the main achievements of this work is the significant sensitivity recovery to low Higgs boson masses. In BSM searches in the fully-hadronic channel, formerly the lowest pseudoscalar mass probed was $m_{\mathrm{A}} = 300$ GeV and 450 GeV for the 13 TeV CMS [17] and ATLAS [131] results, respectively. The latter exhibit only a factor ~ 2 better sensitivity at masses beyond 500 GeV, at the cost of a much larger background rate. In fact, compared with the CMS results in the full-hadronic at 13 TeV, the resulting data sample used in this work is an order of magnitude smaller. The online requirement of a muon within-a-jet acts as a soft b-tag requirement, and it drives down the trigger rates considerably. Looser p_{T} requirements for the di-jet system are then applied at trigger level, thus targeting a better sensitivity at low Higgs boson masses. The other fundamental ingredients needed to optimise the analysis sensitivity are the adoption of the best perfoming b-tagger currently available and the application of b-jet energy regression, which improves

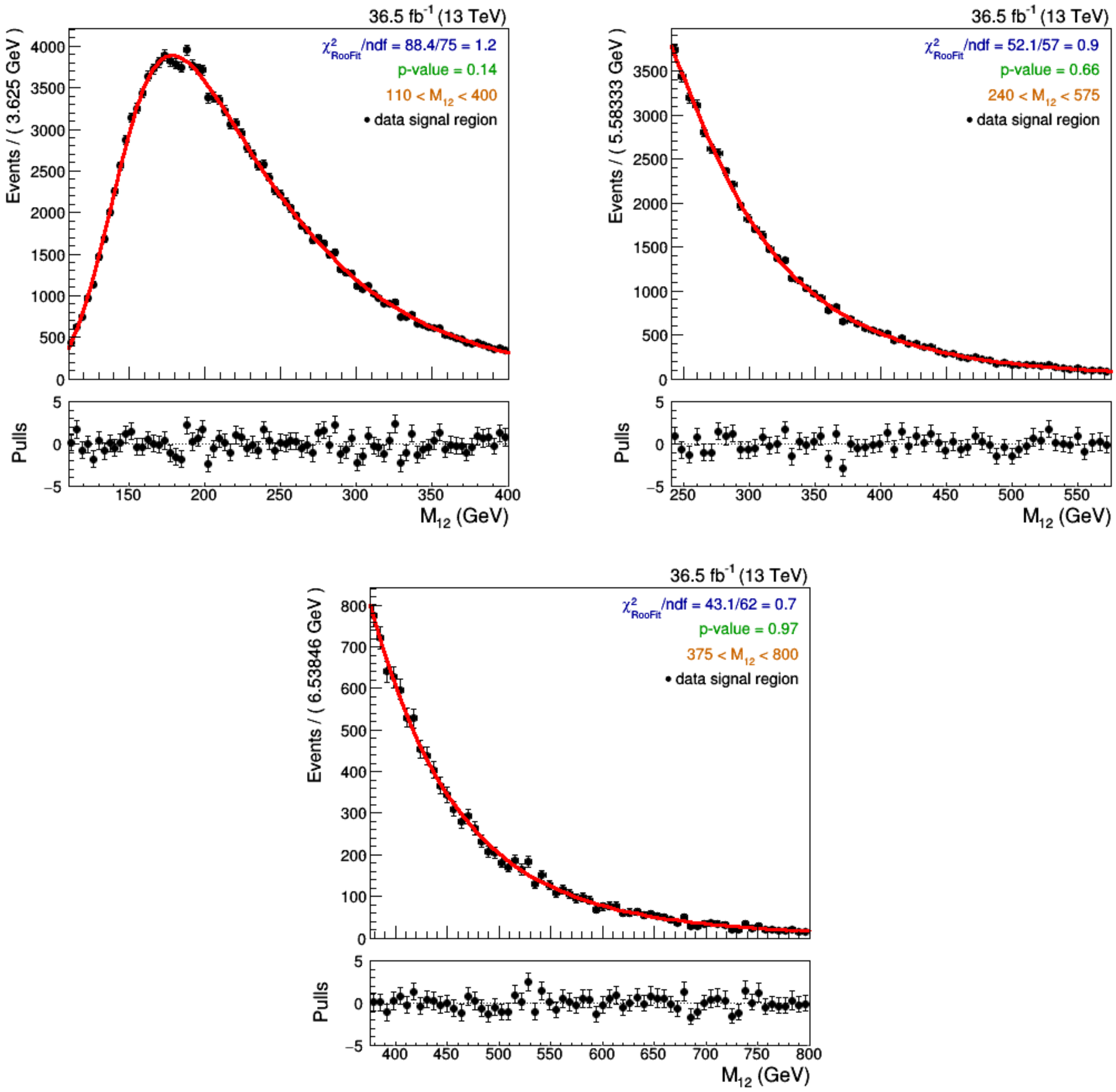

Figure 5.3: Background-only fit (red curve) of the invariant di-jet mass spectrum, M_{12}, in the triple-b-tag (bbb) signal region in three different sub-ranges: $M_{12} = [110, 400]$GeV (top left), $M_{12} = [240, 575]$GeV (top right) and $M_{12} = [375, 800]$GeV (bottom). In each top panel, the black dots denote the data in the signal region while the bottom panel illustrates the data normalised residuals.

Mass [GeV]	-2σ	-1σ	Median	$+1\sigma$	$+2\sigma$	Observed
125	269.17	352.26	481.88	664.35	880.23	541.05
130	168.10	219.99	300.94	406.50	551.53	504.76
140	129.20	171.02	236.25	329.48	446.46	386.23
160	79.22	113.22	159.06	225.64	309.30	147.19
180	47.85	63.34	87.50	121.33	160.91	101.26
200	39.55	48.34	62.50	82.43	105.55	69.11
250	20.32	26.00	35.16	48.61	65.23	21.81
300	18.21	22.67	28.59	36.34	45.63	27.02
350	8.46	11.33	15.81	22.43	30.75	13.95
400	6.31	8.35	11.53	16.08	21.64	14.37
450	4.03	5.34	7.47	10.48	14.25	9.61
500	3.36	4.50	6.28	8.91	12.21	4.80
600	2.14	2.85	3.95	5.53	7.48	6.01
700	1.78	2.37	3.32	4.72	6.51	2.54

Table 5.3: Observed and expected upper limits at 95% C.L. on $\sigma(pp \to bA/H + X)B(A/H \to b\bar{b})$ as a function of the Higgs boson mass $m_{\mathrm{A/H}}$.

the signal efficiency up to 15 % for the lowest signal mass-point. Furthermore, final state radiation recovery yields an additional percent level improvement from the better di-jet mass resolution and scale. Exclusion limits are also derived in several MSSM and 2HDM benchmark scenarios to provide novel constraints on the accessible parameter space of these models.

5.3 Interpretation within the MSSM

As discussed in Section 1.2, the MSSM parameter space is entirely defined at tree-level by two BSM parameters, namely tanβ and m_{A}. The model-independent results are converted into exclusion contours in the $[\tan\beta, m_{\mathrm{A}}]$ plane in the $m_{\mathrm{h}}^{\mathrm{mod+}}$ and the hMSSM benchmark scenarios. The MSSM cross-section times branching fraction of the signal process are computed centrally by the LHC Higgs Cross Section Working Group (LHCHXSWG) [151]. The four- and five-flavour 4(5FS) schemes predictions of the MSSM signal cross section are combined via the Santander matching scheme [132] described in detail in Section 4.2. The 4FS cross section in the MSSM is calculated at NLO accuracy by inclusion of the SUSY QCD corrections [152, 153], while the radiative corrections in the 5FS case are computed up to NNLO accuracy [154]. In the latter, the higher-order loop corrections can be computed, owing to the simpler structure of the signal process involving the presence of only one b-quark in the initial state. The partial decay widths of the

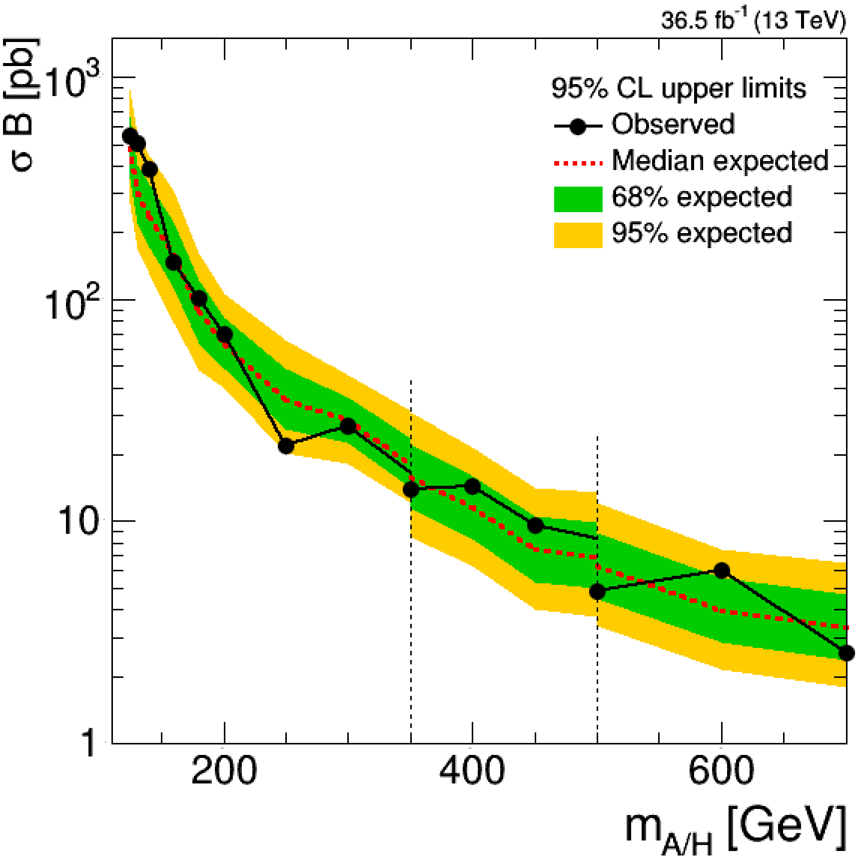

Figure 5.4: Observed and expected upper limits at 95% C.L. on $\sigma(pp \rightarrow bA/H + X)B(A/H \rightarrow b\bar{b})$ versus the Higgs boson mass $m_{\mathrm{A/H}}$. The green and yellow bands indicate respectively one and two-sigma standard deviations from the expected limit derived in the background-only hypothesis (red dashed line), while the observed results are denoted in black dots. The dashed vertical black lines indicate the transition between the adjacent mass sub-ranges defined in the analysis.

$A/H \rightarrow b\bar{b}$ process were determined centrally by the LHCGXSWG, combining the predictions of HDecay [155, 156] for the one-loop SUSY corrections and of FeynHiggs v. 2.12.0 [157–160] for the two-loop level case.

The parameters of the SUSY sector play an important role in the definition of the sensitivity of the analysis. A distinctive feature of the MSSM with respect to non-supersymmetric models featuring an analogous Higgs sector (as in the case of the Type-II 2HDM model) is the existence of additional Higgs boson decay modes into light SUSY particles. In particular, the kinematically allowed decays into a pair of light supersymmetric particles can alter substantially the $A/H \rightarrow b\bar{b}$ branching fraction, particularly for large values of the pseudoscalar mass m_{A}, as outlined in Section 1.2.6. Another important effect is the modification of the bottom Yukawa coupling caused by SUSY radiative corrections, previously discussed in Section 1.2.5. The b-associated production of neutral Higgs bosons decaying into a pair of b-quarks is greatly enhanced for $\tan\beta > 1$ over a vast region of SUSY parameter space. Each $b\bar{b}\phi$ vertex receives a correction by the pre-factor $(1 + \Delta_b)^{-1}$, where the size of the correction to the running bottom mass Δ_b is proportional to the Higgsino mass parameter, i.e. $\Delta_b \propto \mu \tan\beta$. This yields an additional tanβ-dependence on the total rate production of the process of interest which can either enhance or suppress the process depending on the sign of μ.

In the $m_{\mathrm{h}}^{\mathrm{mod+}}$ scenario, the Higgsino mass parameter is set to the conventional value of $\mu = +200$ GeV. In both scenarios the lightest CP-even state h is assumed to be the observed h(125) boson with SM properties. Therefore, its cross section is much smaller than the ones of the other Higgs states in the probed parameter space and the contribution from h is disregarded. The results in the $m_{\mathrm{h}}^{\mathrm{mod+}}$ scenario, shown in Figure 5.5 can be compared with those from the combination of the CMS Run 1 results [129, 130], using both the fully-hadronic and the semi-leptonic channel. In this work, the excluded tanβ region of MSSM parameter spans a $\tan\beta$ range from a minimum at ~ 18 for a pseudoscalar mass around 250 GeV to a maximum of $\tan\beta \sim 56$ around $m_{\mathrm{A}} = 500$ GeV. The present analysis achieves similar or better sensitivity in the full m_{A} range probed than in the Run 1 combination, exploiting a finer grid of signal mass-points.

The results interpreted within the hMSSM benchmark scenario are illustrated in the right plot of Figure 5.5. The exclusion limits range from a minimum of $\tan\beta \sim 16$ for a mass around 250 GeV to a maximum of $\tan\beta \sim 53$ around $m_{\mathrm{A}} = 700$ GeV. The improvement in the exclusion limits with respect to the $m_{\mathrm{h}}^{\mathrm{mod+}}$ scenario can be ascribed to two separate factors. Differently from the other benchmark model, the hMSSM scenario assigns a large characteristic mass $O(\mathrm{TeV})$ to SUSY particles to achieve consistency with the current LHC experimental bounds. This effectively suppresses the competing A/H decay into a pair of SUSY particles, even at large values of m_{A}. Secondly, in the hMSSM scenario the loop-induced SUSY corrections affecting Δ_b, which in the $m_{\mathrm{h}}^{\mathrm{mod+}}$ model can

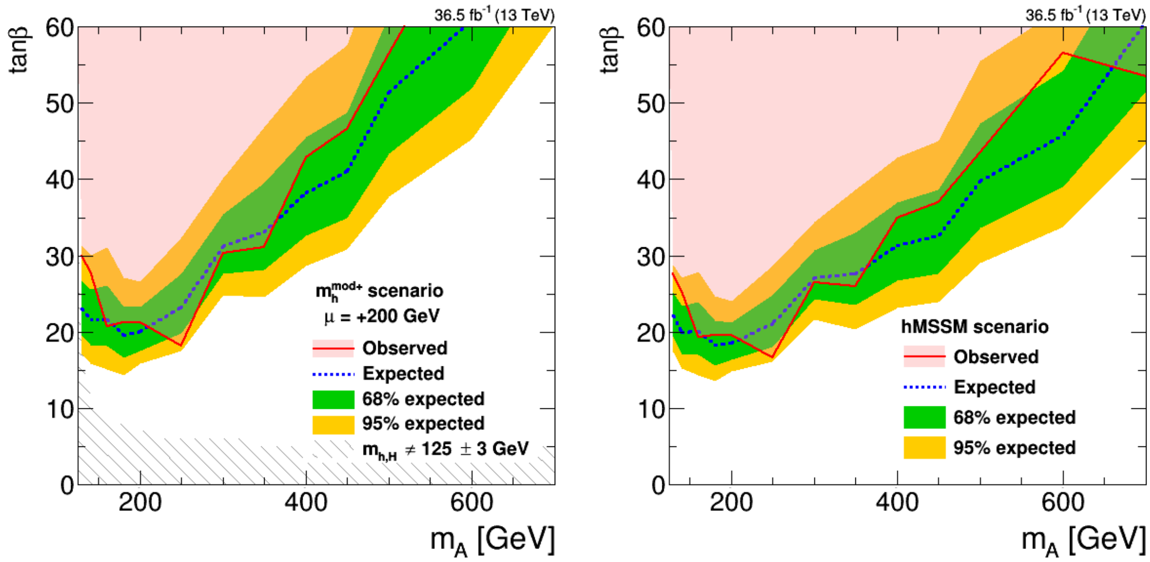

Figure 5.5: Observed and expected limits on the MSSM parameter $\tan\beta$ as a function of the pseudoscalar mass m_{A} in the $m_{\mathrm{h}}^{\mathrm{mod}+}$ benchmark scenario (left), for a Higgsino mass parameter of $\mu = +200$ GeV, and in the hMSSM benchmark scenario (right). The green and yellow bands represent $\pm 1\sigma$ and $\pm 2\sigma$ deviation from background-only expectation, respectively. The hashed pattern indicates the region of parameter space excluded by the observed Higgs boson at 125 GeV.

alter significantly the overall signal cross-section, are not taken into account. These results extend and complement the exclusion limits derived using the constraints of the h(125) Higgs coupling measuremts performed at ATLAS [47] for intermediate $\tan\beta > 25$, and for pseudoscalar masses above 500 GeV. Summary tables of the exclusion limits for both these MSSM scenarios are reported in Appendix C.

5.4 Interpretation within 2HDM

The enlarged Higgs sector foreseen in Two-Higgs-Doublet models has a large number of free parameters, hence a several assumptions are needed to ease the interpretation of the limits. The benchmark "Scenario G" defined in [82] that realises an MSSM-like parameterisation is adopted. In addition, in this analysis, the mass degeneracy of the A and H bosons is assumed at tree-level, while the lightest CP-even scalar state m_h is fixed to 125 GeV. Thus, 2HDM models can be parameterised exclusively as a function of only three parameters at tree-level, namely $\tan\beta$, m_{A} and $\cos(\beta - \alpha)$. Three-dimensional scans of the parameter space have been obtained for the 2HDM cross-sections with the MSSM-like parameterisation in place as described in Section 1.2.8. The results are obtained in the

2HDM Type-II and flipped model, which exhibit the best sensitivity to the $b\bar{b}(\phi \to b\bar{b})$ process, owing to the large enhancement of the bottom Yukawa coupling with respect to the equivalent SM coupling.

The model-independent exclusion limits are translated in the $[\tan\beta, \cos(\beta-\alpha)]$ plane for several representative mass hypotheses, i.e. $m_{\mathrm{A}} = 130$, 200 , 300, 500 GeV for the 2HDM Type-II and the flipped model, portrayed in Figures 5.6 and 5.7, respectively. These limits mirror the fact the $A/H \to b\bar{b}$ is the prevailing decay mode for low pseudoscalar mass below 300 GeV in the central region of $|\cos(\beta-\alpha)|$ in both models, as shown in Figure 1.7. The increased competition from the kinematically allowed bosonic decays $A \to Zh$ and $H \to hh$ at large values of $|\cos(\beta-\alpha)|$ is responsible for the lower sensitivity of the $b\bar{b}$ channel in this region. This effect is particularly prominent for the signal mass-points with a higher value of $m_{\mathrm{A/H}}$ since the coupling to bosons is enhanced for larger Higgs boson mass. The slight asymmetry in the shape of the limits propagates from the one in the H boson partial decay width against $\cos(\beta-\alpha)$, which is caused by the shift of the fermiophobic point with the CP-even mixing angle α.

It is instructive to compare these exclusion limits with the results obtained in the $A \to Zh$ search conducted at CMS [161]. The comparison is exemplified for the intermediate mass-point at 300 GeV, as illustrated in the left plots of Figure 5.8 for the 2HDM Type-II and flipped models, respectively. While the $A \to Zh$ decay channel excludes the region $|\cos(\beta-\alpha)| \gtrsim 0.2$, this analysis achieves unique sensitivity in the phenomenologically viable central $\cos(\beta-\alpha)$ region. This alignment region is of particular interest since the couplings of the lightest scalar in the BSM model coincide with the expected ones of the SM Higgs boson. These results complement and extend in a unique way the indirect constraints on the $[\tan\beta, \cos(\beta-\alpha)]$ plane of the 2HDM Type-II and flipped model from the combined h(125) coupling measurements [47], by probing the exact alignment limit at intermediate tanβ values. The right plots in Figure 5.8, obtained by fixing $\cos(\beta-\alpha) = 0.1$, highlight the excluded $m_{\mathrm{A/H}}$ region for the mass range comprised between 125 and 700 GeV. The probed signal mass-points extend well below the lower bound of $m_{\mathrm{A}} = 400$ GeV accessible in the $A \to ZH$ search, owing to the lower jet p_{T} trigger thresholds used in this work. These upper limits further complement the exclusion contours obtained in the other channel at low and intermediate values of tanβ.

Due to the similar cross-section times branching fractions of the Higgs boson in the flipped and type-II models, a similar sensitivity to the $A/H \to b\bar{b}$ process is achieved. However, in the flipped model the exclusion limits are even more stringent due to the suppression of the second most relevant fermionic decay channel, the $\tau^+\tau^-$ channel, by a factor $\tan^4\beta$ with respect to the dominant $b\bar{b}$ decay mode. For this reason, the present analysis currently provides unique constraints at LHC of the flipped model in the vicinity of the alignment limit for Higgs boson masses below 300 GeV.

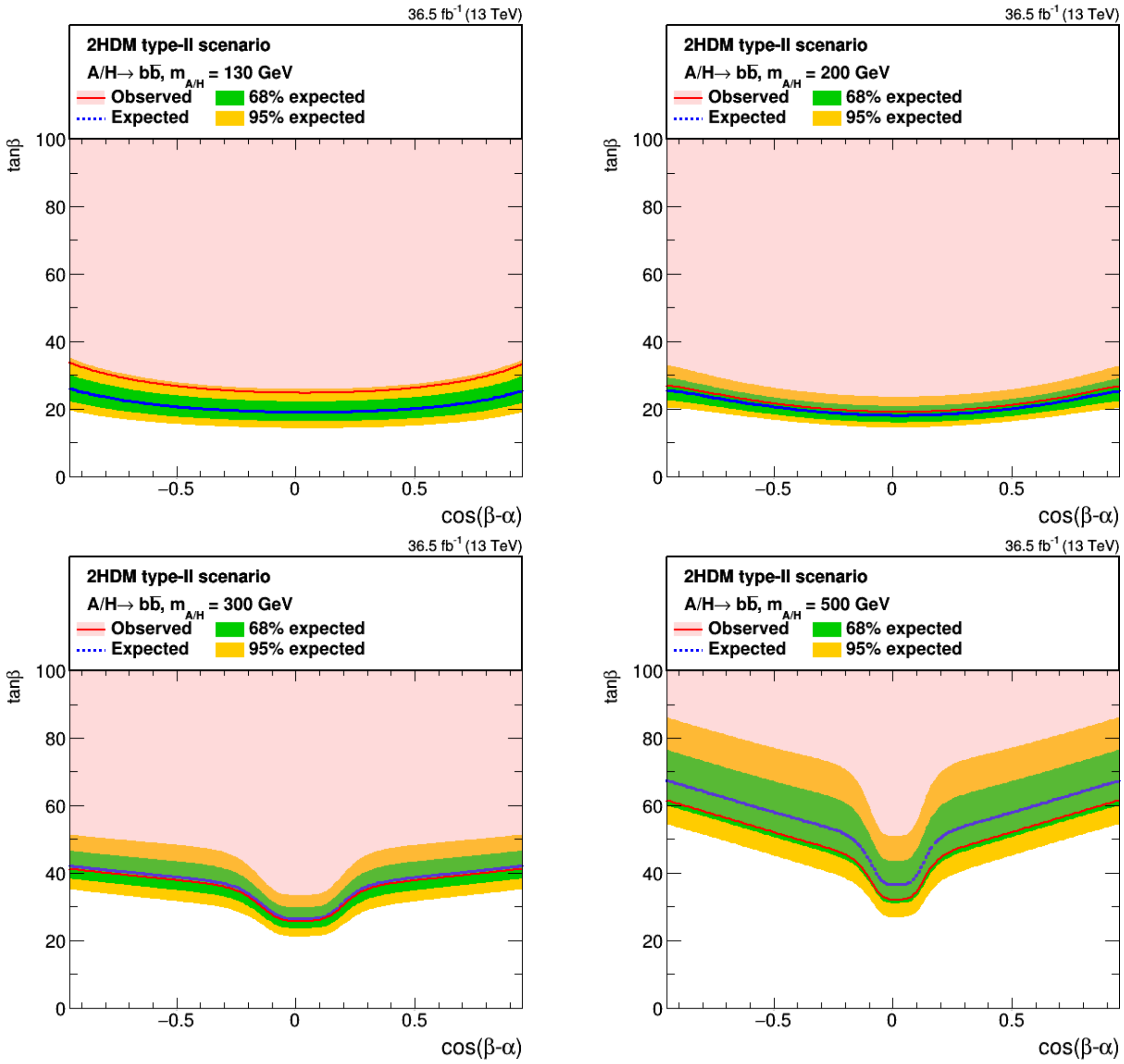

Figure 5.6: Upper limits for the parameter $tan\beta$ at 95% confidence level as a function of $cos(\beta - \alpha)$ for mass values of $m_{H/A}$ = 130,200,300 and 500 GeV in the 2HDM type-II model.

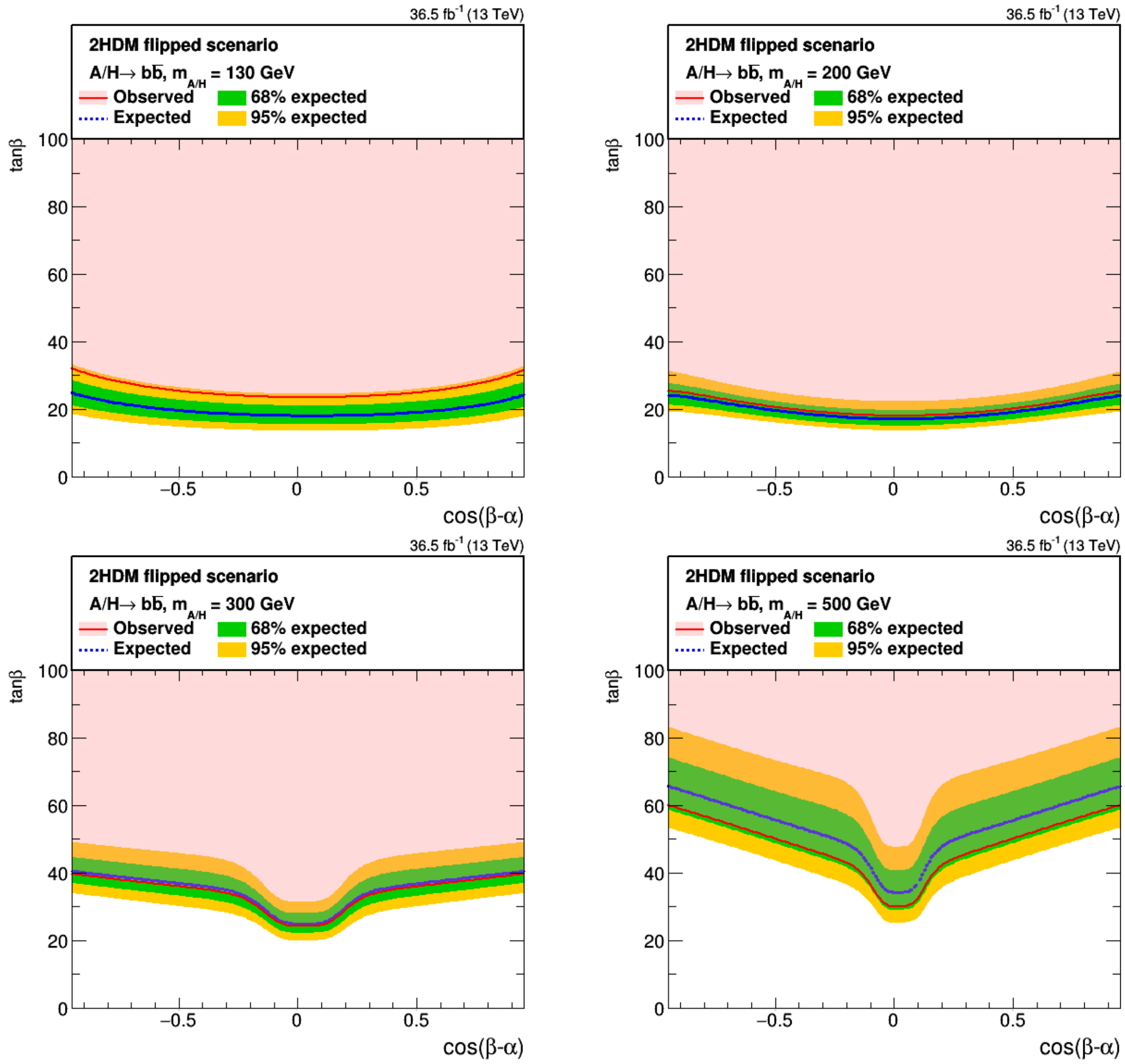

Figure 5.7: Upper limits for the parameter $tan\beta$ at 95% confidence level as a function of $cos(\beta - \alpha)$ for mass $m_{H/A}$ = 130,200,300 and 500 GeV in the flipped model.

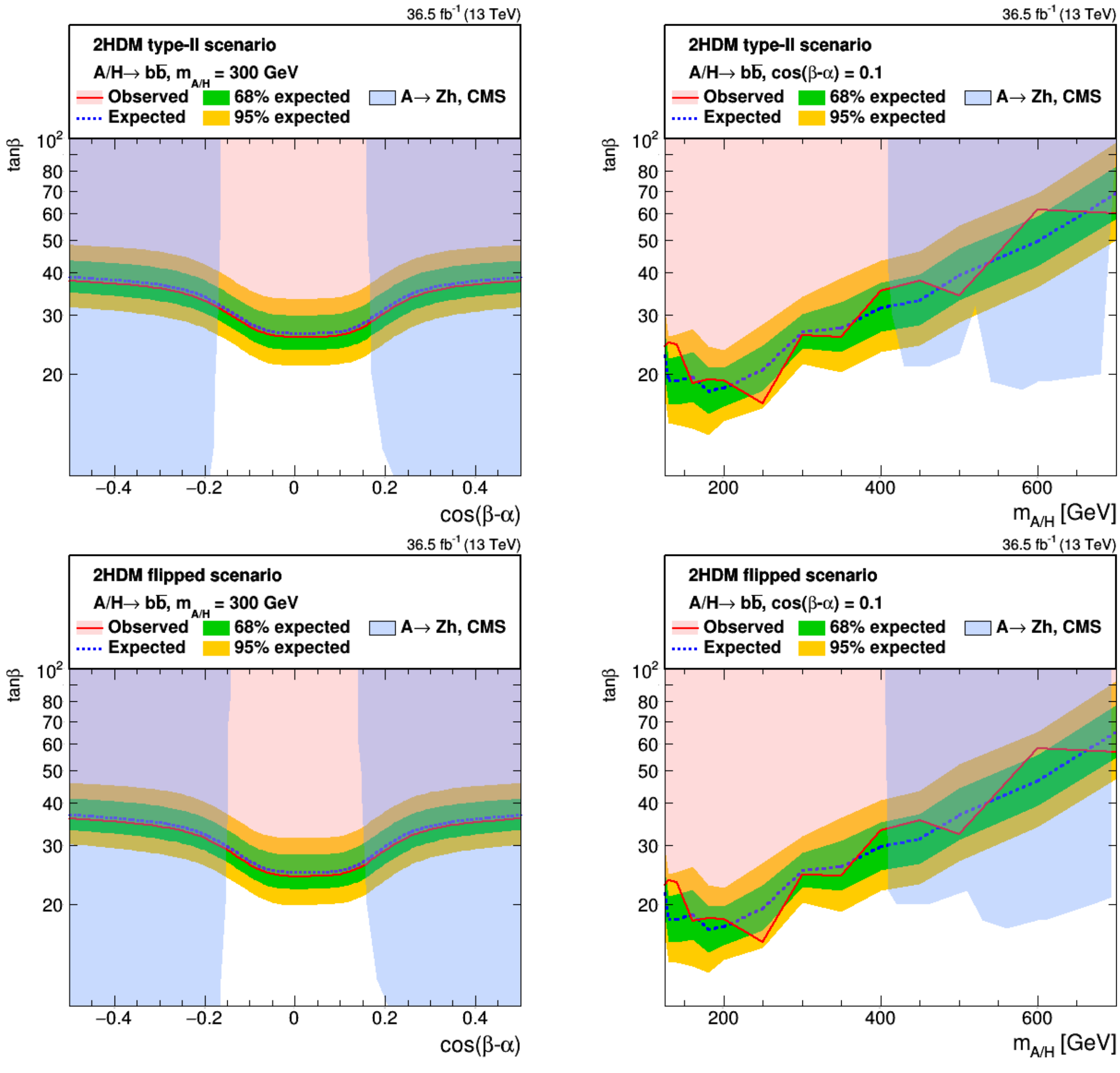

Figure 5.8: Upper limits for the parameter $tan\beta$ at 95% confidence level as a function of $cos(\beta-\alpha)$ for mass $m_{\mathrm{A/H}}$ = 130,200,300 and 500 GeV in the 2HDM type-II (top row) and flipped (bottom row) model.

CHAPTER 6

Summary and Outlook

Several theoretical models comprise an enlarged Higgs sector, such as the Two-Higgs-Doublet Model (2HDM) and the Minimal Supersymmetric Extension of the Standard Model (MSSM). These models predict the existence of additional neutral Higgs bosons, which can be produced at the Large Hadron Collider (LHC), and may be observed by the general purpose detectors, the Compact Muon Solenoid (CMS) and the Toroidal LHC ApparatuS (ATLAS). In a proton-proton collider, the main production mechanisms for such Higgs bosons are gluon-gluon fusion, vector boson fusion, and associated production with either a vector boson or with heavy-flavour quarks. The additional neutral Higgs bosons foreseen in these models decay predominantly into a b-quark pair in a large region of the parameter space.

In this work, Beyond Standard Model (BSM) scenarios in which the bottom Yukawa coupling is enhanced with respect to the Standard Model prediction are studied extensively. The selected production mechanism for the neutral Higgs boson is the b-quark associated production, since it is accompanied by reduced background of multi-jet events. A search for neutral Higgs bosons produced in final states with b-quarks in the semi-leptonic channel using the CMS Run 2 data at a center-of-mass-energy of 13 TeV is presented. This analysis utilises the data collected with the CMS detector in 2017 during proton-proton collisions corresponding to a total luminosity of 36.5 fb^{-1}. The introduction of the semi-leptonic search category at 13 TeV allows extending the sensitivity reach of the search to low Higgs boson masses and complement the full-hadronic category at higher overlapping masses. The excellent performance of the CMS detector in b-tagging and muon reconstruction permits probing a large range of Higgs boson masses. A dedicated semi-leptonic trigger has been implemented, enforcing a double b-jet selection and requiring the presence of a muon within any of the two most energetic b-tagged jets. The muon selection allows triggering on leading jets with softer p_T spectra, which decreases the overall rate by an order of magnitude. The signature of the process, which defines the signal region, is the presence of at least three well-separated, b-tagged jets in the event. The two most energetic ones are identified as the Higgs boson decay products, and they are further categorised on the basis of presence of the selected muon within the jet cone. The third leading jet in transverse momentum is instead regarded as the spectator jet. The signal model is based on fifteen signal samples with next-to-leading order accuracy, simulated with the Monte Carlo generator MADGRAPH5_aMC@NLO. The dominant background source is constituted almost exclusively by the huge QCD multi-jet production. Such background processes involve multiple b-quarks in the final state, and potentially also light-flavoured partons initiating jets that are mis-identified as b-jets. The background model is derived in a fully data-driven way in a signal depleted control region with similar background shape as in the signal region. The control region is obtained by reverting the loose b-tagging requirement on the third leading jet. BSM signal is searched for as an excess in data in the invariant di-jet mass of the two leading b-tagged jets in the signal region.

Since no significant excess over the Standard Model background is observed, upper limits on the overall production rate of the signal process are derived. The observed upper limits at 95 % confidence level cover a range of the cross-section times branching ratio between 541 pb at a Higgs boson mass of 125 GeV, down to 2.54 pb at a mass of 700 GeV. This work extends significantly the sensitivity of this BSM search for neutral Higgs bosons to $m_{\mathrm{A/H}}$ below 300 GeV due to the lower kinematic trigger thresholds applied to the di-jet system. These model-independent limits are further converted into exclusion contours within the parameter space of several MSSM and 2HDM benchmark scenarios. In the former case, the exclusion limits are derived in the $[\tan\beta, m_{\mathrm{A}}]$ plane in the $m_{\mathrm{h}}^{\mathrm{mod+}}$ and hMSSM models respectively. In the first scenario, the observed exclusion limits span tanβ values from a minimum around 18 at 250 GeV to approximately 56 at 500 GeV. These limits achieve similar or better sensitivity exploiting only one search channel than the combination of the Run 1 measurements, performed at center-of mass-energies of 7 and 8 TeV. In the hMSSM scenario, incorporating current constraints from negative searches of supersymmetric particles, the resulting exclusion limits achieve even better sensitivity, due to the suppression of competing decays of the Higgs boson into light SUSY particles. These results also complement the indirect constraints from SM Higgs boson measurement by extending the excluded region to $\tan\beta \gtrsim 20$ at low masses. Within the scope of 2HDM models, the exclusion limits are obtained in the 2HDM Type-II and the flipped model, which predict a substantial enhancement in the overall rate of the process of interest. In both cases, these results exclude a large portion of the 2HDM parameter space. In the vicinity of the alignment limit, they currently provide the most stringent constraints at LHC on the flipped model for Higgs bosons with masses below 300 GeV. This important phenomenologically viable region, not constrained by SM Higgs boson measumerements, is excluded for low pseudoscalar masses at intermediate tanβ values. All the results presented throughout this work have been endorsed by the CMS collaboration.

To conclude, the introduction of the semi-leptonic channel extends the sensitivity of this search to low Higgs boson masses and complements it at higher mass values. Furthermore, the combination with the 2018 data collected with the semi-leptonic trigger will allow improving the statistical power of the analysis. As a closing remark, this approach exploiting a dedicated semi-leptonic trigger could prove essential in the upcoming LHC search programme in the high-luminosity regime to investigate further the possible existence of an extended Higgs sector.

APPENDIX A

The $\boldsymbol{B}(A/H \to b\bar{b})$ in the 2HDM

The predicted branching fraction $B(A/H \to b\bar{b})$ in the 2HDM Type-II an flipped model for the representative signal mass-points at 125 and 500 GeV and for two values of $\tan\beta = 10; 60$ illustrated in Figures A.1 to A.4. The values of the 2HDM decay modes have been computed with next-to-next-to-leading order precision utilising the software package 2HDMC v. 1.7.0 [84].

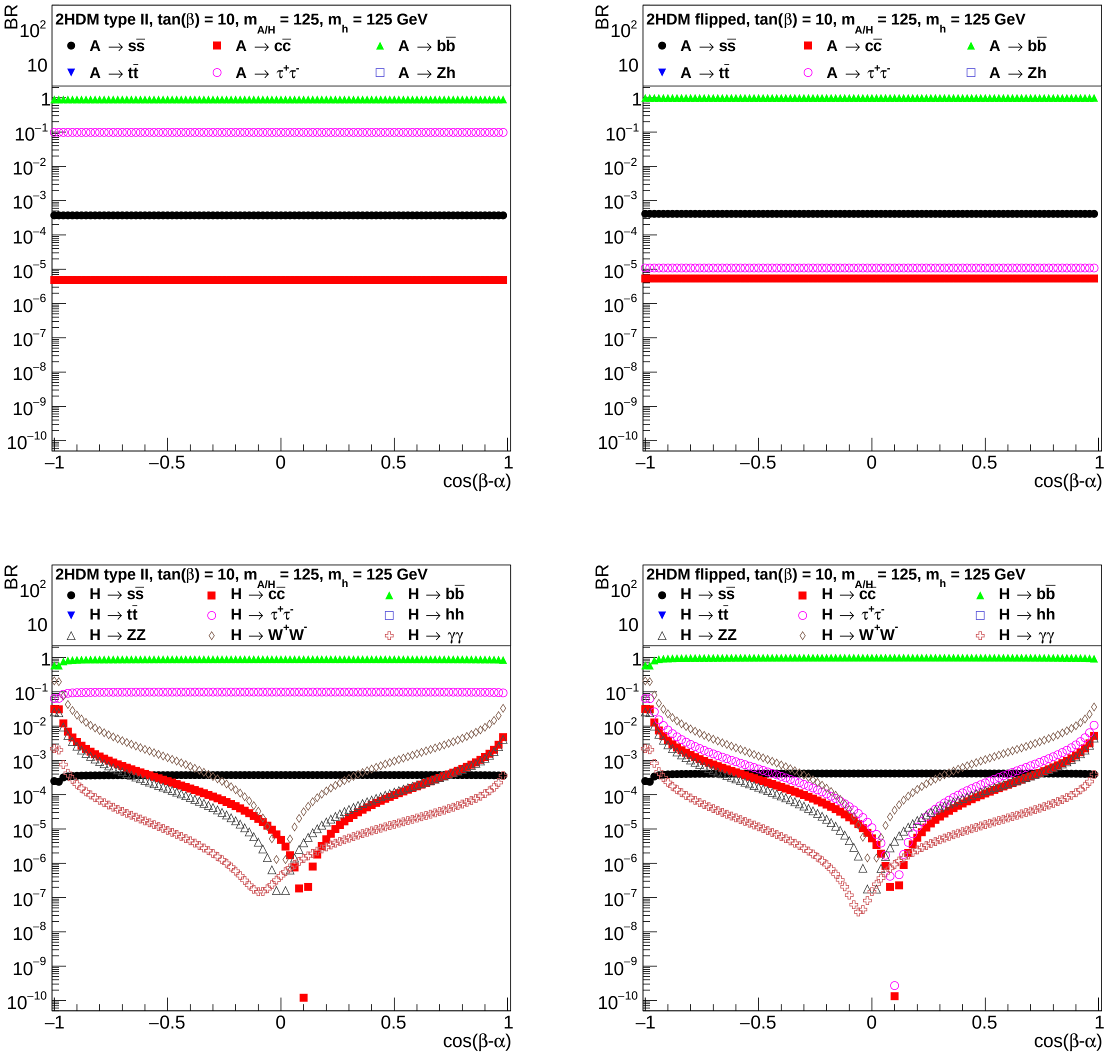

Figure A.1: Branching fractions of the CP-odd A boson (top row) and of the CP-even H boson (bottom row) computed in the type II 2HDM (left column) and in the flipped model (right column) as a function of $\cos(\beta-\alpha)$ for the benchmark masspoint $m_{\mathrm{A/H}} = 125$ GeV at a low value of $\tan\beta = 10$.

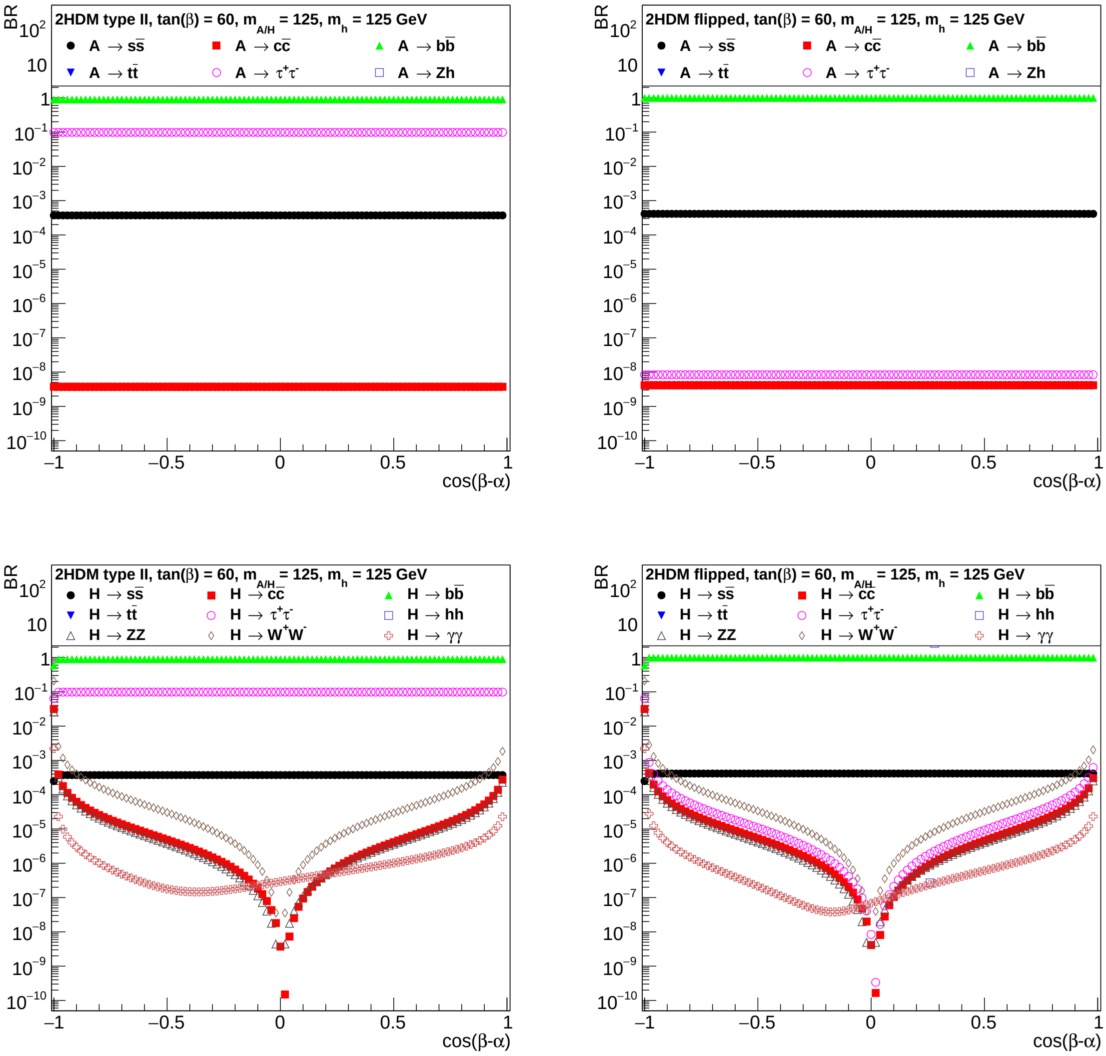

Figure A.2: Branching fractions of the CP-odd A boson (top row) and of the CP-even H boson (bottom row) computed in the type II 2HDM (left column) and in the flipped model (right column) as a function of $\cos(\beta-\alpha)$ for the benchmark masspoint $m_{\mathrm{A/H}} = 125$ GeV at a large value of $\tan\beta = 60$.

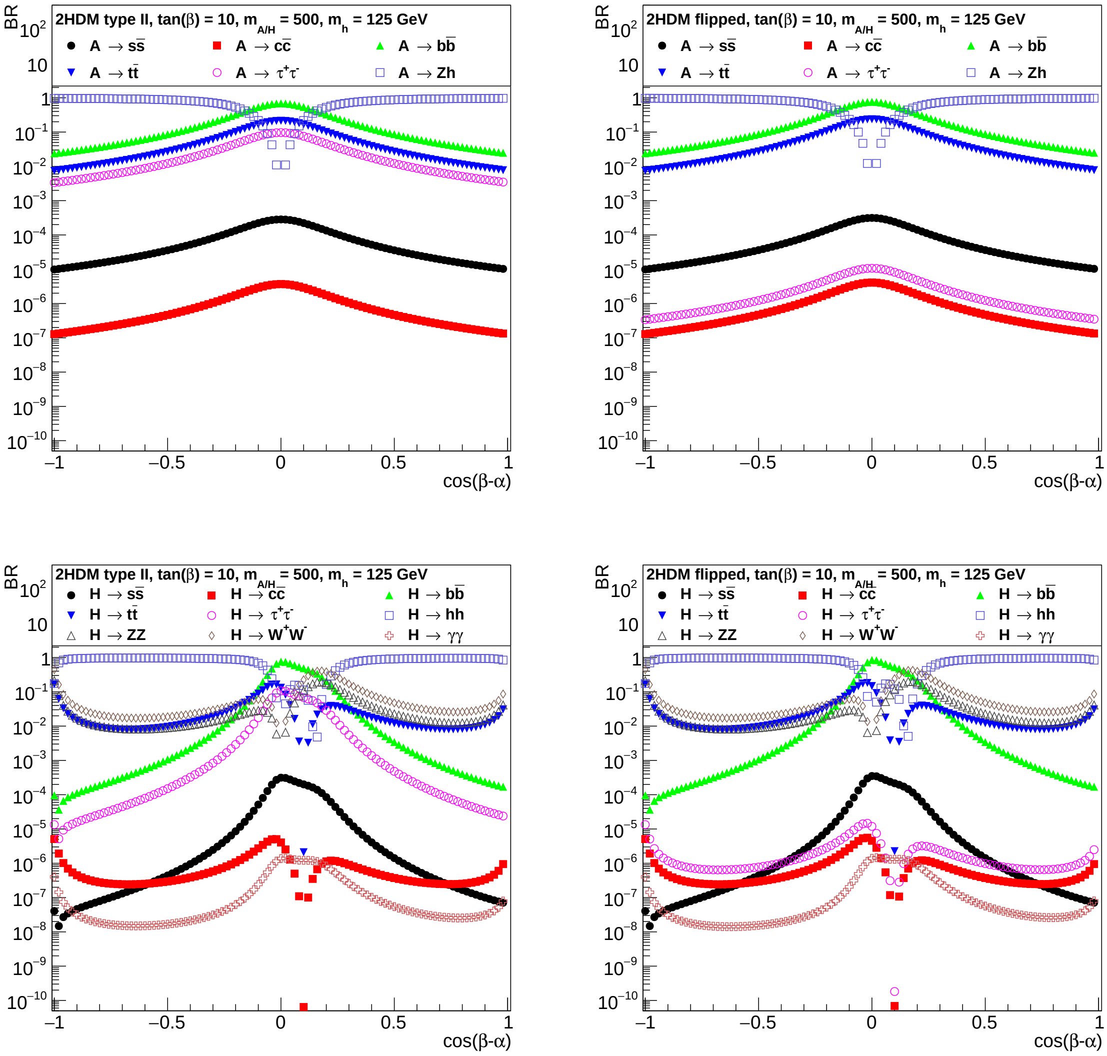

Figure A.3: Branching fractions of the CP-odd A boson (top row) and of the CP-even H boson (bottom row) computed in the type II 2HDM (left column) and in the flipped model (right column) as a function of $\cos(\beta - \alpha)$ for the benchmark masspoint $m_{\mathrm{A/H}} = 500$ GeV at a low value of $\tan\beta = 10$.

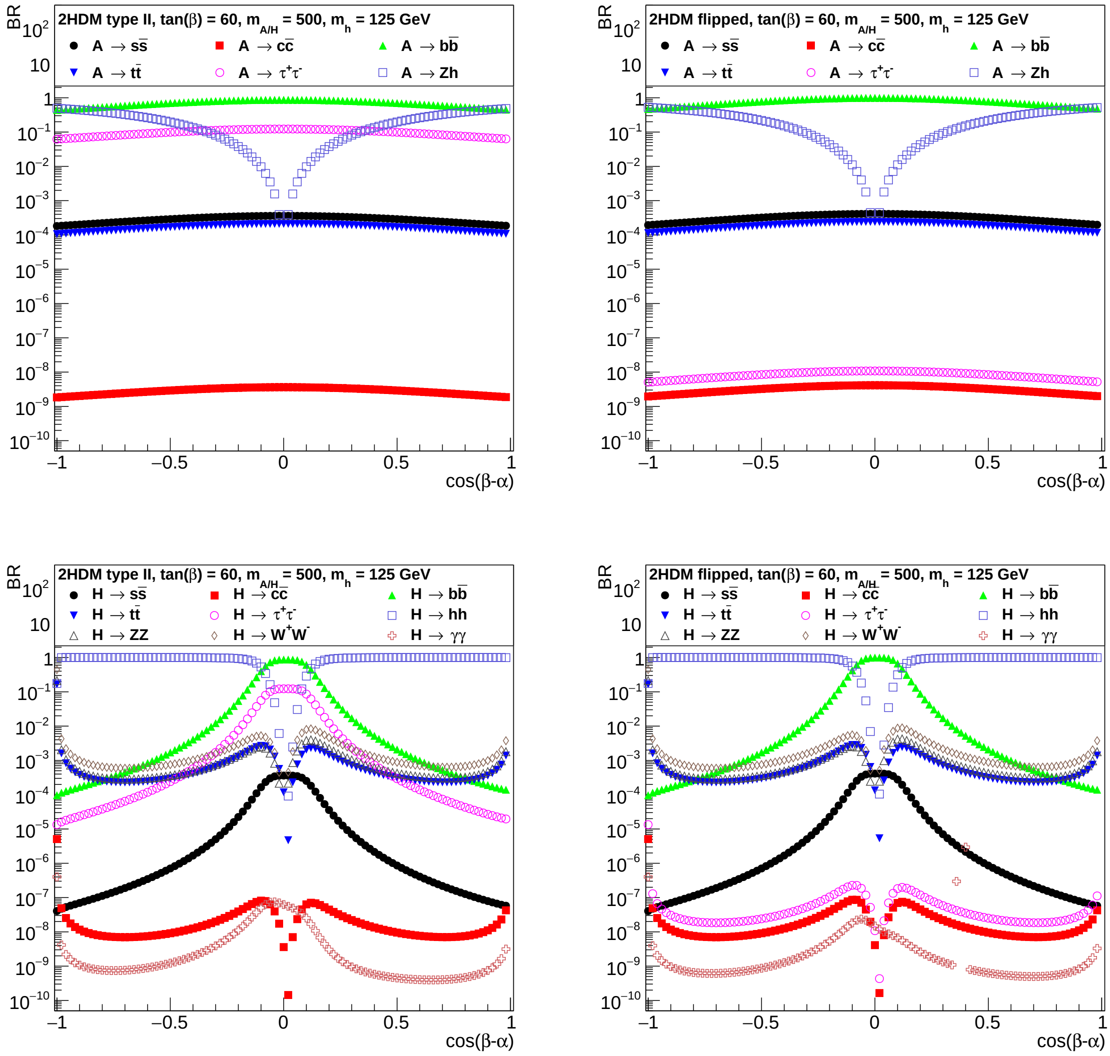

Figure A.4: Branching fractions of the CP-odd A boson (top row) and of the CP-even H boson (bottom row) computed in the type II 2HDM (left column) and in the flipped model (right column) as a function of $\cos(\beta - \alpha)$ for the benchmark masspoint $m_{\mathrm{A/H}} = 500$ GeV at a large value of $\tan \beta = 60$.

APPENDIX B

Trigger study

B.1 L1 rate study

The main semi-leptonic trigger for this analysis was deployed for the first time in the 2017 global trigger menu. Therefore, the corresponding L1 seed had to be emulated in both data and Monte Carlo samples to perform feasibility studies on the expected output rate. A 2016 data sample was obtained with a *zero-bias* trigger used as a reference for the rate measurement. This trigger is activated by simultaneous signals detected in the same bunch crossing by two different beam position monitors. Its rate is kept constant by adjusting the prescale during data-taking according to the instantaneous luminosity. In data, the Level-1 rate of the analysis trigger can be factorised as the product of the selection efficiency ϵ_{L1} of the events passing the L1 requirements and the rate $rate_{ZB}$ of the reference trigger, viz:

$$rate_{L1,data} = \epsilon_{L1} \times rate_{ZB}. \tag{B.1}$$

In simulation, the L1 seed was emulated using the same QCD muon-enriched samples listed in Table 4.3, albeit with the 2016 legacy pixel geometry. The samples with a p_T-bin range between 30 and 170 GeV yield sufficient statistics after the kinematic selection applied at Level-1. The partial trigger rates are obtained in simulation for each p_T bin as follows:

$$(rate_{L1,MC})_i = f_{BX}(1 - e^{-\mu_i \epsilon_{L1,i}}), \tag{B.2}$$

where μ_i is the mean number of pile-up interactions per bunch crossing (BX) for each p_T bin and f_{BX} is the frequency per bunch crossing. The total rate in simulation is then simply computed as the sum:

$$rate_{L1,MC} = \sum_{i=1}^{p_T\ bins} (rate_{L1,MC})_i, \tag{B.3}$$

where the error in the rate is purely statistical. The aim of the study was to keep the expected Level-1 rate below the 5kHz threshold at the value of peak instantaneous luminosity foreseen during 2017 data-taking, i.e. $\mathscr{L} = 2 \times 10^{34}$ cm^{-2} s^{-1}. The latter corresponds under optimal LHC operating conditions to a high pile-up regime corresponding to a mean number of inelastic pp collisions of $\langle\mu\rangle = 56$. The dependence of the L1 rate on the number of pile-up interactions is well-modelled by a parabolic fit both in data and Monte Carlo, as illustrated in Figure B.1. The output Level-1 rate was found to be over a factor ~ 2 larger in simulation than in 2016 data. Following a conservative approach, tight p_T thresholds have been chosen for all Level-1 trigger objects. A final transverse momentum cut of 12 (40) GeV is applied to the muon (di-jet system), from the initial proposal p_{T} thresholds of 10 and 32 GeV, respectively.

B.2 HLT timing study

The large Level-1 input rate, of the order of several kHz, and the available computing resources of HLT farm represent important constraints to the processing time accessible at the high-level trigger [162]. Surpassing this timing threshold for any analysis trigger would imply lowering the overall data-taking efficiency of the experiment. Therefore, it is crucial to determine the HLT timing performance prior to the inclusion of the analysis trigger in the global trigger menu utilised during the data-taking. Since the HLT farm consists of several machines with various hardware architectures and different manufacturers, such timing tests must be carried out running individual tasks on a single core of a specific machine. This precaution is needed in order to avoid performing these measurements under the Hyperthreading mode[1], which would bias the timing results. The timing studies are realised with the "FastTimerSequence" software [163], which measures simultaneously two relevant quantities:

1. the *total real timing* for the target HLT sequence;
2. the mean processing time spent in each module of the offline CMS reconstruction software (CMSSW).

The FastTimerService performs both steps with just a few ms latency time, hence its impact on the actual timing measurement is negligible. Each analysis trigger must fulfill two main conditions in order to be included in the global trigger menu; the mean total real timing must not exceed 10 ms and the average computing time spent in a specific CMSSW module should be lower than 100 ms. The timing study was performed using a skimmed Monte Carlo Neutrino Gun sample with approximately 20,000 events simulated in a very high pile-up environment, i.e. $\langle\mu\rangle \sim 56$. The main semi-leptonic trigger of this

[1]A simultaneous multi-threading of a computational task resulting in its parallelisation on several cores.

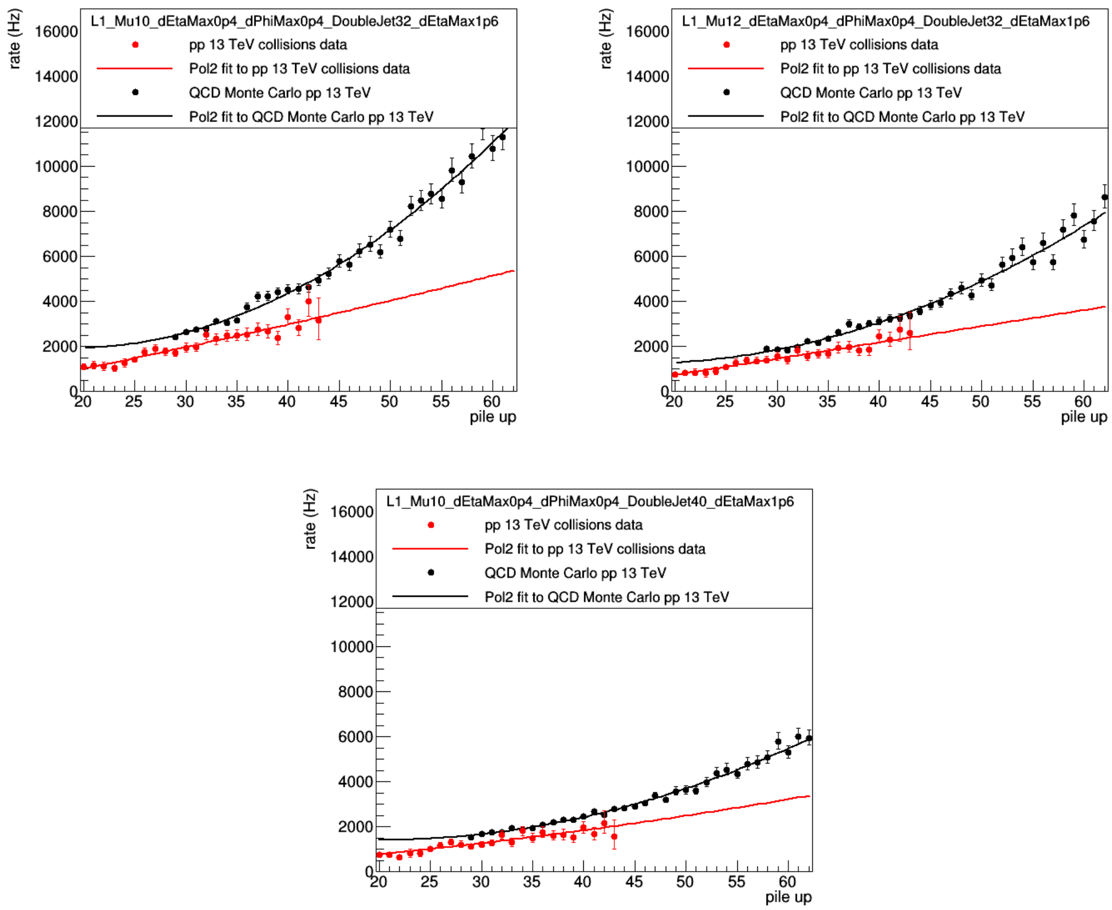

Figure B.1: L1 rate dependence versus the mean number of pile-up interactions in a zero-bias data sample (red) and in a QCD sample (black) modelled with a parabolic fit with different kinematic cuts for the muon $p_T^{(\mu)} > 10; 12$ GeV and for the di-jet system $p_T^{(1,2)} > 32; 40$ GeV.

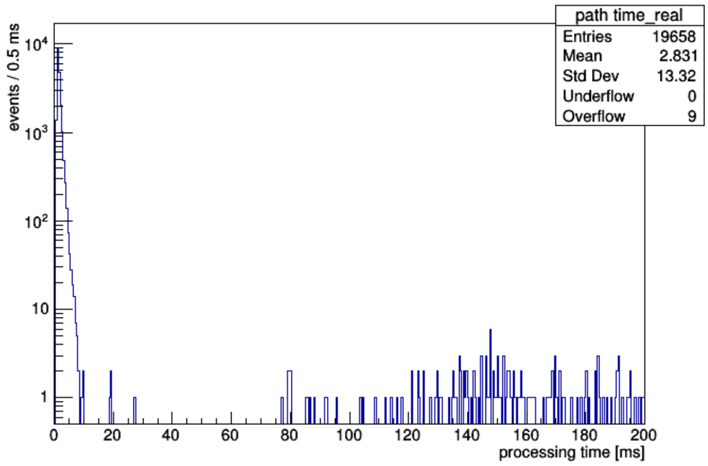

Figure B.2: Processing time for the HLT sequence of the main semi-leptonic trigger used in the analysis simulated in a neutrino gun sample of 20,000 events. The peak region from 0 to 27 ms correspond to signal events failing to meet the L1 requirement, while the tail region contains signal events passing the more complex algorithms in the HLT reconstruction sequence, namely online b-tagging and particle-flow.

analysis meets the first timing condition as illustrated in Figure B.2, since its mean total timing is approximately 2.8 ms. The computing time required for the particle-flow (PF) modules can exceed the threshold of 100 ms, as shown in the tail of the mean timing distribution. However, on average only one event in a thousand passes all the preceding sequential steps, resulting in a negligible impact of the PF modules on the overall mean timing of the trigger.

APPENDIX C

Exclusion limits

The upper limits on $\sigma(pp \to bA/H + X)B(A/H \to b\bar{b})$ listed in Table 5.3 have been translated into the exclusion contours of the MSSM parameter tanβ and m_{A} space for the hMSSM and the $m_{\mathrm{h}}^{\mathrm{mod+}}$ benchmark scenarios, illustrated in Table C.1 and C.2, respectively.

Mass [GeV]	-2σ	-1σ	Median	$+1\sigma$	$+2\sigma$	Observed
130	17.4	19.5	22.2	25.2	28.8	27.7
140	15.2	17.2	20.0	23.4	27.1	25.3
160	14.3	17.0	20.1	23.9	27.9	19.3
180	13.6	15.6	18.3	21.5	24.7	19.6
200	14.9	16.4	18.6	21.3	24.1	19.6
250	16.1	18.1	21.1	24.8	28.7	16.6
300	21.7	24.3	27.2	30.7	34.4	26.5
350	20.3	23.5	27.7	33.0	38.6	26.0
400	23.2	26.7	31.4	37.0	42.9	35.0
450	24.0	27.6	32.6	38.6	45.0	37.0
500	29.1	33.7	39.8	47.4	55.5	43.5
600	33.8	39.0	45.8	54.3	—	56.6
700	44.7	51.6	—	—	—	53.5

Table C.1: Expected and observed upper limits at 95% C.L. in the tanβ– m_{A} parameter space of the hMSSM benchmark scenario. Due to the limited range of the validity of the model predictions to tanβ values below 60, upper limits exceeding this value are omitted. The mass of the lightest CP-even scalar state is set to 125 GeV in the model for consistency with the observed h(125) boson properties, and the corresponding mass-point is disregarded.

Mass [GeV]	-2σ	-1σ	Median	$+1\sigma$	$+2\sigma$	Observed
130	17.2	19.6	23.0	26.8	31.3	29.9
140	15.9	18.3	21.6	25.6	30.1	27.9
160	15.1	18.2	21.7	26.1	31.1	20.8
180	14.4	16.6	19.6	23.3	27.2	21.2
200	15.9	17.6	20.1	23.3	26.6	21.2
250	17.6	19.9	23.3	27.6	32.4	18.2
300	24.8	27.7	31.2	35.5	40.2	30.3
350	24.6	28.2	33.1	39.6	46.9	31.1
400	28.7	32.7	38.3	45.5	53.5	42.9
450	30.8	35.0	41.1	48.8	57.6	46.6
500	37.7	43.4	51.4	—	—	56.4
600	45.3	51.9	—	—	—	—

Table C.2: Expected and observed upper limits at 95% C.L. in the tanβ– m_{A} parameter space of the $m_{\mathrm{h}}^{\mathrm{mod+}}$ benchmark scenario with Higgsino mass parameter$\mu = +200\ GeV$. Due to the limited range of the validity of the model predictions to tanβ values below 60, upper limits exceeding this value are omitted. The mass of the lightest CP-even scalar state is set to 125 GeV model for consistency with the observed h(125) boson properties, and the corresponding mass-point is disregarded.

APPENDIX D

Searches for BSM neutral Higgs bosons in fermionic decays at CMS

In this section, an overview of the main direct searches for BSM neutral Higgs bosons in fermionic decays conducted at CMS using Run 2 data published in [164] is presented. The first part of this review focuses on high-mass Higgs boson resonant searches interpreted within the Two-Higgs-Doublet Model (2HDM) and the Minimal Supersymmetric Standard Model (MSSM) extension. The second part summarises the searches for light pseudoscalars stemming from SM-like Higgs bosons with four fermions in the final state. The existence of these additional states is foreseen in the Next-to Minimal Supersymmetric Standard Model (NMSSM).

PROCEEDINGS OF SCIENCE

Searches for BSM (neutral) Higgs bosons in fermionic decays in CMS

Antonio Vagnerini [1] on behalf of the CMS Collaboration
Affiliation: DESY, Hamburg, Germany
mail: antonio.vagnerini@cern.ch

Abstract: An overview of neutral BSM direct Higgs searches in fermionic decays performed at CMS was presented. The first part focuses on BSM Higgs resonant searches interpreted within the Higgs-Two-Doublet Model (H2DM) framework and in particular the Minimal Supersymmetric Standard Model (MSSM). The second part illustrates the searches for NMSSM light pseudoscalars stemming from SM-like Higgs bosons with four fermions in the final state.

Prospects for Charged Higgs Discovery at Colliders - CHARGED2018
25-28 September 2018
Uppsala, Sweden

[1]Speaker

PoS(CHARGED2018)011

1. Introduction

The Standard Model (SM) of particle physics is one of the most successful theories in the history of physics. However, it suffers from several limitations, notably the inability to provide a solution to the hierarchy problem and a theoretical framework describing the presence of dark matter. The LHC discovery of a Standard-Model-like Higgs H(125) particle in 2012 [1] could be a portal to an extended Higgs sector predicted by several models, such as the Minimal-Supersymmetric Standard Model (MSSM) [2] and the more general Two-Higgs-Doublet Model (2HDM) [3]. The phenomenology of such models can be further enriched by addition of a single scalar gauge in singlet, as in the Next-to-Minimal SuperSymmetric model (NMSSM) [4]. The combination of data collected at 13 TeV with the CMS detector [5] in searches for Higgs decays into invisible constrains the branching fraction BR($H \rightarrow$ inv) to less than 0.26 at 95% CL [6]. Therefore, there is still room for additional Higgs bosons, which are the object of direct BSM Higgs searches. These searches complement the results from indirect constraints on 2HDM from H(125) coupling measurements [7] and rare B-meson decays [8]. In this paper, we shall focus on the most recent neutral BSM Higgs searches in fermionic decays performed at CMS in pp collisions at 13 TeV. These resonant Higgs searches are usually categorized according to the mass range probed and the subsequent theoretical model of interest, which are outlined in the next section. In Section 3, heavy Higgs resonant searches in fermionic decays are interpreted in the light of the 2HDM models. In section 4, the SM-like Higgs decays into light pseudoscalars predicted in the NMSSM with four fermions in the final state are discussed.

2. Theoretical models

The most natural extension of the Standard Model scalar sector is the addition of an extra $SU(2)_L$ doublet. The 2HDM is an effective theory consisting of two complex Higgs doublets (hence with a total of 8 degrees of freedom), which provide masses to both the up-type and the down-type fermions. After electroweak symmetry breaking (EWSB) , there are five physical scalar fields, consisting of neutral bosons φ = h,H,A of which the first two bosons are CP-even, opposed to the A-boson which is CP-odd and of two charged Higgs states $H^{\pm}$. The model is parameterized by the five Higgs masses, $\tan\beta = v_2/v_1$, the ratio of the vacuum expectation values of the two Higgs doublets, and the mixing angle α between the CP-even Higgs states.

In this paper, we focus on searches involving the neutral Higgs bosons only. There exist four types of 2HDM which simultaneously forbid the presence of flavour-changing-neutral currents (FCNC) and preserve CP symmetry:

- In Type I all fermions couple to the second doublet Φ_2. It follows that BR are independent of $\tan\beta$.
- In Type II or MSSM-like scenario, lepton and down-type quarks couple to the first doublet Φ_1, whilst up-type quarks couple to Φ_2 .

- In Type III or lepton specific scenario, quarks couple to Φ_2 while leptons couple to the other doublet.
- In Type IV or flipped model, the coupling of the leptons is reversed with respect to the Type-II model.

The MSSM Higgs sector possesses the same underlying structure as 2HDM Type II but it is described solely by two parameters at tree-level: tanβ and m_{A}. Several benchmark scenarios with different phase space properties have been designed. The results presented in the next section make use of the MSSM m_h^{mod+} scenario, where the mass of the lightest CP-even Higgs state is compatible with H(125) in a large region of the tanβ-m_A plane, and the phenomenological hMSSM scenarios incorporating the observed Higgs boson mass with a fixed mass value of 125 GeV. The NMSSM is a particular case of the 2HDM+S type II representing a viable solution to the μ-problem [4]. The addition of an electroweak singlet S allows to generate dynamically the μ-term in the superpotential $\mu H_u H_d$. After EWSB, due to the additional gauge singlet there are two extra Higgs states, one pseudoscalar a_1 which can be very light and an additional SM-like CP-even state h_1.

3. Heavy Higgs searches : $A/H \rightarrow f\bar{f}$

In this section, we present the most recent Run II results of additional heavy Higgs searches in fermionic decays, with a particular emphasis on 3rd generation fermions particular $h/A/H \rightarrow \tau^+\tau^-$ [9], $b\bar{b}(A/H \rightarrow b\bar{b})$ [10], and also $t\bar{t}(A/H \rightarrow t\bar{t})$ [11]. In the 2HDM type-II model, the cross-section of $\sigma(A/H \rightarrow ff)$ is enhanced for tanβ<1 for the $t\bar{t}$ final state, and for large tanβ in the $b\bar{b}$ and $\tau^+\tau^-$ final states. All three searches have an event categorization based on the number of b-tagged jets and on the Higgs production mechanism. In the $b\bar{b}(A/H \rightarrow b\bar{b})$ search, the production mechanism probed is the b-associate production and at least three b-tagged jets are required in the final state. In the ττ search, since b-associate production dominates at high tanβ while gluon-gluon fusion dominates at low tanβ, there are two separate categories per final state, b-tagged for ggF and non b-tagged jets for bbH. In the $A/H \rightarrow t\bar{t}$ analysis, the Higgs bosons produced in association with the top quarks namely, ttH, tHq and tWH, and decaying to a top quark are included. The key signature is the presence of same-sign dileptons which is a very rare process in the SM. No significant excess over standard model background is observed in any of the model-independent exclusion limits of the above searches, see Figure 1. The most stringent exclusion limits coming from $A/H \rightarrow \tau^+\tau^-$ are translated into exclusion contours in the parameter space of MSSM m_h^{mod+} scenario (Fig. 2). An analogous MSSM-like parameterization is adopted to obtain the exclusion contours for the MSSM $A/H \rightarrow b\bar{b}$ search.

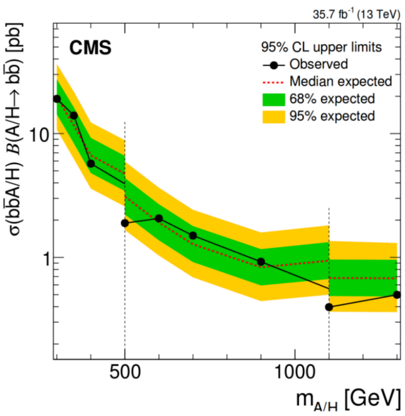

(a) $b\bar{b}(A/H \to b\bar{b})$

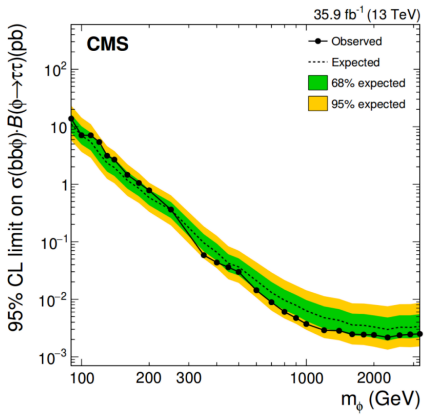

(b) $b\bar{b}(\Phi \to \tau^{+}\tau^{-})$

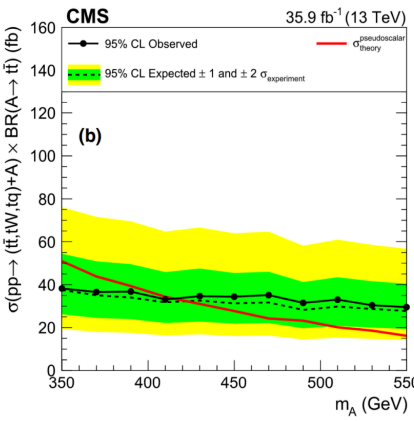

(c) $(t\bar{t},tW,tq)(A \to t\bar{t})$

Figure 1: Upper limits at 95% CL on $\sigma(b\bar{b}A/H)$ x BR($A/H \to b\bar{b}$) [10] (top left), on $\sigma(b\bar{b}\Phi)$ x BR($\Phi \to \tau^{+}\tau^{-}$) [9] (top right) and on σ(tt,tW,tq) x BR($A \to t\bar{t}$) [11] (bottom).

4. Light Higgs Searches: h → aa → 4f

In the NMSSM, the pseudoscalar a_1 boson is identified as the lightest Higgs state. Consequently, SM-like Higgs bosons are allowed to decay into two NMSSM pseudoscalars, which later decay into fermions. Because of the narrow width of the Standard Model Higgs, even a tiny Yukawa coupling Y_{haa} would lead to a measurable BR($h \to aa$) of the order of few percent. In this section, we present the most recent results for $h \to a_1 a_1 \to 2\mu 2\tau$ [12] and $h \to a_1 a_1 \to 2b2\tau$ [13] search channels with 4 (3) final states respectively. The non-boosted τ pair topology restricts the search region of the a-boson mass range 15< m_a < 62.5 GeV. The main observable used for the combined maximum likelihood fit for all final states are the di-muon $m_{\mu\mu}$ and di-tau invariant mass $m_{\tau\tau}$ respectively.

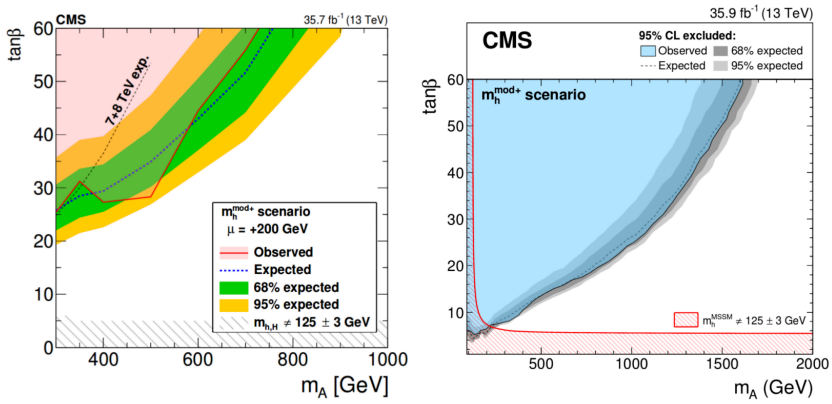

Figure 2: Exclusion contours for the $A/H \rightarrow b\bar{b}$ search [10] (left) and in the $\Phi \rightarrow \tau^+\tau^-$ search [9] (right) in the tanβ-m_A plane for the MSSM m_h^{mod+} benchmark scenario.

The upper limits on the σ_h/σ_{SM} BR($h \rightarrow aa \rightarrow 4f$) illustrated in Fig.3 are translated in exclusion contours of 2HDM+S type II an III. There is a significant improvement in exclusion limits in all 2HDM+S types with respect to Run I results. In the NMSSM BR($h \rightarrow aa$) > 23 % excluded at 95% CL for $m_a = 35$ GeV (see Fig 4.a). This limit was obtained in the $2\tau 2b$ final state probed for the first time at 13 TeV and represents, to date, the most sensitive result at the LHC. In the 2HDM Type III, the upper limits on BR($h \rightarrow aa \rightarrow 2\mu 2\tau$) shown in Fig4 are as low as 1% for m_a =60 GeV.

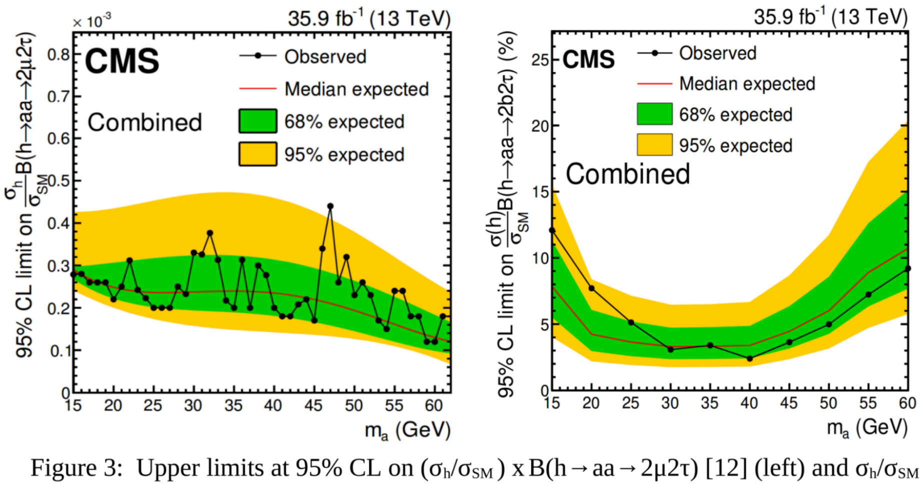

Figure 3: Upper limits at 95% CL on (σ_h/σ_{SM}) x B($h \rightarrow aa \rightarrow 2\mu 2\tau$) [12] (left) and σ_h/σ_{SM} B($h \rightarrow aa \rightarrow 2b2\tau$) [13] (right).

5. Conclusions

The observed Higgs boson at a mass of 125 GeV could be a portal to an extended Higgs sector. Searches for additional neutral Higgs bosons in fermionic decays were presented probing a mass range of $100 < m_\Phi < 1300$ GeV. The results of the searches for $h \rightarrow aa$ decays with four fermions in the final state for low masses $15 < m_a < 62.5$ GeV were also summarized. Since no significant excess was observed over the Standard-Model background, the model-independent limits were translated in exclusion contours in the parameter space of several 2HDM(+S) models.

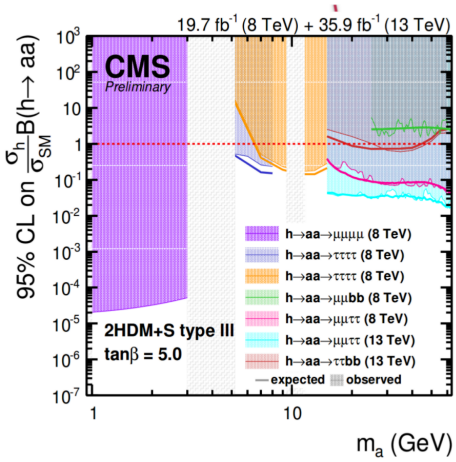

Figure 4: Exclusion limits on $\sigma_h/\sigma_{SM}\, B(h \rightarrow aa)$ in the 2HDM Type III for $\tan\beta = 5$. The upper limits on $B(h \rightarrow aa \rightarrow 2\tau 2b)$ as low as 1% for m_a = 60 GeV [14].

References

[1] CMS Collaboration, *Observation of a new boson at a mass of 125 GeV with the CMS experiment at the LHC,* Phys.Lett. B716 (2012) 30-61

[2] I. J. Aitchison, Supersymmetry and the MSSM: An Elementary Introduction, arXiv:hep-ph/0505105

[3] G. C. Branco et al., *Theory and phenomenology of two-Higgs-doublet models*, arXiv:1106.0034 [hep-ph]

[4] U. Ellwanger, *The Next-to-Minimal supersymmetric Standard Model*, Phys.Rept. 496 (2010) 1-77

[5] CMS Collaboration, *The CMS experiment at the CERN LHC,* JINST 3 S08004 (2008)

[6] CMS Collaboration, *Search for invisible decays of a Higgs boson produced through vector boson fusion in proton-proton collisions at* $\sqrt{s}$ *= 13 TeV, arXiv:1809.05937*

[7] CMS Collaboration, *Precise determination of the mass of the Higgs boson and tests of compatibility of its couplings with the standard model predictions using proton collisions at 7 and 8 TeV*, Eur.Phys.J. C75 (2015) no.5, 212

[8] M. Hussain et al., *Constraints on Two Higgs Doublet Model Parameters in the light of rare B-Decays, arXiv:1703.10845v2* [hep-ph]

[9] CMS Collaboration, *Search for additional neutral MSSM Higgs bosons in the* $\tau\tau$ *final state in proton-proton collisions at* $\sqrt{s}$ *= 13 TeV,* JHEP 1809 (2018) 007

[10] CMS Collaboration, *Search for beyond the standard model Higgs bosons decaying into a bb pair in pp collisions at* $\sqrt{s}$ *= 13 TeV,* JHEP 1808 (2018) 113

[11] CMS Collaboration, *Search for physics beyond the standard model in events with two leptons of same sign, missing transverse momentum, and jets in proton–proton collisions at* $\sqrt{s}$ *= 13 TeV,* Eur.Phys.J. C77 (2017) no.9, 578

[12] CMS Collaboration, *Search for an exotic decay of the Higgs boson to a pair of light pseudoscalars in the final state of two muons and two* τ *leptons in proton-proton collisions at* $\sqrt{s}$ *= 13 TeV, arXiv:1805.04865*

[13] CMS Collaboration, *Search for an exotic decay of the Higgs boson to a pair of light pseudoscalars in the final state with two b quarks and two* τ *leptons in proton-proton collisionst at* $\sqrt{s}$ *= 13 TeV,* Phys.Lett. B785 (2018) 462

[14] CMS Collaboration, *Search for an exotic decay of the Higgs boson to a pair of light pseudoscalars in the final state with two b quarks and two* τ *leptons in proton-proton collisionst at* $\sqrt{s}$ *= 13 TeV,* CMS PAS HIG-17-029

PoS(CHARGED2018)011

Bibliography

[1] G. Galilei, "The Assayer." *Discoveries and opinions of Galileo* (1957) 237–238.

[2] I. Newton, "Philosophiæ Naturalis Principia Mathematica." *England* (1687).

[3] J. C. Maxwell, "Electricity and magnetism." *Volume 2* (1954).

[4] S. L. Glashow, "Partial Symmetries of Weak Interactions." *Nucl. Phys.* **22** (1961) 579–588.

[5] S. Weinberg, "A Model of Leptons." *Phys. Rev. Lett.* **19** (1967) 1264–1266.

[6] A. Salam, "Weak and Electromagnetic Interactions." *Conf. Proc.* **C680519** (1968) 367–377.

[7] H. Fritzsch, M. Gell-Mann, and H. Leutwyler, "Advantages of the Color Octet Gluon Picture." *Phys. Lett.* **47B** (1973) 365–368.

[8] S. F. Novaes, "Standard model: An Introduction." in *Particles and fields. Proceedings, 10th Jorge Andre Swieca Summer School, Sao Paulo, Brazil, February 6-12, 1999*, pp. 5–102, 1999. `hep-ph/0001283`.

[9] W. J. Marciano and H. Pagels, "Quantum Chromodynamics: A Review." *Phys. Rept.* **36** (1978) 137.

[10] J. Mnich, "Overview of standard model results from lep and tevatron." *Czechoslov. J. Phys.* **54** (2004) A193–A205.

[11] CMS Collaboration, "Observation of a new boson at a mass of 125 GeV with the CMS experiment at the LHC." *Phys. Lett. B* **716** (2012) 30 CMS-HIG-12-028, CERN-PH-EP-2012-220, [`arXiv:1207.7235`].

[12] CDF Collaboration, "Observation of top quark production in $\overline{p}p$ collisions with the Collider Detector at Fermilab." *Phys. Rev. Lett.* **74** (1995) 2626.

[13] D. C. Kennedy, "Renormalization of electroweak gauge interactions." in *Theoretical Advanced Study Institute in Elementary Particle Physics (TASI 91): Perspectives in the Standard Model Boulder, Colorado, June 2-28, 1991*, pp. 163–282, 1992.

[14] M. Drewes, "The Phenomenology of Right Handed Neutrinos." *Int. J. Mod. Phys.* **E22** (2013) 1330019, [`arXiv:1303.6912`].

[15] G. C. Branco, P. M. Ferreira, L. Lavoura, M. N. Rebelo, M. Sher, and J. P. Silva, "Theory and phenomenology of two-Higgs-doublet models." *Phys. Rept.* **516** (2012) 1, [`arXiv:1106.0034`].

[16] L. L. Honorez, E. Nezri, J. F. Oliver, and M. H. G. Tytgat, "The Inert Doublet Model: An Archetype for Dark Matter." *J. Cosm. and Astropart. Phys.* **0702** (2007) 028 ULB-TH-06-27, [`hep-ph/0612275`].

[17] CMS Collaboration, "Search for beyond the standard model Higgs bosons decaying into a $\mathrm{b\overline{b}}$ pair in pp collisions at $\sqrt{s} = 13$ TeV." *JHEP* **08** (2018) 113, [`arXiv:1805.12191`].

[18] P. Dirac, "On the theory of quantum mechanics." *Proceedings of The Royal Society A: Mathematical Physical and Engineering Sciences* **112** (1926) 661, [`http://rspa.royalsocietypublishing.org/content/112/762/661.full.pdf`].

[19] A. Zannoni, "On the Quantization of the Monoatomic Ideal Gas." *eprint arXiv:cond-mat/9912229* (1999) [`cond-mat/9912229`].

[20] S. N. Bose, "Planck's law and light quantum hypothesis." *Z. Phys.* **26** (1924) 178–181.

[21] P. J. Mohr, D. B. Newell, and B. N. Taylor, "CODATA Recommended Values of the Fundamental Physical Constants: 2014." *Rev. Mod. Phys.* **88** (2016), no. 3 035009, [`arXiv:1507.07956`].

[22] M. Gell-Mann, "The Eightfold Way: A Theory of strong interaction symmetry." *CTSL-20, TID-12608* (1961).

[23] M. Y. Han and Y. Nambu, "Three Triplet Model with Double SU(3) Symmetry." *Phys. Rev.* **139** (1965) B1006–B1010. [,187(1965)].

[24] E. Fermi, "An attempt of a theory of beta radiation. 1.." *Z. Phys.* **88** (1934) 161–177.

[25] C. S. Wu, E. Ambler, R. W. Hayward, D. D. Hoppes, and R. P. Hudson, "Experimental test of parity conservation in beta decay." *Phys. Rev.* **105** (1957) 1413.

[26] S. L. Glashow, "Partial Symmetries of Weak Interactions." *Nucl. Phys.* **22** (1961) 579–588.

[27] S. Weinberg, "A Model of Leptons." *Phys. Rev. Lett.* **19** (1967) 1264.

[28] J. Goldstone, A. Salam, and S. Weinberg, "Broken Symmetries." *Phys. Rev.* **127** (1962) 965.

[29] N. Cabibbo, "Unitary Symmetry and Leptonic Decays." *Phys. Rev. Lett.* **10** (1963) 531. [,648(1963)].

[30] Particle Data Group Collaboration, M. Tanabashi et al., "Review of particle physics." *Phys. Rev. D* **98** (2018) 030001.

[31] G. 't Hooft, "Renormalizable Lagrangians for Massive Yang-Mills Fields." *Nucl. Phys.* **B35** (1971) 167–188. [,201(1971)].

[32] P. W. Higgs, "Broken Symmetries and the Masses of Gauge Bosons." *Phys. Rev. Lett.* **13** (1964) 508. [,160(1964)].

[33] F. Englert and R. Brout, "Broken Symmetry and the Mass of Gauge Vector Mesons." *Phys. Rev. Lett.* **13** (1964) 321. [,157(1964)].

[34] B. Kors and P. Nath, "Aspects of the Stueckelberg extension." *JHEP* **07** (2005) 069, [`hep-ph/0503208`].

[35] J. Goldstone, A. Salam, and S. Weinberg, "Broken Symmetries." *Phys. Rev.* **127** (1962) 965.

[36] J. Goldstone, "Field Theories with Superconductor Solutions." *Nuovo Cim.* **19** (1961) 154.

[37] ATLAS Collaboration, "Measurement of the Higgs boson mass in the $H \to ZZ^* \to 4\ell$ and $H \to \gamma\gamma$ channels with $\sqrt{s} = 13$ TeV pp collisions using the ATLAS detector." *Phys. Lett.* **B784** (2018) 345–366, [`arXiv:1806.00242`].

[38] CMS Collaboration, "Measurements of Higgs boson properties in the diphoton decay channel in proton-proton collisions at $\sqrt{s} = 13$ TeV." *JHEP* **11** (2018) 185, [`arXiv:1804.02716`].

[39] CMS Collaboration, "Measurements of properties of the Higgs boson decaying into the four-lepton final state in pp collisions at $\sqrt{s} = 13$ TeV." *JHEP* **11** (2017) 047, [`arXiv:1706.09936`].

[40] ATLAS Collaboration, "Evidence for the spin-0 nature of the Higgs boson using ATLAS data." *Phys. Lett. B* **726** (2013) 120 CERN-PH-EP-2013-102, [`arXiv:1307.1432`].

[41] CMS Collaboration, "Constraints on the spin-parity and anomalous HVV couplings of the Higgs boson in proton collisions at 7 and 8 TeV." *Phys. Rev. D* **92** (2015), no. 1 012004 CMS-HIG-14-018, CERN-PH-EP-2014-265, [`arXiv:1411.3441`].

[42] ATLAS Collaboration, "Measurements of the Higgs boson production and decay rates and coupling strengths using pp collision data at $\sqrt{s} = 7$ and 8 TeV in the ATLAS experiment." *Eur. Phys. J. C* **76** (2016), no. 1 6 CERN-PH-EP-2015-125, [`arXiv:1507.04548`].

[43] CMS Collaboration, "Observation of $\mathrm{t\bar{t}H}$ production." *Phys. Rev. Lett.* **120** (2018), no. 23 231801, [`arXiv:1804.02610`].

[44] ATLAS Collaboration, "Observation of Higgs boson production in association with a top quark pair at the LHC with the ATLAS detector." *Phys. Lett. B* **784** (2018) 173, [`arXiv:1806.00425`].

[45] LHC Higgs Cross Section Working Group Collaboration, D. de Florian et al., "Handbook of LHC Higgs Cross Sections: 4. Deciphering the Nature of the Higgs Sector." `arXiv:1610.07922` FERMILAB-FN-1025-T, CERN-2017-002-M, [`arXiv:1610.07922`].

[46] CMS Collaboration, "Combined measurements of Higgs boson couplings in proton–proton collisions at $\sqrt{s} = 13\,\mathrm{TeV}$." *Eur. Phys. J.* **C79** (2019), no. 5 421, [`arXiv:1809.10733`].

[47] ATLAS Collaboration, "Combined measurements of Higgs boson production and decay using up to 80 fb^{-1} of proton-proton collision data at $\sqrt{s} = 13$ TeV collected with the ATLAS experiment." *Phys. Rev.* **D101** (2020), no. 1 012002, [`arXiv:1909.02845`].

[48] ATLAS Collaboration, "Measurement of inclusive and differential cross sections in the $H \to ZZ^* \to 4\ell$ decay channel in pp collisions at $\sqrt{s} = 13$ TeV with the ATLAS detector." *J. High Energy Phys.* **10** (2017) 132 CERN-EP-2017-139, [`arXiv:1708.02810`].

[49] CMS Collaboration, "Observation of the SM scalar boson decaying to a pair of τ leptons with the CMS experiment at the LHC." *Phys. Lett. B* (2017) [`arXiv:1708.00373`].

[50] A. Djouadi, "The Anatomy of electro-weak symmetry breaking. I: The Higgs boson in the standard model." *Phys. Rept.* **457** (2008) 1–216, [hep-ph/0503172].

[51] T. Asaka and K.-i. Hikasa, "Four fermion decay of Higgs bosons." *Phys. Lett.* **B345** (1995) 36–41, [hep-ph/9411297].

[52] CMS Collaboration, "A measurement of the Higgs boson mass in the diphoton decay channel." *Phys. Lett. B* **805** (2020) 135425.

[53] CMS Collaboration, "Observation of the Higgs boson decay to a pair of τ leptons with the CMS detector." *Phys. Lett. B* **779** (2018) 283 CMS-HIG-16-043, CERN-EP-2017-181, [arXiv:1708.00373].

[54] ATLAS Collaboration, "Evidence for the Higgs-boson Yukawa coupling to tau leptons with the ATLAS detector." *JHEP* **04** (2015) 117, [arXiv:1501.04943].

[55] ATLAS Collaboration, "Observation of $H \to b\bar{b}$ decays and VH production with the ATLAS detector." *Phys. Lett.* **B786** (2018) 59–86, [arXiv:1808.08238].

[56] CMS Collaboration, "Observation of Higgs boson decay to bottom quarks." *Phys. Rev. Lett.* **121** (2018), no. 12 121801, [arXiv:1808.08242].

[57] CMS Collaboration, "Search for the Higgs boson decaying to two muons in proton-proton collisions at $\sqrt{s} = 13$ TeV." *Phys. Rev. Lett.* **122** (2019), no. 2 021801, [arXiv:1807.06325].

[58] G. F. Giudice, "Naturally Speaking: The Naturalness Criterion and Physics at the LHC." arXiv:0801.2562.

[59] G. 't Hooft, "Naturalness, chiral symmetry, and spontaneous chiral symmetry breaking." *NATO Sci. Ser. B* **59** (1980) 135 PRINT-80-0083 (UTRECHT).

[60] KATRIN Collaboration, "An improved upper limit on the neutrino mass from a direct kinematic method by KATRIN." *Phys. Rev. Lett.* **123** (2019), no. 22 221802, [arXiv:1909.06048].

[61] H. Nilles, "Supersymmetry, supergravity and particle physics." *Phys. Rep.* **110** (1984), no. 1 1.

[62] S. Coleman and J. Mandula, "All possible symmetries of the s matrix." *Phys. Rev.* **159** (Jul, 1967) 1251–1256.

[63] J. Wess and B. Zumino, "Supergauge Transformations in Four-Dimensions." *Nucl. Phys.* **B70** (1974) 39–50. [,24(1974)].

[64] S. P. Martin, "A Supersymmetry primer." `hep-ph/9709356`. [Adv. Ser. Direct. High Energy Phys.18,1(1998)].

[65] A. B. Lahanas, "LSP as a Candidate for Dark Matter." *Lect. Notes Phys.* **720** (2007) 35–68, [`hep-ph/0607301`].

[66] R. C. Cotta, J. S. Gainer, J. L. Hewett, and T. G. Rizzo, "Dark matter in the MSSM." *New Journal of Physics* **11** (oct, 2009) 105026.

[67] E. Bagnaschi et al., "Benchmark scenarios for low $\tan\beta$ in the MSSM." LHCHXSWG-2015-002.

[68] OPAL, DELPHI, LEP Working Group for Higgs boson searches, ALEPH, L3 Collaboration, "Search for the standard model Higgs boson at LEP." *Phys. Lett. B* **565** (2003) 61 CERN-EP-2003-011, [`hep-ex/0306033`].

[69] CMS Collaboration, "Precise determination of the mass of the Higgs boson and tests of compatibility of its couplings with the standard model predictions using proton collisions at 7 and 8 TeV." *Eur. Phys. J.* **C75** (2015), no. 5 212 CMS-HIG-14-009, CERN-PH-EP-2014-288, [`arXiv:1412.8662`].

[70] CMS Collaboration, "Search for MSSM Higgs bosons decaying to $\mu^+\mu^-$ in proton-proton collisions at $\sqrt{s} = 13$ TeV." *Phys. Lett.* **B798** (2019) 134992, [`arXiv:1907.03152`].

[71] D. Binosi, J. Collins, C. Kaufhold, and L. Theussl, "JaxoDraw: A Graphical user interface for drawing Feynman diagrams. Version 2.0 release notes." *Comput. Phys. Commun.* **180** (2009) 1709 ECT*-08-10, [`arXiv:0811.4113`].

[72] M. Carena, S. Heinemeyer, C. E. M. Wagner, and G. Weiglein, "MSSM Higgs boson searches at the Tevatron and the LHC: Impact of different benchmark scenarios." *Eur. Phys. J.* **C45** (2006) 797 ANL-HEP-PR-05-109, CERN-PH-TH-2005-158, DCPT-05-128, EFI-05-19, FERMILAB-PUB-05-370-T, IPPP-05-64, [`hep-ph/0511023`].

[73] M. Carena, S. Heinemeyer, O. Stål, C. E. M. Wagner, and G. Weiglein, "MSSM Higgs Boson Searches at the LHC: Benchmark Scenarios after the Discovery of a Higgs-like Particle." *Eur. Phys. J.* **C73** (2013), no. 9 2552 ANL-HEP-PR-13-12, EFI-13-2, DESY-13-024, FERMILAB-PUB-13-041-T, [`arXiv:1302.7033`].

[74] H. Bahl, S. Liebler, and T. Stefaniak, "MSSM Higgs benchmark scenarios for Run 2 and beyond: the low $\tan\beta$ region." *Eur. Phys. J.* **C79** (2019), no. 3 279, [`arXiv:1901.05933`].

[75] A. Celis, V. Ilisie, and A. Pich, "LHC constraints on two-Higgs doublet models." *J. High Energy Phys.* **07** (2013) 053 FTUV-13-0217, IFIC-12-89, [`arXiv:1302.4022`].

[76] P. M. Ferreira, R. Santos, M. Sher, and J. P. Silva, "Could the LHC two-photon signal correspond to the heavier scalar in two-Higgs-doublet models?." *Phys. Rev.* **D85** (2012) 035020, [`arXiv:1201.0019`].

[77] DELPHI, OPAL, ALEPH, LEP Working Group for Higgs Boson Searches, L3 Collaboration, S. Schael et al., "Search for neutral MSSM Higgs bosons at LEP." *Eur. Phys. J.* **C47** (2006) 547 CERN-PH-EP-2006-001, [`hep-ex/0602042`].

[78] S. Heinemeyer, W. Hollik, and G. Weiglein, "Constraints on tan Beta in the MSSM from the upper bound on the mass of the lightest Higgs boson." *J. High Energy Phys.* **06** (2000) 9 DESY-99-120, KA-TP-12-1999, [`hep-ph/9909540`].

[79] H. Bahl, E. Fuchs, T. Hahn, S. Heinemeyer, S. Liebler, S. Patel, P. Slavich, T. Stefaniak, C. E. M. Wagner, and G. Weiglein, "MSSM Higgs Boson Searches at the LHC: Benchmark Scenarios for Run 2 and Beyond." `arXiv:1808.07542`.

[80] S. L. Glashow and S. Weinberg, "Natural conservation laws for neutral currents." *Phys. Rev. D* **15** (1977) 1958.

[81] E. A. Paschos, "Diagonal neutral currents." *Phys. Rev. D* **15** (1977) 1966.

[82] H. E. Haber and O. Stål, "New LHC benchmarks for the CP-conserving two-Higgs-doublet model." *Eur. Phys. J.* **C75** (2015), no. 10 491 SCIPP-15-10, [`arXiv:1507.04281`]. [Erratum: Eur. Phys. J.C76,no.6,312(2016)].

[83] R. V. Harlander, S. Liebler, and H. Mantler, "SusHi: A program for the calculation of Higgs production in gluon fusion and bottom-quark annihilation in the Standard Model and the MSSM." *Comput. Phys. Commun.* **184** (2013) 1605 WUB-12-28, LPN12-134, [`arXiv:1212.3249`].

[84] D. Eriksson, J. Rathsman, and O. Stål, "2HDMC: Two-Higgs-Doublet Model Calculator Physics and Manual." *Comput. Phys. Commun.* **181** (2010) 189, [`arXiv:0902.0851`].

[85] A. Buckley, J. Ferrando, S. Lloyd, K. Nordström, B. Page, M. Rüfenacht, M. Schönherr, and G. Watt, "LHAPDF6: parton density access in the LHC precision era." *Eur. Phys. J. C* **75** (2015) 132 GLAS-PPE-2014-05, MCNET-14-29, IPPP-14-111, DCPT-14-222, [`arXiv:1412.7420`].

[86] L. Evans and P. Bryant, "LHC machine." *Journal of Instrumentation* **3** (aug, 2008) S08001–S08001.

[87] DØ Collaboration, "Observation of the top quark." *Phys. Rev. Lett.* **74** (1995) 2632.

[88] CMS Collaboration, "CMS Physics: Technical Design Report Volume 1: Detector Performance and Software." *Technical Design Report CMS* (2006).

[89] CMS Collaboration, "Luminosity: 2017 proton-proton 13 tev collisions." `https://twiki.cern.ch/twiki/bin/view/CMSPublic/LumiPublicResults` Accessed: 2019-09-30.

[90] J. Wenninger, "LHC status and performance." *PoS* **CHARGED2018** (2019) 001.

[91] T. Sjöstrand, S. Mrenna, and P. Z. Skands, "A Brief Introduction to PYTHIA 8.1." *Comput. Phys. Commun.* **178** (2008) 852, [`arXiv:0710.3820`].

[92] CMS Collaboration, "Cms tracking pog performance plots for 2017 with phasei pixel detector." `https://twiki.cern.ch/twiki/bin/view/CMSPublic/TrackingPOGPerformance2017MC#CMS_Tracking_POG_Performance_Plo` Accessed: 2019-09-30.

[93] CMS Collaboration, "Interactive Slice of the CMS detector." CMS-OUTREACH-2016-027.

[94] CMS Collaboration, "The CMS Experiment at the CERN LHC." *JINST* **3** (2008) S08004.

[95] A. Saha, "Phase 1 upgrade of the CMS pixel detector." *Journal of Instrumentation* **12** (feb, 2017) C02033–C02033.

[96] L. Feld, W. Karpinski, K. Klein, M. Lipinski, M. Preuten, M. Rauch, S. Schmitz, and M. Wlochal, "The DC-DC conversion power system of the CMS Phase-1 pixel upgrade." *JINST* **10** (2015), no. 01 C01052.

[97] CMS, "Failure of DCDC modules in the CMS pixel system during the 2017 run - Executive Summary ." `https://project-dcdc.web.cern.ch/project-dcdc/public/Documents/ExecutiveSummary2018.pdf` Accessed: 2019-07-30.

[98] CMS HCAL/ECAL Collaboration, "The CMS Barrel Calorimeter Response to Particle Beams from 2 to 350 GeV/c." Tech. Rep. CMS-NOTE-2008-034, CERN, Geneva, 2008.

[99] P. Adzic et al., "Energy resolution of the barrel of the CMS electromagnetic calorimeter." *J. Instrum.* **2** (2007) P04004 CERN-CMS-NOTE-2006-148.

[100] CMS Collaboration, "HCAL Out Of Time Pileup Subtraction and Energy Reconstruction." tech. rep., May, 2018.

[101] CMS Collaboration, "The CMS muon project: Technical Design Report." *Technical Design Report CMS* (1997).

[102] CMS Collaboration, A. Tapper and D. Acosta, "CMS Technical Design Report for the Level-1 Trigger Upgrade." Tech. Rep. CERN-LHCC-2013-011. CMS-TDR-12, Jun, 2013.

[103] CMS Collaboration, "Level-1 muon trigger performance in 2017 data and comparison with the legacy muon trigger system.".

[104] CMS Collaboration, "Particle-flow reconstruction and global event description with the CMS detector." *J. Instrum.* **12** (2017), no. 10 P10003, [`arXiv:1706.04965`].

[105] P. Billoir and S. Qian, "Simultaneous pattern recognition and track fitting by the Kalman filtering method." *Nucl. Instrum. Methods Phys. Res. A* **294** (1990), no. 1 219.

[106] CMS Collaboration, "CMS Tracking POG Performance Plots For 2017 with PhaseI pixel detector." `https://twiki.cern.ch/twiki/bin/view/CMSPublic/TrackingPOGPerformance2017MC#Vertex_Resolutions` Accessed: 2019-08-09.

[107] K. Rose, "Deterministic annealing for clustering, compression, classification, regression, and related optimization problems." *Proceedings of the IEEE* **86** (1998), no. 11 2210–2239.

[108] W. Waltenberger, "Adaptive vertex reconstruction." Tech. Rep. CERN-CMS-NOTE-2008-034, CERN, Geneva, 2008.

[109] CMS Collaboration, "Performance of the CMS muon detector and muon reconstruction with proton-proton collisions at $\sqrt{s} = 13$ TeV." *JINST* **13** (2018), no. 06 P06015, [`arXiv:1804.04528`].

[110] E. Widl and R. Fruhwirth, "Application of the Kalman alignment algorithm to the CMS tracker." *J. Phys. Conf. Ser.* **219** (2010) 032065.

[111] CMS Collaboration, "Reference muon id, isolation and trigger efficiencies for 2017 data." `https://twiki.cern.ch/twiki/bin/viewauth/CMS/MuonReferenceEffs2017` Accessed: 2019-09-30.

[112] M. Cacciari, G. P. Salam, and G. Soyez, "The Anti-k(t) jet clustering algorithm." *J. High Energy Phys.* **04** (2008) 063 LPTHE-07-03, [`arXiv:0802.1189`].

[113] CMS Collaboration, "Cms jet and missing energy results." `https://twiki.cern.ch/twiki/bin/view/CMSPublic/PhysicsResultsJME` Accessed: 2019-09-30.

[114] CMS Collaboration, "Jet energy resolution and corrections (jerc) subgroup.." https://twiki.cern.ch/twiki/bin/viewauth/CMS/JetEnergyScale Accessed: 2019-09-30.

[115] CMS Collaboration, "Jet energy resolution." https://twiki.cern.ch/twiki/bin/view/CMS/JetResolution Accessed: 2019-09-25.

[116] L3 Collaboration, "Measurement of the branching ratios b $\rightarrow$ eνX, $\mu\nu$X, $\tau\nu$X and νX." *Z. Phys. C* **71** (Apr, 1996) 379–389. 27 p.

[117] CMS Collaboration, "Identification of b-quark jets with the CMS experiment." *J. Instrum.* **8** (2013) P04013 CMS-BTV-12-001, CERN-PH-EP-2012-262, [arXiv:1211.4462].

[118] CMS Collaboration, "Cms b-tagging and vertexing results." https://twiki.cern.ch/twiki/bin/view/CMSPublic/PhysicsResultsBTV Accessed: 2019-09-30.

[119] CMS Collaboration, "Identification of heavy-flavour jets with the CMS detector in pp collisions at 13 TeV." *J. Instrum.* **13** (2018), no. 05 P05011 CMS-BTV-16-002, CERN-EP-2017-326, [arXiv:1712.07158].

[120] M. Stoye, J. Kieseler, H. Qu, L. Gouskos, and M. Verzetti, "Deepjet: Generic physics object based jet multiclass classification for lhc experiments.".

[121] ATLAS Collaboration, "Observation of a new particle in the search for the Standard Model Higgs boson with the ATLAS detector at the LHC." *Phys. Lett. B* **716** (2012) 1 CERN-PH-EP-2012-218, [arXiv:1207.7214].

[122] CMS Collaboration, "Observation of a new boson with mass near 125 GeV in pp collisions at $\sqrt{s} = 7$ and 8 TeV." *J. High Energy Phys.* **06** (2013) 081 CMS-HIG-12-036, CERN-PH-EP-2013-035, [arXiv:1303.4571].

[123] M. Hussain, M. Usman, M. A. Paracha, and M. J. Aslam, "Constraints on Two Higgs Doublet Model Parameters in the light of rare B-Decays." *Phys. Rev.* **D95** (2017), no. 7 075009, [arXiv:1703.10845].

[124] R. Assmann, M. Lamont, and S. Myers, "A brief history of the LEP collider." *Nucl. Phys. Proc. Suppl.* **109B** (2002) 17 CERN-SL-2002-009-OP. [,17(2002)].

[125] S. Holmes, R. S. Moore, and V. Shiltsev, "Overview of the Tevatron Collider Complex: Goals, Operations and Performance." *J. Instrum.* **6** (2011) T08001 FERMILAB-PUB-11-245-AD-APC, [arXiv:1106.0909].

[126] CDF Collaboration, "Search for Higgs Bosons Produced in Association with b-quarks." *Phys.Rev.* **D85** (2012) 032005, [arXiv:1106.4782].

[127] DØ Collaboration, "Search for neutral Higgs bosons in the multi-b-jet topology in 5.2fb^{-1} of $p\bar{p}$ collisions at $\sqrt{s} = 1.96$ TeV." *Phys.Lett.* **B698** (2011) 97–104, [arXiv:1011.1931].

[128] CDF, DØ Collaboration, "Search for Neutral Higgs Bosons in Events with Multiple Bottom Quarks at the Tevatron." *Phys. Rev. D* **86** (2012) 091101 FERMILAB-PUB-12-385-E, [arXiv:1207.2757].

[129] CMS Collaboration, "Search for neutral MSSM Higgs bosons decaying into a pair of bottom quarks." *J. High Energy Phys.* **11** (2015) 071 CMS-HIG-14-017, CERN-PH-EP-2015-133, [arXiv:1506.08329].

[130] CMS Collaboration, "Search for a Higgs boson decaying into a b-quark pair and produced in association with b quarks in proton–proton collisions at 7 TeV." *Phys. Lett. B* **722** (2013) 207 CMS-HIG-12-033, CERN-PH-EP-2012-375, [arXiv:1302.2892].

[131] ATLAS Collaboration, "Search for heavy neutral Higgs bosons produced in association with b-quarks and decaying to b-quarks at $\sqrt{s} = 13$ TeV with the ATLAS detector." arXiv:1907.02749.

[132] R. Harlander, M. Krämer, and M. Schumacher, "Bottom-quark associated Higgs-boson production: reconciling the four- and five-flavour scheme approach." arXiv:1112.3478 CERN-PH-TH-2011-134, FR-PHENO-2011-009, TTK-11-17, WUB-11-04, [arXiv:1112.3478].

[133] CMS Collaboration, "Measurement of the $t\bar{t}$ production cross section using events with one lepton and at least one jet in pp collisions at $\sqrt{s} = 13$ TeV." *JHEP* **09** (2017) 051, [arXiv:1701.06228].

[134] J. Alwall, R. Frederix, S. Frixione, V. Hirschi, F. Maltoni, O. Mattelaer, H. S. Shao, T. Stelzer, P. Torrielli, and M. Zaro, "The automated computation of tree-level and next-to-leading order differential cross sections, and their matching to parton shower simulations." *J. High Energy Phys.* **07** (2014) 079, [arXiv:1405.0301].

[135] P. Connor, "Precision measurement of the inclusive b jet production in proton proton collisions with the CMS experiment at the LHC at $\sqrt{s} = 13\,\mathrm{TeV}$" , Ph.D. thesis, Hamburg U. (2018).

[136] CMS Collaboration, "Jet identification for the 13 tev data run 2017." https://twiki.cern.ch/twiki/bin/viewauth/CMS/JetID13TeVRun2017#Jet_Identification_for_the_13_Te Accessed: 2019-09-30.

[137] CMS Collaboration, "A deep neural network for simultaneous estimation of b jet energy and resolution." arXiv:1912.06046.

[138] CMS Collaboration, "B-jet energy regression at 13 tev." `https://twiki.cern.ch/twiki/bin/view/Main/BJetRegression#DNN_producer_implementation_AN1` Accessed: 2019-09-30.

[139] M. Matsumoto and T. Nishimura, "Mersenne twister: A 623-dimensionally equidistributed uniform pseudo-random number generator." *ACM Trans. Model. Comput. Simul.* **8** (1998), no. 1 3.

[140] Belle Collaboration, "A detailed test of the CsI(Tl) calorimeter for BELLE with photon beams of energy between 20-MeV and 5.4-GeV." *Nucl. Instrum. Meth. A* **441** (2000) 401 KEK-PREPRINT-99-70, BELLE-PREPRINT-99-3, NWU-HEP-99-02, TIT-HPE-99-10.

[141] R. A. Fisher, "On the interpretation of χ^2 from contingency tables, and the calculation of p." *Zenodo* (jan, 1922).

[142] J. E. Gaiser, "Charmonium Spectroscopy From Radiative Decays of the J/ψ and ψ'." *SLAC* (1982).

[143] G. Cowan, K. Cranmer, E. Gross, and O. Vitells, "Asymptotic formulae for likelihood-based tests of new physics." *Eur. Phys. J. C* **71** (2011) 1554, [`arXiv:1007.1727`]. [Erratum: Eur. Phys. J.C73,2501(2013)].

[144] ATLAS Collaboration, CMS Collaboration, LHC Higgs Combination Group Collaboration, "Procedure for the LHC Higgs boson search combination in Summer 2011." Tech. Rep. CMS-NOTE-2011-005. ATL-PHYS-PUB-2011-11, CERN, Geneva, 2011.

[145] L. Moneta, K. Cranmer, G. Schott, and W. Verkerke, "The RooStats project." in *Proceedings of the 13th International Workshop on Advanced Computing and Analysis Techniques in Physics Research. February 22-27, 2010, Jaipur, India. http://acat2010.cern.ch/*, p. 57, 2010. `arXiv:1009.1003`.

[146] A. L. Read, "Presentation of search results: The CL(s) technique." *J. Phys.* **G28** (2002) 2693. [,11(2002)].

[147] F. James, "MINUIT Function Minimization and Error Analysis: Reference Manual Version 94.1." CERN-D-506, CERN-D506.

[148] J. Ocariz, "Probability and Statistics for Particle Physicists." in *Proceedings, 1st Asia-Europe-Pacific School of High-Energy Physics (AEPSHEP): Fukuoka, Japan, October 14-27, 2012*, p. 253, 2014. `arXiv:1405.3402`. [,253(2014)].

[149] S. S. Wilks, "The Large-Sample Distribution of the Likelihood Ratio for Testing Composite Hypotheses." *Annals Math. Statist.* **9** (1938), no. 1 60.

[150] CMS Collaboration, C. Collaboration, "CMS luminosity measurement for the 2017 data-taking period at $\sqrt{s} = 13$ TeV.".

[151] LHC Higgs Cross Section Working Group Collaboration, "LHC Higgs Cross Section Working Group." `https://twiki.cern.ch/twiki/bin/view/LHCPhysics/LHCHXSWG` Accessed: 2019-10-02.

[152] S. Dittmaier, M. Krämer, and M. Spira, "Higgs radiation off bottom quarks at the Tevatron and the CERN LHC." *Phys. Rev. D* **70** (2004) 074010 EDINBURGH-2003-13, MPP-2003-49, PSI-PR-03-14, [`hep-ph/0309204`].

[153] S. Dawson, C. B. Jackson, L. Reina, and D. Wackeroth, "Exclusive Higgs boson production with bottom quarks at hadron colliders." *Phys. Rev. D* **69** (2004) 074027 BNL-HET-03-17, FSU-HEP-2003-1015, UB-HET-03-05, [`hep-ph/0311067`].

[154] R. V. Harlander and W. B. Kilgore, "Higgs boson production in bottom quark fusion at next-to-next-to leading order." *Phys. Rev. D* **68** (2003) 013001 BNL-HET-03-4, CERN-TH-2003-067, [`hep-ph/0304035`].

[155] A. Djouadi, J. Kalinowski, and M. Spira, "HDECAY: A Program for Higgs boson decays in the standard model and its supersymmetric extension." *Comput. Phys. Commun.* **108** (1998) 56 DESY-97-079, IFT-96-29, PM-97-04, [`hep-ph/9704448`].

[156] A. Djouadi, M. M. Mühlleitner, and M. Spira, "Decays of supersymmetric particles: The Program SUSY-HIT." *Acta Phys. Polon. B* **38** (2007) 635 CERN-PH-TH-2006-200, [`hep-ph/0609292`].

[157] G. Degrassi, S. Heinemeyer, W. Hollik, P. Slavich, and G. Weiglein, "Towards high-precision predictions for the MSSM Higgs sector." *Eur. Phys. J. C* **28** (2003) 133 DCPT-02-126, IPPP-02-63, LMU-11-02, MPI-PHT-2002-73, RM3-TH-02-19, [`hep-ph/0212020`].

[158] M. Frank, T. Hahn, S. Heinemeyer, W. Hollik, H. Rzehak, and G. Weiglein, "The Higgs boson masses and mixings of the complex MSSM in the Feynman-diagrammatic approach." *J. High Energy Phys.* **02** (2007) 047 DCPT-06-160, IPPP-06-80, MPP-2006-158, PSI-PR-06-14, [`hep-ph/0611326`].

[159] S. Heinemeyer, W. Hollik, and G. Weiglein, "FeynHiggs: A program for the calculation of the masses of the neutral CP even Higgs bosons in the MSSM." *Comput. Phys. Commun.* **124** (2000) 76 KA-TP-16-1998, DESY-98-193, CERN-TH-98-389, [`hep-ph/9812320`].

[160] S. Heinemeyer, W. Hollik, and G. Weiglein, "The Masses of the neutral CP - even Higgs bosons in the MSSM: Accurate analysis at the two loop level." *Eur. Phys. J. C* **9** (1999) 343 KA-TP-17-1998, DESY-98-194, CERN-TH-98-405, [`hep-ph/9812472`].

[161] CMS Collaboration, “Search for a heavy pseudoscalar boson decaying to a Z and a Higgs boson at $\sqrt{s}$ = 13 TeV.” *Eur. Phys. J.* **C79** (2019), no. 7 564, [`arXiv:1903.00941`].

[162] C. Richardson, “CMS high level trigger timing measurements.” *Journal of Physics: Conference Series* **664** (dec, 2015) 082045.

[163] CMS Collaboration, “The FastTimerService.” `https://twiki.cern.ch/twiki/bin/viewauth/CMS/FastTimerService` Accessed : 2019-09-30.

[164] A. Vagnerini, “Searches for BSM (neutral) Higgs bosons in fermionic decays in CMS.” *PoS* **CHARGED2018** (2019) 011.

Acknowledgements

During my doctoral studies, I have had the honour to collaborate with several remarkable people, whom I have learnt to appreciate for their intellectual and moral stature.
Firstly, I would like to thank wholeheartedly my supervisor Dr. Roberval Walsh. His invaluable guidance and immense knowledge of the field has been an essential condition for the successful completion of this doctorate. His technical comments and wise mentoring have proven priceless throughout my time as a doctoral student at DESY in several, diverse areas. I have had the pleasure to be under his supervision already as a summer student, and back then I was already impressed by his meticulous dedication and passion for physics. I am extremely grateful for his inspirational, daily guidance throughout my scientific work, as well as his great care in proof-reading this thesis.
This doctoral thesis would have not been possible without the limitless support of my co-supervisor Prof. Dr. Elisabetta Gallo, to whom I would like to express my deepest gratitude for granting me the opportunity for this PhD project. It is extremely difficult to condense in a few words my admiration for her profile as a researcher, as she exemplifies all the ideal qualities that any group leader should treasure. I am absolutely stunned by her exceptional scientific knowledge, as well as her incredible positive listening attitude and patience. I am very pleased to thank the coordinator of our CMS Higgs working group Dr. Rainer Mankel. He has been an endless source of insightful comments and has provided many suggestions on how to improve substantially the project strategy and refine the presentation of the results.
A very special gratitude goes to my dear Ukrainian colleague Dr. Rostyslav Shevchenko for his pioneering work in searches for neutral Higgs bosons with multiple bottom quarks in the final state, which has laid the foundations for my PhD project. I would also like to mention the precious contribution of Dr. Chayanit Asawatangtrakuldee and Dr. Gregor Mittag to the development of the analysis framework, and of Dr. Alexei Raspereza for his guidance through the bias studies. I am also eternally grateful to my co-worker and friend Paul Asmuss for his valuable support in delivering in a timely manner the model-dependent interpretation of the results, and to Andrea Cardini for his great supply of Tuscan delicacies needed for the proof-reading. My sincere gratitude goes to Dr. Patrick L.S. Connor for the opportunity to work in an interesting project involving the development of a new dedicated trigger for the Alignment group. I remember vividly our endless discussions in French about *le taux du déclencheur de haut niveau*, or perhaps more succinctly, the HLT rate. It is impossible to provide an exhaustive list of all my friends from DESY and other research institutes who played a major role in my personal well-being, but I will give it a try anyways. In sparse order, I would like to thank Ilya, Sam, Valeria, Olena, Fang-Ying, Asya, Daniel, David, Nikita, Andrej, Matteo, Aliya, Leonid, Merijn, Yiwen. A special thought goes to Jyhun, a candid soul to whom the secrets of the universe have prematurely disclosed. *Dulcis in fundo*, I owe a very important debt of gratitude to my family for their unconditional love and to my heart-warming friends from my hometown Buch, Babba, Cast, Robby, Friz and Carlo, as well as my university friends Pier, Nadia, Carlotta, Piotrek, Lydia, Joned and many others for their support. I would also like to thank my life-companion for always being present in my heart.